Structure, Function, and Neutralization of SARS-CoV-2 Spike Glycoproteins

by

Dhiraj Mannar

B.Sc., University of British Columbia, 2019

A DISSERTATION SUBMITTED IN PARTIAL FULFILLMENT OF THE

REQUIREMENTS FOR THE DEGREE OF

DOCTOR OF PHILOSOPHY

in

THE FACULTY OF GRADUATE AND POSTDOCTORAL STUDIES

(Biochemistry and Molecular Biology)

THE UNIVERSITY OF BRITISH COLUMBIA

(Vancouver)

June 2023

The following individuals certify that they have read, and recommend to the Faculty of Graduate and Postdoctoral Studies for acceptance, the dissertation entitled:

Structure, Function, and Neutralization of SARS-CoV-2 Spike Glycoproteins

submitted by Dhiraj Mannar

in partial fulfillment of the requirements for the degree of Doctor of Philosophy

in Biochemistry and Molecular Biology

Examining Committee:
Dr. Sriram Subramaniam, Professor, Biochemistry and Molecular Biology, UBC
Supervisor

Dr. Calvin K. Yip, Associate Professor, Biochemistry and Molecular Biology, UBC
Supervisory Committee Member

Dr. Theodore Steiner, Professor, Department of Medicine, UBC
Supervisory Committee Member

Dr. Robert Hancock, Professor, Microbiology and Immunology, UBC
University Examiner

Dr. Robert Molday, Professor, Biochemistry and Molecular Biology, UBC
University Examiner

Dr. Joanne Lemieux, Professor, Biochemistry, University of Alberta
External Examiner

Additional Supervisory Committee Members:

Torsten Nielsen, Professor, Pathology & Laboratory Medicine, UBC
Supervisory Committee Member

Abstract

The COVID-19 pandemic erupted in 2019 and went on to have devastating impacts on global health and economies. The causative agent of COVID-19 is a novel coronavirus known as severe acute respiratory syndrome coronavirus 2 (SARS-CoV-2), which was found to cause respiratory illness in humans, with symptoms ranging from mild to life threatening (pneumonia, multi-system organ failure). Like previous disease-causing coronaviruses, SARS-CoV-2 relies on a spike glycoprotein to recognize and infect human cells; and antibodies that target the spike protein can prevent viral entry from occurring, effectively neutralizing the virus. However, viruses possess the ability to evolve, and previous experience with other coronaviruses has set the precedence for spike proteins evolving altered antigenic properties and epitopes, permitting escape from neutralizing antibodies. This thesis represents efforts to respond to the COVID-19 pandemic in real time, as we sought to first define the antigenic properties and vulnerabilities of the SARS-CoV-2 spike protein, and then proceed to characterize emerging spike protein mutations and variants, with an emphasis on spike protein structure, receptor binding, and antibody neutralization. We identified antigenic and vulnerable regions in the spike protein amino terminal domain and receptor binding domain and describe heterogenous ways in which antibodies can bind epitopes within these regions. Over the course of the pandemic, significant mutational drift was observed within these regions. We found that mutations within the receptor binding domain were modular in nature, and when combined to represent variant strains of SARS-CoV-2, served to simultaneously prevent recognition of neutralizing antibodies, and enhance or preserve receptor binding affinity. Analysis of variant spike proteins showed that there was high architectural conservation across most variants, with one glaring exception revealing a novel dimers-of-trimers assembly. All variant spike proteins were antibody evasive, with some exhibiting concerning escape from immunized

and convalescent sera. Structural analyses on the amino terminal and receptor binding domains of these variants revealed mutational mechanisms underpinning antigenic drift and rationalizing antibody escape. Finally, we structurally defined an epitope on the spike protein that enables broad neutralization of several variants, offering hope for the development of broadly effective therapies to combat variants of SARS-CoV-2.

Lay Summary

The COVID-19 pandemic has had devastating effects on health, economies, and society. The emergence of SARS-CoV-2 variants poses a threat to vaccines and therapeutic antibodies which showed initial efficacy. These variants, called "Variants of Concern" or "Variants of Interest," show increased infectivity and resistance to antibodies. New variants are continually emerging, and viral evolution is ongoing. The spike protein in SARS-CoV-2 variants plays a crucial role in infecting human cells and is targeted by antibodies and vaccines. Spike mutations can enhance viral infectivity by altering the spike's structure and making it harder for the immune system to recognize and neutralize. This research aims to understand how antibodies recognize the spike protein, assess the impact of mutations on spike structure and receptor binding, and identify vulnerabilities common to all variant spikes. Structural knowledge of variant spikes is crucial for updating vaccines and designing therapies that can effectively target emerging SARS-CoV-2 variants.

Preface

All serum samples were collected and used for the studies presented in this thesis under the following UBC ethics oversights and approvals:

BCCDC Samples: Patient derived sera samples were collected according to the CARE COVID Study (http://www.bccdc.ca/health-professionals/clinical-resources/covid-19-care/covid-19-serology-care-covid-study) with ethics approval from the UBC Clinical Research Ethics Board.

COVID-19 Immunity Study Samples were collected by Dr. Ted Steiner, with UBC ethic approval, certificate number: H20-00966.

Unless otherwise specified, this work was conducted at the Centre for Brain Health at the University of British Columbia, Vancouver Campus in Prof. Sriram Subramaniam's Lab (Department of Biochemistry, University of British Columbia [UBC], British Columbia [BC] Canada).

Chapter 2: Most of this work is published, except for the polyclonal Fab-spike complex structural work of which I performed in entirety except for microscopy which was performed by Dr. Alison Bezeruk. This portion is the focus of a manuscript in preparation. Below are the publications from which the data in this chapter were taken (# denotes equal contribution):

Mannar, D., Leopold, K. & Subramaniam, S. Glycan reactive anti-HIV-1 antibodies bind the SARS-CoV-2 spike protein but do not block viral entry. Scientific Reports, 11(1), 1-9 (2021). – Dr. Karoline Leopold and myself performed protein purification. I performed all other experiments with technical help from Steven Zhou.

Li, W., Schäfer, A., Kulkarni, S.S., Liu, X., Martinez, D.R., Chen, C., Sun, Z., Leist, S.R., Drelich, A., Zhang, L., Ura, M.L., Berezuk, A., Chittori, S., Leopold, K., **Mannar D**., Srivastava, S.S., Zhu, X., Peterson, E.C., Tseng, C.-T., Mellors, J.W., Falzarano, D., Subramaniam, S., Baric, R.S., Dimitrov, D.S., High potency of a bivalent human VH domain in SARS-CoV-2 animal models, Cell, 183(2), 429-441 (2020). - Myself, Dr. Karoline Leopold, and Dr. Shanti Srivastava performed protein purification and negative stain experiments. Microscopy was performed by Dr. Alison Bezeruk, and electron microscopy data processing was performed by Dr. Xing Zhu. Structural interpretation was performed collectively.

Dhiraj Mannar#, James W Saville#, Zehua Sun#, Xing Zhu, Michelle M Marti, Shanti S Srivastava, Alison M Berezuk, Steven Zhou, Katharine Tuttle, Michele D Sobolewski, Andrew Kim, Benjamin R Treat, Priscila Mayrelle Da Silva Castanha, Jana L Jacobs, Simon M Barratt-Boyes, John W Mellors, Dimitrov S Dimiter, Wei Li, Sriram Subramaniam. SARS-CoV-2 variants of concern: spike protein mutational analysis and epitope for broad neutralization. Nat Communications, 13(1), 4696 (2022). -Myself, James Saville, and Seven Zhou performed all molecular cloning and protein purification. Myself and James Saville performed the ELISA experiments. I performed the neutralization experiments and the interpretation.

Chapter 3: This work was published in 2 manuscripts:

Zhu X#, **Mannar D#**, Srivastava SS#, Berezuk AM#, Demers JP, Saville JW, Leopold K, Li W, Dimitrov DS, Tuttle KS, Zhou S, Chittori S, Subramaniam S. Cryo-electron microscopy structures of the N501Y SARS-CoV-2 spike protein in complex with ACE2 and 2 potent neutralizing antibodies. PLoS Biol. 19(4):e3001237, 2021. – Cloning, protein purification, and biochemical

assays were performed by myself, James Saville, Dr. Karoline Leopold and Steven Zhou. ELISA experiments were performed by myself and James Saville. Microscopy was performed by Dr. Alison Bezeruk, Dr. Sagar Chittori, and Dr Jean-Phillipe Demers. Kathrine Tuttle performed grid vitrification. Electron-microscopy data processing was performed by Dr. Xing Zhu. Structural interpretation was performed collectively. Biolayer interferometry was performed at the University of Pittsburgh by the group of Dr. Dimitrov.

Mannar, D#., Saville, J#., Zhu, X., Srivastava, S., Berezuk, A., Zhou, S., Tuttle, K., Ki,, A., Li, W., Dimitrov, D., Subramaniam, S. Structural Analysis of Receptor Binding Domain Mutations in SARS-CoV-2 Variants of Concern That Modulate ACE2 and Antibody Binding. Cell Reports, 37(12), 110156, 2021. – Myself, James Saville, and Steven Zhou performed cloning and protein purification. Myself and James Saville performed ELISA binding assays. Microscopy was performed by Dr. Alison Bezeruk. Kathrine Tuttle performed grid vitrification. Cryo-EM data processing was performed by Dr. Xing Zhu. Structural interpretation was performed by myself, James Saville, and Drs. Xing Zhou, Shanti Srivastava and Sriram Subramaniam. Biolayer interferometry was performed at the University of Pittsburgh by the group of Dr. Dimitrov.

Chapter 4: This work was published across 4 manuscripts with the exception of the BA.2 variant neutralization data, which was performed by myself and James Saville, and the mouse ACE2 ELISA experiment which was performed by Dr. Faezeh Vahdatihassani and myself.

Saville, J#., **Mannar, D#.,** Zhu, X., Srivastava, S., Berezuk, Demers, JP., A., Zhou, S., Tuttle, K., Sekirov, I., Ki., A., Li, W., Dimitrov, D., Subramaniam, S. Structural and Biochemical Rationale for Enhanced Spike Protein Fitness in Delta and Kappa SARS-CoV-2 Variants. Nature Communications 13(1), 742, (2022). - Myself, James Saville, and Seven Zhou performed all

molecular cloning and protein purification. Myself and James Saville performed the antibody binding (ELISA) and neutralization experiments. Microscopy was performed by Dr. Alison Bezeruk and Dr. Jean-Phillip Demers. Kathrine Tuttle performed grid vitrification. Electron microscopy data processing was performed by Dr. Xing Zhu. Structural interpretation was performed by myself, James Saville, and Drs. Xing Zhou, Shanti Srivastava and Sriram Subramaniam. Biolayer interferometry was performed at the University of Pittsburgh by the group of Dr. Dimitrov.

Dhiraj Mannar#, James W Saville#, Zehua Sun#, Xing Zhu, Michelle M Marti, Shanti S Srivastava, Alison M Berezuk, Steven Zhou, Katharine Tuttle, Michele D Sobolewski, Andrew Kim, Benjamin R Treat, Priscila Mayrelle Da Silva Castanha, Jana L Jacobs, Simon M Barratt-Boyes, John W Mellors, Dimitrov S Dimiter, Wei Li, Sriram Subramaniam. SARS-CoV-2 variants of concern: spike protein mutational analysis and epitope for broad neutralization. Nat Communications, 13(1), 4696, (2022). -Myself, James Saville, and Steven Zhou performed all molecular cloning and protein purification. Myself and James Saville performed the antibody binding (ELISA) and neutralization experiments. Microscopy was performed by Dr. Alison Bezeruk. Kathrine Tuttle performed grid vitrification. Cryo-EM data processing was performed by Dr. Xing Zhu. Structural interpretation was performed by myself, James Saville, and Drs. Xing Zhou, Shanti Srivastava and Sriram Subramaniam. Biolayer interferometry was performed at the University of Pittsburgh by the group of Dr. Dimitrov. Live virus neutralization assays were performed at the University of Pittsburgh by members of the Barrat-Boyles and Mellors labs.

Mannar, D#., Saville, J#., Zhu, X., Srivastava, S., Berezuk, A., Tuttle, K., Ki, Marquez, C, A., Sekirov, I., Subramaniam, S., SARS-CoV-2 Omicron variant: Antibody evasion and cryo-EM structure of spike protein–ACE2 complex. Science, 375(6582), 760-764, (2022). Myself and

James Saville performed all experiments including protein purification. Microscopy was performed by Dr. Alison Bezeruk. Kathrine Tuttle performed grid vitrification. Cryo-EM data processing was performed by Dr. Xing Zhu. Structural interpretation was performed by myself, James Saville, and Drs. Xing Zhou, Shanti Srivastava and Sriram Subramaniam.

James W. Saville#, **Dhiraj Mannar#,** Xing Zhu, Alison Berezuk, Spencer Cholak, Katherine Tuttle, Faezeh Vahdatihassani, Sriram Subramaniam. Structural Analysis of Receptor Engagement and Antigenic Shift within the BA.2 Spike Protein. Cell Reports, 42(1), 111964, 2023. – Myself and James Saville conducted all experiments including protein purification and cloning. I optimized protocols for constructing antigen specific columns and performed the domain specific polyclonal antibody binding ELISA studies. Dr. Faezeh Vahdatihassani and Spencer Cholak assisted with mouse ACE2 and monoclonal antibody ELISA experiments. Microscopy was performed by Dr. Alison Bezeruk. Kathrine Tuttle performed grid vitrification. Cryo-EM data processing was performed by Dr. Xing Zhu. Structural interpretation was performed by myself, James Saville, and Drs. Xing Zhou, and Sriram Subramaniam.

Table of Contents

List of Tables

List of Figures

List of Abbreviations

2D	Two Dimensional
3D	Three Dimensional
ab	Antibody
ANOVA	Analysis of Variance
AUC	Area Under the Curve
BLI	Biolayer Interferometry
CDC	Center for Disease Control
CoV	Coronavirus
Cryo-EM	Cryo-electron Microscopy
CTF	Contrast Transfer Function
CV	Column Volume
DNA	Deoxynucleic Acid
EC50	Effective Concentration to achieve 50% Response
EDTA	Ethylenediaminetetraacetic acid.
EER	Electron Event Registration
ELISA	Enzyme-linked Immunosorbent Assay
EMDB	Electron Microscopy Data Base
Fab	Fragment Antigen-Binding region
Fc	Fragment Crystallizable region
GF	Gel Filtration
GISAID	Global Initiative on Sharing all Influenza Data
hACE2	Human Angiotensin Converting Enzyme 2

HEK293	Human Embryonic Kidney Cell Line
HIV	Human Immunodeficiency Virus
IgA	Immunoglobulin A
IgG	Immunoglobulin G
IgM	Immunoglobulin M
K_D	Dissociation Constant
$K_{D,app}$	Apparent Dissociation Constant
kV	Kilovolt
mAb	Monoclonal Antibody
mACE2	mouse Angiotensin Converting Enzyme 2
MERS-CoV	Middle Eastern Respiratory Syndrome Coronavirus
NTD	Amino Terminal Domain
OD	Optical Density
pAb	Polyclonal Antibody
PBS	Phosphate Buffered Saline
PDB	Protein Data Bank
RBD	Receptor Binding Domain
SARS-CoV	Severe Acute Respiratory Syndrome Coronavirus
SARS-CoV-2	Severe Acute Respiratory Syndrome Coronavirus 2
SEC	Size Exclusion Chromatography
SPR	Surface Plasmon Resonance
TBS	Tris Buffered Saline
TEM	Transmission Electron Microscope

TMPRSS2	Transmembrane serine protease 2
VH	Variable heavy chain
VL	Variable light chain
VoC	Variant of Concern
VoI	Variant of Interest
WHO	World Health Organization
WT	Wild-Type

Acknowledgements

I want to thank everyone at the Subramaniam lab for their intense efforts on this project. Without the collective expertise of the excellent graduate students, post doctoral researchers, technicians, and staff in the Subramaniam lab, this thesis would not be possible. Dr. Xing Zhu is one of the worlds top experts in Cryo-EM data processing and I wish to thank him very much for working with us on these projects, and his readiness to teach and share his knowledge and his expertise was truly invaluable. Dr. Alison Berezuk is an expert microscopist and biochemist who facilitated much of this work – thank you Alison for translating your knowledge of both biochemistry and microscopy into meaningful feedback as we strove to collect top notch datasets. Kate Tuttle, thank you so much for your attention to detail and meticulous help in generating Cryo-EM grids. Drs Karoline Leopold and Shanti Srivastava have extensive experience in protein biochemistry, and I want to thank you both for sharing your knowledge and your amazing work on these projects. I really enjoyed our many hours spent interpreting results, planning exciting experiments, and just having fun! Dr. Faezeh Vahdatihassani, thank you for bringing your skills in molecular biology and knowledge in pharmacology to this work – it was a pleasure to work with you (and thank you for putting up with some of my infamous lab messes). Susan Hooper – thank you for your unending work in scheduling meetings, placing orders (and fiercely following up with vendors when they stall on delivery), and overall efforts to keep us organized. Spencer Cholak, thank you for always bringing such a positive attitude to the lab, I will miss our many deep dives into various scientific concepts, lively discussions with James and others, runs, and data processing “parties”. James Saville, thank you so much for leveraging your talent and experience in protein biochemistry to kickstart this work. From our late nights in the lab endlessly purifying proteins and pipetting into 384 well plates, to our almost nightly phone

calls, and exciting experimental planning sessions, it has been a pleasure, and I am very lucky to have been able to work so closely with you. I would also like to thank my supervisor Dr. Sriram Subramanian for the opportunity to join the lab and work with the amazing, talented, and friendly team he assembled and leads. Thank you for your patience, and always keeping me on track and focused (and allowing me my multiple research tangents along the way).

My time working with you all has taught me the true meaning of teamwork and collaboration. You have taught me that it is together that we do amazing things, and I will embrace the power of interdisciplinary collaboration modelled by you all in my future endeavours.

I would also like to thank my friends, parents, sisters, and in-laws for their unending support and love. Thank you all for putting up with my many scientific monologues at family dinners and social events.

Finally, I want to thank my amazing wife Jenna for her incredible love and patience through the late nights, missed dinners, and cancelled vacations. Your support means the world.

Chapter 1: Introduction

1.1 Viruses and Respiratory Infections

Viruses have existed for billions of years and have evolved to be able to infect organisms from all areas of life[1]. There are an estimated 10^{31} virus particles on earth[2], belonging to numerous viral taxa, many of which have yet to be discovered. A staggering amount of these viruses (an estimated 320,000 kinds) are thought to infect mammals[3], and around 270 are known to infect humans[4]. Since the discovery of viruses, humanity has devoted significant resources and efforts to understanding and combating disease causing viruses, which enact pathogenic effects through a variety of mechanisms. Of these viruses, a select group are known to cause respiratory infections via infection of the lung and other areas of the respiratory tract[5] (Table 1.1.). Respiratory viruses are known to cause the common cold – a self-limiting viral illness of the upper respiratory tract, along with more acute and severe viral infections of the lower respiratory tract and lung parenchyma, leading to pneumonia. Epidemiological studies from the 20th century suggested respiratory infections to be the leading cause of common illnesses in humans of all ages across the world[6]. Thus, the study and prevention of respiratory viruses has been a key area of investigation for centuries, with relevance to both basic and clinical sciences.

Table 1.1. Viruses that infect the respiratory system.

Virus	Genome Type	Genome Size
Rhinovirus	Single-stranded RNA, positive sense	~7.2 kilobases
Coronavirus	Single-stranded RNA, positive sense	~30 kilobases
Respiratory syncytial virus	Single-stranded RNA, negative sense	~15 kilobases
Metapneumovirus	Single-stranded RNA, negative sense	~13 kilobases
Adenovirus	Double-stranded DNA	~26-45 kilobases
Influenza	Single-stranded RNA, negative sense	~13.5 kilobases
Parainfluenza	Single-stranded RNA, negative sense	~16 kilobases
Bocavirus	Single-stranded DNA, negative sense	~5.5 kilobases
Enterovirus	Single-stranded RNA, positive sense	~7.5 kilobases
Cytomegalovirus	Double-stranded DNA	~235 kilobases
Varicella-zoster virus	Double-stranded DNA	~125 kilobases

1.2 Coronaviruses and Zoonotic Potential

Coronaviruses are a group of viruses that belong to the family *Coronaviridae*, and are large, enveloped viruses with a positive sense single stranded RNA genome. Four seasonal endemic coronaviruses are responsible for causing an estimated 10-30% of common colds in humans[7] (Table 1.2.), and importantly several coronaviruses are known to circulate in animal reservoirs with high zoonotic transmission potential. Devastating examples of coronaviral zoonotic events have been observed in history, with the 2003 severe acute respiratory syndrome coronavirus (SARS-CoV) pandemic achieving zoonotic transmission from a horseshoe bat reservoir[8], and the Middle East respiratory syndrome coronavirus (MERS) which achieved zoonotic transmission from dromedary camel reservoirs[9] and spread to 27 countries since its discovery in 2012. SARS-CoV and MERS cause a range of clinical symptoms including life threatening viral pneumonia and respiratory failure.

Table 1.2. Coronaviruses circulating in humans.

Coronavirus name	Genus	Endemic/Epidemic
NL63	Alphacoronavirus	Endemic
229E	Alphacoronavirus	Endemic
OC43	Betacoronavirus	Endemic
HKU1	Betacoronavirus	Endemic
SARS-CoV	Betacoronavirus	Epidemic
MERS-CoV	Betacoronavirus	Epidemic
SARS-CoV-2	Betacoronavirus	Epidemic

1.3 The Coronavirus Replication Cycle and Viral Infection Process

Coronaviruses infect humans through direct entry of the respiratory tract via aerosols and droplets, or direct contact with virions and subsequent exposure to the respiratory tract[10]. It is generally accepted that there exists a viral load threshold upon which exposure will lead to productive infection and symptoms. Infection requires exposure to permissive cells and subsequent viral replication. Coronavirus particles are enveloped and spherical with a range of 118-140 nm in size[11]. These particles are covered by spike proteins which protrude out 16-21 nm from the viral envelope and appear as a "crown" or "corona" in Latin, endowing them their name. These spike proteins are responsible for orchestrating the first step of the coronavirus replication cycle, which involves host cell recognition and subsequent fusion of host and viral membranes[12]. Upon entry of the viral genome into the host cell cytoplasm, viral gene expression occurs via hijacking of host cell ribosomes, with the central goal of generating the machinery to replicate the viral RNA genome and synthesize the structural proteins required to form new virions and package full-length genomes within these virions prior to viral egress. The viral proteins required for genome replication are referred to as the "non-structural proteins" (Nsp's), and found within the first two thirds of the 5' end of the viral genome, within two large open reading frames named ORF1a and ORF1b[13], while the proteins required for virion assembly and packaging are referred to as the

"structural proteins" and are found within the last third of the genome, along with the "accessory proteins" which are thought to play a role in diminishing antiviral responses[13]. Correct production of the non-structural viral proteins involves translational regulation through a ribosomal frameshift process which generates the polypeptide fragments pp1a and pp1ab from ORF1a and ORF1b respectively[13–16]. Specifically, there is a programed -1 ribosomal frameshift at the overlap between the boundary of these fragments. Once ORF1a and ORF1b have been translated, pp1a and pp1ab are post translationally modified by proteolytic cleavage via viral cysteine proteases into functional non-structural proteins[13,17–19]. Replication of the viral genome is mediated by the viral replication/transcription complex (RTC), which is comprised of non-structural proteins Nsp2-16 and harbours the critical RNA dependent RNA polymerase (RdRP) encoded by Nsp12[13,20,21]. Transcription of the positive sense viral genome yields negative sense genomic strands which are then utilized for production of positive sense genomes for viral packaging. Transcription of the viral genome also occurs in a discontinuous manner, resulting in shorter negative sense segments known as "subgenomic RNA" (sgRNA)[13,22,23]. The mechanism of discontinuous transcription involves interruption of transcription upon the RTC encountering a "transcription regulatory sequence" (TRS) which are upstream of most open coding reading frames in the 3' most third of the viral genome. Upon interruption of transcription, synthesis of the negative strand RNA is re-initiated at a leader sequence located at the 5' end of the viral genome, yielding a set of chimeric negative sense RNA segments. These segments can again be transcribed into positive sense "subgenomic messenger RNA" (sgmRNA), which are then translated to produce the structural and accessory proteins encoded in the viral genome[13,22,23]. The structural proteins are comprised of the nucleocapsid (N), envelope (E), membrane (M), and spike (S) proteins which are all embedded within the viral membrane. The M,N, and E proteins are involved in biogenesis of viral particles

within the endoplasmic reticulum (ER) to Golgi compartments[13,24–26]. Specifically, the N protein binds viral genomic RNA, promoting the packaging of the viral genome within viral particles[11,27,28]. The M protein functions in inducing viral particle formation and is the most abundant structural protein in the viral membrane[11,29,30], and the E protein is comparatively scarce within the viral envelope and may act as ion channels of unknown importance[11,31]. Fully formed viral particles are thought to be released from infected cells via exocytosis[13,32–34].

As mentioned above, coronaviruses rely on their spike proteins to enable the critical step of host cell recognition and entry, without which viral infection and replication cannot proceed. Coronavirus spike proteins belong to the family of homotrimeric class I fusion glycoproteins and are comprised of two general functional regions known as S1 and S2[13,31]. The S1 region is the surface accessible portion and is responsible for recognizing host receptors, while the S2 region contains the machinery required for host and viral membrane fusion to occur. Coronaviruses recognize several different host receptors (Table 1.3.) and share low sequence conservation within the S1 region. In contrast, the S2 region plays a role independent of cell recognition and is therefore highly conserved across coronaviruses[11]. A feature of most coronaviral spike proteins is that they must be proteolytically processed to allow dissociation of the S1 and S2 regions as a prerequisite for membrane fusion, wherein the S2 region undergoes a dramatic conformational change. The cleavage sites and host cell proteases responsible for this event vary across coronavirus spike proteins[11], thus the host cell receptor and protease combinations utilized by coronaviruses likely have effects at the level of cellular tropism.

Table 1.3 Receptors recognized by various human infecting coronaviruses.

Coronavirus name	Receptor
229E	Aminopeptidase N
NL63	Angiotensin Converting Enzyme 2
SARS-CoV	Angiotensin Converting Enzyme 2
OC43	Sialic acid units
HKU1	Sialic acid units
MERS-CoV	Dipeptidyl peptidase 4
SARS-CoV-2	Angiotensin Converting Enzyme 2

1.4 Adaptive Immune Responses to Coronaviruses

Significant efforts to understand how the immune system responds to coronavirus infection have been made since the emergence of the highly pathogenic coronaviruses SARS-CoV and MERS-CoV. While the innate immune system recognizes universal pathogen-associated molecular patterns (PAMPs) - which are not unique to coronaviruses - the adaptive immune system performs tailored responses against specific coronaviral antigens[35]. Studies have determined a role for cellular immunity in limiting but not preventing SARS-CoV and MERS-CoV infection[35]. The structural proteins (S, M, E and N) are the main antigens recognized by both CD4 and CD8 T cell responses, with the majority of reactivity seen against the spike (S) protein[35]. These cellular responses against coronavirus structural proteins are long lived and persistent[35]. Exposure to MERS-CoV and SARS-CoV have been shown to elicit neutralizing antibody responses which target the spike protein, highlighting the spike protein as a dominant antigen for effective viral neutralization[36,37]. Neutralizing antibodies against MERS-CoV and SARS-CoV spike proteins have been shown to be effective in protecting against lethal challenge using mouse models, demonstrating the vulnerability of spike proteins during coronavirus infections[37,38]. Detailed studies have identified most neutralizing epitopes to be within the S1 region of these spike proteins, with many falling within the portions responsible for receptor binding, implying disruption of host

cell recognition as an important mechanism of neutralization[37,39]. Several less frequently recognized epitopes within the S2 regions have been identified as well, suggesting inhibition of the membrane fusion event as an additional mechanism of neutralization[37,40].

1.5 Evolution of Coronaviruses

Viral evolution can be described as an interaction between selective pressures and mutational rate. The mutational rate of viruses is generally dependent on the fidelity of genome replication. Typically, RNA viruses have increased mutational frequencies relative to DNA viruses, due to their reliance on RNA-dependent RNA polymerases (RdRp) which lack proofreading activity[41]. While the fidelity of RdRps may be low, it does not approach that of reverse transcriptase enzymes, which are utilized by retroviruses, and have comparatively higher mutational rates[41]. Importantly, coronavirus genomes encode for a 3'-5' exoribonuclease that provides an RdRp-independent proofreading activity. This exoribonuclease activity reduces mutation rates introduced by the RdRp relative to other RNA viruses[41]. The discontinuous nature of genome transcription inherent to coronaviruses poses an additional mutational mechanism. Discontinuous transcription in cells co-infected with multiple coronavirus species can result in the production of chimeric sgRNA strands from multiple genomes via "strand switching" by the RdRp[42]. Thus, mutational mechanisms in coronaviruses include i) RdRp errors that survive proofreading and ii) the formation of chimeric sgRNA during discontinuous transcription within co-infected cells. The development and optimization of genetic sequencing technologies has enabled the tracking of coronavirus evolution over time, allowing for insight into the relevant selection pressures. Genetic tracking of various coronaviruses has revealed several areas of genetic diversity, from mutations in various genes, to the gain and loss of individual genes. These genetic changes are thought to represent selection pressures in host tropism during zoonosis[43]. A high rate of mutational plasticity

has been noted in the spike proteins of coronaviruses, thought to be a result of selection pressures in receptor usage during zoonosis[43], and perhaps also due to immune pressures as some mutations have been noted to evade neutralizing antibodies[44–47].

1.6 Emergence of a Novel Coronavirus Pandemic in 2019

On December 31, 2019, several related cases of pneumonia in workers at a live animal market were reported in Wuhan, China. This raised suspicion of a zoonotic event and sequencing efforts identified the etiological agent of these cases to be a novel coronavirus, initially named 2019-nCoV and later named SARS-CoV-2. Patients infected with SARS-CoV-2 displayed varied symptoms consistent with respiratory infections, including cough, fever, sore throat, runny nose, fatigue, and in severe cases, respiratory distress, pneumonia, multiple organ failure, and death. The disease caused by SARS-CoV-2 infection is referred to as COVID-19. In the following two months, SARS-CoV-2 had achieved alarmingly rapid spread to over 90 countries, causing unprecedented international concern. On March 11, 2020, the world health organization (WHO) declared the SARS-CoV-2 outbreak a pandemic, calling for international efforts in preventing SARS-CoV-2 transmission, which occurs through exposure to infectious respiratory fluids (droplet and aerosol products of respiration). SARS-CoV-2 would go on to spread across the entire globe and have devastating effects on global health, economies, and society[48–54]. At the time of writing this thesis in 2023, analyses suggest a sobering death toll of 6.8 million people due to COVID-19.

Sequencing of SARS-CoV-2 revealed it to contain a genome of around 30 kilobase pairs coding for 29 proteins, which can be divided into 16 non-structural proteins, 4 structural proteins, and 9 accessory proteins[12], as expected for coronaviruses. Armed with decades worth of knowledge on coronavirus biology from studying SARS-CoV, MERS-CoV and other coronaviruses, the international science community immediately began to focus intensely on the spike protein given

its crucial role in cell entry and its vulnerability to neutralization. The SARS-CoV-2 spike protein shares ~76% amino acid similarity with that of SARS-CoV, suggesting that SARS-CoV-2 uses the same receptor: angiotensin converting enzyme 2 (ACE2)[55]. This was confirmed to be the case by several studies[55–57], also finding that like SARS-CoV, SARS-CoV-2 is processed by TMPRRS2[58]. Interestingly, a novel furin cleavage site was identified in the SARS-CoV-2 spike protein, enabling the spike protein to be cleaved during maturation in the golgi system, which seems to be key for its pathogenesis[59] and transmission[60]. Several mRNA vaccine platforms were adapted to target the SARS-CoV-2 spike at record speed, as it represented the top antigen choice for a vaccine candidate.

1.7 Structural and Functional Techniques for Characterizing Coronavirus Spike Proteins

Structural and functional investigation of coronavirus spike proteins involves several challenges that must be overcome. Given that coronavirus spike proteins are multidomain homotrimers which bind receptors and antibodies, there exists a great deal of conformational heterogeneity intrinsic to the structural study of such complexes. Additionally, these complexes are quite large (>400kDa) and combined with the high conformational heterogeneity, are not amenable to crystallization or NMR based structural studies (although such studies can certainly be performed using minimal subdomains). These spike proteins are membrane embedded, undergo cleavage events, and spontaneously perform large-scale structural transitions to post-fusion conformations. All of these factors increase the technical difficulty of structural and biochemical studies on coronavirus spike proteins. Researchers have developed methods to stabilize these spike proteins in un-cleaved, pre-fusion, and soluble forms, overcoming these barriers, and facilitating detailed structural and biophysical experiments[61–63].

The large size, flexibility, and conformational heterogeneity of the SARS-CoV-2 spike protein makes it a strong candidate for structural investigation via single particle electron microscopy. Briefly, single particle electron microscopy involves the analysis of biomolecules which have been deposited onto various surfaces and imaged using transmission electron microscopes. The main variations in this technique are at the level of specimen preparation, where samples can be stained with an electron dense material such as uranyl formate (in what is called negative stain electron microscopy), or unstained and frozen with the biomolecule suspended in vitreous ice (in what is known as cryo-electron microscopy). Specimens are then subjected to electron bombardment, and a detector collects electrons that pass through the sample, converting the raw data into images or movies. These electrons have interacted with the specimen and therefore contain important information with regards to the coulombic potential of the sample. Due to the high electron scattering potential of the stain used, negative stain electron microscopy delivers high contrast, low resolution images or movies of biomolecules, while cryo-electron microscopy delivers low contrast, high resolution images or movies. Thus, negative stain analysis is fundamentally limited to resolving structures of biomolecules at low resolution with a general maximum limit of ~20 Å, while cryo-electron microscopy is amenable to atomic resolution analysis of biomolecule structure. Assuming optimal sample generation and specimen preparation, these images ideally contain projection images of the biomolecule in question from multiple angles of observation. Single particle analysis therefore attempts to combine many projections into coherent 3D reconstructions by selecting, averaging, and assigning angular coordinates to the various particle projections within these images. This process involves numerous computational tasks (the details of which are beyond the scope of this introduction) aimed at correcting for movement of particles due to electron bombardment, aberrations and defocusing of the microscope, and generally many

iterative rounds of particle selection, particle averaging, and angular assignments yielding 3D volumes. We employ both negative stain and cryo-electron microscopy as techniques within this thesis for generation of low- and high-resolution structural insights respectively.

The main challenge when attempting to study functionality of coronavirus spike proteins within the context of cell entry and neutralization is one of biosafety. An ideal experiment would require use of intact and native virions; however, coronaviruses such as SARS-CoV, MERS-CoV, and SARS-CoV-2 pose a significant health risk to humans and require biosafety level 3 working conditions, which are not generally readily available to researchers. To overcome this challenge, researchers utilize a pseudo-virus system that attempts to mimic the critical first infectious step of cell entry. These systems make use of replication incompetent virus particles that lack an intact genome but harbour a reporter gene (such as GFP or luciferase) and are adorned with a spike protein of the researchers choosing. These particles can be administered onto mammalian cells expressing the relevant receptors, either in the absence or presence of antibodies and or entry inhibitors, and viral entry can then be quantified as a function of the reporter gene activity after a certain amount of time. These pseudo-virus systems generally make use of lentivirus, murine leukemia virus (MLV), or vesicular stomatitis virus (VSV) virions, and facilitate experimentation under less stringent biosafety level conditions.

1.8 General Architecture of the SARS-CoV-2 Spike Glycoprotein

Cryoelectronic tomography (Cryo-ET) based studies of whole SARS-CoV-2 virions revealed the viral envelope to contain SARS-CoV-2 spike proteins in both pre and post-fusion states[64–66]. This finding confirmed that the SARS-CoV-2 spike protein is capable of spontaneous S1-S2 dissociation and transition from the pre to post fusion state independent of ACE2 engagement. Cryogenic electron microscopy (Cryo-EM) studies using full-length spike proteins[67] revealed

similar findings, determining the structures of both pre-fusion and post-fusion conformations of the spike protein (Figure 1.1). The pre-fusion state of viral spike proteins is considered the relevant antigenic target when considering neutralizing antibody elicitation, as post-fusion conformations represent a fusion event that has already occurred and do not generally represent a vulnerability of the virus. Importantly, a Cryo-ET study using SARS-CoV-2 virions that were chemically inactivated with β-propiolactone revealed most spike proteins to be in the post-fusion state, cautioning against the use of inactivated SARS-Cov-2 vaccines[68]. As previously mentioned, researchers have developed methods to stabilize viral spike proteins in pre-fusion states[61], and rapid identification of i) stabilizing proline substitutions, ii) replacement of the transmembrane helices with a T4 foldon trimerization motif, and iii) abrogation of the furin cleavage site enabled detailed structural and biochemical studies of the SARS-CoV-2 pre-fusion spike protein ectodomain[55,69]. These investigations allowed detailed views of the S1 and S2 regions and enabled description of the conformational heterogeneity within the spike protein, typical of coronavirus spike proteins (Figure 1.2). The SARS-CoV-2 S1 region contains the amino terminal domain (NTD) and the receptor binding domain (RBD). The RBD exists in multiple conformations within the spike trimer, with its two conformational extremes being dubbed “up” or “down”, referring to its accessibility and positioning[70]. The RBD recognizes the host cell receptor ACE2, only when it is in the “up” conformation[70]. Thus, the SARS-CoV-2 spike protein forms a trimeric complex with multiple possible architectures which can be reduced and simplified for study via pre-fusion stabilization.

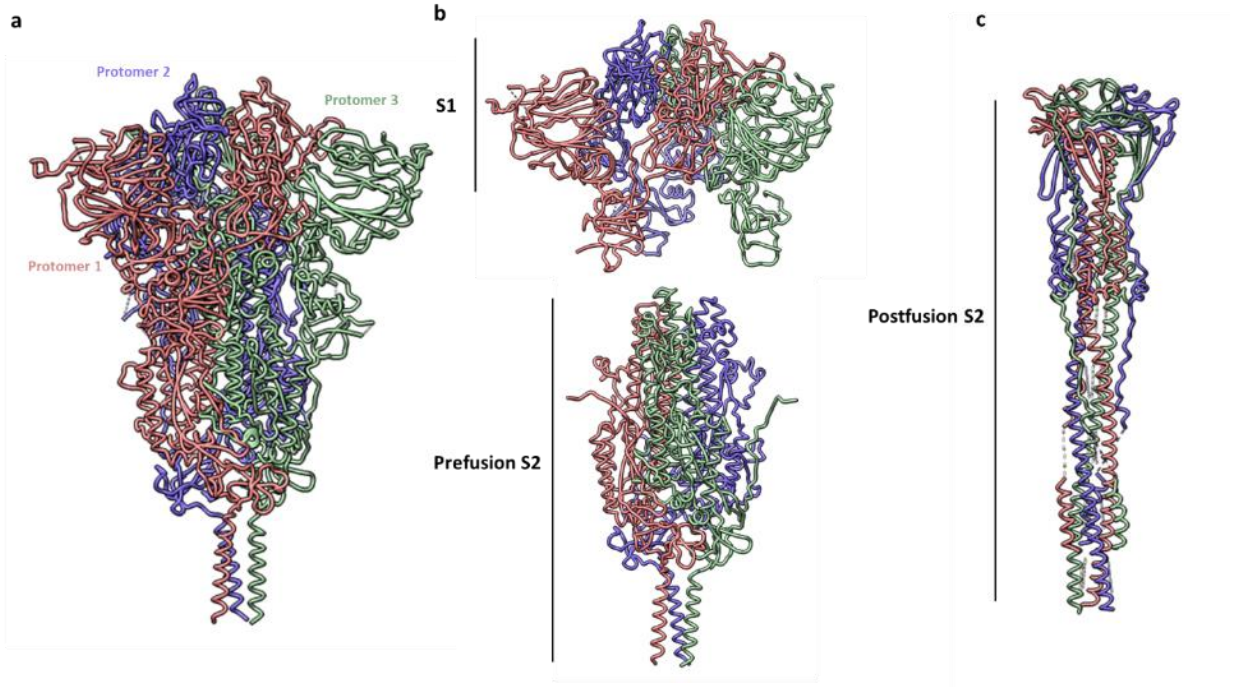

Figure 1.1. **Cryo-EM structures of full length un-stabilized SARS-CoV-2 trimers**. (a) Structure of a prefusion spike trimer in the closed state with all RBDs down (PDB 6XR8). (b) Same as in (a) but the S1 and S2 regions are shown separately to mimic S1 dissociation. (c) Structure of the post-fusion S2 region (PDB 6XRA).

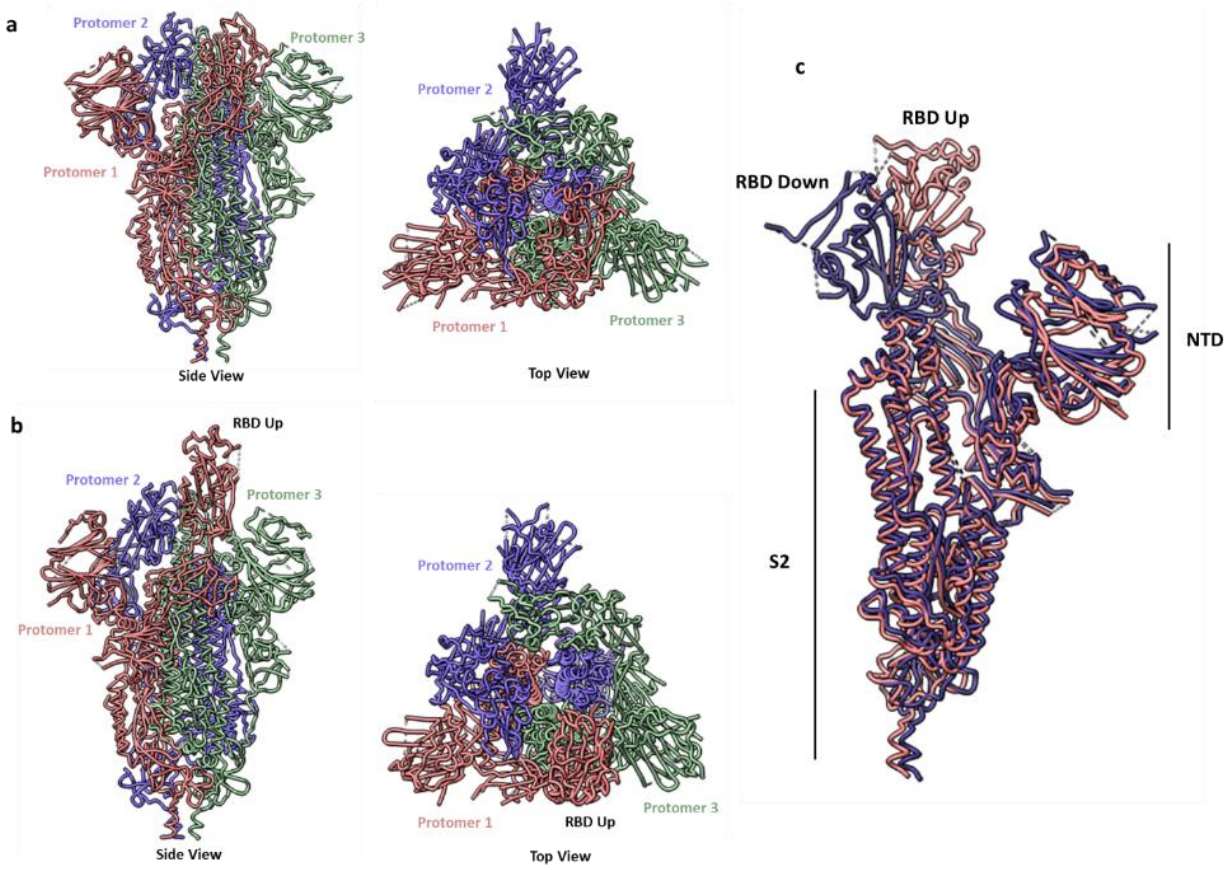

Figure 1.2. **Cryo-EM structures of the pre-fusion stabilized SARS-CoV-2 spike ectodomain**. (a) Structure of a closed spike trimer ectodomain with all RBDs in the down position (PDB 6VXX). (b) Structure of an open spike trimer ectodomain with 2 RBDs in the down position and one in the up position (PDB 6YVB). (c) Superposition of a single protomer either with the RBD up or down. Domains are annotated within the protomer superposition.

1.9 Structure and Function of Angiotensin Converting Enzyme 2 (ACE2)

ACE2 is a type I integral membrane carboxypeptidase which functions as the terminal peptidase in the multi-step processing of angiotensinogen within the renin-angiotensin system[71]. The peptide products generated by ACE2 serve to maintain homeostasis in the renin-angiotensin system, with a major role in vasoconstriction[72]. Interestingly, ACE2 was found to be the critical host receptor for NL-63[73], SARS-CoV[74], and SARS-CoV-2[58] coronaviruses. Gene expression studies have found high levels of ACE2 expression in intestinal enterocytes, renal tubules, gallbladder cells,

cardiomyocytes, male reproductive cells, placental trophoblasts, ductal cells, ocular cells, vasculature cells[75], and adipose cells[76], but low to medium levels of expression within the lung[75,76]. Within the lung, higher apical expression of ACE2 was observed in alveolar epithelial cells compared to bronchial epithelial cells, implicating the lung parenchyma as the initial site of infection for respiratory coronaviruses that utilize ACE2[77]. Crystallography studies of the extracellular domain of ACE2 revealed its active site to exist as a cleft between the amino terminal and carboxy terminal sub-domains[78], and that both NL63 and SARS-CoV spike protein RBDs bind ACE2 at the carboxy terminal sub-domain[79,80].

1.10 Structural Insights into Receptor Binding by the SARS-CoV-2 Spike Glycoprotein

Crystal structures of the SARS-CoV-2 RBD in complex with ACE2[81,82] revealed a similar binding interface and mode to that of SARS-CoV, as expected due to high sequence homology between both viral spike proteins. One notable difference observed between these complexes is the conformation of RBD loop at the ACE2 binding ridge (Figure 1.3), wherein additional ACE2 contacts are established by SARS-CoV-2, partially rationalizing its near 10-fold increased ACE2 affinity relative to SARS-CoV[81,82].

The initial crystal structures made use of soluble monomeric ACE2, however the true receptor for SARS-CoV-2 is the membrane embedded dimeric form of ACE2. Cryo-EM investigations revealed the complex formed by membrane embedded dimeric ACE2 could interact with one RBD per ACE2, suggesting that two different spike trimers can engage with a single receptor at once, but not 2 RBDs from the same trimer[83] (Figure 1.4). Thus, the SARS-CoV-2 spike protein shares a largely conserved receptor interaction interface with SARS-CoV and can give rise to multiple interactions with receptors by virtue of its trimeric nature.

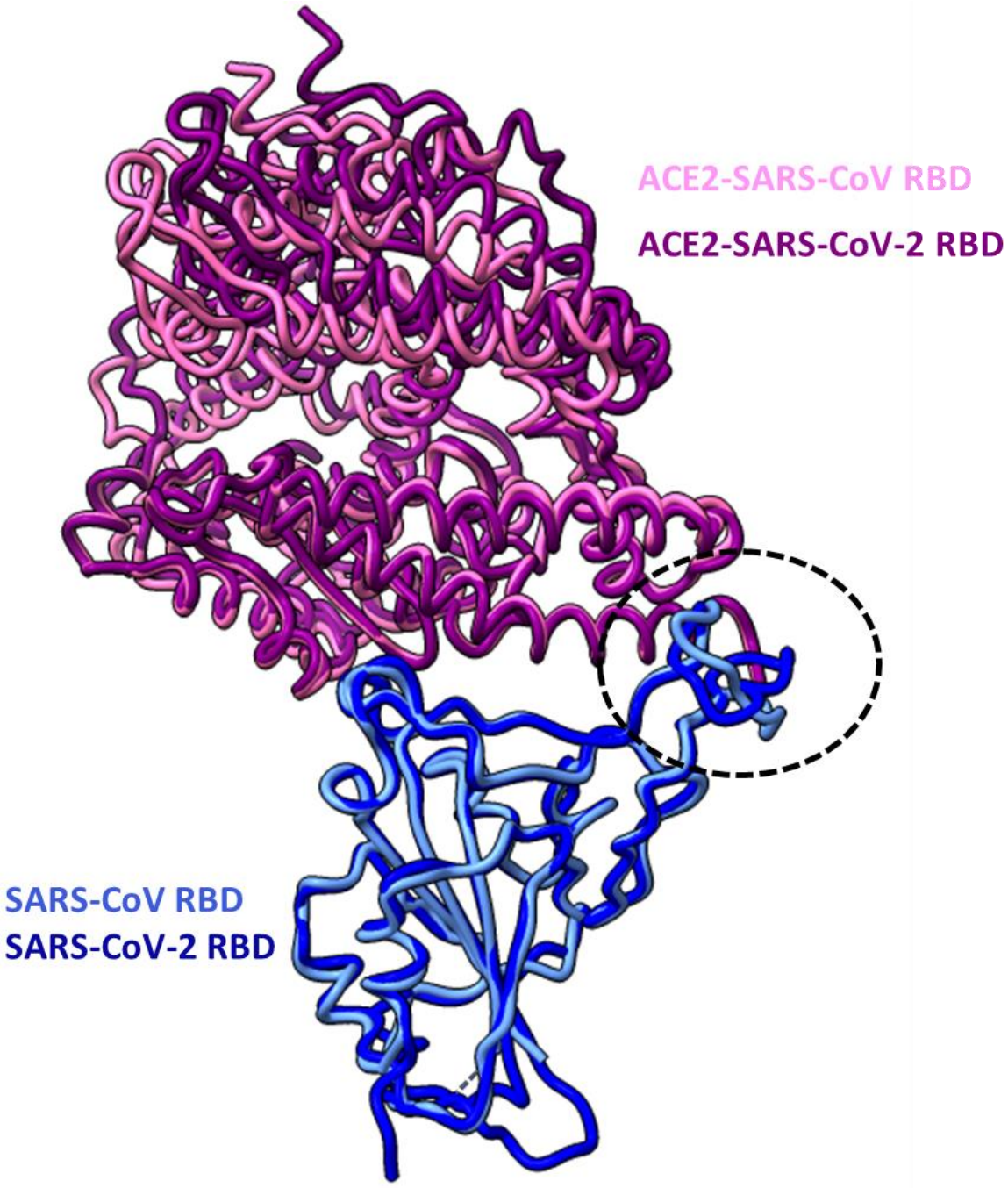

Figure 1.3. **Structural comparison of ACE2 bound SARS-CoV RBD and SARS-CoV-2 RBD complexes.** The loops in the ACE2-binding ridge are highlighted for comparison. Structures were aligned on the RBD portions.

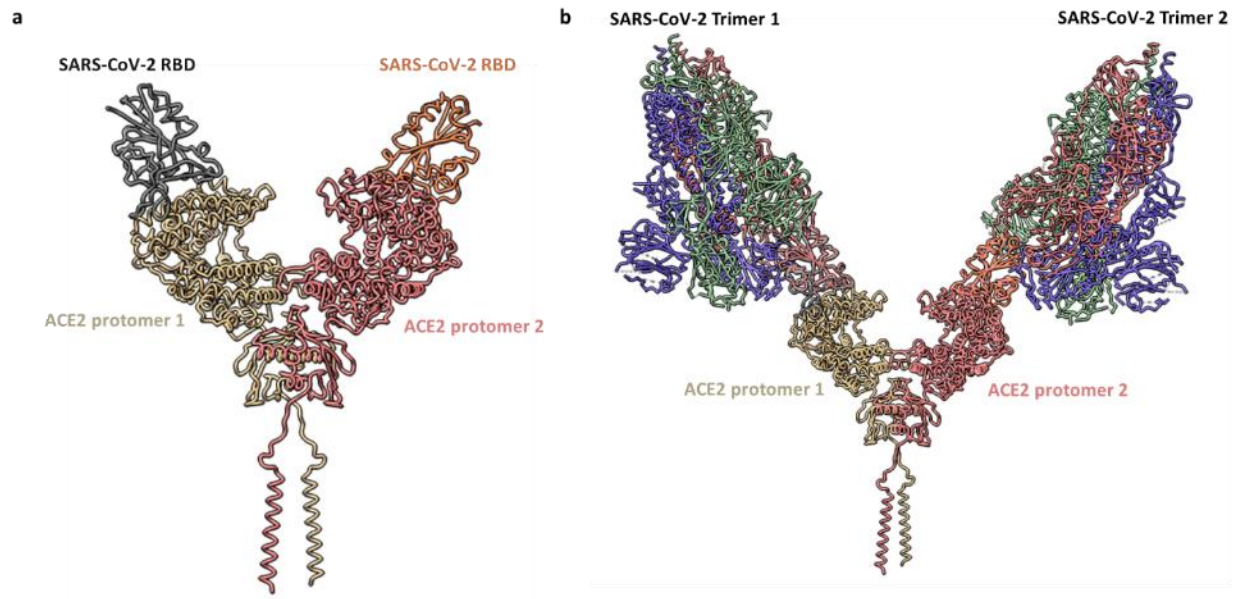

Figure 1.4 **Structure of the SARS-CoV-2 RBD – dimeric ACE2 complex**. (a) Structure of full-length membrane embedded dimeric ACE2 bound to two RBDs. (b) the open stabilized pre-fusion spike trimer model (PDB 6YVB) is superposed onto each RBD from (a) to simulate dual occupancy on dimeric ACE2.

1.11 Thesis goals

The work presented in this thesis spans the very rapid progression and evolution of the first three years of the COVID-19 pandemic, with the SARS-CoV-2 spike protein as a focal point of study. The early phase of the pandemic was marked by an urgent need to understand the vulnerabilities of the SARS-CoV-2 spike protein to neutralization and to develop effective therapies. Thus, characterizing spike protein vulnerabilities is our central focus in chapter 2 of this thesis. As with previous coronaviruses, mutational drift within the spike protein was expected and occurred in the later years of the pandemic. Studies on the effects of these mutations with regards to spike protein

structure, function, and antigenicity are therefore of high relevance. In chapter 3, we provide a comprehensive molecular analysis focusing on the effects of mutations present in the spike protein RBD. In chapter 4, we expand our analyses to variant spike proteins harbouring mutations both within and outside the RBD and focus on characterizing conserved vulnerabilities shared by these variant spike proteins.

The goals of this thesis are:

1) To investigate vulnerabilities within the SARS-CoV-2 spike glycoprotein (Chapter 2).
2) To understand the molecular impact of mutations within the SARS-CoV-2 spike RBD (Chapter 3).
3) To investigate structural, functional, and antigenic differences between emerged SARS-CoV-2 variant spike proteins, and to identify any conserved vulnerabilities (Chapter 4).

Chapter 2: Exploration of SARS-CoV-2 Spike Glycoprotein Vulnerabilities

2.1 Introduction

As discussed in chapter 1, coronavirus spike proteins adorn the viral surface and mediate the initial step of host cell entry during the viral replicative cycle. Due to their accessibility and critical function, they represent a vulnerability, and previous studies highlight the role of coronavirus spike proteins as targets for neutralizing antibodies[37,38]. The SARS-CoV-2 spike protein is thus considered to be a key vulnerability that can be exploited to neutralize the virus via effective antibodies. Such antibodies may be naturally elicited by infection, vaccination, or may be discovered via *in vitro* approaches such as phage display. In some cases, exposure to a different virus may elicit antibodies that are capable of reacting with several different viruses, and such antibodies are deemed "cross-reactive". Significant efforts were made to understand the vulnerability and antigenicity of the SARS-CoV-2 spike protein during the initial phase of the pandemic, by the identification and characterization of cross-reactive antibodies that target the SARS-CoV-2 spike, mechanistic investigation into SARS-CoV-2 spike directed antibodies, and antigenic descriptions of the SARS-CoV-2 spike. This chapter contains efforts on these fronts as we explore vulnerabilities of the SARS-CoV-2 spike protein. We first begin with efforts to identify and characterize glycan-reactive HIV directed antibodies that cross-react with SARS-CoV-2. We then proceed to provide structural and mechanistic insight into two potently neutralizing SARS-CoV-2 directed antibodies, and finally end by providing serological and structural descriptions of the antigenic sites within the SARS-CoV-2 spike protein using polyclonal antibodies in human sera.

2.2 Results and Discussion

2.2.1 Studies on Cross-Reactive, Glycan-Directed anti-HIV antibodies

Viral spike proteins are typically populated by a variable array of host-derived glycans, which serve multiple functions, including epitope occlusion and immune system evasion[84]. Such viral glycosylation patterns themselves may be sufficiently antigenic to elicit antibody responses and may even confer viral neutralization when bound. Indeed, there exist multiple broadly neutralizing antibodies against the HIV spike gp120, whose epitopes involve critical glycan contacts[85]. The SARS-CoV-2 spike contains 22 N linked glycosylation sites which are variably glycosylated with mixtures of Man9GlcNAc2 to Man5GlcNAc2 N-glycans, afucosylated and fucosylated hybrid-type glycans, along with complex glycans[86], suggesting the potential for glyco-epitope mediated cross reactivity. A study has reported SARS-CoV-2 S glyco-epitope recognition by mannose directed Fab-dimerized antibodies against HIV gp120[87], confirming that glycosylation mediated cross-reactivity is possible. We aimed to further investigate such cross-reactivities using a panel of broadly neutralizing anti-HIV antibodies which recognize glycan and peptide epitopes within gp120.

To investigate the existence of cross-reactive glyco-epitopes within the SARS-CoV-2 spike, we subjected a panel of glycan-reactive anti-HIV-1 gp120 antibodies to an ELISA-based cross-reactivity screen (Figure 2.1). We selected nine anti-gp120 antibodies whose epitopes have been shown to involve glycans, along with two anti-gp120 antibodies which recognize the gp120 CD4-binding site as negative controls (Table 2.1) and assessed the ability of these antibodies to bind SARS-CoV-2 spike ectodomain. While the CD4-binding site directed antibodies VRC01 and VRC03 were unable to bind the SARS-CoV-2 spike ectodomain, we observed varying degrees of cross-reactivity for most of the screened glycan-reactive antibodies, the most potent of which were

2G12, PGT128 and PGT126 (Figure 2.1). Glycan-dependent cross-reactivity of 2G12 with the SARS-CoV-2 spike has been recently described[87], and as 2G12, PGT128 and PGT126 exhibited similar levels of cross-reactivity, we selected these antibodies for further investigation.

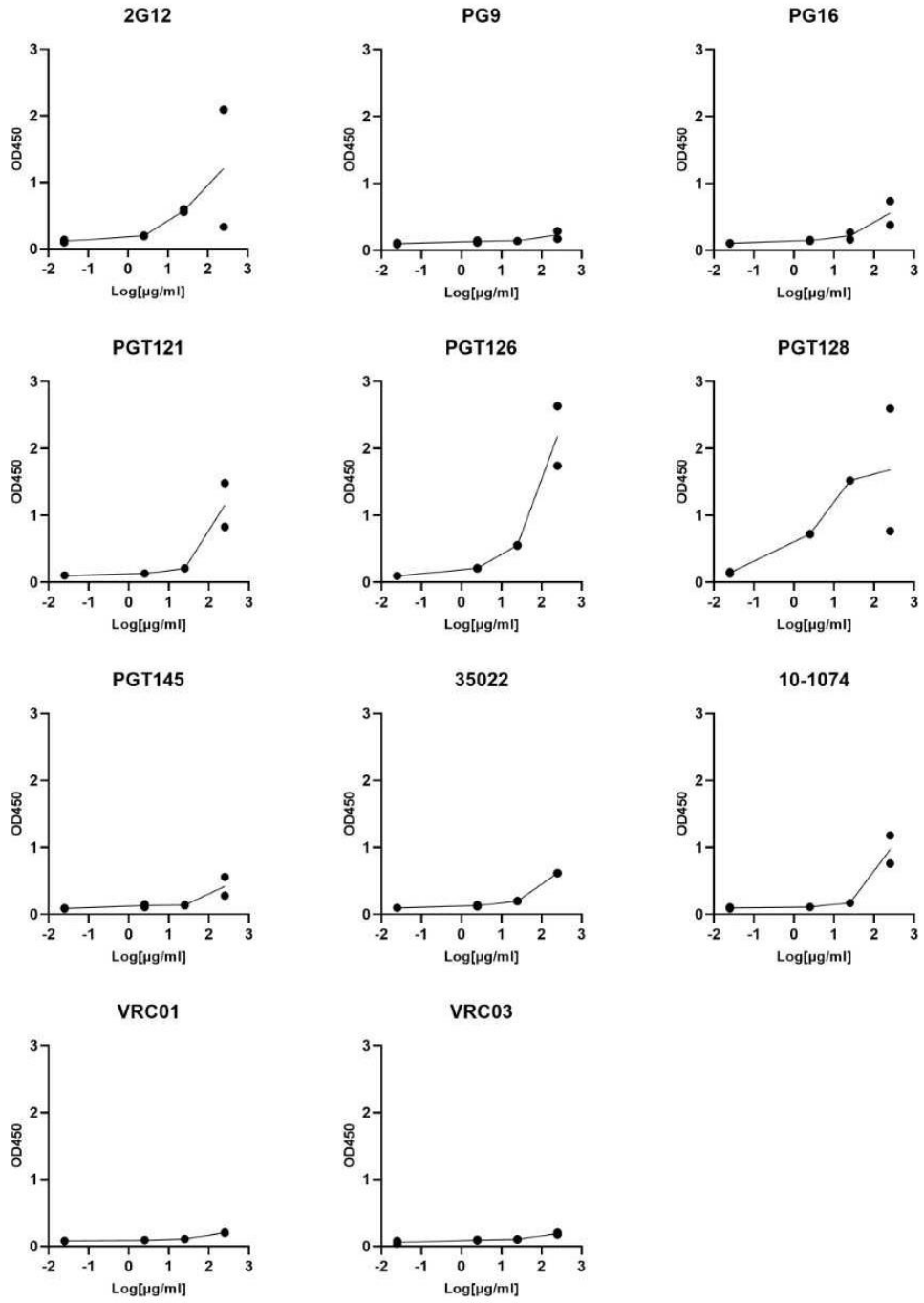

Figure 2.1 **ELISA screen of glycan directed anti-gp120 antibody cross-reactivities to the SARS-CoV-2 Spike.** Serial dilutions of the indicated mAbs were assessed for SARS-CoV-2 S protein binding. VRC01 and VRC03 target the CD4 binding site within gp120 and are included here as negative controls. All ELISAs were performed using BSA-based buffers (see methods). Experiments were done in technical duplicate (n = 2) and results are plotted as points.

Table 2.1. HIV gp120 epitopes recognized by antibodies selected for SARS-CoV-2 S cross reactivity screening.

Antibody	gp120 epitope	Reference
2G12	N-linked glycans in the C2, C3, V4, and C4 domains	[88]
PGT121	N332-centered oligomannose patch on the V3 loop, GDIR motif in V3 loop	[89–91]
PGT126	N332-centered oligomannose patch of the V3 loop, GDIR motif in V3 loop	[89–91]
PGT128	V3-glycan, GDIR motif in V3 loop	[89,92,93]
PGT145	V1-V2 Glycans, residues within C-strand of V1/V2 and the C1 region near the base of V1	[89,94]
PG9	V1-V2 Glycans, residues within C strand of V1/V2	[95,96]
PG16	V1-V2 Glycans, residues within V1–V2	[39,95,97]
10-1074	V3-glycan, N332 glycosylation dependent, GDIR motif in V3 loop	[98,99]
35O22	Glycan and peptides at the gp120–gp41 interface	[100]
VRC01	CD4-binding site	[101]
VRC03	CD4-binding site	[101]

We next sought to determine the neutralization capabilities of these cross-reactive antibodies, via use of a SARS-CoV-2 S pseudotyped virus entry assay (Figure 2.2). No neutralization capabilities were detected for 2G12, PGT128, and PGT126 over a wide range of concentrations, demonstrating these antibodies to be non-neutralizing.

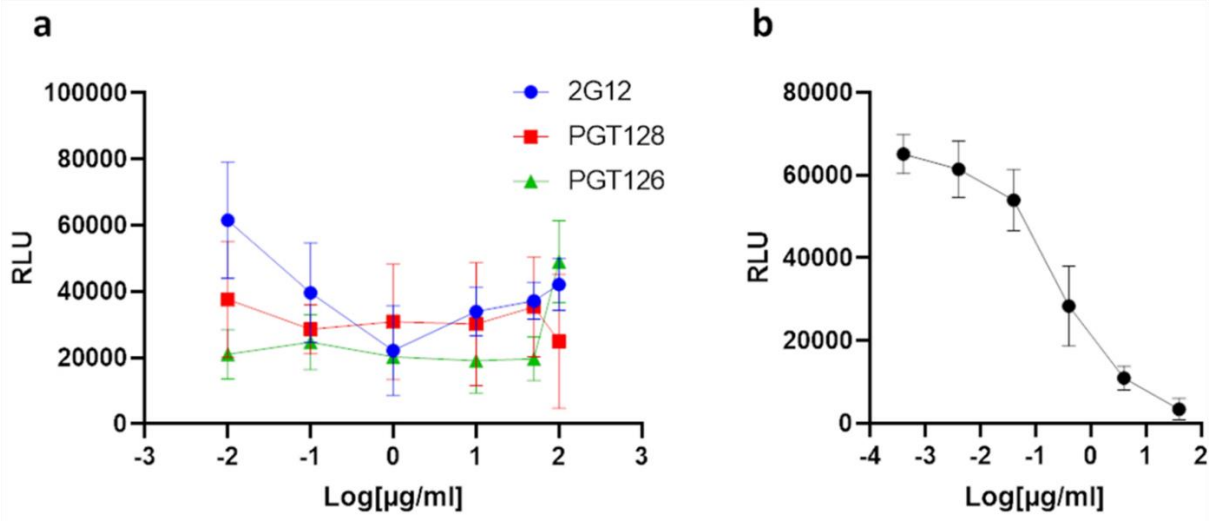

Figure 2.2. **2G12, PGT128 and PGT126 do not neutralize SARS-CoV-2 S pseudo-typed virus.** (a) HEK293-T cells stably overexpressing ACE-2 were incubated with SARS-CoV-2 S pseudo-typed virus harbouring a luciferase reporter gene, in the presence of serial dilutions of the indicated anti-gp120 antibodies. (b) Positive control neutralizing antibody ab8 subjected to the same assay described in (a) Luciferase activities in cellular lysates were determined 48 hours post-infection. (RLU: relative luciferase units). Experiments were done in technical triplicate; error bars indicate standard deviation (n = 3).

To further characterize the cross-reactivity of 2G12, PGT128 and PGT126 with the SARS-CoV-2 spike protein, we assessed the immunoreactivity of these antibodies with the SARS-CoV-2 spike ectodomain via Western blot (Figure 2.3a). Immunoreactivity was observed for 2G12, PGT128, and PGT126, while VRC01 immunoreactivity was not detected, consistent with the results of our initial ELISA screen. We next aimed to assess the ability of these antibodies to cross-react with full-length SARS-CoV-2 spike under native conditions. To this end, we performed immunoprecipitation experiments utilizing lysate generated from cells transiently expressing the full-length SARS-CoV-2 spike (Figure 2.3b). The full-length SARS-CoV-2 spike was successfully immunoprecipitated by 2G12, PGT128 and PGT126, but not by VRC01, implicating these cross-reactive epitopes to be present in the full-length spike under non-denaturing conditions. Furthermore, we demonstrate interactions between 2G12, PGT128, and PGT126 but not VRC01

and cell-associated full-length SARS-CoV-2 spike via a cell-based ELISA assay (Figure 2.3c) corroborating our immunoprecipitation results.

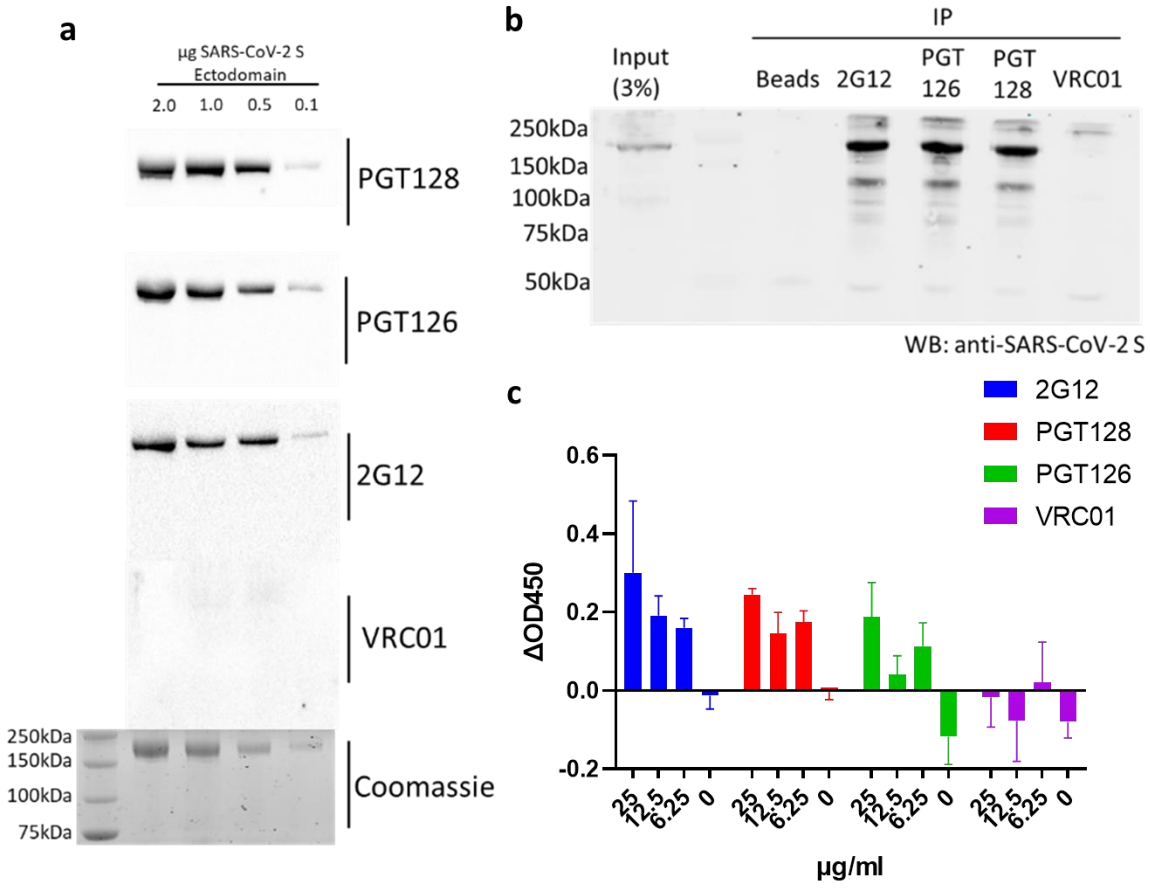

Figure 2.3. **SARS-CoV-2 S binding capabilities of selected cross-reactive anti-gp120 antibodies.** (a) Immunoreactivity of selected anti-gp120 antibodies with the SARS-CoV-2 S ectodomain was assessed via western blot, membranes were probed with the indicated antibodies prior to detection via HRP-anti-human IgG. A Coomassie-stained gel is included as a loading control. (b) Immunoprecipitation (IP) of full-length SARS-CoV-2 S by selected anti-gp120 antibodies. Lysates generated from HEK293T cells transiently expressing full-length SARS-CoV-2 S were incubated with the indicated antibodies and subjected to immunoprecipitation using protein A beads prior to Western blot (WB) analysis with a commercially available antibody targeting SARS-CoV-2 S. An immunoprecipitation condition using protein A beads alone is included as a control. Shown is a representative blot from 2 independent experiments. (c) Cell-based ELISA of cell-associated full-length SARS-CoV-2 S binding by the indicated anti-gp120 antibodies. Assays were carried out on chemically fixed HEK293T cells either transfected with plasmid encoding full-length SARS-CoV-2 S, or empty plasmid (mock). The difference in signal between these conditions is presented. Experiments were done in technical triplicate; error bars indicate standard deviation (n = 3).

Having characterized the cross-reactivities of 2G12, PGT128 and PGT126 with the SARS-CoV-2 spike, we proceeded to investigate the potential contribution of glycans in these interactions. We had observed abolished cross-reactivities when using casein-based blocking buffers (Figure 2.4) compared to BSA-based blocking buffers (Figure 2.1) in our initial cross-reactivity screens. Given the high carbohydrate content of casein[102], it suggested a possibility that these interactions may be glycan sensitive. We first assessed these cross-reactive interactions in the presence of methyl α-d-mannopyranoside, a stabilized mannose analogue, via ELISA (Figure 2.5a). Disruption of cross-reactivity was observed for all three antibodies with increasing concentrations of methyl α-d-mannopyranoside, demonstrating the glycan sensitivity of these interactions. We next evaluated the cross-reactivities exhibited by these antibodies with differentially glycosylated SARS-CoV-2 spike preparations. We expressed SARS-CoV-2 S ectodomain in cells grown either in the presence or absence of kifunensine, a mannosidase inhibitor which facilitates the production of highly glycosylated, high mannose glycoproteins[103]. SDS-PAGE analysis of the resulting purified proteins revealed SARS-CoV-2 S ectodomain produced in kifunensine treated cells exhibits a hindered electrophoretic mobility relative to ectodomain produced in untreated cells (Figure 2.5b), consistent with the higher extent of glycosylation expected with kifunensine treatment. All three antibodies exhibited increased relative affinities and observed extents of binding with SARS-CoV-2 S ectodomain produced in cells treated with kifunensine compared to ectodomain produced in untreated cells (Figure 2.5 c-d), further highlighting the participation of glycans within these cross-reactive interactions. Taken together, these results implicate 2G12, PGT128 and PGT126 as targeting cross-reactive glyco-epitopes within the SARS-CoV-2 spike.

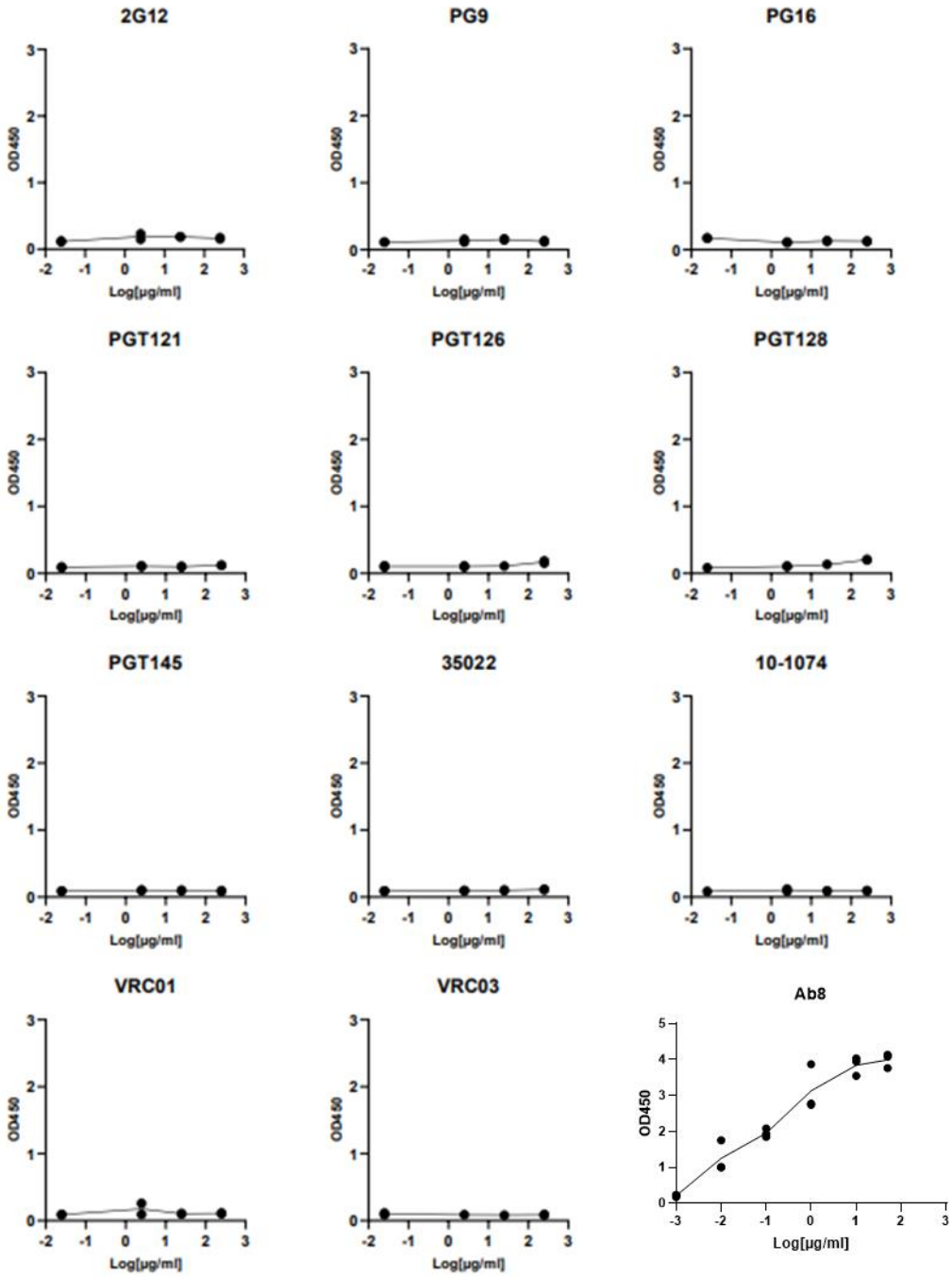

Figure 2.4. **ELISA screen of glycan directed anti-gp120 antibody cross-reactivities to the SARS-CoV-2 Spike using the casein-based buffer.** Serial dilutions of the indicated mAbs were assessed for SARS-CoV-2 S protein binding. VRC01 and VRC03 target the CD4 binding site within gp120 and are included here as negative controls. Ab8 targets the SARS-CoV-2 RBD and is included as a positive control. All ELISAs were performed using casein-based buffers (see methods). Experiments were done at least in duplicate and results are plotted as points.

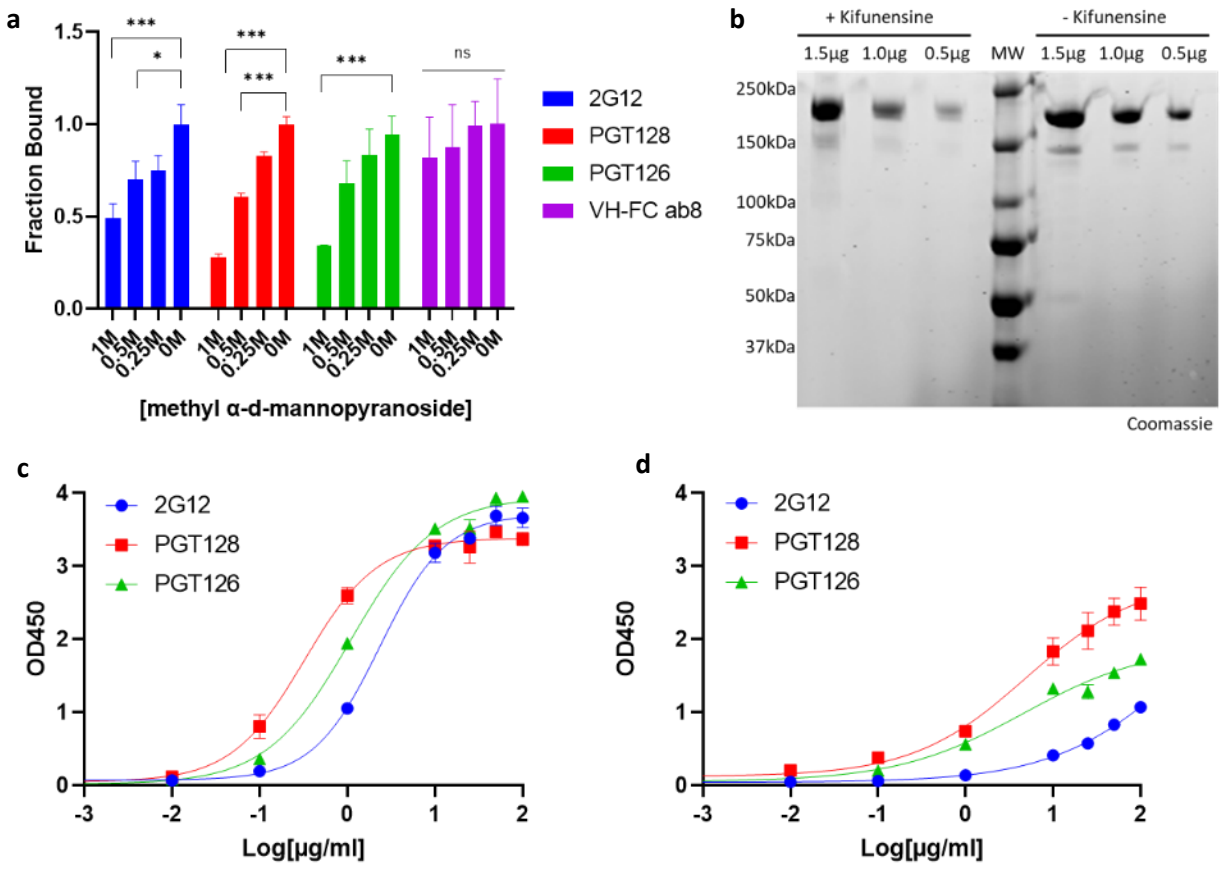

Figure 2.5. **2G12, PGT128 and PGT126 cross-react with the SARS-CoV-2 Spike in a glycan dependent manner.** (a) SARS-CoV-2 S ectodomain binding by anti-gp120 antibodies in the presence of methyl α-d-mannopyranoside. Plates were coated with SARS-CoV-2 S ectodomain and incubated with dilutions of methyl α-d-mannopyranoside along with a constant amount of the indicated antibodies. Antibody binding was quantified via ELISA. (b) SDS-PAGE analysis of varying amounts of purified SARS-CoV-2 S ectodomain expressed in cells either in the presence or absence of kifunensine. (MW: molecular weight ladder). (c – d) ELISA analysis of anti-gp120 antibody interactions with SARS-CoV-2 S ectodomain expressed in cells either in the presence (c) or absence of kifunensine (d). Experiments were done in triplicate; error bars indicate standard deviation (n = 3). Statistical significance was tested by two-way ANOVA with Dunnett post-test ($p > 0.05$ [ns, not significant], $p \leq 0.05$ [∗], $p \leq 0.01$ [∗∗], $p \leq 0.001$ [∗∗∗]).

As the cryo-EM structure of 2G12 bound to the SARS-CoV-2 spike protein has been reported, we attempted to perform structural studies in hopes of identifying the cross-reactive glyco-epitopes on the SARS-CoV-2 spike protein recognized by PGT126 and PGT128. We performed negative stain electron microscopy analyses of spike proteins mixed with excesses of either antibody, both in IgG and Fab fragment format. We were unable to resolve any classes of spike-mAb complexes

in 2D or 3D classification analyses (data not shown). Likely the low affinity of these interactions and possible multiple binding sites on the spike protein preclude structural investigation via low spike protein occupancy and averaging out of any bound species due to heterogenous positioning, respectively. Evidence to this first point is available as the cryo-EM analysis of 2G12 bound to the SARS-CoV-2 spike protein revealed only ~15% of spike protein particles to be bound by 2G12 under a large molar excess of 2G12[87], which can be expected to be of similarly low potency to PGT126 and PGT128.

2.2.2 Characterization of Potent RBD-Directed SARS-CoV-2 Neutralizing Antibodies

Having exhausted efforts to characterize cross-reactive, non neutralizing epitopes within the SARS-CoV-2 spike protein, we next shifted our focus to mapping out epitopes recognized by potent, SARS-CoV-2 directed, neutralizing antibodies. We selected two antibodies which were identified by our collaborators via phage display technology using libraries from human sequences: ab8 which is a V_H fragment amenable to dimerization via fusion to an FC region[104] and ab1, a canonical immunoglobulin G antibody[105]. Both antibodies were identified based on their ability to bind the SARS-CoV-2 Spike protein RBD and compete with receptor binding. We first performed pseudo-virus neutralization experiments, confirming the potent neutralizing activity of both antibodies (ab1 EC50 = 0.4nM, ab8 EC50 = 2nM) (Figure 2.6a). To confirm the receptor competing nature of these antibodies we performed competition ELISA experiments in 2 complementary formats (Figure 2.6b). First, we preincubated spike proteins with each antibody before adding increasing amounts of ACE2 and measuring the residual antibody binding levels. Second, we preincubated spike proteins with ACE2 before adding increasing amounts of each antibody and measuring the residual ACE2 binding levels. Competition between ACE2 and both antibodies was observed across each assay format.

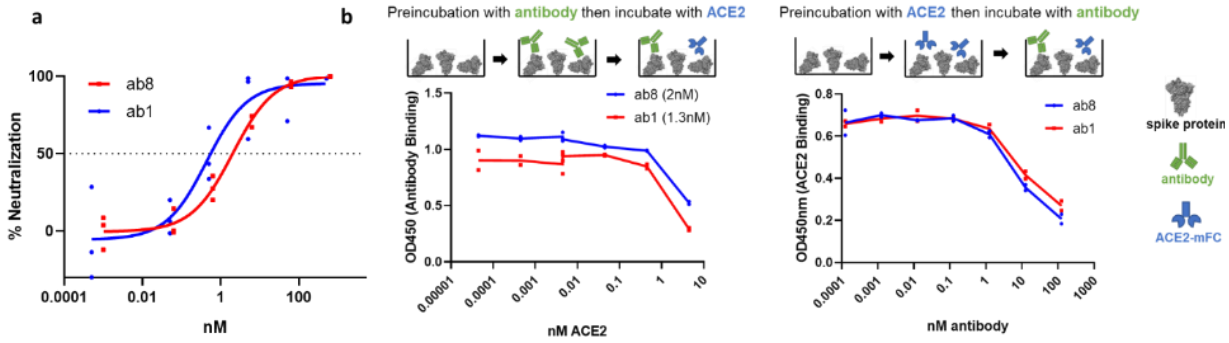

Figure 2.6. **Biochemical analysis of SARS-CoV-2 neutralizing antibodies ab1 and ab8.** (a) Pseudo-virus neutralization assay for V_H-FC ab8 and IgG ab1. (b) Complementary ELISA analyses of ACE2 competition for spike protein binding with V_H-FC ab8 and IgG ab1. Experimental schematics are depicted above each assay. Left: Spike proteins were preincubated with antibodies prior to ACE2 incubation, and the remaining antibody was measured. Right: spike proteins were preincubated with ACE2 prior to incubation with antibodies, and the remaining ACE2 was measured. Note "mFC" refers to a mouse FC tag on ACE2. Experiments were performed in technical triplicate (n=3) and data are shown as points.

To explore structural aspects of SARS-CoV-2 neutralization by ab8, we performed negative stain electron microscopy analysis of the complex formed between the spike protein ectodomain and V_H ab8 or soluble ACE2 (Figure 2.7). The resultant density maps showed that both V_H ab8 and ACE2 were bound to the ectodomain in a quaternary conformation in which two of the protomers in the trimer are in the ''down'' conformation, with the third one in the ''up'' conformation (Figure 2.7a-b). One molecule of V_H ab8 was observed bound to each RBD domain (Figure 2.7a). In the ACE2-S complex, one molecule of ACE2 was bound to the S protein trimer, straddling one ''up'' and one ''down'' RBD region (Figure 2.7b). Superposition of the two density maps reveals that the binding site of V_H ab8 directly overlaps with the ACE2 one, precluding simultaneous occupancy on the S protein ectodomain (Figure 2.7c). To better understand the spatial relationship between the site of V_H ab8 binding and that of ACE2 binding, we created a molecular model for ACE2 bound S trimer by aligning the RBD region of the crystal structure of SARS-CoV-2 RBD bound ACE2 (PDB:6M0J) to the ''up'' RBD region in the cryo-EM structure of the trimer (PDB:

6YVB). Superposition of this chimeric structure with the density map of V_H ab8-bound S protein trimers reveals that the bound ACE2 has extensive overlap with the space occupied by bound V_H ab8 (Figure 2.7d). The direct spatial overlap between bound V_H ab8 and ACE2 provides a structural mechanism for the observed competition between ab8 and ACE2 for spike protein binding.

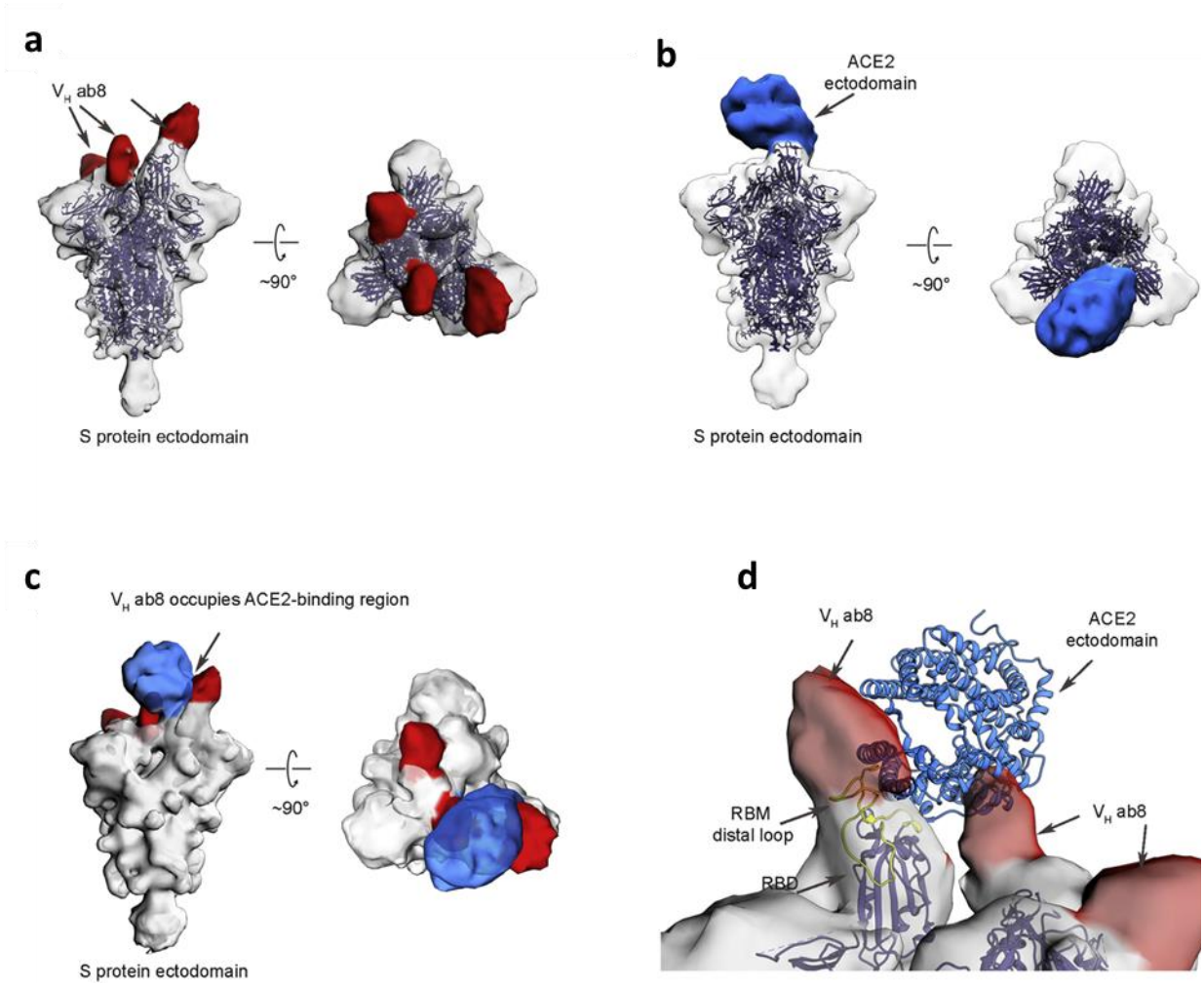

Figure 2.7. **Electron Microscopic Analysis of the SARS-CoV-2 S Protein Ectodomain Complexed with V_H ab8** (a) Side and top views of the density map of S protein ectodomain (shown in gray) in complex with V_H ab8. The density that we associate with the bound V_H domain is colored red. The open-state structure of the SARS-CoV-2 S protein ectodomain (PDB: 6VYB, blue color ribbon) fits well into the map with the exception of the tip of the RBD from the "up" protomer. There appears to be a slight outward shift in the V_H ab8 complex.
(b) Side and top views of the density map of S protein ectodomain in complex with soluble human ACE2 domain, with density for bound ACE2 shown in blue. (c) Superposition of the density maps from (a) and (b). (d) A closer view of the binding site that incorporates the known atomic model for the structure of the ACE2 complex with the RBD in the "up" conformation, delineating the regions of contact with the V_H density. A ribbon representation of the RBM distal loop and the F486 side chain are highlighted in yellow.

We next performed cryo-electron microscopy studies on the spike protein trimer incubated in the presence of the Fab fragment of ab1. We were able to obtain low resolution 3D reconstructions of the spike trimer with 2 RBDs and all 3 RBDs bound by Fab ab1 (Figure 2.8). In contrast to V_H ab8, Fab ab1 seems to only bind the RBD in the "up" conformation, and the unbound RBD in the reconstruction with 2 RBDs bound is in the "down" conformation. Alignment of the ACE2 bound RBD crystal structure to the "up" RBD bound by ab1 reveals significant steric incompatibility between ACE2 and ab1 binding, providing mechanistic insight into the ACE2 competitive nature of ab1 (Figure 2.8).

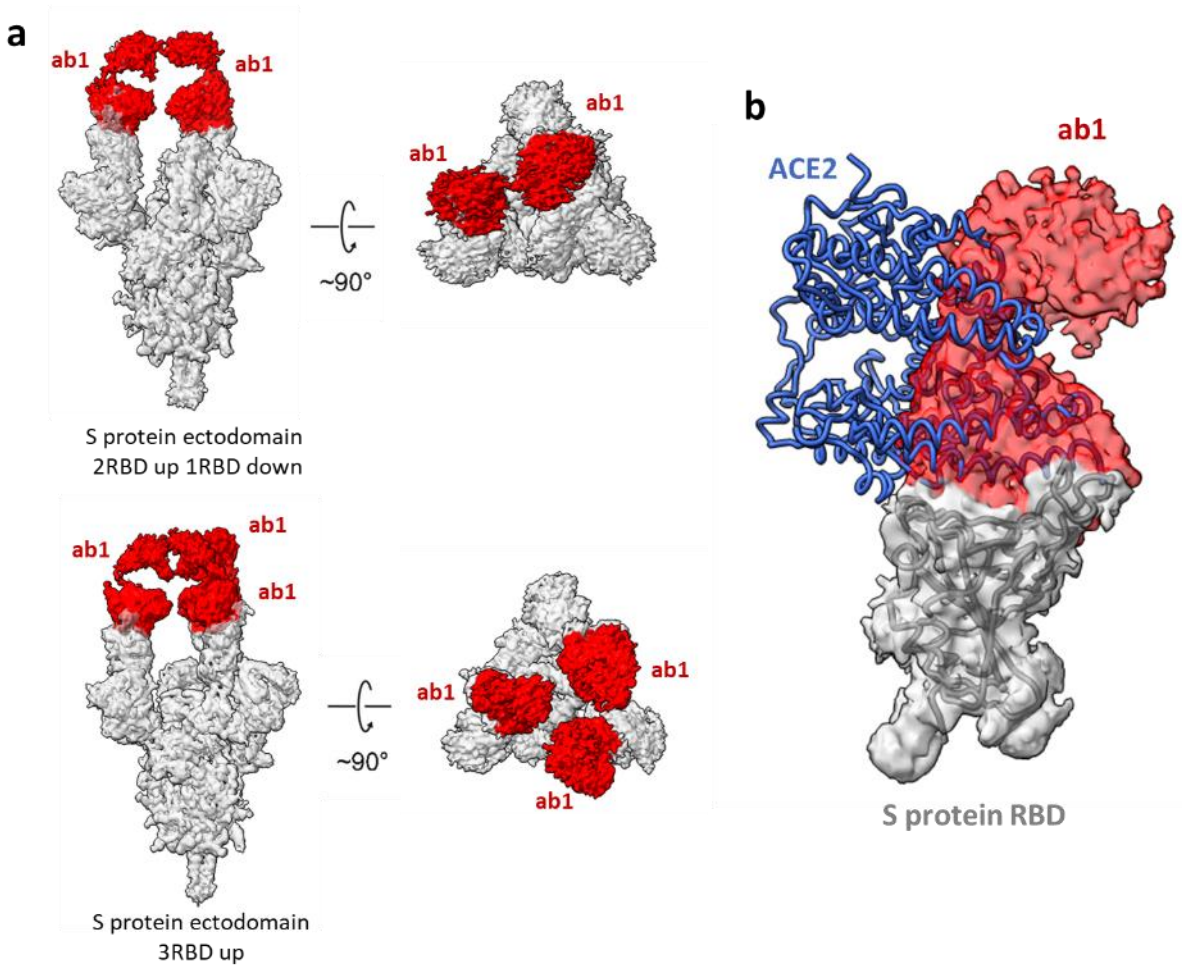

Figure 2.8. **Electron Microscopic analysis of the SARS-CoV-2 spike protein complexed with Fab ab1.** (a) global cryo-electron microscopy reconstructions for spike protein ectodomains bound with either 2 (top) or 3 (bottom) ab1 Fab fragments (coloured in red). (b) Focused view of an RBD bound by ab1, incorporating the crystal structure of ACE2 bound RBD (PDB 6M0J). The atomic model was docked into the reconstruction map in ChimeraX using the fit in map function.

2.2.3 Serological Analysis of SARS-CoV-2 Reactive Polyclonal Antibodies

With a better understanding of the antigenicity of the SARS-CoV-2 spike protein and the vulnerability of the RBD, we next aimed to evaluate the ability of human antibody responses to recognize and neutralize the SARS-CoV-2 spike protein. Sera were collected from a spectrum of patients with varying COVID-19 infection histories and vaccination statuses (Table 2.2). These

sera were subjected to neutralization and binding assays using the spike protein ectodomain, NTD, and RBD (Figure 2.9). Potent neutralization of WT spike pseudovirus was observed in all COVID-19 positive or vaccinated samples but not with pre-pandemic sera from uninfected patients (referred to as negative samples from here on), suggesting limited pre-existing immunity (Figure 2.9a). Negative samples contained spike ectodomain reactive IgG but not IgA or IgM antibodies (Figure 2.9c), and further analysis of the spike reactive IgG component from these samples revealed low recognition of the NTD and RBD domains, with a small increase in NTD recognition over the RBD (Figure 2.9d). Thus, the spike protein reactive antibodies within the negative sera are predominantly directed to epitopes outside the NTD and RBD. The COVID19/Vaccinated samples also predominantly contained spike reactive IgG antibodies when compared to IgA or IgM (Figure 2.9e). In contrast to the negative samples, the spike protein reactive IgG within the COVID19/Vaccinated samples displayed reactivity to the NTD and RBD, although reactivity to these regions was significantly lower to overall spike protein reactivity in these samples (Figure 2.9f). The enhanced neutralization potency and recognition of the NTD and RBD by the COVID19/Vaccinated samples suggested that neutralizing antibodies may preferentially recognize the NTD and RBD. Indeed, while serum levels of spike ectodomain binding antibodies correlated poorly with wild-type spike neutralization, strong correlations were observed between NTD and RBD binding antibody levels and neutralization (Figure 2.10). This finding is in agreement with several studies conducted over similar time intervals, which corroborate the dominance of neutralizing epitopes within the NTD and RBD[106–108].

Table 2.2. Patient demographics for donor serum samples.

Sample ID	Sample Status	Vaccine Dose	Immunization to Serum Draw Time
P0	Vaccine post-COVID19	1st	4 Weeks
P1	Vaccine	1st	3 Weeks
P2	Negative	n/a	n/a
P3	Vaccine	1st	6 Weeks
P4	Negative	n/a	n/a
P5	Vaccine	1st	1 Week
P6	Vaccine	1st	3 Weeks
P7	Negative	n/a	n/a
P8	Vaccine post-COVID19	1st	9 Weeks
P9	Vaccine post-COVID19	1st	7.5 Weeks
P10	Vaccine post-COVID19	1st	6.5 Weeks
P11	Vaccine post-COVID19	1st	7 Weeks
P12	Vaccine post-COVID19	1st	8.5 Weeks
P13	COVID19	n/a	n/a (2 Weeks post-infection)
P14a	Vaccine	2^{nd}	3 Weeks
P14b	Vaccine	2^{nd}	4 Weeks
P16	Negative	n/a	n/a
P17	Negative	n/a	n/a
P19	Negative	n/a	n/a

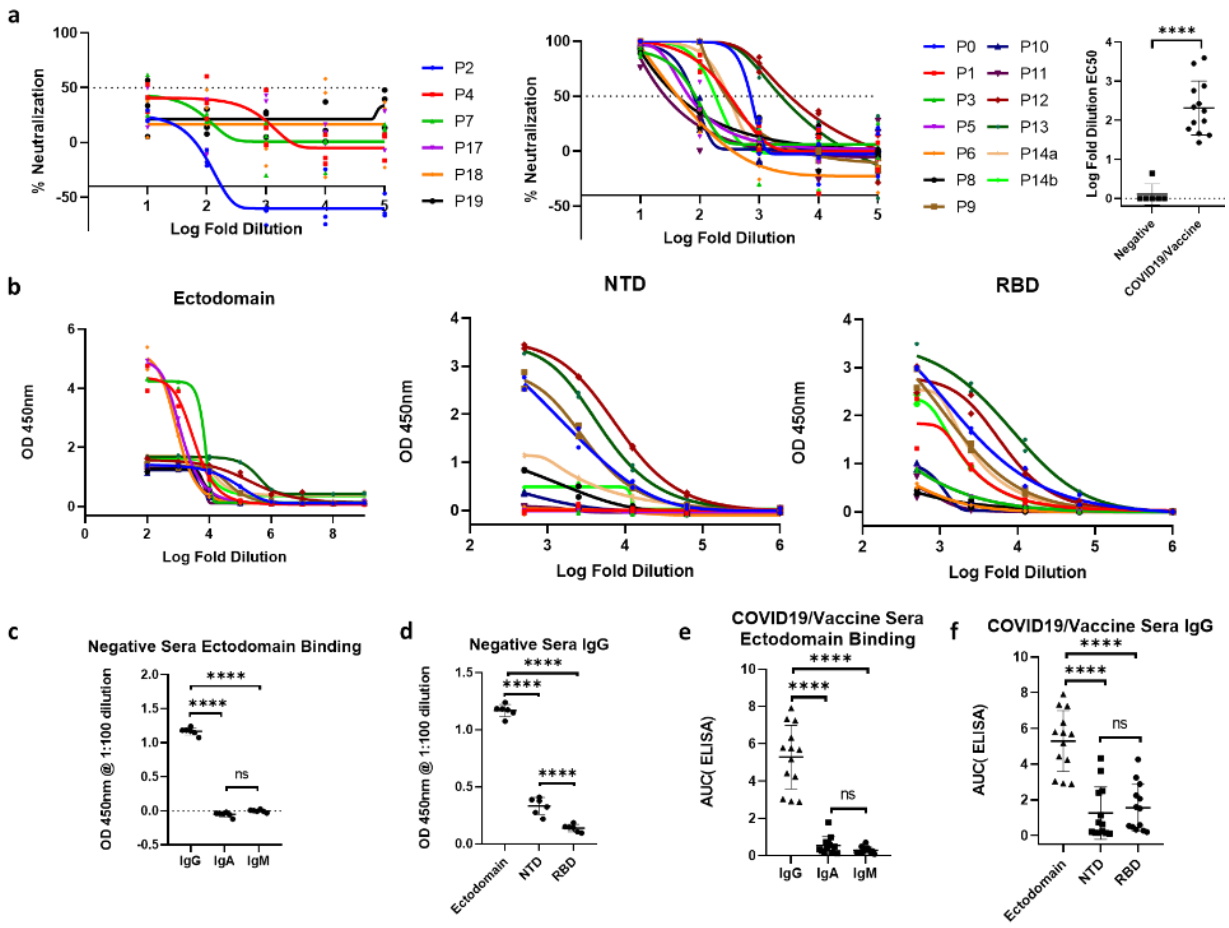

Figure 2.9. **Serological analysis of antibody responses to the SARS-CoV-2 spike protein from various donors**. (a) Pseudo-virus neutralization curves for pre-pandemic (negative) samples (left) and samples from COVID19 positive/vaccinated donors (right). Summary EC50 serum dilution values are shown at the far right. Statistical significance was tested by an unpaired t test ($p \leq 0.0001$ [****]). (b) ELISA curves assessing IgG binding of SARS-CoV-2 spike protein ectodomain, NTD, and RBD from COVID19 positive/vaccinated donors. For neutralization and binding assays, experiments were performed at least in technical duplicate and are shown as individual points. (c) ELISA analysis of SARS-CoV-2 spike protein ectodomain binding IgG, IgA, and IgM at a 1:100 dilution for negative samples. (d) ELISA analysis of SARS-CoV-2 spike protein ectodomain, NTD, and RBD binding IgG at a 1:100 dilution for negative samples. (e) ELISA analysis of SARS-CoV-2 spike protein ectodomain binding IgG, IgA, and IgM in COVID19 positive/vaccinated samples. (f) ELISA analysis of SARS-CoV-2 spike protein ectodomain, NTD, and RBD binding IgG in COVID19 positive/vaccinated samples. For e and f, area under the curve (AUC) values were generated from ELISA binding curves. For c- f, statistical significance was tested using one-way ANOVA with Tukey's correction for multiple comparisons. ($p > 0.05$ [ns, not significant], $p \leq 0.05$ [*], $p \leq 0.01$ [**], $p \leq 0.001$ [***], $p \leq 0.0001$ [****]).

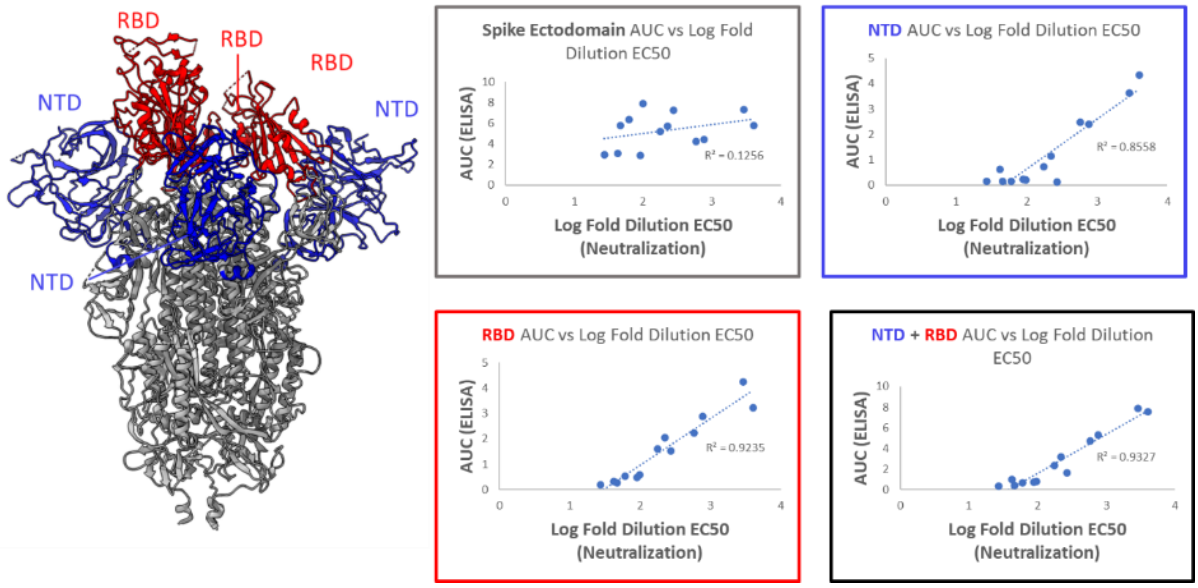

Figure 2.10. **Correlation between SARS-CoV-2 Spike ectodomain, NTD, and RBD binding IgG and neutralization potency in sera obtained from COVID19/Vaccinated donors.** A model of the SARS-CoV-2 spike protein with one RBD up (PDB 7DK3) is shown with the NTD and RBD regions highlighted. Linear correlations between area under the curve (AUC) values generated from ELISA experiments and pseudo-virus neutralization EC50 values are shown.

2.2.4 Structural Analysis of SARS-CoV-2 Spike Protein-Polyclonal Serum Antibody Complexes

Given the observed antigenic importance of the NTD and RBD in our analyses, we next aimed to structurally define vulnerabilities within these regions by studying the complexes formed when spike ectodomains are incubated with polyclonal antibodies from sera. To accomplish this, we utilized negative stain epitope mapping (NSEM) which traditionally requires millilitres of sera[109]. Since we initially only had access to low (~100 microliter) volumes of sera per patient, we first aimed to develop methods to perform NSEM using much smaller volumes of serum. We employed a microscale affinity approach where we selected 30 microliters of plasma from a convalescent patient drawn 1 month after a single dose of the Pfizer mRNA vaccine, purified the IgG component from this sample using protein A chromatography, and subsequently generated bulk polyclonal

Fab fragments via papain cleavage. We incubated these Fabs in excess with spike protein ectodomain (1mg/ml of Fabs to 0.015mg/ml spike protein) along with 5 microliters of Ni-NTA agarose resin in a final volume of 20 microliters overnight at room temperature. After washing to remove unbound Fabs, spike protein was eluted directly onto grids for negative stain electron microscopy analysis. Inspection of the micrographs collected from this sample revealed a low density of spike proteins with visible Fab particles in the background (Figure 2.11), indicating dissociation of Fab-spike protein complexes or incomplete resin washing. Nevertheless, we were able to reconstruct a spike protein trimer class bound by a single Fab fragment from this dataset. The Fab fragment recognizes the top face of the NTD spike protein trimer, which is in a closed state with all RBDs in the "down" position. We hypothesised that the low spike protein particle density would pose an intrinsic limitation to this microscale affinity approach. Therefore, we next aimed to perform a large-scale experiment and employ size exclusion chromatography to isolate Fab - spike protein complexes. Given our limited supply of sera, we pooled equal volumes of samples from all COVID19/Vaccinated patients to a final volume of 620 microliters. We generated polyclonal Fabs and incubated 1mg/ml of Fabs with 0.6mg/ml of spike ectodomain in a 100-microliter volume overnight. We then injected this mixture onto a size exclusion column to separate our free Fab proteins from spike proteins and spike-Fab complexes. Comparison of the elution profiles between spike protein alone and spike protein incubated with bulk Fabs does not indicate an appreciable shift (Figure 2.12a), however given the small mass and size change expected for a Fab fragment (~50kDa) binding the spike protein trimer (~450kDa), this finding does not necessarily imply failure of spike-Fab complexes to form. Indeed, when measuring spike protein binding via ELISA it is apparent that spike reactive Fabs are depleted from the free Fab pool after incubation with spike protein, implying complexation (Figure 2.12b). We analysed the

putative spike protein-Fab complex fractions by negative stain electron microscopy, obtaining more densely populated micrographs which are predominantly comprised of spike proteins and a small amount of free Fab proteins, suggesting complex dissociation after size exclusion chromatography. 2D classification efforts enabled the visualization of several Fab-spike protein classes, identifying NTD and RBD directed classes (Figure 2.12c). However, we were unable to resolve convincing 3D reconstructions for any of these classes, likely due to complex dissociation and the high level of heterogeneity intrinsic to the exercise of analysing pooled antibodies from many individual donors. We next obtained 1ml of serum from a quadruple vaccinated donor with a previous history of COVID-19 infection and proceeded to perform a similar large scale complexation experiment in hopes that the donor homogeneity and enhanced vaccination status would be of benefit in our efforts. Indeed, we were able to obtain several 3D reconstructions from a dataset collected using this sample (Figure 2.13), highlighting both NTD and RBD directed antibodies. We observed an NTD directed Fab which approached the spike protein from the bottom face (in contrast to the previous top face NTD binding Fab we identified in the microscale affinity approach). We additionally observed Fabs which bound to the RBD in the "up" position, either binding the "up" RBD head on, or at a 45-degree angle of approach. We were able to generate a 3D reconstruction of a spike protein trimer bound simultaneously by both kinds of Fabs on a single RBD (Figure 2.13).

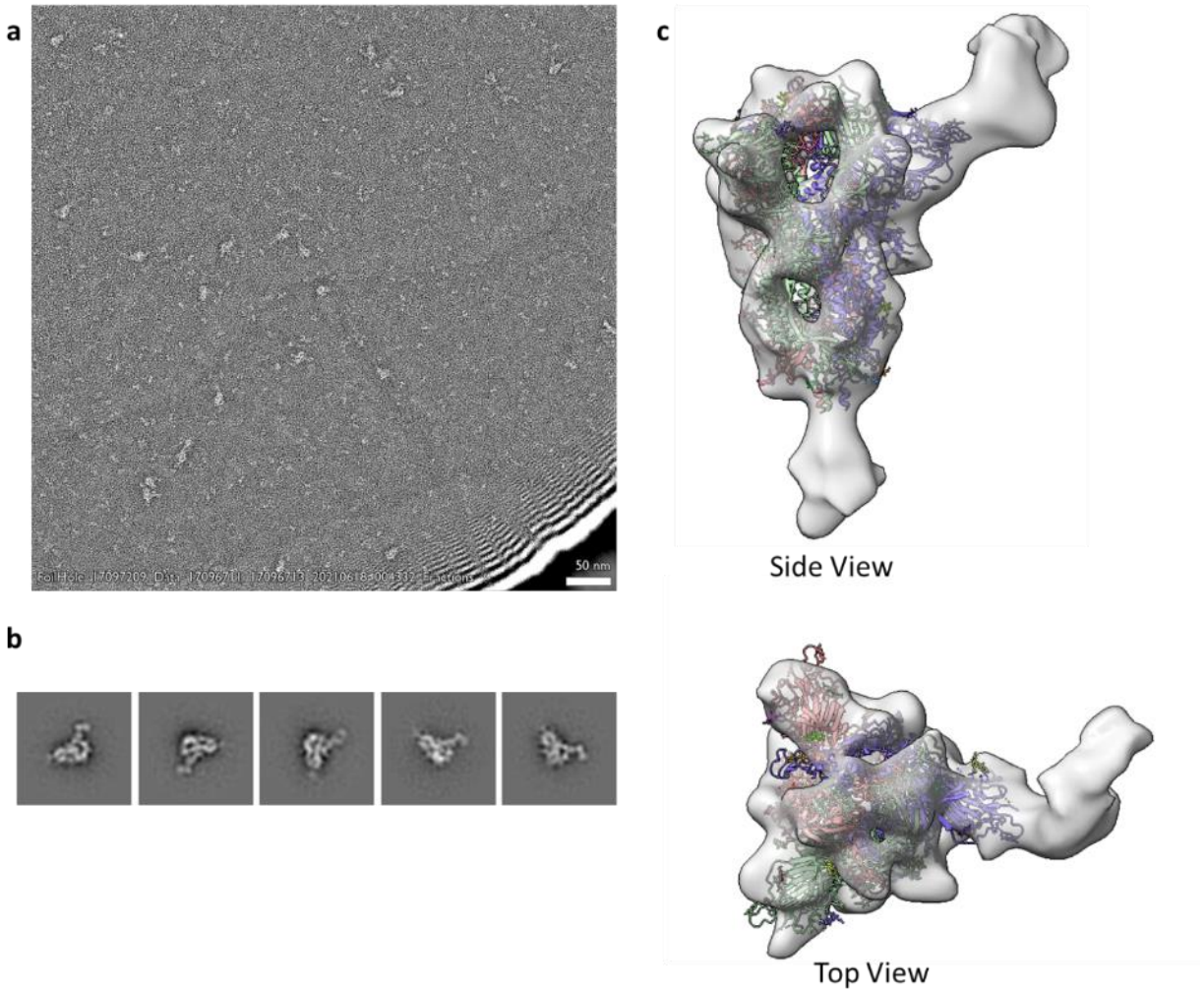

Figure 2.11**. Negative stain electron microscopic analysis of polyclonal Fab – spike protein complexes isolated via microscale affinity chromatography from a single donor.** (a) Micrograph of the negatively stained specimen. (b) selected 2d classes depicting spike proteins with additional Fab fragment densities near the NTD. (c) 3D reconstruction of a closed spike protein trimer bound by a single Fab fragment targeting the top face of the NTD. A molecular model of the SARS-Cov-2 spike protein in the closed state is docked into the reconstruction (PDB 7DF3). The atomic model was docked into the reconstruction map in ChimeraX using the fit in map function.

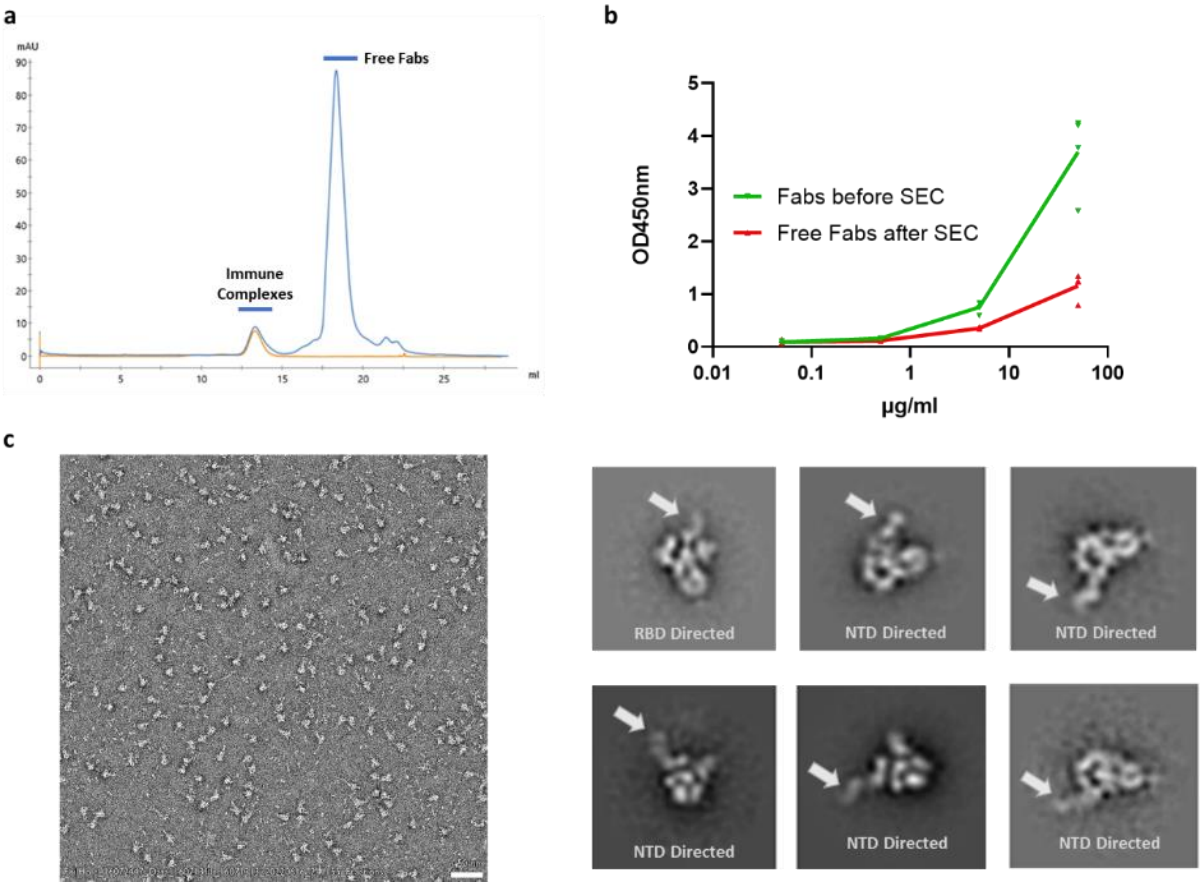

Figure 2.12. **Biochemical and Negative stain electron microscopic analysis of polyclonal Fab – spike protein complexes prepared using pooled serum.** (a) Size exclusion chromatogram traces of spike protein alone (orange) and spike protein – polyclonal Fab mixture (blue). The peak corresponding to free Fab fragments and immune complexes are annotated. (b) ELISA analysis of spike protein reactivity in bulk polyclonal Fabs before incubation with spike protein and in the free Fab fragment fraction after incubation with spike protein and size exclusion chromatography (SEC). The assay was performed in technical triplicate (n=3) and is shown as individual points. (c) Representative negative stain micrograph and selected 2D class averages from electron microscopic analysis of the immune complexes isolated. Fab fragment densities are highlighted and annotated based on the putative domain recognized.

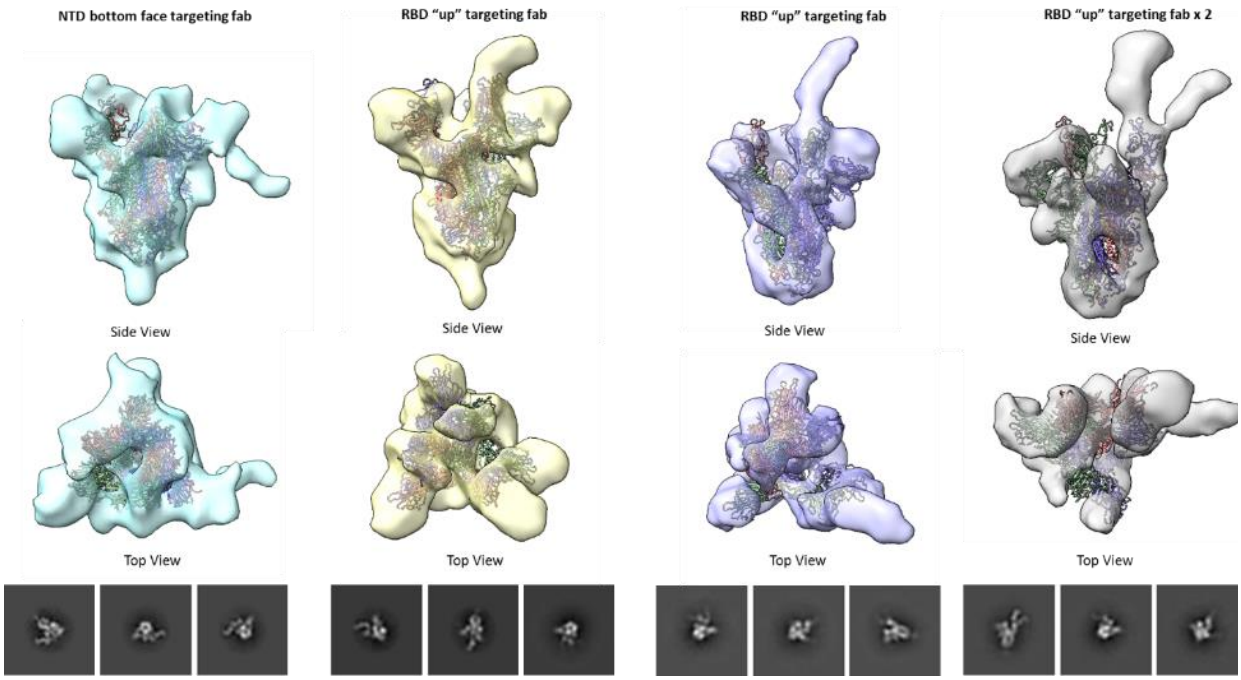

Figure 2.13. **Negative stain electron microscopic analysis of polyclonal Fab – spike protein complexes prepared from a single donor.** Side view and top views for each unique 3D reconstruction are shown, with representative 2D class averages below. Annotation of the antigenic regions recognized by Fab fragments in each reconstruction is provided at the top. Molecular models of spike proteins in various conformations are docked into each reconstruction (NTD bottom face reconstruction: open trimer with one RBD up and 2 down, PDB 6VYB, all others: open trimer with 3 RBDs up, PDB 7A98). The atomic models were docked into the reconstruction map in ChimeraX using the fit in map function.

Encouraged by our NSEM results we next sought to perform cryo-electron microscopy to better visualize the interactions made by polyclonal Fabs and the spike protein. To this end we concentrated the complexes formed from the single donor experiment and performed cryo-EM analysis (Figure 2.14). We first obtained a spike protein map imposing C3 symmetry, with the goal of performing symmetry expansion and focused 3D classification. Our initial map reached a global resolution of 2.66 Å, although it is clear that features of the RBD and NTD are poorly defined, likely due to the inherent flexibility of these regions and the averaging of multiple conformations. In contrast, the core S2 region of the spike protein is clearly visualized at high resolution (Figure

2.14c), demonstrating the dominance of this region during particle alignment. For 3D classification, we employed spherical masks covering either the RBD or the NTD regions (Figure 4e). We were unsuccessful at identifying any NTD bound classes, and we could only identify a single putative RBD bound class (Figure 4f-e). This class appears to have density corresponding to the variable regions of a Fab fragment bound to an RBD in the "down" position, although density for this region is relatively weak compared to the S2 core of the spike. Local refinement of this region did not appreciably improve the weak density and low resolution at this interface. Additional in-depth data processing methods will be required to confidently identify and visualize the numerous Fab-spike protein classes within this sample via cryo-EM.

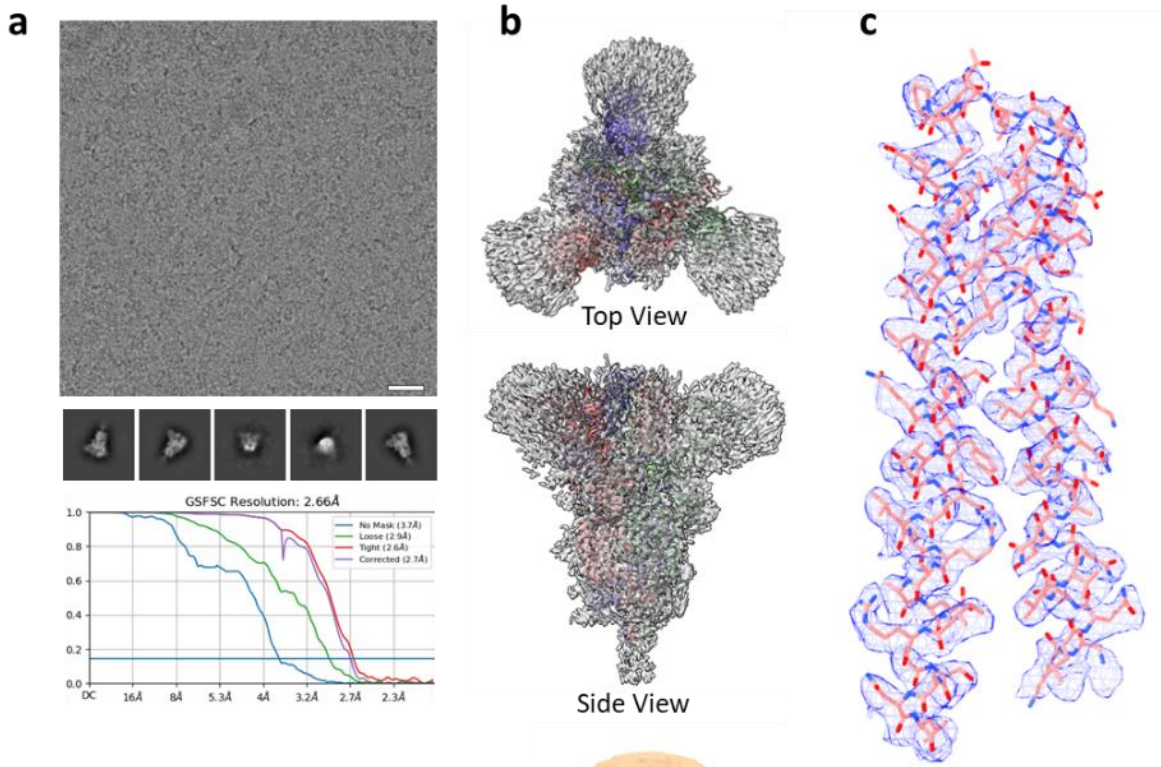
a
b
c
Top View
Side View
GSFSC Resolution: 2.66Å
No Mask (3.7Å)
Loose (2.9Å)
Tight (2.6Å)
Corrected (2.7Å)
1.0
0.8
0.6
0.4
0.2
0.0
DC
16Å
8Å
5.3Å
4Å
3.2Å
2.7Å
2.3Å
d
e
f
g

Figure 2.14. **Cryo-electron microscopic analysis of polyclonal Fab – spike protein complexes prepared from a single donor.** (a) Representative cryo-electron micrograph of the sample, selected 2D class averages corresponding to spike protein particles, and gold-standard Fourier shell correlation (GSFSC) resolution estimate of resulting global reconstruction presented in (b). (b) top and side views of resulting reconstruction with imposed C3 symmetry. The atomic model of SARS-CoV-2 S trimer in a closed state (PDB 7DF3) is fit within the map. (c) map quality and resolution within the S2 core. Residues 946-1024 from the model in b) are presented along with the experimentally determined map for a single protomer. (d-e) map and masks used for focused classification on symmetry expanded particles. A map covering a single RBD region (brown) and NTD region (green) were selected. (f) 3D reconstruction of a putative Fab-spike protein complex after 3D classification using an RBD mask. (g) Focused view of the putative Fab-RBD region. The RBD from the model in b) is shown in orange, along with corresponding RBD density from (f), and an atomic model for a generic Fab fragment coloured in blue (PDB 7FAB) is fit into the putative Fab density from (f). The atomic models were docked into the reconstruction maps in ChimeraX using the fit in map function.

In this chapter we have explored both neutralizing and non-neutralizing antibodies which bind the SARS-CoV-2 spike protein. Our analysis on glycan-reactive anti-gp120 antibodies underscores the potential for cross-reactive antibodies to bind but not neutralize SARS-CoV-2. Our results suggest that glycans on the SARS-CoV-2 spike protein do not represent an isolated vulnerability in general, although combined glycan-protein features may comprise important neutralizing epitopes for some SARS-CoV-2 directed antibodies. We have provided structural insights to the mechanism of receptor competition by 2 potent RBD directed neutralizing antibodies, highlighting differences in RBD positioning requirements for antibody binding. Our serological analysis revealed strong correlations between the level of NTD and RBD directed polyclonal antibodies, suggesting the presence of important neutralizing epitopes within these regions. Finally, we have developed methods to structurally characterize polyclonal Fab fragments bound to spike proteins, further confirming the antigenicity of the NTD and RBD. We found that patient derived polyclonal antibodies recognize the NTD and RBD at multiple sites, highlighting the vulnerability of these domains. Importantly, we observed some recurrent structural features of spike protein directed polyclonal Fabs across our experiments using different sera (see the bottom face NTD targeting

Fab reconstruction in Figure 2.13 and the 2D class average in Figure 2.12 for example). This demonstrates the existence of public antibody responses targeting the NTD and RBD across individuals, at the level of antigen recognition. Overall, the data presented in this chapter contribute to a growing body of evidence demonstrating that neutralizing antibodies target the NTD and RBD at multiple sites and in multiple conformations[106–108,110–113].

2.3 Methods

2.3.1 Cell culture and DNA constructs

Expi293 cells were purchased from Thermo Fisher Scientific (Cat# A14527) and cultured in Expi293 expression medium, according to the manufacturer's specifications. HEK293T cells (ATCC CRL-3216) were a kind gift from Dr. Annie Vogel Ciernia. HEK293T-ACE2 cells were obtained from BEI resources (NR-52511). HEK293T and HEK293T-ACE2 cells were cultured at 37 °C, 5% CO2 in Dulbecco's Modified Eagle medium (DMEM) supplemented with 10% fetal bovine serum (FBS) and 100 U/mL of penicillin–streptomycin. The codon-optimized SARS-CoV-2 2P S protein ectodomain construct (GenBank: YP_009724390.1) was C-terminally tagged with 8xHis and a twin Strep-tag and cloned into the mammalian expression vector pcDNA 3.1 (Synbio). The full-length SARS-CoV-2 S construct, pTwist-EF1alpha-SARS-CoV-2-S-2xStrep-IRES-Puro was a gift from Dr. Nevan Krogan. The SARS-CoV-2 hexapro construct was a kind gift from Jason McLellan.

C-terminal 7x his tagged NTD (amino acids 1–305) and RBD (amino acids 319–541) constructs were PCR amplified from full-length spike ORFs. NTD constructs were cloned into pcDNA 3.1 using NheI and MssI restriction enzyme cloning, while the RBD constructs were introduced in

frame to the mu phosphatase signal sequence and incorporated within pcDNA3.1 via Gibson assembly (NEBuilder HiFi DNA Assembly Cloning Kit, New England Biolabs).

2.3.2 Monoclonal Antibodies

All anti-gp120 IgG antibodies were obtained through the NIH AIDS Reagent Program, Division of AIDS, NIAID, NIH: Anti-HIV-1 gp120 Monoclonal (2G12) from Polymun Scientific, Anti-HIV-1 gp120 Monoclonal (PG9) from IAVI (cat# 12,149), Anti-HIV-1 gp120 Monoclonal (PG16) from IAVI, Anti-HIV-1 gp120 Monoclonal (PGT121) from IAVI (cat# 12,343), Anti-HIV-1 gp120 Monoclonal (PGT128) from IAVI (cat# 13,352), Anti-HIV-1 gp120 Monoclonal (PGT145) from IAVI (cat# 12,703), Cat# 12,586 Anti-HIV-1 gp41/gp120 Monoclonal (35O22), from Drs. Jinghe Huang and Mark Connors, Anti-HIV-1 gp120 Monoclonal (10-1075) from Dr. Michel C. Nussenzweig (cat# 12,477), Anti-HIV-1 gp120 Monoclonal (VRC01), from Dr. John Mascola (cat# 12,033), Anti-HIV-1 gp120 Monoclonal (VRC03), from Dr. John Mascola (cat# 12,032). ab8 and ab1 constructs were a gift from Dr. Dimiter S. Dimitrov.

2.3.3 Protein expression and purification

To express the SARS-CoV-2 2P S ectodomain, or the SARS-CoV-2 Hexapro ectodomain, NTD, and RBD constructs, Expi293 cells were transfected at a density of 3 × 106 cells/ml using linear polyethylenimine (PEI) (Polysciences). For Kifunensine treatment, cultures were treated with 5 μM Kifunensine 3 h post-transfection. At 24 h post-transfection, cultures were supplemented with 2.2 mM valproic acid. The supernatant was harvested by centrifugation after 5 days, filtered and loaded onto a 5 mL HisTrap Excel column (Cytiva). The column was washed with buffer (20 mM Tris pH 8.0, 500 mM NaCl, 20 mM imidazole) and the protein was eluted with buffer (20 mM Tris pH 8.0, 500 mM NaCl, 500 mM imidazole). Purified protein was concentrated and loaded onto a

Superose 6 column (Cytiva) equilibrated with GF buffer (20 mM Tris pH 8.0 and 150 mM NaCl). Peak fractions were pooled, concentrated and flash frozen. Freestyle293 cells were used to express the SARS-CoV-2 2P S ectodomain for the ab8-spike protein negative stain studies.

For purification of the RBD and NTD constructs, the supernatant was harvested after 7 days of expression and incubated with 300 µL of Ni-NTA resin (Qiagen) at 4 °C overnight. The resin was washed three times with 5 mL of PBS, then three times with 5 mL of PBS supplemented with 20 mM of imidazole. Proteins were eluted in PBS containing 300 mM of imidazole and then buffer exchanged into PBS and concentrated to 5–10 mg/mL (Amicon Ultra 10 kDa cut off, Millipore Sigma) before flash freezing and storage at −80 °C.

2.3.4 Enzyme-linked immunosorbent assay (ELISA)

For cross-reactive antibody binding studies, 100 µl of SARS-CoV-2 2P S protein preparations were coated onto 96-well MaxiSorp plates at 1 µg/ml in PBS overnight at 4 °C. All washing steps were performed 5 times with PBS + 0.05% Tween 20 (PBS-T). After washing, wells were either incubated with BSA-based blocking buffer (PBS-T + 2% BSA) or Casein-based blocking buffer (TBS + 0.05% Tween 20 + 1% Casein) for 1 h at room temperature. After washing, wells were incubated with dilutions of primary antibodies in either BSA-based blocking buffer or Casein-based blocking buffer for 2 h at room temperature. After washing, wells were incubated with goat anti-human IgG (Jackson ImmunoResearch) at a 1:10,000 dilution in either BSA-based blocking buffer or Casein blocking buffer, for 1 h at room temperature. After washing, the substrate solution (Pierce 1-Step) was used for colour development according to the manufacturer's specifications. Optical density at 450 nm was read on a Varioskan Lux plate reader (Thermo Fisher Scientific). The same protocol was conducted for methyl α-d-mannopyranoside competition assays, keeping

the concentration of the indicated primary antibodies at 5 µg/ml while including dilutions of methyl α-d-mannopyranoside as indicated.

For ACE2-antibody competition studies, wells were coated as stated above using the SARS-CoV-2 hexapro ectodomain and either antibodies or ACE2-mFC (Sino Biological) was incubated in PBST+1% BSA for 1hr at room temperature before washing, then incubation with ACE2-mFC or antibodies occurred in PBST+1% BSA for 1 hr at room temperature. After washing, either goat anti-human IgG (Jackson ImmunoResearch) or Goat Anti-Mouse IgG Fc Secondary Antibody, HRP (Invitrogen) in PBS-T + 0.5% BSA buffer was added for 1 h at room temperature. After washing signal was developed as above.

For polyclonal antibody binding analyses, wells were coated as above using the SARS-CoV-2 hexapro ectodomain and NTDs, and RBDs were coated onto wells at 2 µg/mL in PBS + 1% casein overnight at 4 °C., All washing steps were performed 3 times with PBS + 0.05% Tween 20 (PBS-T). After washing, wells were incubated with blocking buffer (PBS-T + 1% casein) for 1 h at room temperature. After washing, wells were incubated with dilutions of sera in PBS-T + 1% Casein buffer for 1 h at room temperature. After washing, wells were incubated with goat anti-human IgG, IgM, or IgA (Jackson ImmunoResearch) at a 1:8000 dilution in PBS-T + 1% casein buffer for 1 h at room temperature. After washing, signal was developed as above.

2.3.5 Western blotting

Either purified or unpurified SARS-CoV-2 2P spike ectodomain was subjected to SDS-PAGE and transferred onto nitrocellulose membranes prior to blocking in TBS + 0.05% Tween 20 (TBS-T) + 2% BSA for 1 h at room temperature. Membranes were then incubated with the indicated anti-gp120 antibodies at 2 µg/ml in TBS-T + 2% BSA overnight at 4 °C. After washing,

membranes were incubated with goat anti-human IgG (Jackson ImmunoResearch) at a 1:5,000 dilution in TBS-T + 2% BSA for 1 h at room temperature. After washing, membranes were visualized using SuperSignal chemiluminescent substrate (Thermo Fisher Scientific).

2.3.6 Cell-based ELISA

HEK293T cells were seeded in 96 well plates and transfected with either a plasmid encoding the full-length SARS-CoV-2 spike (pLVX-EF1alpha-SARS-CoV-2-S-2xStrep-IRES-Puro) or mock plasmid (pcDNA3.1) using branched PEI (Sigma). Media was switched 24 h post-transfection. At 48 h post-transfection, cells were washed 5 times with PBS prior to fixation with 4% paraformaldehyde in media for 30 min at 4 °C. All further washing steps were performed 5 times with PBS + 0.05% Tween 20 (PBS-T). Cells were washed prior to blocking in blocking buffer (PBS-T + 2% BSA) for 1 h at room temperature. After washing, cells were incubated with dilutions of primary antibodies in blocking buffer for 2 h at room temperature. After washing, cells were incubated with goat anti-human IgG (Jackson ImmunoResearch) at a 1:5,000 dilution in blocking buffer for 1 h at room temperature. After washing, substrate solution (Pierce 1-Step) was used for colour development according to the manufacturer's specifications. Optical density at 450 nm was read on a Varioskan Lux plate reader (Thermo Fisher Scientific). The difference in signals between cells transfected with full-length spike and mock plasmid was calculated.

2.3.7 Immunoprecipitations

Immunoprecipitations were performed using the Dynabeads immunoprecipitation kit (Invitrogen). 100 µL of Dynabeads was incubated with 10 µg of either PGT126, PGT128, 2G12, VRC01, or PBS + 0.05% Tween 20 (PBS-T) as a beads-only control for 30 min at room temperature. Cellular lysates were generated from HEK-293 T cells transiently expressing full-length SARS-CoV-2

spike (transfections as described for cell-based ELISA). Cells were solubilized in ice-cold 20 mM Tris–HCl, pH 7.4, 150 mM NaCl, 1 mM EDTA and 1% Triton X-100 with 1 mM PMSF added fresh, and further disrupted via sonication. Lysates were then centrifuged at 12,000 g for 2 min and the supernatant was retrieved for immunoprecipitation input. After washing 3 times with 1 ml of PBS-T, antibody-bead complexes were incubated with lysate for 1 h at room temperature on a rocking platform. Beads were washed 3 times with PBS-T and bound proteins were eluted directly into 4 × Laemmli buffer with 10% dithiothreitol and boiled. The samples were then subjected to Western blot analysis and detected using an anti-SARS-CoV-2 spike glycoprotein antibody (Abcam–ab27504) or an anti-strep tag antibody (Bio-Rad–MCA2489).

2.3.8 Pseudo-virus Neutralization Assay

SARS-CoV-2 S pseudotyped retroviral particles were produced in HEK293T. Briefly, a lentiviral packaging system was utilized in combination with plasmids encoding the full-length SARS-CoV-2 spike, along with a transfer plasmid encoding luciferase and GFP as a dual reporter gene. Pseudoviruses were harvested 60 h after transfection, filtered with 0.45 µm PES filters, and frozen. For cell-entry and neutralization assays, HEK293T-ACE2 cells were seeded in 96 well plates at 50,000 cells per well. The next day, pseudoviral preparations were incubated with dilutions of the indicated antibodies, serum, or media alone for 1 h at 37 °C prior to addition to cells and incubation for 48 h. Cells were then lysed and luciferase activity assessed using the ONE-Glo™ EX Luciferase Assay System (Promega) according to the manufacturer's specifications. Detection of relative luciferase units was carried out using a Varioskan Lux plate reader (Thermo Fisher Scientific). Percent neutralization was calculated relative to signals obtained in the presence of the virus alone for each experiment.

2.3.9 Negative Stain Electron Microscopy for the SARS-CoV-2 Spike-ab8 complex

Purified S protein ectodomain (0.04 mg/ml) was mixed with VH ab8 (0.02 mg/ml) and incubated on ice for 10 mins. The mixtures (4.8 µl) were applied to 300-mesh copper grids coated with continuous ultrathin carbon. Grids were plasma cleaned using an H2/O2 gas mixture for 15 s in a Solarus plasma cleaner (Gatan Inc.) prior to adding the sample. Samples were allowed to adsorb for 30 s before blotting away excess liquid, followed by a brief wash with MilliQ H2O. Grids were stained by three successive applications of 2% (w/v) uranyl formate (20 s, 20 s, 60 s). Grids were imaged using a 200 kV Glacios transmission electron microscope (ThermoFisher Scientific) equipped with a Falcon3 camera operated in linear mode. Using EPU automated acquisition software (ThermoFisher Scientific), 15-frame movies were collected at 92,000x magnification.

Motion correction and CTF estimation were performed in RELION (3.1). Particles were picked by crYOLO (1.7.4) with pre-trained model for negative stain data. After extraction, particles were imported to cryoSPARC live (v2.15.1) and subjected to 2D classification and 3D heterogeneous classification. Final density maps were obtained by 3D homogeneous refinement. Figures were prepared using UCSF Chimera.

2.3.10 Cryogenic Electron Microscopy for the SARS-CoV-2 Spike-ab1 complex

SARS-CoV-2 spike hexapro ectodomain preparations were deposited on grids at a concentration of 2.25 mg/ml. Complexes were prepared by incubating spike protein with Fab ab1 at a 1:8 molar ratio (spike trimer to ab1) for 20 minutes on ice prior to centrifugation at 14,000g for 10 minutes. Grids were plasma cleaned using an H2/O2 gas mixture for 15 s in a Solarus II Plasma Cleaner (Gatan) before 1.8 µl of protein suspension was applied to the surface of the grid. Using a Vitrobot Mark IV (Thermo Fisher Scientific), the sample was applied to UltrAuFoil Holey Gold 300 mesh

grids at a chamber temperature of 10°C with a relative humidity level of 100%, and then vitrified in liquid ethane after blotting for 12 s with a blot force of −10. All cryo-EM grids were screened using a 200-kV Glacios (Thermo Fisher Scientific) TEM equipped with a Falcon4 direct electron detector followed by high-resolution data collection on a 300-kV Titan Krios G4 (Thermo Fisher Scientific) TEM equipped with a Falcon4 direct electron detector in electron event registration (EER) mode.

Data processing was performed in cryoSPARC v.2.15 and v.3.0.1. Motion correction in patch mode, CTF estimation in patch mode, reference-free particle picking, and particle extraction were performed on-the-fly in cryoSPARC. After preprocessing, particles were subjected to 2D classification and 3D heterogeneous classification. The consensus maps were obtained by 3D homogeneous refinement. Structural analyses and figure generation were performed in ChimeraX.

2.3.11 Generation of Polyclonal Fab Fragments

First bulk IgG was isolated from sera as follows: sera was dilutied 5 times in PBS before incubation with Protein A Agarose (Thermo Fisher) for 1 hour at room temperature. After washing the resin with 5 column volumes (CVs) of PBS IgG was eluted batchwise with 100mM Glycine pH 3.5 immediately into $1/10^{th}$ of the elution volume of 1M Tris pH 8.0. Papin-agarose (Sigma) was then added to the IgG fractions and the mixture was supplemented to 10mM EDTA and 10mM L-Cystine. After incubation at 37 degrees overnight, the reaction was centrifuged to remove the papain-agarose. The supernatant was then added to Protein A agarose resin and allowed to incubate for 20 minutes to an hour at room temperature before the flow through was collected and the resin washed with 3 CVs. The wash and flow through fractions were pooled and Fabs were concentrated (Amicon Ultra 10 kDa cut off, Millipore Sigma) before storage at 4 degrees Celsius in 0.02% sodium azide.

2.3.12 Microscale Affinity Pulldowns of SARS-CoV-2 Spike Immune Complexes

20 microliters of Fab fragments at 1mg/ml were incubated with spike hexapro ectodomain at 15micrograms/ml along with 5 microliters of NiNTA-agarose (Qiagen) overnight at room temperature. The incubation was added to microcentrifuge tubes and spun down. The resin was washed with 500 microliters of PBS twice. Immune complexes were eluted in 5 microliters of PBS + 250mM Imidazole. The specimen was immediately negatively stained and data was collected as described for the s-ab8 complex.

2.3.13 Size Exclusion Chromatography Purification of Immune Complexes

For the Fab fragments generated from pooled samples, 60 micrograms of spike hexapro ectodomain was incubated with 1mg of Fabs in 100 microliters of PBS overnight at room temperature. For the Fab fragments generated from a single donor, 60 micrograms of spike hexapro ectodomain was incubated with 3mg of Fabs in 300 microliters of PBS overnight at room temperature. Size exclusion chromatography was performed using a Superose 6 Increase column (Cytiva) in PBS. Immune complexes were pooled and negatively stained and imaged as described above. For the Cryo-EM dataset, immune complexes were concentrated to 1.2mg/ml (Amicon Ultra 10 kDa cut off, Millipore Sigma) and deposited onto glow discharged Cu 200 R1.2/1.3 grids as described above. Data collection was performed on a 300-kV Titan Krios G4 (Thermo Fisher Scientific) TEM equipped with a Falcon4 direct electron detector in electron event registration (EER) mode.

2.3.14 Image Processing for Negative Stain Immune Complex Datasets

Data processing was performed in CryoSPARC v4.0.1. Patch motoion correction was performed, constant CTF values were output upon movie import. For the microscale affinity dataset, 449

particles were manually picked and used to generate templates for template picking. After several rounds of 2D classification, particles were selected for ab-inito reconstruction and subsequent homogenous refinement. For the pooled sample immune complexes isolated via size exclusion chromatography, blob picking was used, followed by 2D classification to generate templates for subsequent template picking. Several rounds of 2D classification on selected particles were then performed. For the immune complexes generated from a single donor and isolated via size exclusion chromatography, blob picking was employed followed by several rounds of 2D classification, ab-inito reconstructions, and either homogenous or heterogenous classification. Structural analyses, including docking of protein models within experimental maps using the "fit in map" function was performed in ChimeraX.

2.3.15 Image Processing for Cryo-EM Immune Complex Datasets

Data processing was performed in CryoSPARC v4.0.1. Patch motion correction was performed, followed by patch CTF estimation. Blob picking was employed followed by 2D classification, after which selected particles were subjected to ab-inito reconstruction, followed by heterogenous refinement with C3 symmetry imposed. Select classes were then subjected to homogenous refinement with C3 symmetry imposed. The class reaching high resolution (2.66 Å) in the core was then subjected to symmetry expansion, followed by multiple rounds of 3D classification using various spherical masks. The class showing putative Fab density was selected for homogenous reconstruction. Structural analyses, including docking of protein models within experimental maps using the "fit in map" function was performed in ChimeraX.

Chapter 3: Molecular Analysis of SARS-CoV-2 Spike Protein RBD Mutations

3.1 Introduction

As demonstrated in chapter 2, the SARS-CoV-2 spike protein RBD is an important antigenic target for neutralizing antibodies. In addition to harbouring neutralizing epitopes, the RBD itself plays a critical role in the viral replicative cycle as it is responsible for recognition of the receptor ACE2. As discussed in chapter 1, the exact molecular details of this interaction have been described through Xray crystallography studies[81,82], and cryo-EM studies[83] revealing an intricate network of interactions involving multiple residues which have been collectively dubbed the receptor binding motif (RBM) within the RBD. The structural details of the SARS-CoV-2 RBD in complex with ACE2 and several neutralizing antibodies permit an understanding of the role of RBD residues with regards to ACE2 binding and neutralizing epitope recognition. This adds crucial context in the monitoring of emergent variants of SARS-CoV-2 which harbour mutations within the spike protein RBD. Starting in late 2020, the world saw the emergence of several SARS-CoV-2 variants, such as the Alpha (B.1.1.7, first observed in the United Kingdom), Beta (B.1.351, first observed in South Africa), Gamma (P.1, first observed in Brazil), and Epsilon (B.1.427 and B.1.429, first observed in California) variants, which were identified by the CDC as either variants of concern (VoCs) or variants interest (VoIs) based on enhanced transmissibility and infectivity. These variants harboured RBD mutations, many of which fell within the RBM and several neutralizing epitopes, and which were conserved across several variants. This chapter aims to provide a molecular analysis of the effect of emergent RBD mutations on spike protein structure, ACE2 binding, and antibody recognition. The results of these efforts will be presented in the form of two manuscripts, in chronological order of publication as we responded to emerging RBD mutations in real time.

3.2 Results and Discussion

3.2.1 Studies on the N501Y Mutant Spike Protein

In December 2020, new variants of SARS-CoV-2 carrying several mutations in the spike protein were documented in the UK and South Africa[114], and were named "Alpha" and "Beta" variants respectively. Early epidemiological and clinical findings have indicated that these variants show increased transmissibility in the population[115]. Despite being phylogenetically distinct, a common feature of both the UK and South African variants is the mutation of residue 501 in the RBD from Asn to Tyr (N501Y). X-ray crystallography and Cryo-EM structural studies have identified N501 as a key residue in the spike protein at the interface between RBD and ACE2 that is involved in critical contacts with several ACE2 residues[81–83]. Studies carried out in a mouse model[116] and via deep mutational scanning[117] before the identification of the new UK variant suggested that mutations of residue 501 could be linked to increased receptor binding and infectivity. Understanding the impact of N501Y on antibody neutralization, ACE2 binding, and viral entry is therefore of fundamental interest in the efforts to prevent the spread of COVID-19.

3.2.1.1 Visualization of Y501 in contact with ACE2

To understand the structural effects of the N501Y mutation on ACE2 binding, we expressed and purified spike (S) protein ectodomains with and without the N501Y mutation and conducted microscopy studies on the ACE2–spike complexes. A cryo-EM structure of the spike protein ectodomain with the N501Y mutation was obtained at an average resolution of approximately 2.8 Å. The structure shows no significant global changes in secondary or quaternary structure as a result of the mutation when compared to the previously published structure of the spike protein

ectodomain with an Asn residue at position 501 (referred to here as the “unmutated” form (Figure 3.1).

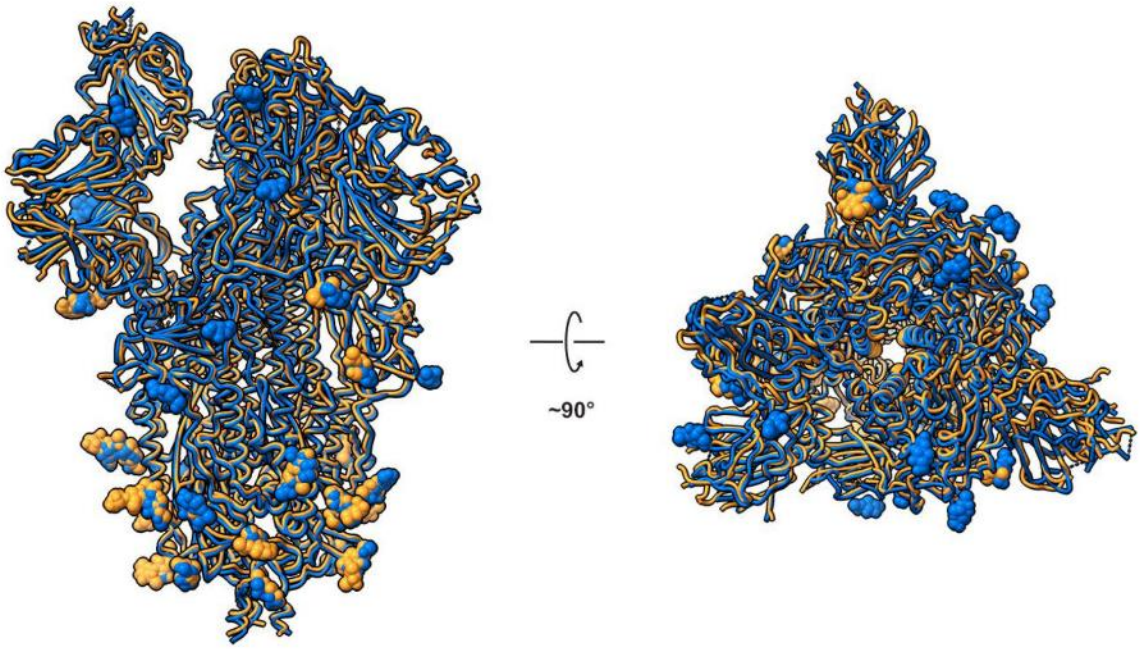

Figure 3.1. **Superposition of the structure of the N501Y spike protein ectodomains (**light orange) with the previously published structure of the unmutated construct (blue; PDB ID 6XKL).

Cryo-EM structural analysis of the complex formed between the N501Y spike protein ectodomain and the ACE2 receptor ectodomain provides a detailed glimpse of both the overall structure of the receptor and the binding interface between the RBD and ACE2 (Figure 3.2). The ACE2 receptor is bound to the “up” position of the RBD (Figure 3.2a). The overall structure of the complex was determined at a global resolution of 2.9 Å. Local refinement of the RBD–ACE2 interface improves the local resolution at the binding interface to approximately 3.3 Å (Figure 3.2b), resulting in unambiguous delineation of the Y501 side chain and other residues in the vicinity (Figure 3.2c). The overall structure at the binding site is almost identical to that of the unmutated version (Figure

3.2d) with the exception of local rearrangements that result in the aromatic ring of Y501 being accommodated in a cavity that is sandwiched between Y41 and K353 of the ACE2 receptor (Figure 3.2e). Y501 in the spike protein and Y41 in the ACE2 receptor form a perpendicular y-shaped π–π stacking interaction[118].

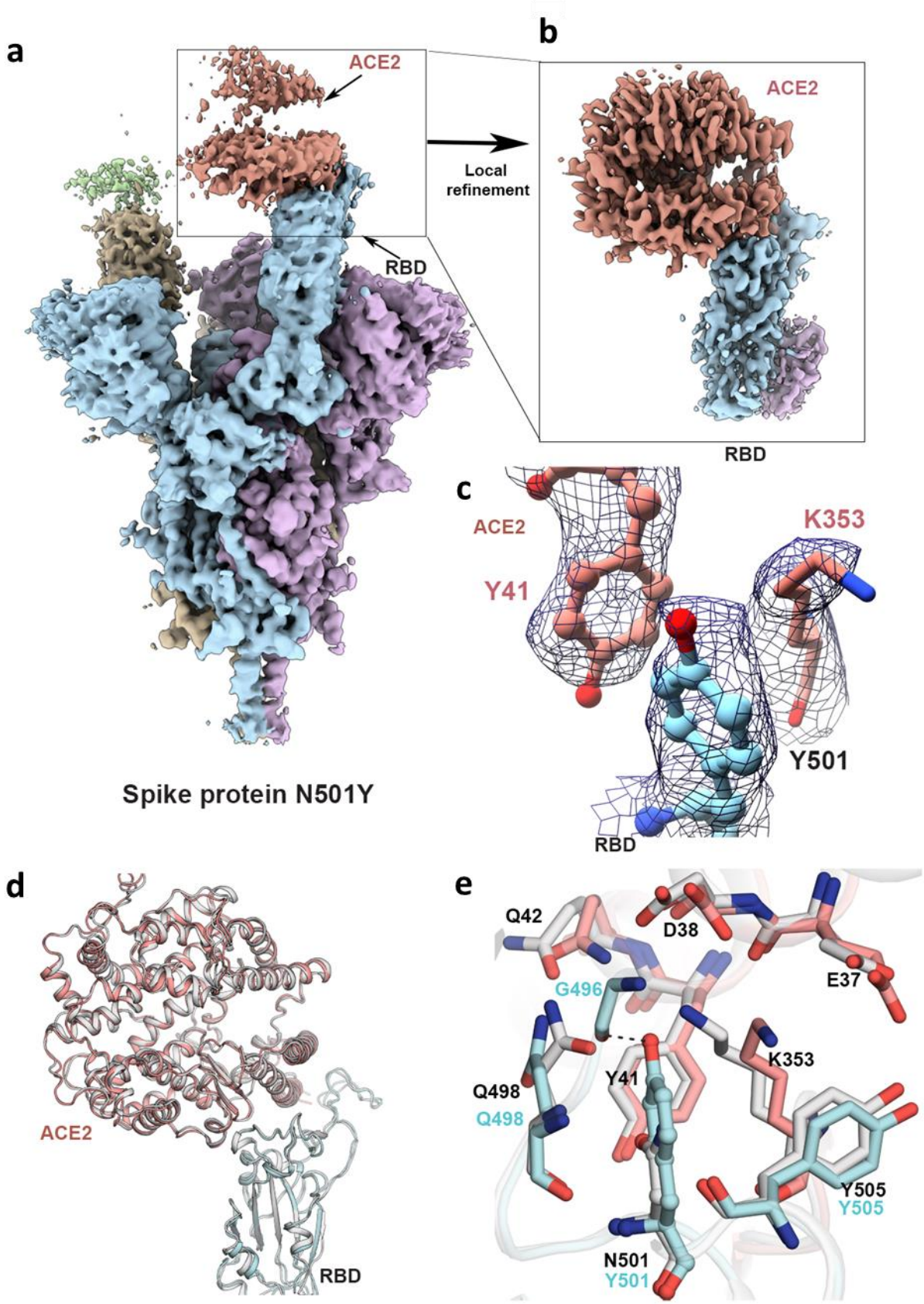
a
ACE2
RBD
Local refinement
b
ACE2
RBD
Spike protein N501Y
c
ACE2
K353
Y41
Y501
RBD
d
ACE2
RBD
e
Q42
D38
E37
G496
K353
Y41
Q498
Q498
Y505
Y505
N501
Y501

Figure 3.2. **Structure of the SARS-CoV-2 N501Y mutant spike protein ectodomain bound to the ACE2 ectodomain.** (a) Density map for the overall complex at the end of global structure refinement. The 3 spike protein protomers are colored in cyan, purple, and yellow, with the density for the strongly and weakly bound ACE2 proteins in pale red and green, respectively. (b) Improved density map at the contact zone between the receptor binding domain (RBD) and the strongly bound ACE2 protein ectodomain. (c) Visualization of density at the contact zone for Y501 in the RBD and residues Y41 and K353 in ACE2. (d). Ribbon diagram with superposition of the unmutated and N501Y RBD–ACE2 complex (PDB ID 7KMB). (e) Zoomed-in view of the interface, showing a superposition of the structures of unmutated and N501Y mutant spike proteins in complex with ACE2. The carbon atoms of residues in the N501Y mutant and ACE2 in our structure are colored in cyan and pale red, respectively, while those in the structure of the complex between unmutated spike protein and ACE2 are in light gray.

Potent neutralization of SARS-CoV-2 has been achieved with a number of antibodies, including 2 recently reported examples, V_H Fc ab8 and IgG ab1, both derived from a large human library of antibody sequences and introduced in chapter 2. We compared the efficiencies of these 2 antibodies, as well as the ACE2 receptor ectodomain, to bind spike proteins with and without the N501Y mutation. We also determined the relative efficiency of neutralization of pseudoviruses expressing either the N501Y mutant or unmutated form of the spike protein.

3.2.1.2 The N501Y mutation confers increased ACE2 binding affinity

To test the influence of the N501Y mutation on ACE2 binding, we used a luciferase reporter to measure the infectivity of pseudotyped viruses presenting N501Y or unmutated spike proteins for cells overexpressing ACE2 (Figure 3.3). The higher relative luminescence unit (RLU) intensity from cells infected by the N501Y mutant compared to control viruses expressing the unmutated form suggests that the N501Y mutation may result in increased infectivity, assuming equal incorporation of spike proteins within the pseudotyped particles utilized. This finding is in agreement with a recent report demonstrating increased cell entry of pseudoviral particles incorporating the N501Y and D614G mutations relative to D614G alone[119]. To investigate whether

the N501Y mutation increases the binding strength of the SARS-CoV-2 spike to ACE2, we measured the binding parameters between ACE2 and either unmutated or N501Y spike protein ectodomain trimers via biolayer interferometry (BLI). This revealed that the N501Y mutation confers a modest increase in affinity for ACE2, mainly driven by a reduction in the dissociation rate constant (k_{off}) (Figure 3.3). Notably, several studies have demonstrated that the N501Y mutation confers much larger increases (3- to 16-fold) in ACE2 binding affinity when using minimal RBD constructs[120–122]. We also measured the efficiency of exogenously added soluble ACE2-mFc proteins to neutralize unmutated and N501Y pseudoviruses via preincubation prior to cell infection (Figure 3.3b). The comparison of neutralization profiles shows that the IC_{50} for neutralization of the N501Y mutant is lower, suggesting that full-length spikes bearing the N501Y mutation bind ACE2-mFc to a higher extent. Taken together, these 3 results are consistent with the hypothesis that the greater infectivity of the N501Y mutant stems from improved binding to ACE2.

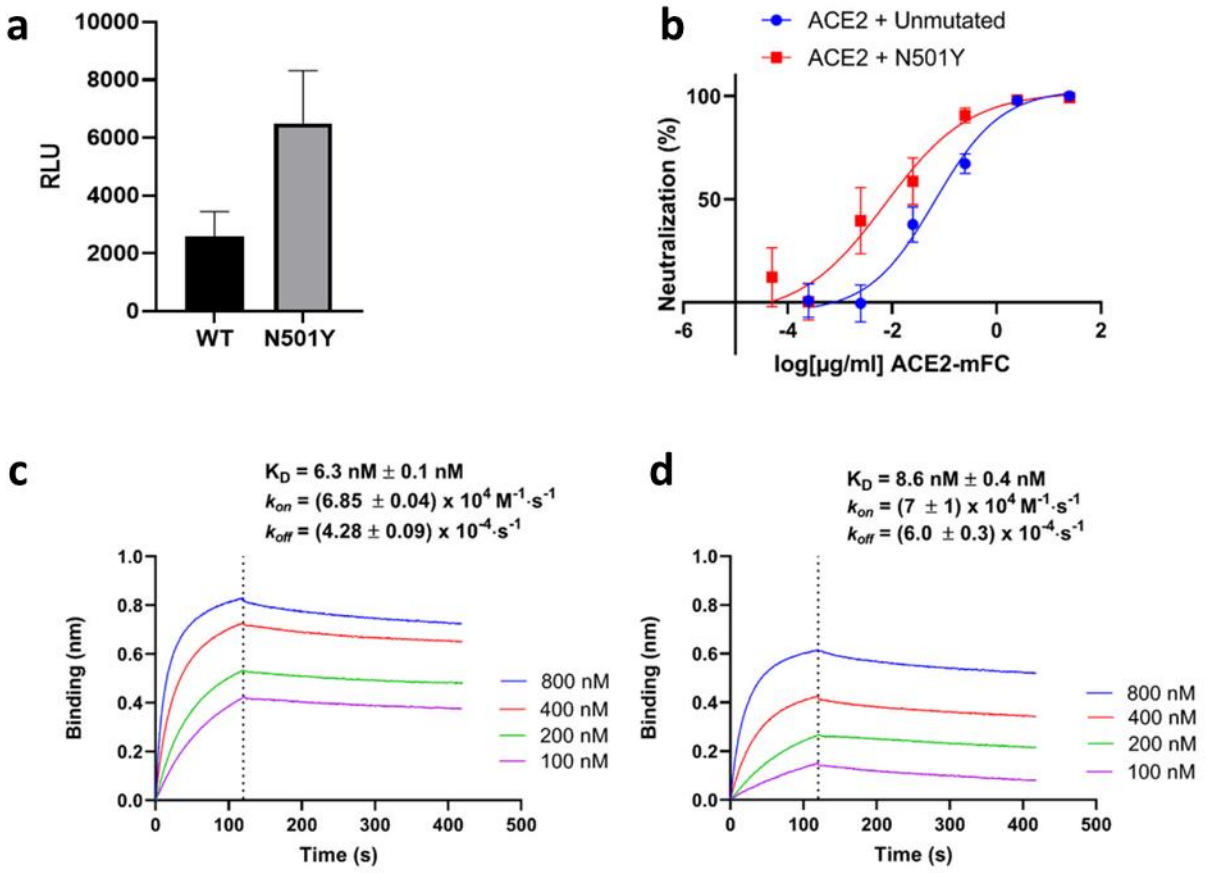

Figure 3.3. **Analysis of ACE2 interactions with N501Y and unmutated spike.** (a) Analysis of cell entry of N501Y or unmutated SARS-CoV-2 S pseudotyped viral particles. N501Y or unmutated SARS-CoV-2 S pseudotyped virus was normalized for p24 levels and incubated with HEK293T-ACE2 cells for 48 h prior to cell lysis and luciferase activity quantification. (RLU: relative luminescent units). (b) Analysis of N501Y or unmutated SARS-CoV-2 S pseudotyped virus neutralization by soluble ACE2-mFC. The IC_{50} of soluble ACE2-mFC neutralization is 0.066 µg/ml (95% CI 0.026–0.17 µg/ml) for unmutated pseudotyped virus, and 0.0074 µg/ml (95% CI < 0.043 µg/ml; lower bound not accurately determined) for N501Y pseudotyped virus. (c and d) Biolayer interferometry analysis of immobilized ACE2 binding by increasing concentrations of either N501Y (a) or unmutated (b) spike ectodomain. Shown is the extent of binding as determined by shift in wavelength (nm: nanometers). Biophysical parameters (K_D, k_{on}, k_{off}) are shown as mean ± standard deviation.

3.2.1.3 N501Y has minimal effects on the binding and potency of 2 neutralizing antibodies with RBD epitopes

Next, we tested the effect of the N501Y mutation on the relative strengths of binding and neutralization potency of V_H Fc ab8 and IgG ab1 (Figure 3.4). ELISA analysis of IgG ab1 and V_H Fc ab8 interactions with unmutated or N501Y spike ectodomains demonstrates that the N501Y mutation has no significant effect on V_H Fc ab8 binding but results in a slightly higher EC_{50} for IgG ab1 (Figure 3.4a). Second, competition experiments establish that IgG ab1 more efficiently prevents ACE2 binding of the unmutated ectodomain compared to the N501Y mutant (Figure 3.4c), while V_H Fc ab8 prevents ACE2 binding of unmutated and N501Y mutant spike proteins to similar extents (Figure 3.4d). Consistent with these measurements, neutralization experiments carried out with V_H Fc ab8 show that it can neutralize the N501Y mutant with a potency similar to that of the unmutated form, while IgG ab1 exhibits a slightly diminished neutralization potency for the N501Y mutant relative to pseudo-viruses expressing the unmutated form (Figure 3.4b). Overall, binding and neutralization analyses show that the N501Y mutation results in enhanced ACE2 binding, minimal effects on the binding and potency of V_H Fc ab8, and a small reduction in the binding and potency of IgG ab1.

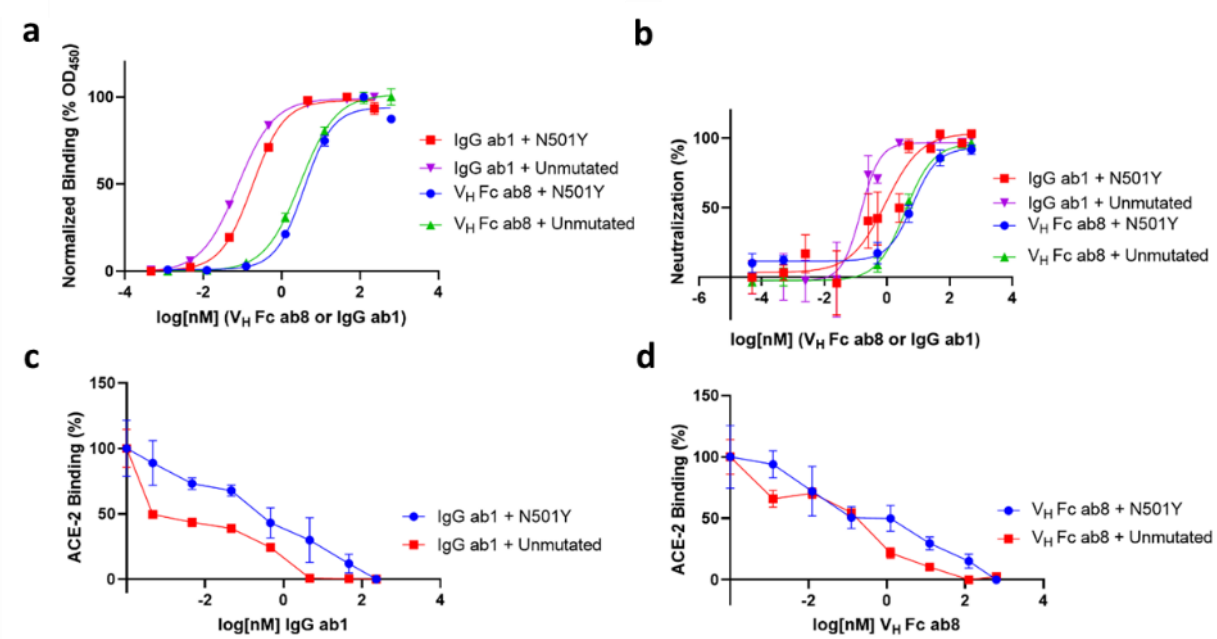

Figure 3.4. **Analysis of V_H Fc ab8 and IgG ab1 interactions with N501Y and unmutated spike.** (a) ELISA analysis of antibody interactions with either N501Y or unmutated spike ectodomain. (b) N501Y or unmutated SARS-CoV-2 S pseudotyped virus neutralization by either V_H Fc ab8 or IgG ab1. (C and D) ELISA analysis of N501Y or unmutated SARS-CoV-2 spike ectodomain binding by soluble ACE2-mFc in the presence of serial dilutions of either (c) IgG ab1 or (d) V_H Fc ab8. ELISA experiments were done at least in duplicate while neutralization experiments were performed twice at least in duplicate, and the average values are shown. Error bars denote the standard error of the mean (SEM).

3.2.1.4 Neutralizing antibodies bind N501Y spikes in different conformational states

To understand the effects of these antibodies at a structural level, we next determined cryo-EM structures of the complexes formed by V_H ab8 (variable domain of the bivalent fusion construct V_H FC Ab8) and Fab ab1 (the antigen binding fragment of IgG ab1) with the N501Y mutant spike protein ectodomain. Cryo-EM structural analysis of the complex formed between V_H ab8 and the N501Y spike protein ectodomain shows a single dominant conformation with 2 V_H ab8 fragments bound to RBDs in the down conformation and weak density for the other RBD, which is flexible

and primarily in the up position (Figure 3.5a). This architecture is similar to the negative stain electron microscopic analysis performed on the unmutated spike in chapter 2. The global average resolution of the map is approximately 2.8 Å, with lower local resolution in the RBD regions, but local refinement yields maps of the V_H ab8–RBD interface at a resolution of approximately 3 Å (Figure 3.5b). Cryo-EM density maps unambiguously show the location of residue 501 in the N501Y mutant spike protein ectodomains (Figure 3.5c). The interface between the RBD and V_H ab8 is well defined, with key interactions at the interface mediated by residues in the stretch between V483 and S494, along with a few other interactions contributed by non-contiguous RBD residues (Figure 3.5 d-e)). Residue 501 of the spike protein RBD is at the periphery of the footprint of V_H ab8 and shows no evidence of interactions with the antibody. The presence of the mutation thus appears not to influence interactions between the RBD and V_H ab8.

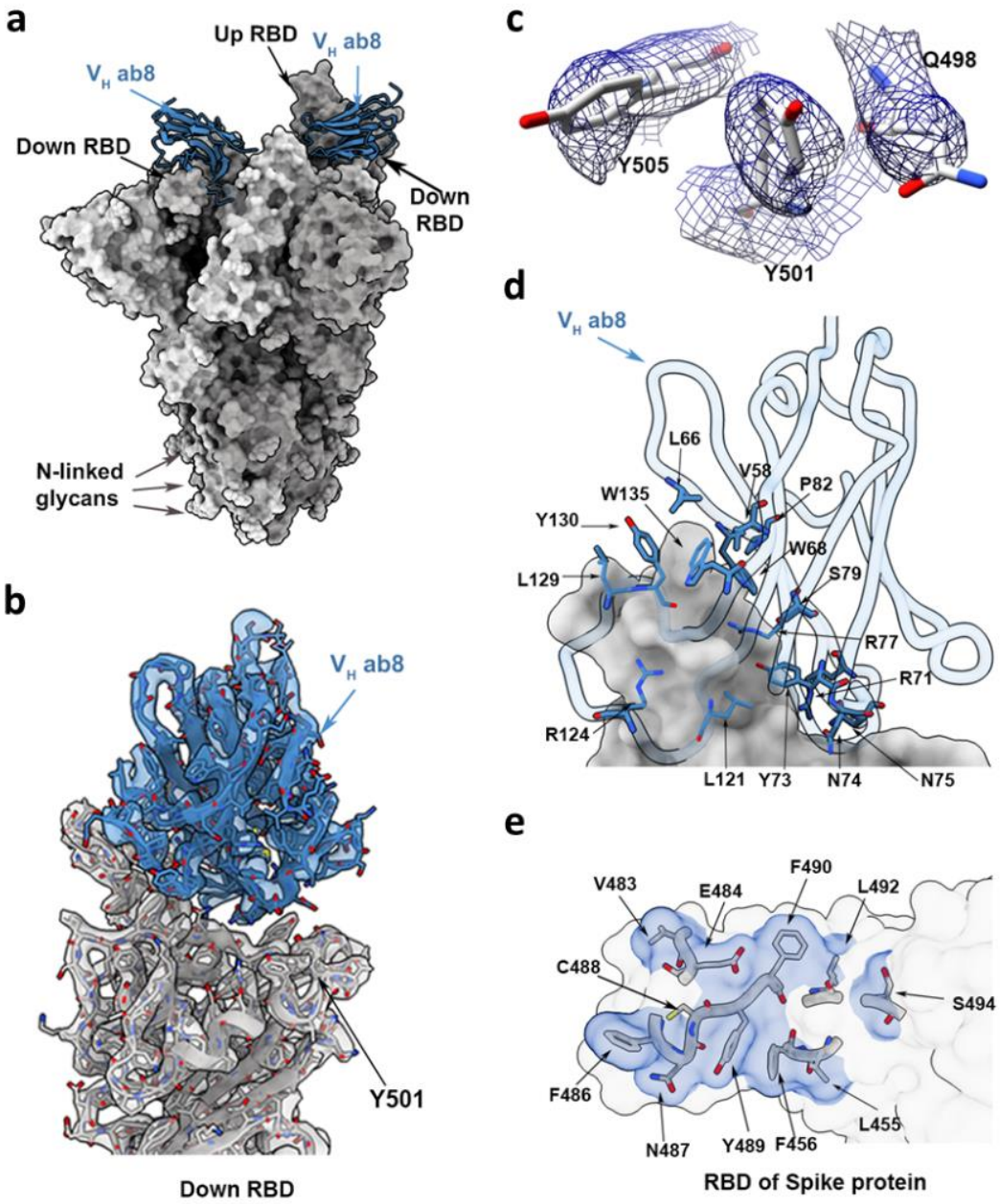

Figure 3.5. **Structure of V_H ab8 bound to the N501Y mutant spike protein trimer.** (a) Atomic model for the structure of the complex of V_H ab8 (blue) with the N501Y mutant spike protein ectodomain (gray). The structure has 2 receptor binding domains (RBDs) in the down position with well-resolved densities for the bound V_H ab8. The third RBD is in the up position. (b) Cryo-electron microscopy density map after local refinement with fitted coordinates for the contact zone between the RBD and V_H ab8. (c) Density map in the region near 501 for the N501Y mutant spike protein ectodomain showing density for residues Q498, Y501, and Y505. (d and e) Close-up views of the contact zone between the RBD region and ACE2 highlighting residues involved.

Similar cryo-EM analyses of the complex between the mutated spike protein and Fab ab1 show that in contrast to the V_H ab8 complex, Fab ab1 binding involves either 2 or 3 RBDs, all being in the up position, similar to the architectures resolved in chapter 2 using unmutated spike protein. (Figure 3.6a-b). Local refinement of the RBD–Fab ab1 interface improves the resolution to approximately 3 Å, enabling unambiguous placement of Y501 as well as the residues involved in the contact between the RBD and Fab ab1 (Figure 4.6c-d). Residue 501 is at the periphery of the Fab ab1 footprint, with Ser 30 of Fab ab1 in a position to interact with this residue (Figure 4.6e-f). The N501Y mutation would thus be expected to have a small effect on the antibody binding epitope. Together, the cryo-EM structures are fully consistent with the studies presented in Figure 3.4 that show a small but significant effect of the N501Y mutation on Fab ab1 binding and neutralization, but with no measurable effects on V_H ab8 binding or neutralization.

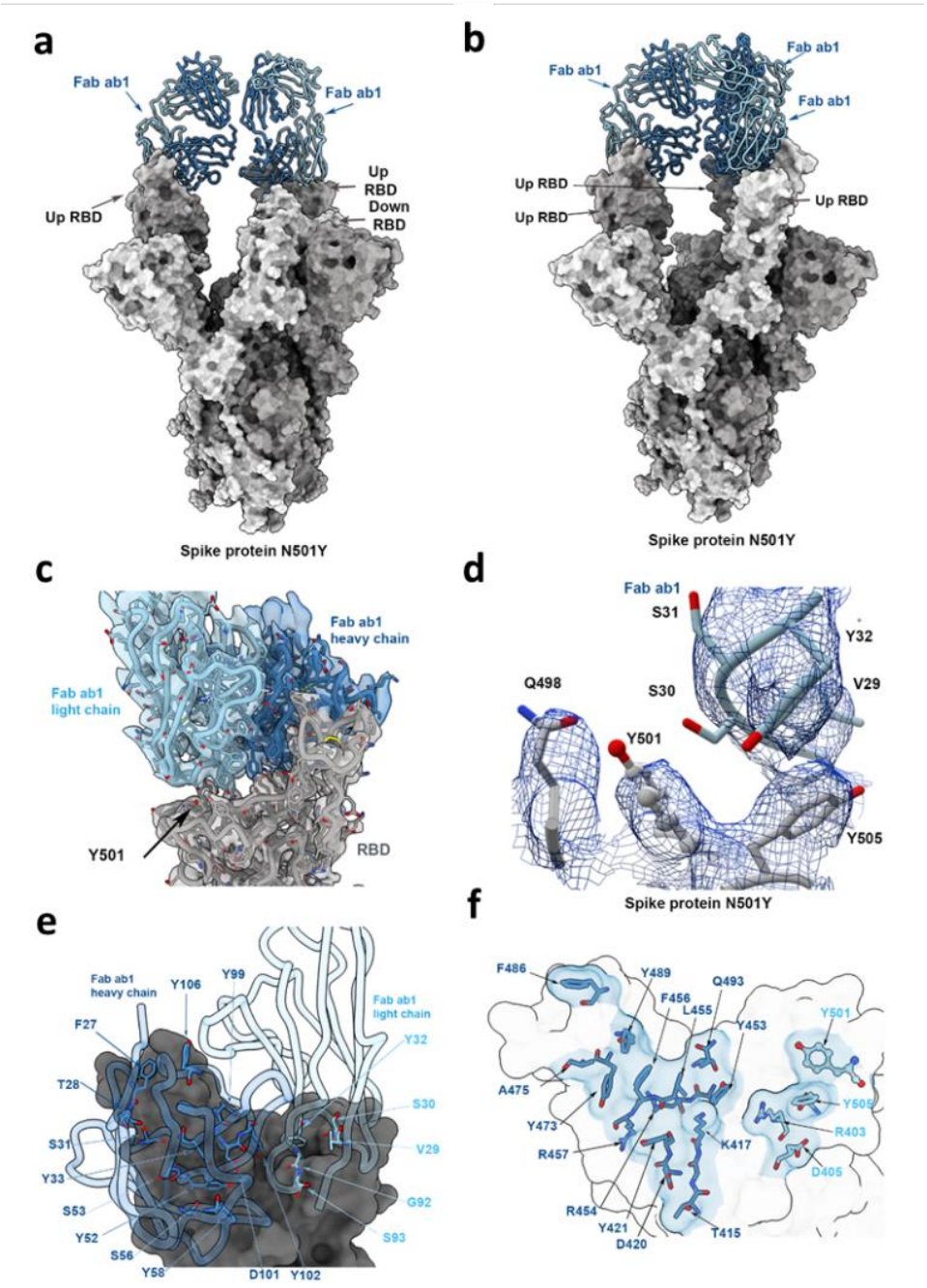

Figure 3.6. **Structure of Fab ab1 bound to the N501Y mutant spike protein trimer.** (a and b) Atomic models for the 2 predominant conformations of the spike protein (gray) observed with Fab ab1 (blue) bound to either 2 (a) or 3 (b) receptor binding domains (RBDs) in the up position. (c) Cryo-electron microscopy density map after local refinement with fitted coordinates for the contact zone between the RBD and Fab ab1. (d) Density map in the region near 501 for the N501Y mutant spike protein ectodomain showing density for residues Q498, Y501, and Y505 in the spike protein and a loop in Fab ab1 that includes S30, the residue closest to Y501. (e and f) Close-up views of the contact zone between the RBD region and ACE2 highlighting residues involved.

Our studies with the N501Y mutant are consistent with the expectation that the rapid spread of VOC202012/01 variant of SARS-CoV-2 is likely due to the virus being more infectious. While there can be multiple origins for the increased infectivity, our biochemical studies suggest that the N501Y mutation results in increased ACE2 binding efficiency. Our structural studies establish the molecular basis underpinning the observed increase in ACE2 binding efficiency conferred by the N501Y mutation. Competition assays with a strongly neutralizing antibody show that it competes for binding with the spike trimer–ACE2 interaction in a concentration-dependent manner. Our results suggest that despite the higher infectivity of SARS-CoV-2 viruses carrying the N501Y mutation, the availability of the extended epitope surface on the RBD enables effective neutralization by V_H ab8 and Fab ab1.

3.2.2 Studies on RBD mutations within the D614G background

The emergence of the N501Y mutation in several SARS-CoV-2 variants was followed shortly by several other RBD mutations, which all shared the globally dominant D614G mutation outside of the RBD (figure 3.7). We now shift the focus to the mutational effects of these RBD mutations, within the background of the D614G mutation. By early 2021, genomic surveillance efforts tracking the global spread of SARS-CoV-2 had identified the emergence and rapid spread of several variants. These variants are designated as having evidence demonstrating increased transmissibility, increased disease severity, and/or a significant impact on diagnostics, treatments, and vaccines[123–126]. Figure 3.7b-c shows the S protein mutations present in each of the emergent variants, with the majority of common mutations found within the RBD. Additionally, three of the four VoC RBD mutations (L452R, E484K, and N501Y) are located within the receptor binding motif (RBM), which comprises the interaction interface between the S protein and ACE2. The one RBD mutation occurring outside of the RBM, K417N/T, additionally exhibits ambiguity in

mutation, with the P.1 strain mutated to threonine (K417T) and the B.1.351 strain mutated to asparagine (K417N) (Figure 3.7b). We sought to understand the individual and combinatorial contributions that each of these common VoC/VoI RBD mutations has on enhancing aspects of viral fitness such as receptor binding and antibody evasion.

Using 11 S proteins with different complements of mutations (Figure 3.7d), we systematically dissect the contributions of RBD mutations toward increasing ACE2 affinity and evading neutralizing antibodies using Cryo-EM structural analyses and assays that measure ACE2 and antibody binding. We also constructed spike proteins harbouring combinations of RBD mutations that had not been observed at the time, to explore the properties of variants that in some cases, later emerged after the time of experimentation.

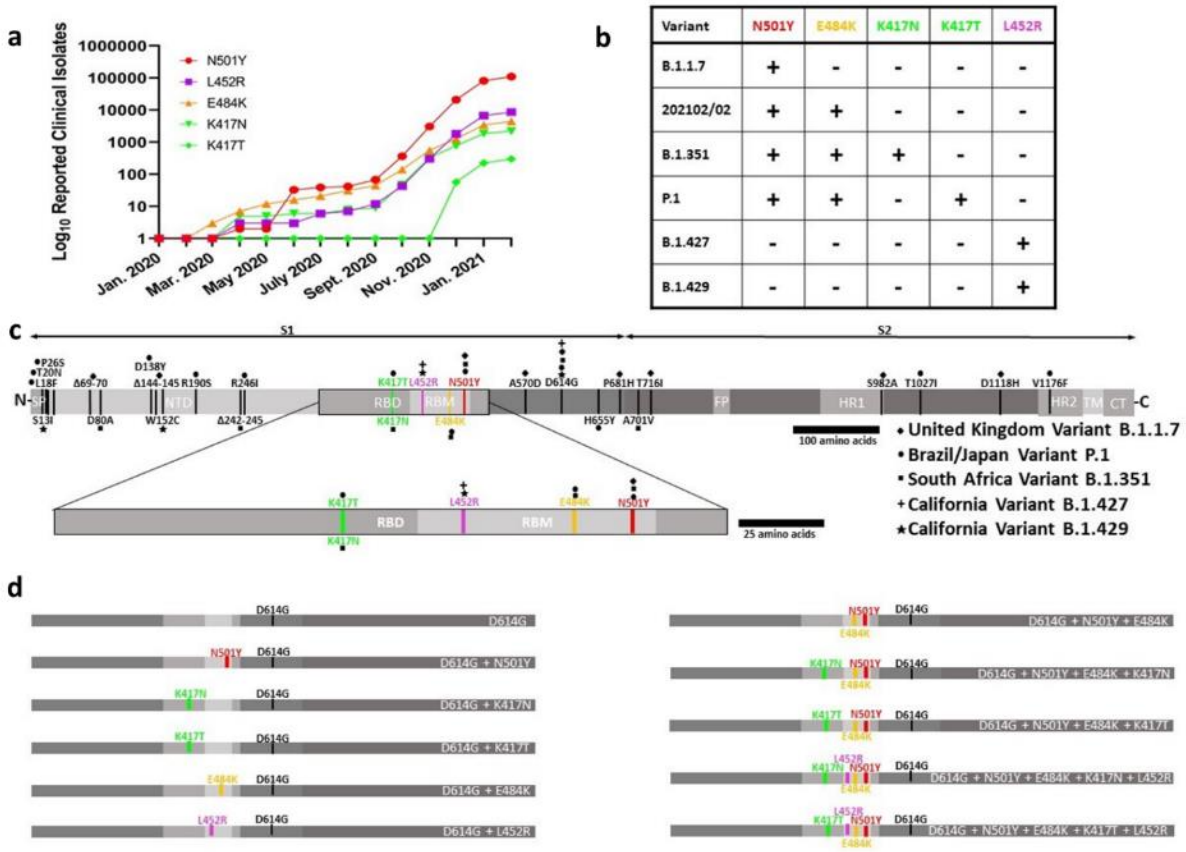

Figure 3.7. **The global prevalence of SARS-CoV-2 VoC/VoI RBD mutations and their locations within the S protein.** (a) Global occurrences of each VoC/VoI RBD mutation over time, computed using the sum of clinical isolate entries each month deposited into the GISAID database (https://www.gisaid.org/). (b) Summary of the RBD mutations present in each variant. (c) SARS-CoV-2 spike glycoprotein amino acid open reading frame (ORF) with variant mutations indicated. An expanded portion of the RBD is provided to highlight the common RBD mutations between the variants. Relevant features are indicated: SP, signal peptide; NTD, N-terminal domain; RBD, receptor binding domain; RBM, receptor binding motif; FP, fusion peptide; HR1, heptad repeat 1; HR2, heptad repeat 2; TM, transmembrane domain; CT, cytoplasm domain. (d) Summary of the SARS-CoV-2 spike glycoprotein constructs used in this study. VoC/VoI RBD mutations were expressed in isolation, in naturally occurring combinations, and in novel combinations to assess the relative individual and combinatorial effects of these mutations. All constructs contain the D614G mutation as background, and this was defined as the wild-type construct throughout the study.

3.2.2.1 The N501Y, E484K, and L452R mutations drive increased S protein-ACE2 binding affinity

To investigate the effects of VoC/VoI RBD mutations on ACE2 binding, we expressed and purified recombinant spike ectodomain proteins bearing RBD mutations in isolation and combination, which we used in biolayer interferometry (BLI) experiments (Figure 3.8a-b). Compared with wild-type (D614G), spikes harboring combinations of RBD mutations found in circulating variants exhibited increased ACE2 binding affinities. The individual addition of N501Y, E484K, or L452R mutations increased ACE2 binding affinity, and the increased affinity conferred by the N501Y and E484K mutations in isolation was preserved in combination in the D614G + N501Y + E484K construct, yielding the highest affinity ACE2 binder. Mutations at the 417 position (K417N/T) decreased the affinity for ACE2 both in isolation (D614G + K417N/T) and when introduced into the D614G + N501Y + E484K construct. Interestingly, the K417N mutation reduced ACE2 affinity to a greater extent than the K417T mutation (both in isolation and when combined with D614G + N510Y + E484K). Taken together, these results demonstrate that the amalgamation of spike RBD mutations present in circulating VoC/VoIs enables increased ACE2 affinity, which is driven mainly by N501Y (B.1.1.7), L452R (B.1.427/B.1.429), and the combinatorial effect of both N501Y and E484K (P.1, B.1.351, and VOC 202102/02).

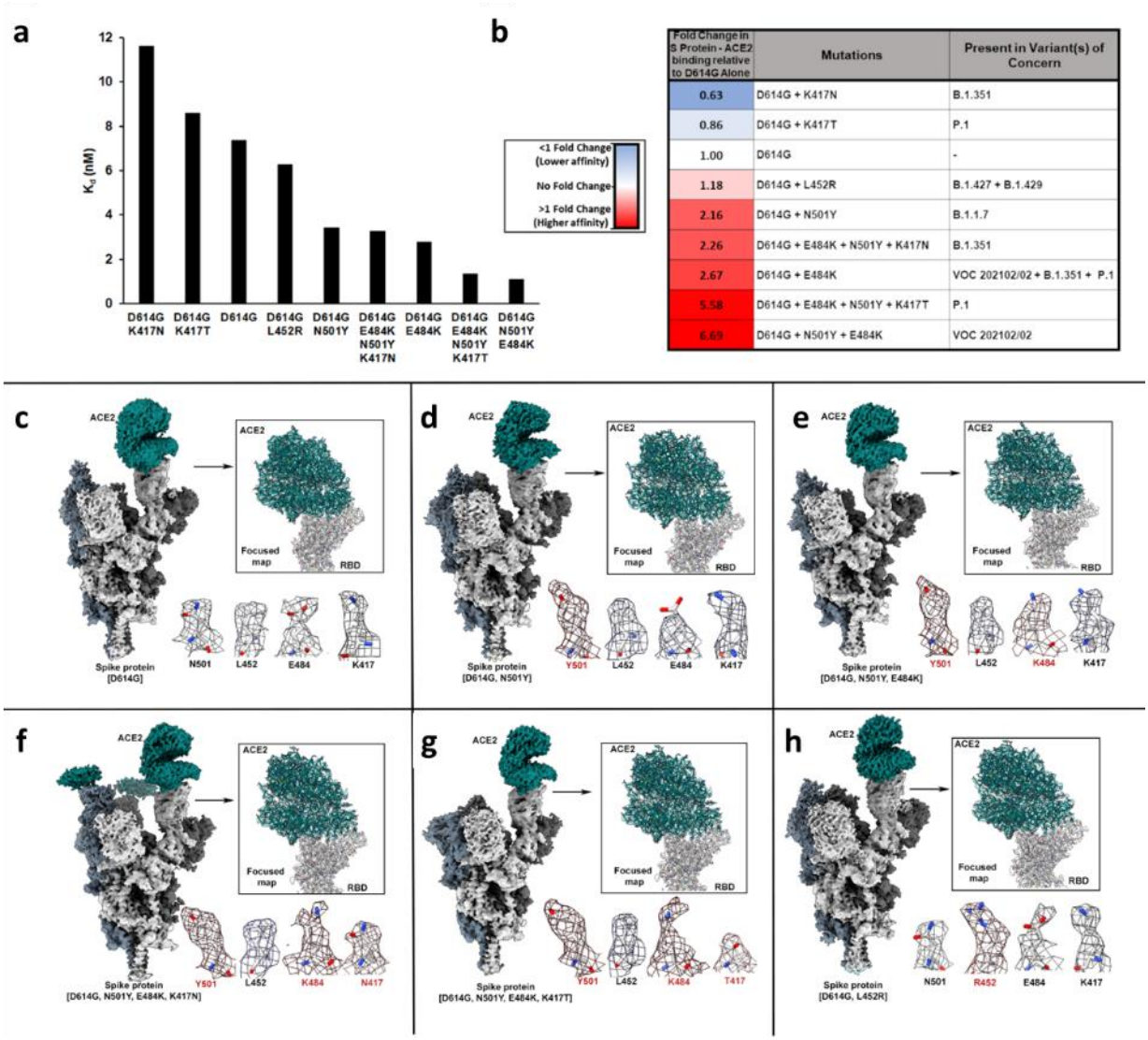

Figure 3.8. **Complete sets of VoC/VoI RBD mutations increase S protein trimer-ACE2 binding affinity.** (a) Affinity (Kd) measurements for VoC/VoI RBD mutant S protein-ACE2 binding as measured by biolayer interferometry (BLI). (b) Relative fold change differences in S protein-ACE2 affinity (Kd) relative to D614G alone. (c-h) Structures of VoC/VoI spike-ACE2 complexes characterized in this study. Shown for each complex studied are density maps for the overall complex at the end of global structure refinements, improved focused density maps at the ACE2-RBD contact zones, and visualization of densities at mutational positions within each variant spike. Densities at sites harboring mutations are highlighted with red text.

3.2.2.2 Mutational effects on ACE2 binding are mediated by subtle side-chain rearrangements at the S protein-ACE2 interface

To understand the structural effects of the various VoC/VoI RBD mutations on ACE2 binding, we conducted cryo-EM studies on unbound spike trimers and ACE2-spike complexes (Figure 3.8c-h). Resulting structures were obtained at average resolutions of ~2.3–3 Å. The *apo*- and ACE2-complexed S protein structures show no significant global changes in secondary or quaternary structure as a result of the various mutations compared with D614G (Figure 3.9). However, focused refinement of the S protein-ACE2 interface revealed side-chain rearrangements that may account for the observed differences in binding affinity as outlined below.

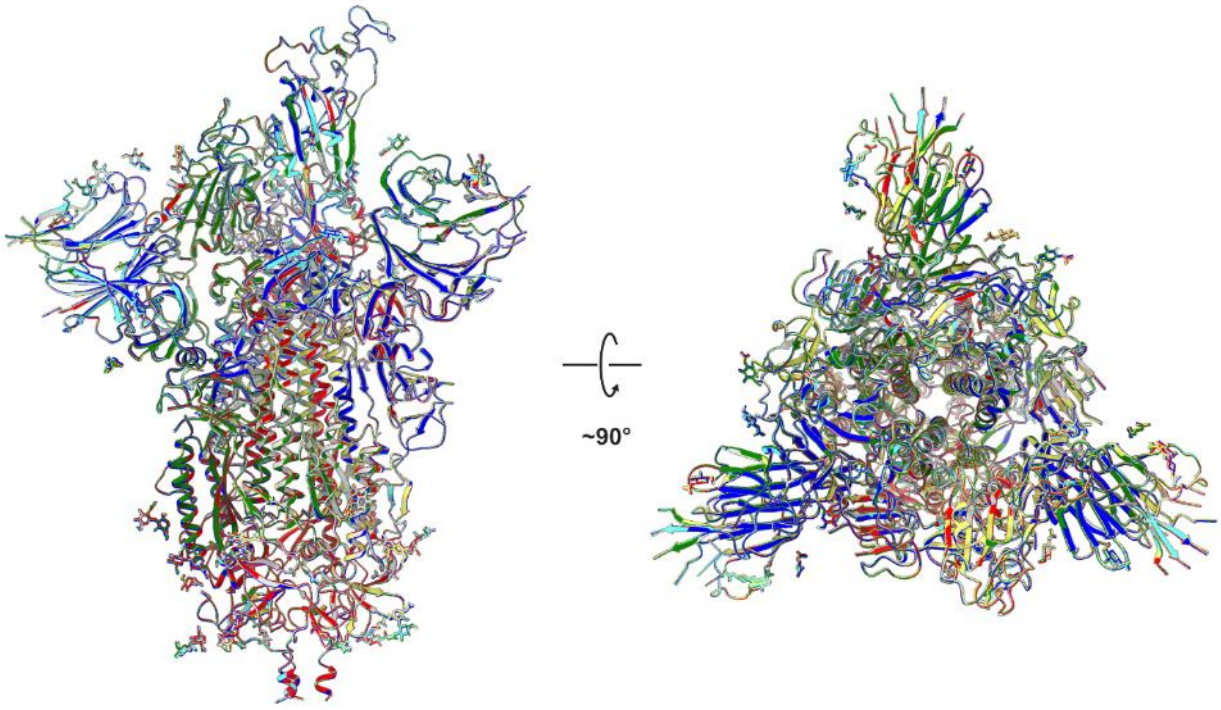

Figure 3.9. **Superposition of all mutant ectodomain structures characterized in this study.** Gray: D614G, Red: D614G + N501Y, Green: D614G + N501Y + E484K, Blue: D614G + N501Y + E484K + K417N, Yellow: D614G + N501Y + E484K + K417T, Cyan: D614G + L452R

D614G + N501Y

The cryo-EM structure of ACE2 bound to the D614G + N501Y mutant spike (Figures 3.10b and 3.11b) shows the same features at the RBD-ACE2 interface as in the structure of the N501Y-ACE2 complex in the absence of the D614G mutation. Y501 in the spike protein and Y41 in the ACE2 receptor engage in a perpendicularly shaped π-π stacking interaction. Additionally, superposition of the RBD in all RBD-ACE2 structures reveals a ~2.4 Å displacement of an ACE2 helix distal to the RBD binding helix compared with complexes with N and Y at residue 501 reflecting the impact of this change (Figure 3.11c).

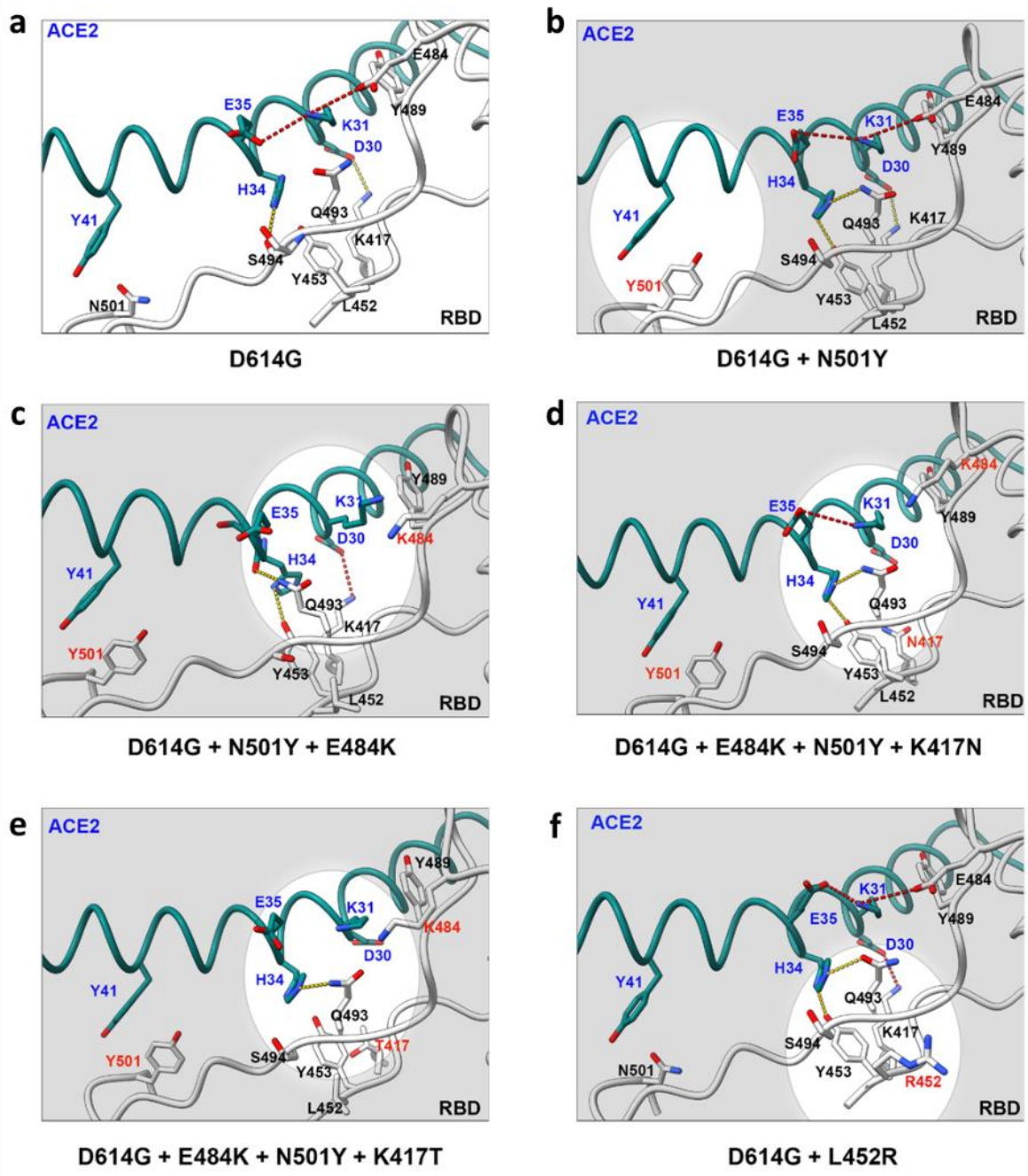

Figure 3.10. **CryoEM structures of wild-type and VoC RBD-ACE2 interfaces (A–F) Zoomed-in views of the RBD-ACE2 binding interfaces for the six S protein-ACE2 structures.** Focused refinement of the RBD-ACE2 interface reveals distinct S protein and ACE2 side-chain rotamer arrangements for the various variants. Mutated residues are labeled in red, and adjacent residues of interest are highlighted within ovals. ACE2 residues are labeled in blue, while RBD residues are labeled in black. Hydrogen bonds and electrostatic interactions are shown as yellow and red dotted lines, respectively. Oxygen and nitrogen heteroatoms are colored in red and blue, respectively

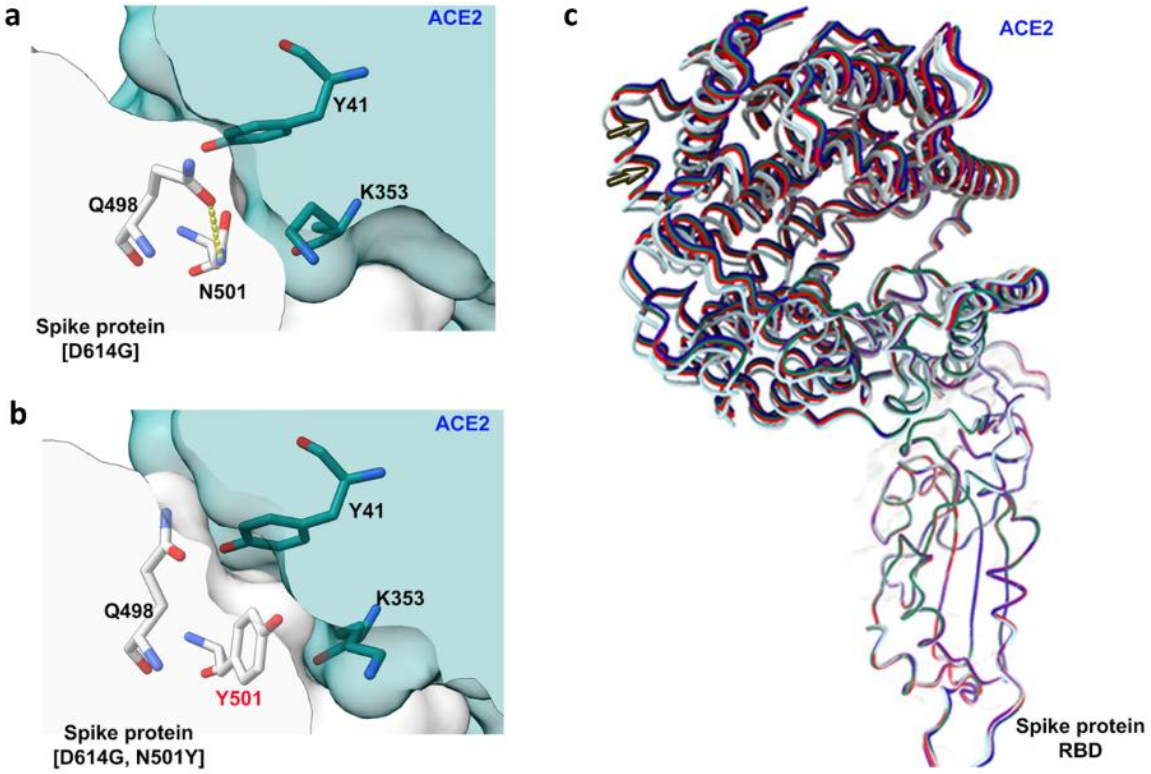

Figure 3.11. **Structural effects of the N501Y mutation on RBD-ACE2 complexes.** (a) Zoomed in view of position 501 and adjacent residues at the D614G RBD-ACE2 interface. (b) Zoomed in view of position 501 and adjacent residues at the D614G, N501Y RBD-ACE2 interface. (c) Superposition of the RBD in the RBD-ACE2 structures from all complexes reported in this study. Cyan and grey models correspond to structures harboring N at position 501, all other models correspond to structures harboring Y and position 501. Movement of the ACE2 helix distal to the RBD binding interface is highlighted with arrows.

D614G + N501Y + E484K

Analysis of the D614G + N501Y + E484K mutant spike in complex with ACE2 reveals local rearrangements resulting in unambiguous rotamer placement of both H34 within ACE2 and Q493 within the spike RBD (Figure 3.10c, Figure 3.12c)). The resulting H34 rotamer yields space that accommodates an alternative Q493 rotamer closer to ACE2 relative to the D614G spike, allowing it to be positioned within hydrogen-bonding distance of the main chain carbonyl of H34. Additionally, the positioning of K31 within ACE2 is shifted relative to the D614G spike, adopting a position within pi-cation bonding distance to Y489 within the RBD (Figure 3.12c). K484 extends parallel to the RBD-ACE2 plane of interaction, likely because of electronic repulsion from K31, and adopts a position ~7.5 Å from E35. These subtle changes in intermolecular interactions enabled upon H34 repositioning suggest a basis for the enhanced ACE2 affinity observed for the D614G + N501Y + E484K mutant spike relative to D614G + N501Y.

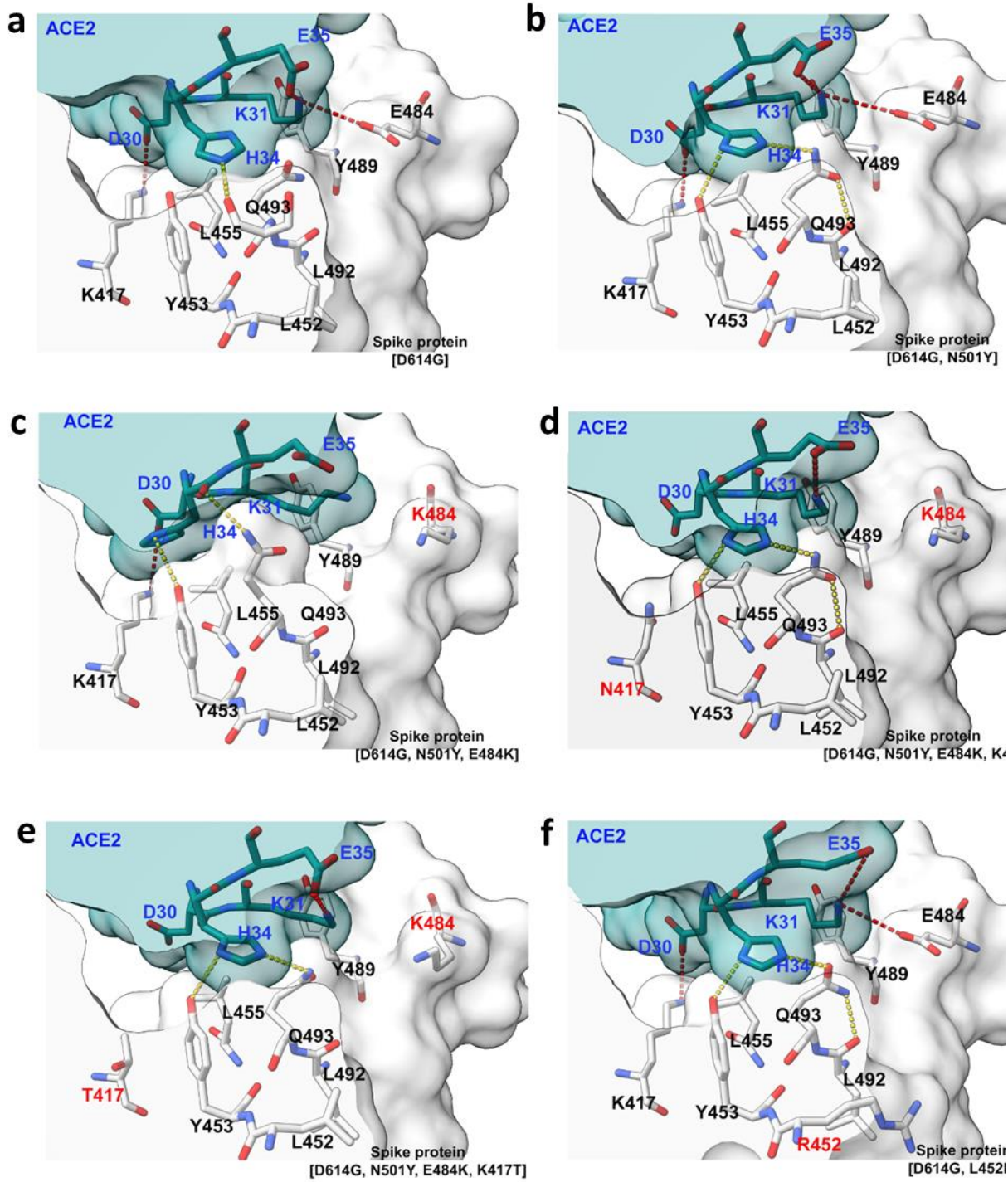

Figure 3.12. **Analysis of RBD-ACE2 interactions.** (a – f) Zoomed in views of residue H34 within ACE2, residue Q493 within the RBD, and adjacent residues at the RBD-ACE2 interface

for all complexes studied. Mutated residues are highlighted in red. Hydrogen bonds are shown as dotted yellow lines, electrostatic interactions are shown as red dotted lines.

D614G + N501Y + E484K + K417T/N

The mutation of K417 to T or N resulted in loss of the K417-D30 salt bridge within the ACE2-spike complex, providing a basis for the decreased ACE2 binding affinities conferred by these two mutations (Figure 3.10d-e, Figure 3.12d-e). In contrast to the D614G + N501Y + E484K-ACE2 complex, H34 rotamer placement is ambiguous within these complexes, with the predominant densities corresponding to H34 facing toward the K484 interface. Additionally, Q493 adopts a rotamer that faces away from ACE2, and K31 is positioned to face both H34 and Q493.

D614G + L452R

Structural comparison of D614G-ACE2 and D614G + L452R-ACE2 complexes reveals no significant changes at the RBD-ACE2 interface (Figure 3.10f, Figure 3.12f), indicating that the enhanced ACE2 affinity afforded by L452R is not due to modulation of direct ACE2 contacts. In contrast to L452, the side chain of R452 extends farther away from the RBD core (Figure 3.12f) and is better exposed to solvent, suggesting that R452 may enhance the solvation of the RBD in the up position. In addition to solvation effects, the L452R substitution introduces a positive charge at position 452 that may increase the electrostatic complementarity between the RBD and ACE2. Figure 3.13 shows the increase in electropositivity at position 452 upon L452R substitution, with position 452 approximately 13 Å away from the highly electronegative site on ACE2 centered at E35. Thus, in contrast to the local rearrangements observed at the RBD-ACE2

interface for the N501Y, E484K, and K417N/T mutations, the binding effect of the L452R mutation is likely mediated by solvation and/or electrostatic complementarity effects.

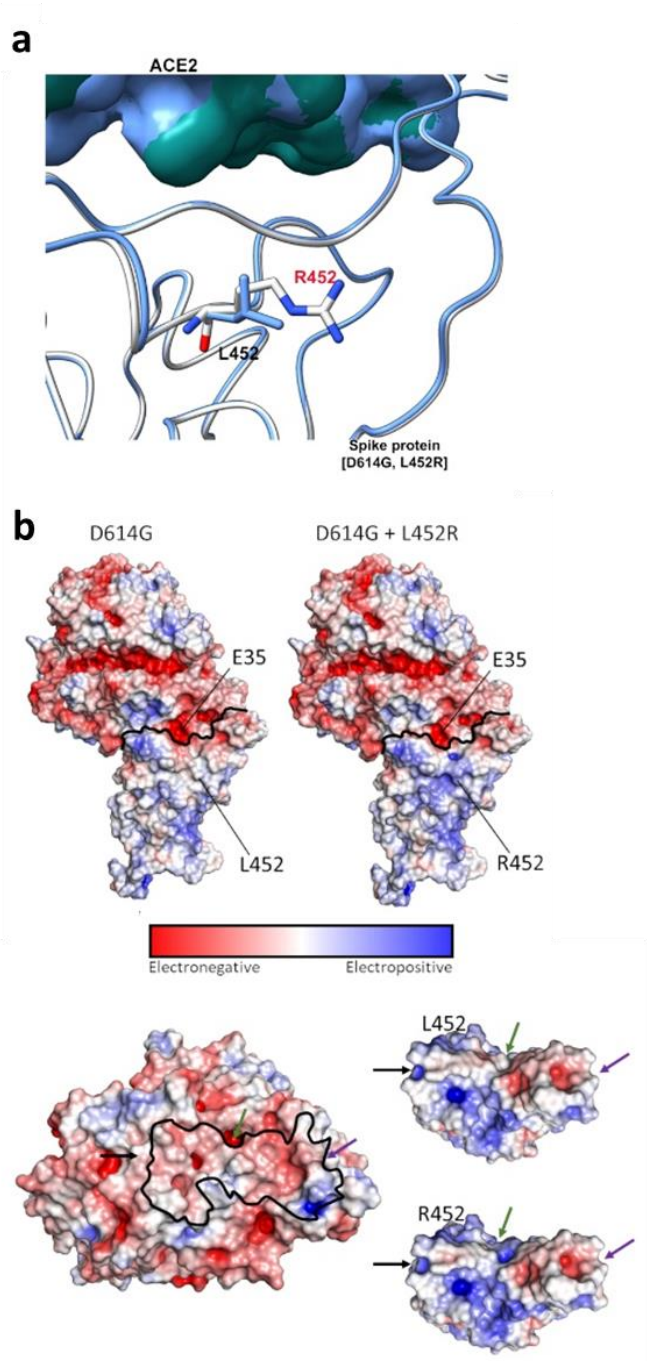

Figure 3.13. **L452R enhances electrostatic complementarity between ACE2 and the SARS-CoV-2 RBD.** (a) Superposition of D614G (blue) and D614G +L452R (white) RBD-ACE2 interfaces. (b) Left: Electrostatic surface representations of CryoEM structures of wild-type (D614G) and L452R RBD-ACE2 complexes. Right: Electrostatic surface representation of ACE2, wild-type (D614G) RBD and L452R RBD in isolation. The RBD binding interface on ACE2 is outlined in black and arrows for orientation are provided for both ACE2 and RBD surface representations.

3.2.2.3 Mutations E484K, L452R, and K417N/T facilitate decreased antibody binding.

We next sought to evaluate the effect of VoC/VoI RBD mutations on antibody binding. We selected a panel of previously reported antibodies that cover the four distinct anti-RBD antibody classes[106] (Table 3.1, Figure 3.14a) and an ultrapotent antibody, S2M11, that uniquely binds two neighboring RBDs[127] Antibody binding was quantified via enzyme-linked immunosorbent assay (ELISA) (Figure 3.14b). As expected, class 3 (S309) and class 4 (CR3022) antibodies, whose footprints did not span VoC/VoI mutations, exhibited relatively unchanged binding across all variant spikes (Figure 3.14b). Mutations at position 417 of the S protein to either N or T abolished or significantly reduced ab1[105] (class 1 like) binding, demonstrating the importance of K417 within the molecular epitope of ab1. Similarly, the E484K mutation resulted in loss of binding to ab8[104] (class 2) and S2M11, highlighting the critical nature of E484 within the epitopes of these antibodies. L452 sits peripherally within the footprint of S2M11, and mutation of this residue to R452 reduced but did not abolish its binding, possibly via steric or charge-mediated effects or by allosteric modulation of direct contacts. Taken together, these results suggest the escape of antibody binding from the four major anti-RBD classes is primarily mediated by modulation of direct contacts at mutational sites.

Table 3.1. Antibody class definitions and categorization of the antibodies in the present study.

Antibody Class	Antibody Class Description	Antibodies in the Present Study
1	Neutralizing antibodies that block ACE2 and bind only to ‘up’ RBDs.	ab1
2	ACE2-blocking neutralizing antibodies that bind both up and ‘down’ RBDs and can contact adjacent RBDs.	ab8
3	Neutralizing antibodies that bind outside the ACE2 site and recognize both up and down RBDs.	S309
4	Previously described antibodies that do not block ACE2 and bind only to up RBDs.	CR3022

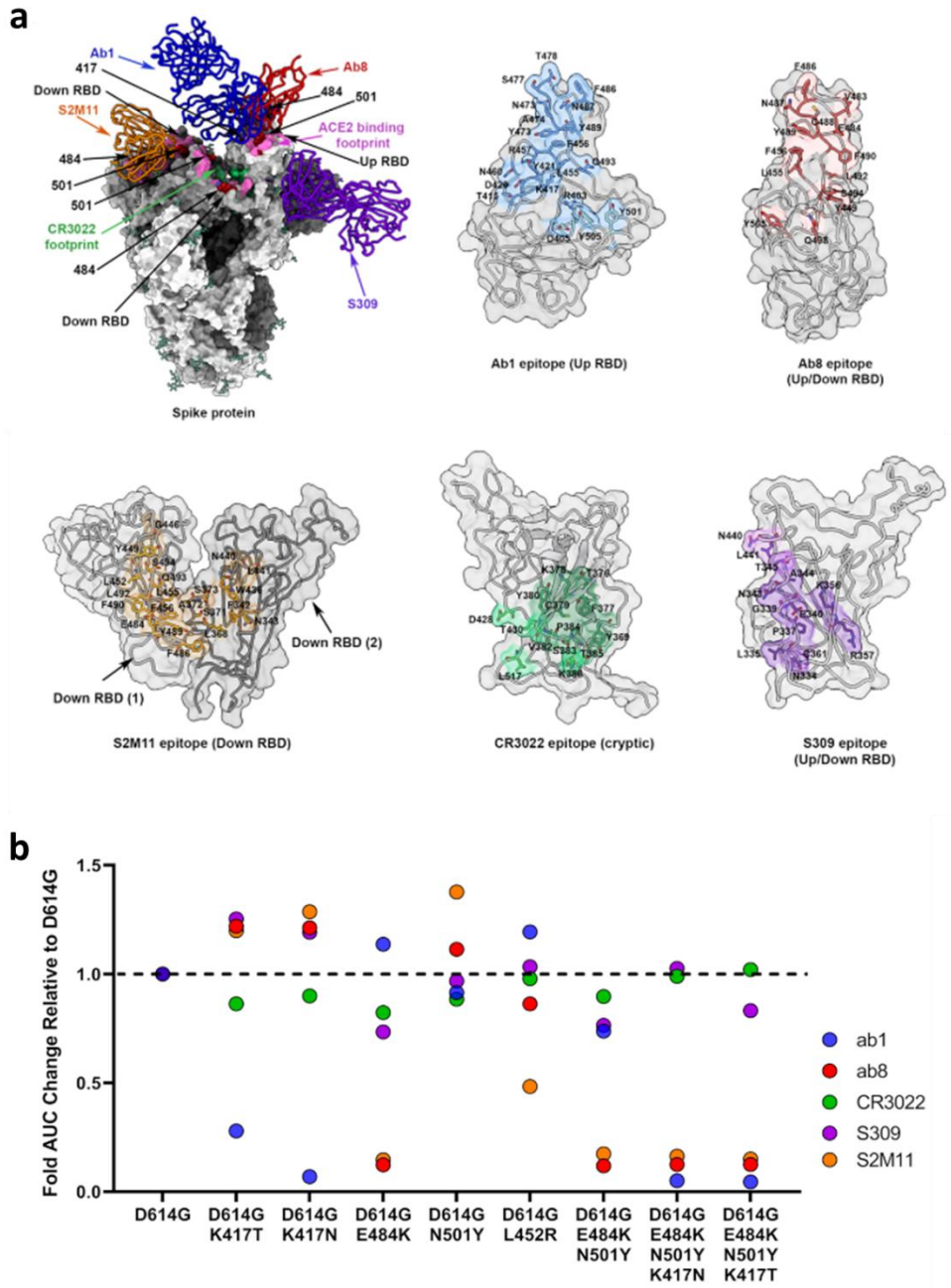

Figure 3.14. **Monoclonal antibody binding against SARS-CoV-2 S proteins containing VoC/VoI RBD mutations.** (a) Mapping of Ab1, Ab8, CR3022, S309, and S2M11 antibody footprints onto SARS-CoV-2 trimers and RBDs. Direct amino acid contacts for each individual antibody footprint are highlighted separately. (b) Area under the curve (AUC) fold changes in ELISA binding assays relative to D614G alone for Ab1, Ab8, CR3022, S309, and S2M11.

3.2.2.4 Novel RBD mutant combinations preserve but do not enhance effects on ACE2 affinities and antibody binding

Having determined that all full complements of VoC/VoI RBD mutations result in increased ACE2 binding and various extents of antibody evasion, we aimed to assess the functional effects of novel RBD mutational combinations that at the time had not yet been reported but represent combinations of mutations already observed. Variants harbouring N501Y exhibit a spectrum of additional RBD mutations (B.1.1.7: N501Y; VOC 202102/02: E484K, N501Y; B.1.351: E484K, N501Y, K417N; and P.1: E484K, N501Y, K417T), while variants containing L452R (B.1.427/B.1.429) seemingly exclude N501Y, K417N/T, and E484K mutations, although the Kappa (B.1.617.1) variant which emerged later during the pandemic, contained the E484Q co-mutation with L452R in its spike protein. In order to assess if such patterns of evolution are due to incompatibility of these mutations, we constructed and expressed recombinant spike ectodomains combining L452R with the full complement of either B.1.351 or P.1 RBD mutations and evaluated ACE2 and antibody binding of these mutants (Figure 3.15). Neither of these novel combinations conferred enhanced ACE2 affinities compared with B.1.351 and P.1 RBD mutant spikes. Notably, both novel combinatorial mutants still exhibited enhanced ACE2 binding compared with wild-type (Figure 3.15b). The addition of L452R to both constructs preserved the antibody-evasive properties for K417N/T against ab1 and E484K against both ab8 and S2M11 (Figure 3.15c). These results indicate that although the L452R mutation is not mutually exclusive with the complement of RBD mutations in B.1.351 and P.1 variants with regard to reduction of neutralizing antibody binding, the increase in ACE2 binding affinity conferred by the L452R mutation in isolation (Figure 3.8a-b) is absent when combined with B.1.351 and P.1 RBD mutations.

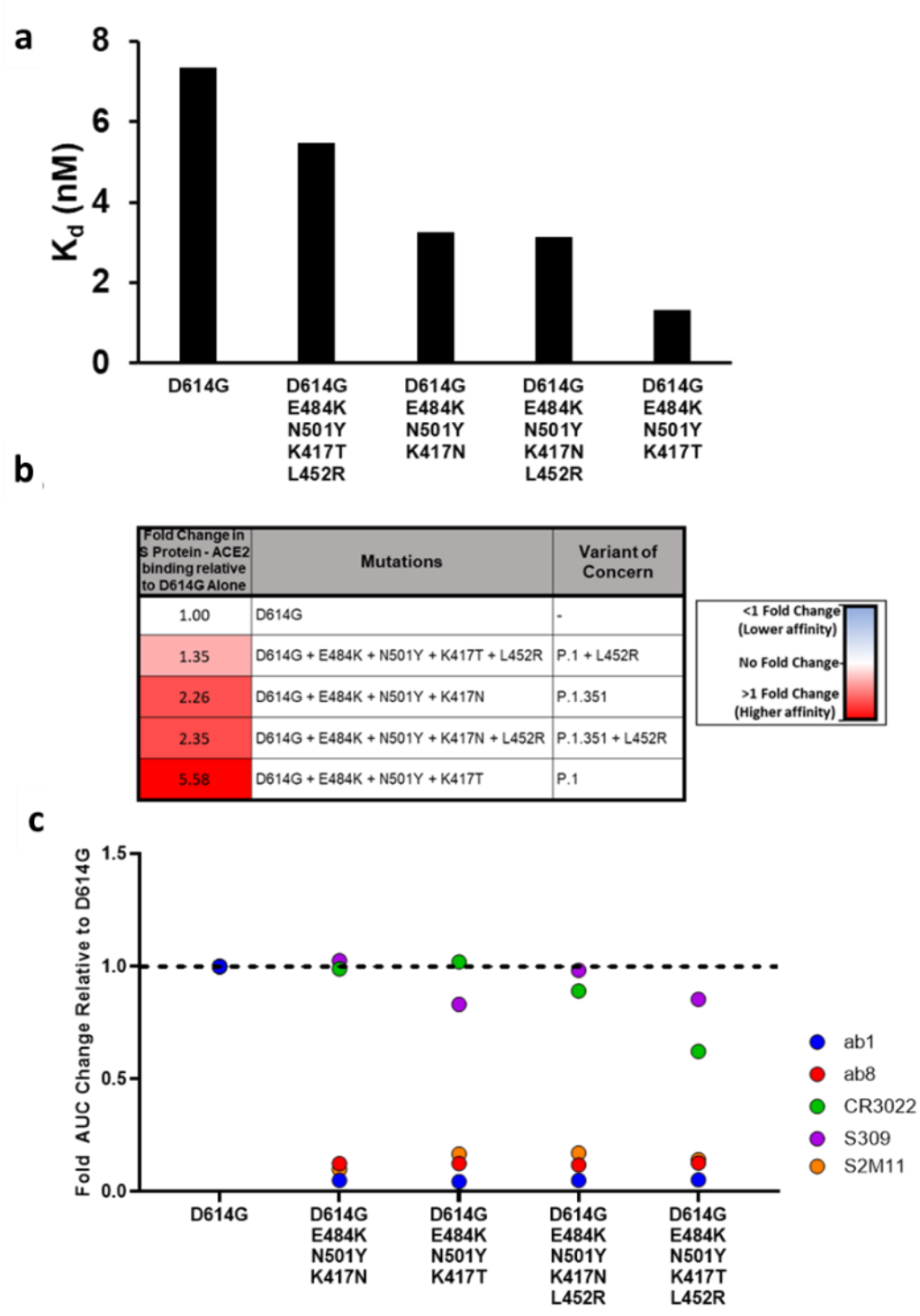

Figure 3.15. **ACE2 and antibody binding to next-generation combinatorial VoC RBD mutations.** (a) Affinity (Kd) measurements as measured by biolayer interferometry (BLI). (b) Relative fold change differences in S protein - ACE2 affinity (Kd) relative to D614G alone. (c) Area under the curve (AUC) fold changes in ELISA binding assays relative to D614G alone for ab1, ab8, CR3022, S309, S2M11.

3.2.3 General Observations

This work dissected the relative roles of circulating VoC/VoI RBD mutations with regard to both ACE2 affinity and antibody binding (Figure 3.16). Our results demonstrated that individual mutations may be classified as resulting in (1) increased RBD-ACE2 affinity (N501Y), (2) reduced ACE2 affinity and reduced antibody binding (K417N/T), or (3) a simultaneous increase in ACE2 affinity and reduced antibody binding (E484K, L452R). These individual effects are preserved when mutations are combined to reflect full complements of VoC/VoI RBD mutations, demonstrating their modular nature. Furthermore, these results suggested that RBD evolution follows a trajectory aimed at simultaneous enhancement of receptor affinity and reduction of neutralizing antibody binding. Although our analyses did not reveal the N501Y mutation to be highly antibody evasive, its presence within the footprint of several neutralizing antibodies may have implications for antibody escape (Figure 3.17a-d), although it has been suggested that main antibody evasive impact of the N501Y mutation is one of competition, whereby receptor binding is favoured over antibody binding due to increased ACE2 affinity[128]. It is noteworthy that all VoCs containing K417N/T mutations also contain the N501Y and E484K mutations. Given that K417N/T mutations serve to diminish antibody binding at a cost to ACE2 affinity, the conditional presence of ACE2 affinity enhancing mutations may represent a compensatory mutational mechanism. Consistent with this hypothesis, analysis of deposited spike sequences in the GISAID database deposited between January 2020 and May 2021 reveals that K417N/T mutations did not occur independently of N501Y and E484K mutations (Figure 3.18). In contrast, K417N/T mutations were not a prerequisite for the occurrence of mutations that increase ACE2 affinity (N501Y) or simultaneously increase ACE2 affinity and decrease antibody binding (E484K, L452R) (Figure 3.18).

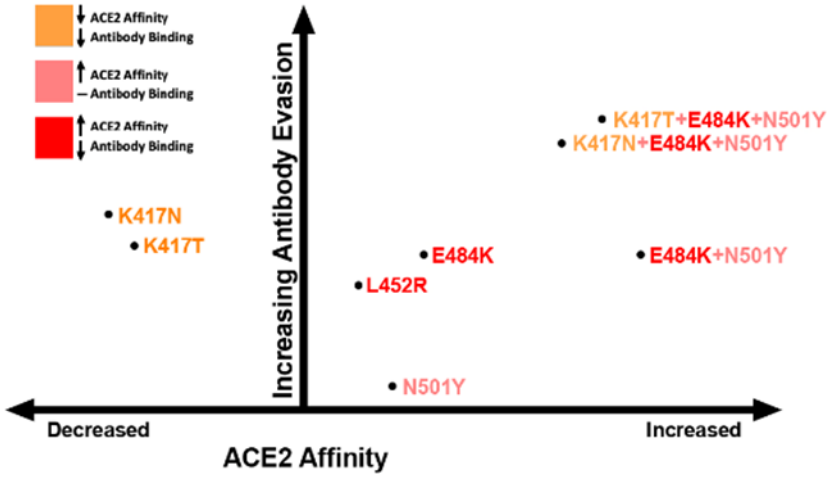

Figure 3.16. **Qualitative two-dimensional (2D) plot describing pre-omicron VoC RBD mutational effects on ACE2 and antibody binding.** The mutations are grouped into three colour categories: orange, mutations that decrease ACE2 affinity and antibody binding; pink, mutations that increase ACE2 affinity and do not significantly affect antibody binding; and red, mutations that increase ACE2 affinity and decrease antibody binding.

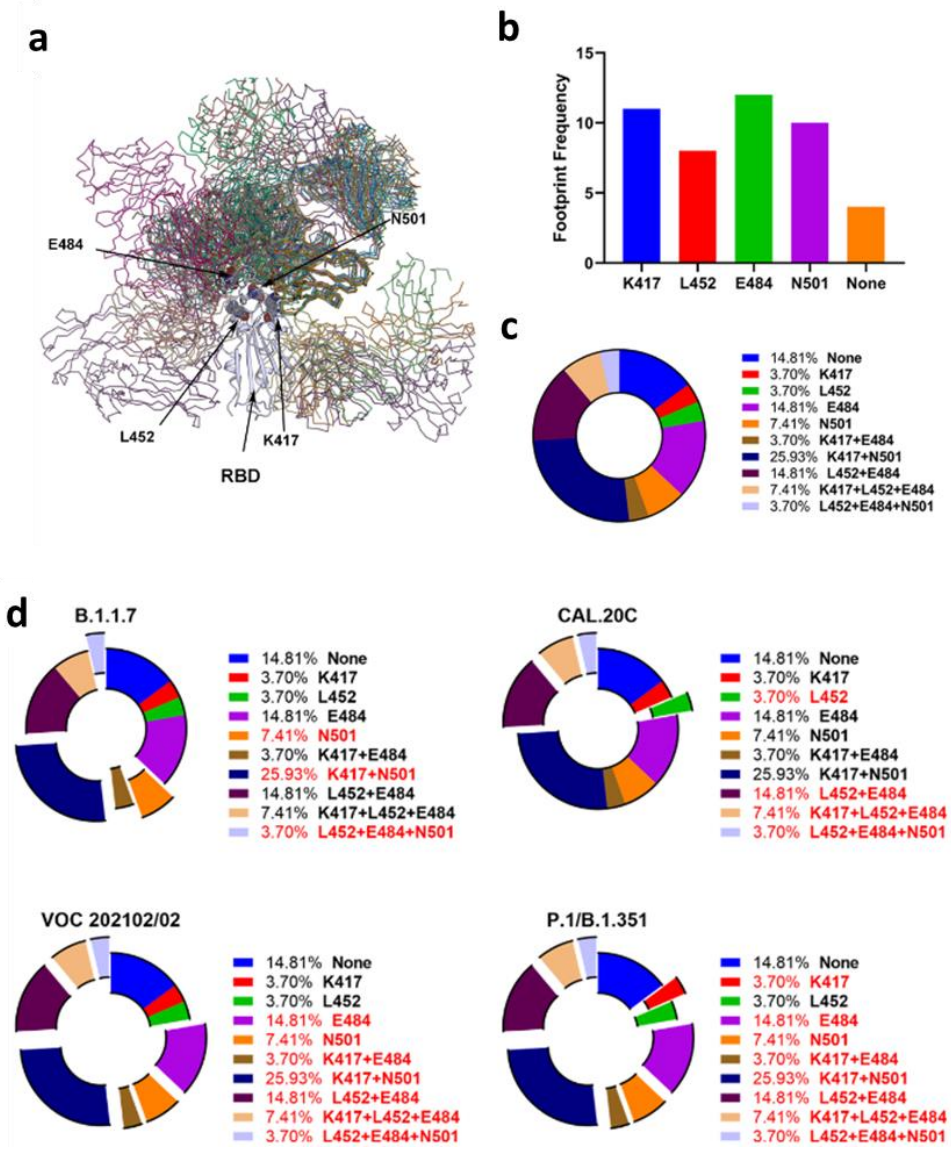

Figure 3.17. **Analysis of RBD mutations in PDB entries of SARS-CoV-2 spike or RBD complexes with antibody fragments isolated from convalescent patients.** See Table 3.2 for PDB entries included in this analysis. (a) Structural overlap of all antibodies selected on the SARSCoV-2 RBD. Mutational positions within the RBD are highlighted. (b) Frequency of each of the RBD positions that are mutated in VoCs within the footprints of selected antibody-spike/RBD structures. (c) Proportional analysis of distinct variant RBD positional compositions within the footprints of selected antibody-spike/RBD structures. (d) Analysis of the overlap between the mutational composition of various VoCs and distinct variant RBD positional compositions within the footprints of selected antibody-spike/RBD structures. Footprints including at least one position mutated within a given VoC are highlighted in red and depicted as slices graphically. Table 3.2 lists the antibodies and PDB entries selected.

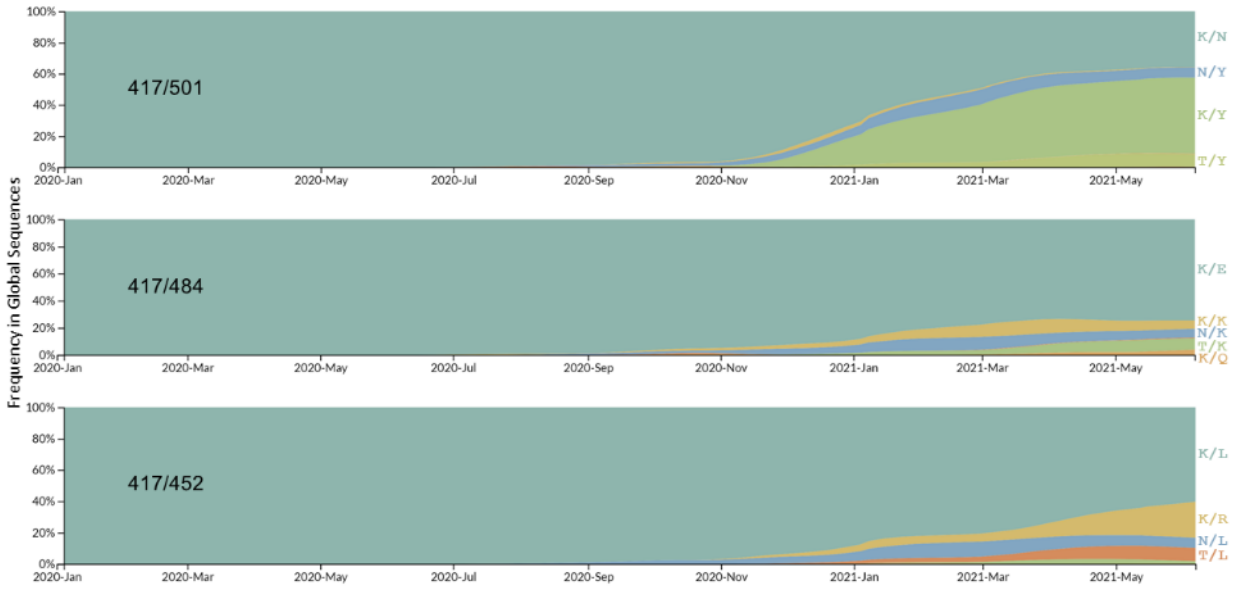

Figure 3.18. **Analysis of co-mutational prevalence at positions 417, 452, 484, and 501 within the SARS-Cov-2 Spike.** Data from the GISAID sequence databank was analyzed for mutational prevalence between January 2020 and May 2021 at the indicated residue combinations.

Our described effects on ACE2 binding and antibody evasion imparted by VoC/VoI RBD mutations are in agreement with other reports[120,121,129–134], with the exception of the enhanced ACE2 affinity conferred by E484K. Several studies have reported conflicting data surrounding the effect of E484K on ACE2 binding, where both decreased[135–137] and increased[121,138] affinities are observed. A variety of biophysical techniques, spike protein domains, and ACE2 constructs were used across these studies, which could account for the contrasting results. Most important, the E484K mutation was among several mutations selected via *in vitro* evolution to affinity-mature the RBD for enhanced ACE2 binding[139], demonstrating a clear role for increasing ACE2 binding affinity.

This study highlighted the potential for antibody evasion by VoC RBD mutations via antibody binding assays using a panel of monoclonal antibodies. To estimate the potential effect of VoC RBD mutations on RBD binding by naturally acquired antibodies during SARS-CoV-2 infection, we selected PDB entries of SARS-CoV-2 spike or RBD complexes with antibody fragments isolated from convalescent patients (Table 3.2). Using these structural data, we evaluated the frequency of positions corresponding to RBD mutations in VoC/VoIs within the footprint of 27 selected antibodies. The majority of deposited human-derived neutralizing antibodies bound the RBD with footprints spanning at least one of the positions corresponding to RBD mutation in VoC/VoIs (Figure 3.17b). Of these antibodies, the majority interacted with more than one position corresponding to RBD mutations in VoC/VoIs (Figure 3.17c). Of these variants, B.1.351, P.1, and VOC 202102/02 possessed mutations that were collectively recognized by the majority of the antibodies selected and suggested that these variants could exhibit the greatest RBD-directed antibody escape during human infection (Figure 3.17d).

Table 3.2. Antibodies and PDB entries for antibody-RBD complexes selected for analysis in figure 3.17.

Antibody	PDB	References
CB6	7C01	Shi *et al.* Nature 2020 [140]
b38	7BZ5	Wu *et al.* Science 2020 [111]
P2B-2F6 Fab	7BWJ	Ju *et al.* Nature 2020 [141]
EY6A	6ZER	Zhou *et al.* Nature Structure and Molecular Biology 2020 [112]
COVA2-39	7JMP	Wu *et al*. Cell Reports 2020 [142]
COVA2-04	7JMO	Wu *et al*. Cell Reports 2020 [142]
CC12.1	6XC2	Yuan *et al.* Science 2020 [137]
CC12.3	6XC4	Yuan *et al.* Science 2020 [137]
CV30	6XE1	Hurlburt *et al.* Nature Communications 2020[143]
Fab 2-4	6XEY	Liu *et al.* Nature 2020 [144]
S2H13	7JV2	Piccoli *et al.* Cell 2020 [107]
S2A4	7JVA	Piccoli *et al.* Cell 2020 [107]
S2H14	7JX3	Piccoli *et al.* Cell 2020 [107]
S2X35	7JX3	Piccoli *et al.* Cell 2020 [107]
910-30	7KS9	Banach *et al.* Cell Reports 2021 [145]
C102	7K8M	Barnes *et al.* Nature 2020 [106]
C105	6XCM	Barnes *et al.* Cell 2020 [146]
C144	7K90	Barnes *et al.* Nature 2020 [106]
C121	7K8X	Barnes *et al.* Nature 2020 [106]
C002	7K8S	Barnes *et al.* Nature 2020 [106]
C135	7K8Z	Barnes *et al.* Nature 2020 [106]
C110	7K8V	Barnes *et al.* Nature 2020 [106]
C104	7K8U	Barnes *et al.* Nature 2020 [106]
C119	7K8W	Barnes *et al.* Nature 2020 [106]
bd23	7BYR	Cao *et al.* Cell 2020 [147]
COVA2-39	7JMP	Wu *et al*. Cell Reports 2020 [142]
CT-P59	7CM4	Kim *et al.* Nature Communications 2021 [113]

We additionally generated novel combinations of RBD mutations by introducing L452R into B.1.351 and P.1 constructs. Although these mutational combinations enabled enhanced ACE2 binding compared with wild-type spikes, the increase in ACE2 binding affinity conferred by the L452R mutation in isolation was not preserved. We demonstrated that these novel constructs retained antibody-evasive properties when tested for antibody binding using a panel of monoclonal antibodies. Although there are many factors governing viral evolution, these results suggested that the independent evolution of L452R-bearing spikes and N501Y-, K417N/T-, and E484K-bearing spikes may be explained by a lack of synergistic increase in ACE2 binding upon combination of these mutations.

The cryo-EM structures of all five VoC/VoI RBD-mutated spike trimers, both in isolation and in complex with ACE2, provided insights regarding the molecular basis for observed changes in ACE2 affinities. The combination of enhanced intermolecular interactions due to the concomitant repositioning of H34 and Q493 in the D614G + N501Y + E484K-ACE2 complex provided a structural rationale for the increased ACE2 binding affinity relative to the D614G + N501Y spike. Although hydrogen bonding with Y453 is possible in both H34 rotamers (Figure 3.11), the dominant rotamer positioning of H34 in the D614G + N501Y + E484K-ACE2 complex enables it to participate in additional favourable intermolecular interactions with Y453 (hydrogen bond + OH/π) and L455 (CH/π), yielding estimated interaction energies of −10.29 and −2.75 kcal/mol, respectively[148]. The mechanism of H34 rotamer stabilization in response to the E484K mutation is unclear, although the repositioning of Q493 in this structure permits the formation of an intermolecular hydrogen bond with the main chain carbonyl of H34. This is in contrast to all other structures of spike protein-ACE2 complexes in which Q493 is positioned in close proximity to the main chain RBD carbonyls of F490 and L492 and is well poised to participate in intramolecular

hydrogen bonds (Figure 3.12). Finally, the positioning of K31 within pi-cation bonding distance to Y489 in this structure suggested an additional intermolecular interaction that may enhance ACE2 affinity (Figure 3.12c). It should be noted that although the intermolecular K31-E484 salt bridge was lost upon inclusion of the E484K mutation, this electrostatic interaction is likely intramolecularly distributed between ACE2 residues E35 and K31, thus limiting the contribution of the K31-E484 interaction with regard to ACE2-RBD binding. The positioning of H34 away from residue 484 in all RBD-ACE2 crystal structures reported (PDB: 6M0J, PDB: 6VW1, and PDB: 7NXC) agrees with our assessment that this represents the more energetically favourable rotamer with regard to the stability of the RBD-ACE2 complex. This structural basis is consistent with previous reports implicating H34 as a major contributor to the SARS-CoV-2 RBD-ACE2 interaction[149] and reports demonstrating the H34A mutation in ACE2 enhances SARS-CoV-2 spike binding[138,150]. This is likely due to closer positioning and flexibility of RBD residues such as Q493. Studies have suggested that the E484K mutation may enhance ACE2 binding via increasing electrostatic complementarity between ACE2 and the RBD [130,151], and the structures reported here are consistent with that hypothesis. The combination of the L452R mutation with either Beta or Gamma variant RBD mutations (D614G + N501Y + E484K + K417N/T) did not further increase ACE2 affinity. This may be explained by electrostatic complementarity effects; namely, E484K already introduces complementary electropositivity near the electronegative site on ACE2 (centered at residues E35 and K31), so the addition of further electropositivity at the more distal L452 position (by the addition of L452R) likely does not additionally enhance the S protein-ACE2 electrostatic complementarity. The structural basis for the observed discrepancies in ACE2 binding between the K417T and K417N mutations is unclear.

As L452 is distal to the ACE2-RBD interface, it has been previously suggested that the L452R mutation may increase ACE2 affinity via allosteric modulation of the residues promoting the RBD-ACE2 interaction[152] or via electrostatic effects[153]. We did not observe any allosteric changes in our structures; rather we highlighted the enhanced RBD-ACE2 electrostatic complementarity and potentially increased RBD solvation as explanations for the increased ACE2 affinity conferred by R452. Protein-protein interaction studies have predicted that long-range electrostatic complementarity plays a role in determining complex association rates[154]. Therefore, the increased electrostatic complementarity between ACE2 and the RBD due to R452 may enhance ACE2 affinity by increasing the probability of forming favourable RBD-ACE2 binding orientations. The increased solvation and electrostatic complementarity explanations are not mutually exclusive and may contribute to increased ACE2 affinity in combination.

3.3 Methods

3.3.1 Cloning, expression, and purification of recombinant spike protein constructs

Mutations were introduced to the SARS-CoV-2 hexapro ectodomain construct by site-directed mutagenesis (Q5 Site-Directed Mutagenesis Kit, New England Biolabs). Successful subcloning and mutation were confirmed by Sanger sequencing (Genewiz). Spike proteins were expressed and purified as described in section 2.3.3.

3.3.2 Antibody Production

ab8, ab1 and CR3022 were a gift from Drs. Dimitrov and Li. Plasmids encoding light and heavy chains for Fab S309 and S2M11 were synthesized (Synbio). Heavy chains were designed to incorporate a C terminal 6x histidine tag. Expi293 cells were transfected at a density of 3 x 10ˆ6 cells/mL using linear polyethylenimine (Polysciences Cat# 23966-1). 24-hours following

transfection, media was supplemented with 2.2 mM valproic acid and expression carried out for 3-5 days at 37°C, 8% CO2. The supernatant was harvested by centrifugation and filtered through a 0.22 μM filter prior to loading onto a 5 mL HisTrap excel column (Cytiva). The column was washed for 20 CVs with wash buffer (20 mM Tris pH 8.0, 500 mM NaCl), 5 CVs of wash buffer supplemented with 20 mM imidazole and the protein eluted with elution buffer (20 mM Tris pH 8.0, 500 mM NaCl, 500 mM imidazole). Elution fractions containing the protein were pooled and concentrated (Amicon Ultra 10 kDa cut off, Millipore Sigma) for gel filtration. Gel filtration was conducted using a Superose 6 10/300 GL column (Cytiva) pre-equilibrated with GF buffer (20 mM Tris pH 8.0, 150 mM NaCl). Peak fractions corresponding to soluble protein were pooled and concentrated to 8 - 20 mg/mL (Amicon Ultra 10 kDa cut off, Millipore Sigma). Protein samples were stored at 4°C until use.

3.3.3 Pseudo-virus Neutralization Assay

Assays were performed as described in section 2.3.8.

3.3.4 Enzyme-linked immunosorbent assay (ELISA)

Competition ELISAs were performed as described in section 2.3.4. For antibody binding studies 100 μl of wild-type or VoC RBD mutant SARS-CoV-2 S protein preparations were coated onto 96-well MaxiSorp™ plates at 2 μg/ml in PBS overnight at 4°C. All washing steps were performed 5 times with PBS + 0.05% Tween 20 (PBS-T). After washing, wells were either incubated with blocking buffer (PBS-T + 2% BSA) for 1 hr at room temperature. After washing, wells were incubated with dilutions of primary antibodies in PBS-T + 0.5% BSA buffer for 1 hr at room temperature. After washing, wells were incubated with goat anti-human IgG (Jackson ImmunoResearch) at a 1:8,000 dilution in PBS-T + 0.5% BSA buffer for 1 hr at room temperature.

After washing, the substrate solution (Pierce™ 1-Step™) was used for colour development according to the manufacturer's specifications. Optical density at 450 nm was read on a Varioskan Lux plate reader (Thermo Fisher Scientific).

3.3.5 Biolayer interferometry (BLI)

The binding kinetics of SARS-CoV-2 trimers and human ACE2 was analyzed with the biolayer interferometer BLItz (ForteBio). Protein-A biosensors (ForteBio, 18–5010) were coated with ACE2-mFc (40 μg/ml) for 2 min and incubated in DPBS (pH = 7.4) to establish baselines. For the N501Y mutation study, concentrations of 100 nM, 200 nM, and 400 nM spike trimers were used for association for 2 min followed by dissociation in DPBS for 5 min. For the RBD mutation in the D614G background study, concentrations of 125, 250, 500 and 1000 nM spike trimers were used. The association (kon) and dissociation (koff) rates were derived from the sensorgram fitting and used to calculate the binding equilibrium constant (K_D).

3.3.6 Cryo-EM sample preparation and data collection

S-protein samples were prepared at 2.25 mg/mL, with and without the addition of ACE2 (~1:1.25 S-protein trimer:ACE2 molar ratio) (New England Biolabs). For ab8 and ab1 complexes the same spike concentration was used but with a 1:9 and 1:8 molar ratio to ab8 and ab1 respectively. Vitrified samples of S-protein constructs with and without ACE2/antibody were prepared by first glow discharging Quantifoil R1.2/1.3 300 mesh holey carbon copper grids for 1 minute using a Pelco easiGlow glow discharge unit (Ted Pella, Redding CA) and then applying 1.8 μL of protein suspension to the surface of the grid. Grids were blotted (12 sec, blot force -10) and plunge frozen into liquid ethane using a Vitrobot Mark IV (Thermo Fisher Scientific) at a temperature of 10°C and a humidity level of 100%. All cryo-EM samples were imaged using a 300 kV Titan Krios G4

transmission electron microscope (ThermoFisher Scientific) equipped with a Falcon4 direct electron detector in electron event registration (EER) mode.

3.3.7 Cryo-EM Image Processing

In general, all data processing was performed in cryoSPARC v.2.15 or v.3.0.1 unless stated otherwise. Motion correction in patch mode, CTF estimation in patch mode, reference-free particle picking and particle extraction were performed on-the-fly in cryoSPARC. After preprocessing, particles were subjected to 2D classification and/or 3D heterogeneous classification. Final 3D refinement was done with per particle CTF estimation and aberration correction. For complexes of spike protein ectodomain and human ACE2, focused refinements were performed with a soft mask covering single RBD and its bound ACE2. Local refinements with a soft mask covering a single RBD and its bound VH ab8 or ACE2 resulted in improvement of the binding interfaces. C3 symmetry expanded particles were used for local refinement of RBD and its bound Fab ab1. Global resolution and focused resolution were according to the gold-standard FSC.

3.3.8 Model Building and Refinement

Coordinates of PDB 6WGJ and 7CH5 were used as initial models to build the VH ab8 and Fab ab1, respectively. Individual domains of SARS-CoV-2 HexaPro S trimer (PDB ID 6XKL) were docked into cryo-EM density using UCSF Chimera v.1.15 . Initial models were first refined against sharpened locally refined maps, followed by iterative rounds of refinement against consensus map in Coot v.0.9.3 and Phenix v.1.19. For models of complex of spike protein ectodomain and human ACE2, the RBD-ACE2 subcomplex was built using coordinates of PDB code 7MJN as an initial model and refined against focused refinement maps. Then it was docked into global refinement maps together with individual domains of spike protein. Glycans were added at N-linked

glycosylation sites in Coot. Model validation was performed using MolProbity. Structural analyses and figure generation were performed in ChimeraX.

3.3.9 Analysis of convalescent patient antibody footprints

PDB entries of SARS-CoV-2 spike or RBD complexes with antibody fragments isolated from convalescent patients were selected. Antibody footprints were determined by consulting respective depositing studies along with analysis of protein-protein contacts using PDBsum[155].

Chapter 4: Structure, Receptor Engagement, and Antibody Neutralization of Variant SARS-CoV-2 Spike Proteins

4.1 Introduction

Since 2020 there have been many variants of SARS-CoV-2 that have emerged, with a select few that have managed to achieve global domination (Figure 4.1). Many of these variants exhibit enhanced infectivity and transmissibility, achieving global spread[121,130–132,136,152,153,156–158] , and have been designated variants of concern (VoCs) or variants of interest (VoIs) by the WHO. Each of these variants possesses defining mutations within their spike glycoproteins. In chapter 3 we provided a comprehensive analysis of mutations falling within the RBD, finding overall a balance between increasing ACE2 binding affinity and enabling antibody evasion. However, variant spike proteins harbour numerous mutations in addition to those within the RBD. Importantly, all major variants possess mutations within the NTD, a site of antigenic significance as revealed in chapter 2 and by several major studies[107,108]. Therefore, in this chapter we aim to evaluate the impact of the totality of mutations within each variant spike protein on structure, function in ACE2 binding, and recognition by antibodies. Given the mutational variation observed in SARS-CoV-2 variant spike proteins, we additionally aim to identify any conserved epitopes that may confer broad neutralization of circulating variants.

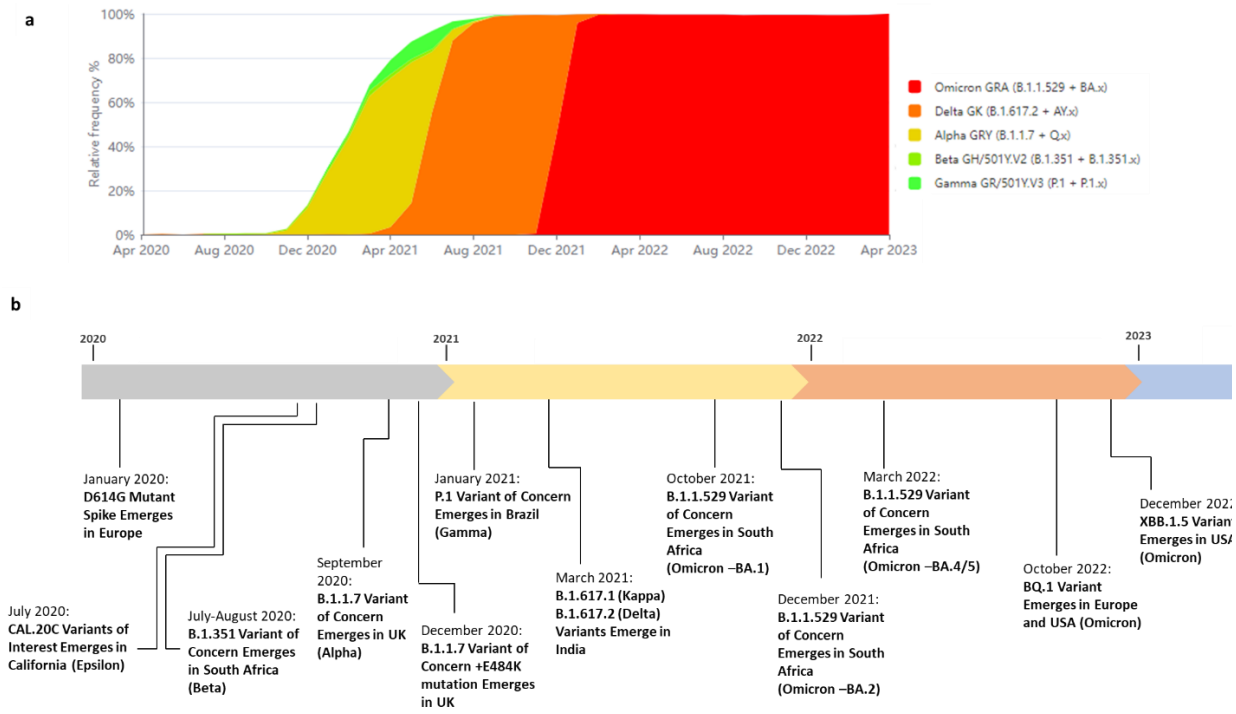

Figure 4.1. **Timeline of SARS-CoV-2 variants.** (a) Global frequencies for SARS-CoV-2 variant sequences deposited in the GISAID database. (b) Chronological timeline of SARS-CoV-2 variant emergence. Experiments in this chapter were all completed by June 2022 and do not include variants that emerged after.

4.2 Results and Discussion

4.2.1 Studies on "First Generation" Variant Spike Proteins

This chapter will take a chronological approach to characterizing variant spike proteins as we responded to groups of emerging variants in real time. We will first group our efforts to characterize the "first generation" variant spike proteins (those that emerged between 2020-2021) (Figure 4.1, Figure 4.2) before proceeding to the Omicron generation spike proteins which began emerging in late 2021 and into 2022 (Figure 4.1).

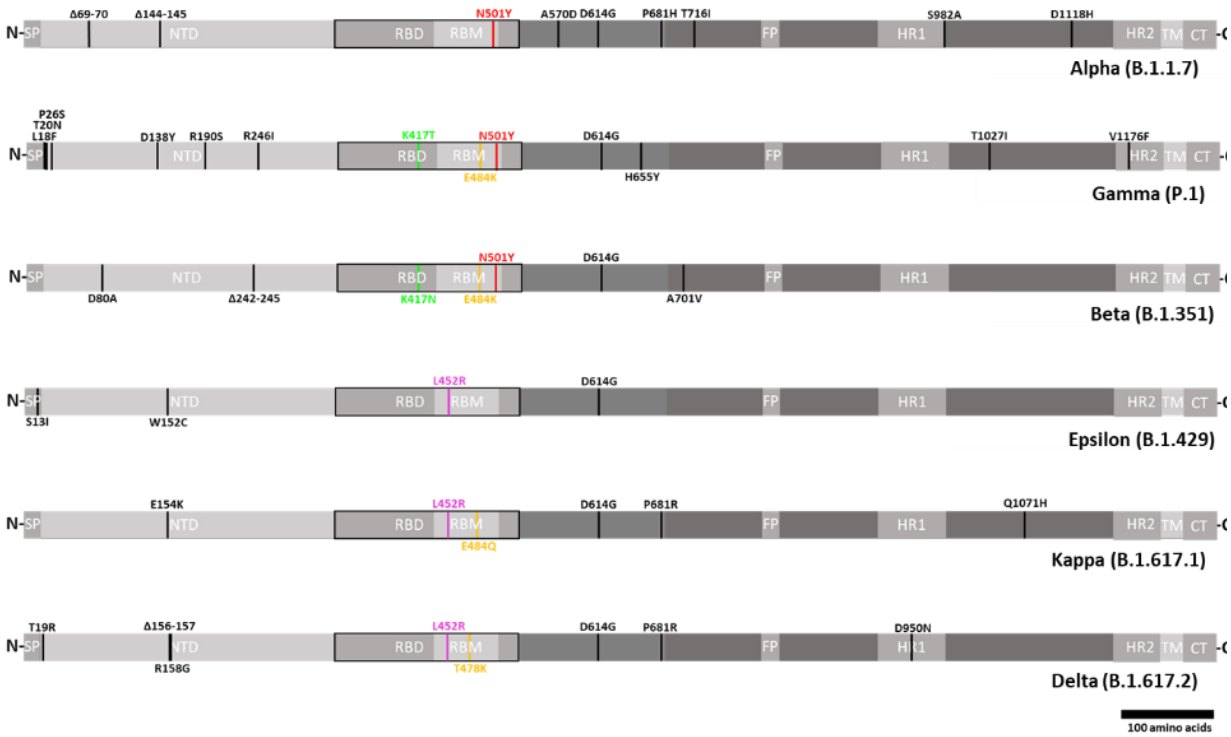

Figure 4.2. **Spike protein mutations present within selected "first generation" variants studied in this chapter.** Relevant features are indicated: SP, signal peptide; NTD, N-terminal domain; RBD, receptor binding domain; RBM, receptor binding motif; FP, fusion peptide; HR1, heptad repeat 1; HR2, heptad repeat 2; TM, transmembrane domain; CT, cytoplasm domain. RBD mutations are coloured.

4.2.1.1 Receptor Binding by Variant Spike Proteins

To investigate the ACE2 binding potential of SARS-CoV-2 variant spikes, recombinant S protein ectodomains bearing variant spike mutations were used in biolayer interferometry (BLI) experiments. While the Kappa spike protein showed comparable ACE2 binding compared to the D614G spike protein, all other mutant spikes exhibited modest increases in ACE2 binding (Figure 4.3a). In chapter 3 the impact of RBD mutations on ACE2 binding affinity was evaluated, allowing the identification of enhancing and reducing mutations, which acted in a modular fashion when combined to represent variant spike proteins. When ranking the relative increases in ACE2 binding for variant spike proteins bearing full complements of mutations and spike proteins harbouring

only RBD mutations, there is agreement in the relative ranking (Figure 4.3a), further demonstrating the modular nature of these mutations. The structural basis for the impacts of these mutations on ACE2 binding are explored in chapter 3 and will not be considered here. However, the Kappa variant RBD contains the E484Q mutation, and the Delta variant contains the T478K mutation, neither of which were included in our previous studies as these variants had not emerged at the time. To understand the impact of these mutations on ACE2 binding we performed cryo-EM investigations of the Kappa and Delta variant spike proteins in complex with ACE2.

The focus-refined atomic structure of the Kappa variant S protein in complex with ACE2 reveals limited structural changes at the RBD-ACE2 interface (Figure 4.3b). The Kappa variant E484Q mutation results in the loss of an electrostatic interaction between residue E484 and residue K31 within ACE2, likely resulting in a weaker interaction at this site. However, the enhanced electrostatic complementarity afforded by the accompanying L452R mutation, seen in chapter 3 and in the Epsilon variant (Figure 4.3a), likely presents a compensatory mutation accounting for the lost E484–K31 interaction (Figure 4.3c). The combination of these two opposing mutations, one diminishing ACE2 affinity (E484Q), and the other increasing ACE2 binding (L452R), is consistent with the unchanged overall affinity of the Kappa S protein–ACE2 binding interaction (Figure 4.3a). Precedence for compensatory mutations towards increasing ACE2 affinity while decreasing antibody binding was shown in chapter 3.

As was seen for the Kappa variant, the Delta variant S protein–ACE2 complex focus-refined cryo-EM structure also reveals limited sidechain rearrangement at the RBD-ACE2 interface (Figure 4.3b). The Delta variant lacks the E484Q substitution which preserves the E484–K31 electrostatic interaction, while the L452R mutation likely increases ACE2 binding by enhancing electrostatic

complementarity as previously described. Further, the Delta variant lysine substitution at position 478 (T478K) extends its positively charged sidechain towards an electronegative region on ACE2 (centred at position E87) (Figure 4.3c). Therefore, the combination of enhanced electrostatic complementarity afforded by the L452R and T478K Delta variant substitutions likely accounts for the moderate increase in ACE2 affinity (Figure 4.3a).

Overall, our analysis of these SARS-CoV-2 variant spike proteins revealed either marginally enhanced or unchanged ACE2 binding affinities compared to the ancestral Wild-Type D614G spike protein. Thus, it is unlikely that ACE2 binding affinity alone represents the sole critical selection pressure for evolution of these variant spike proteins. It is likely that there exists a required ACE2 binding affinity threshold that must be at least preserved as SARS-CoV-2 undergoes mutational drift. The presence of both ACE2 affinity enhancing and reducing mutations in variant spike proteins (Beta, Gamma, Kappa) further substantiates the notion of compensatory mutations that balance ACE2 binding with other aspects of spike protein fitness such as immune evasion.

a

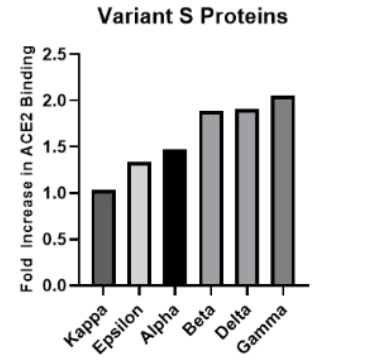

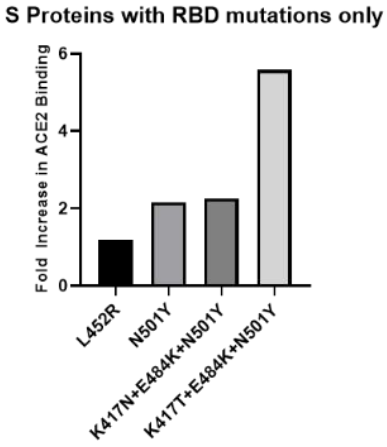

Variant	RBD Mutations	Variant S Protein Fold Increase in ACE2 Binding	S Protein + RBD Mutations Fold Increase in ACE2 Binding
Kappa (B.1617.1)	L452R E484Q	1.0	n/a
Epsilon (B.1429)	L452R	1.3	1.2
Alpha (B.1.1.7)	N501Y	1.5	2.2
Beta (B.1.351)	K417N E484K N501Y	1.9	2.3
Delta (B.1.617.2)	T478K L452R	1.9	n/a
Gamma (P.2)	K417T E484K N501Y	2.1	5.6

Red – Increase ACE2 Affinity
Blue – Decrease ACE2 Affinity

b

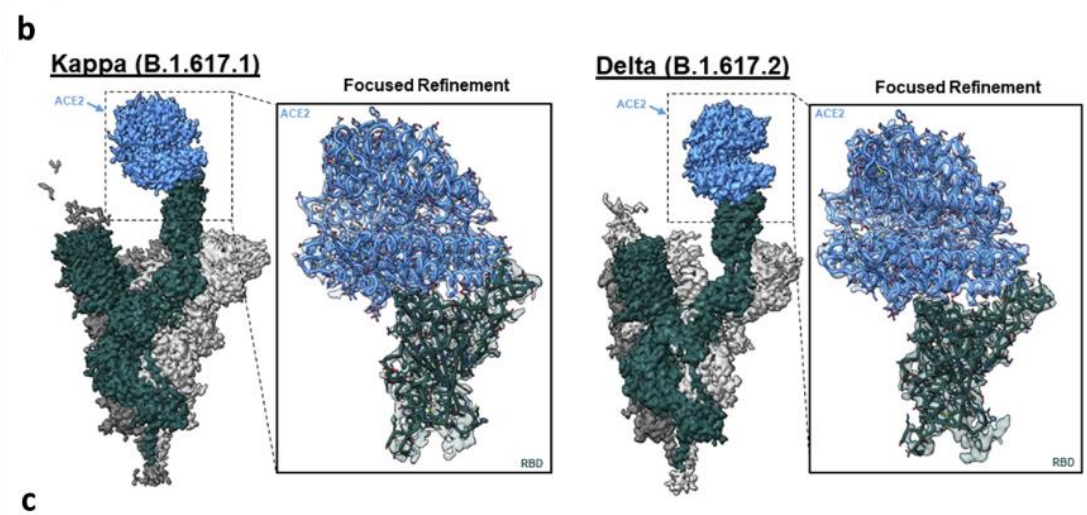

c

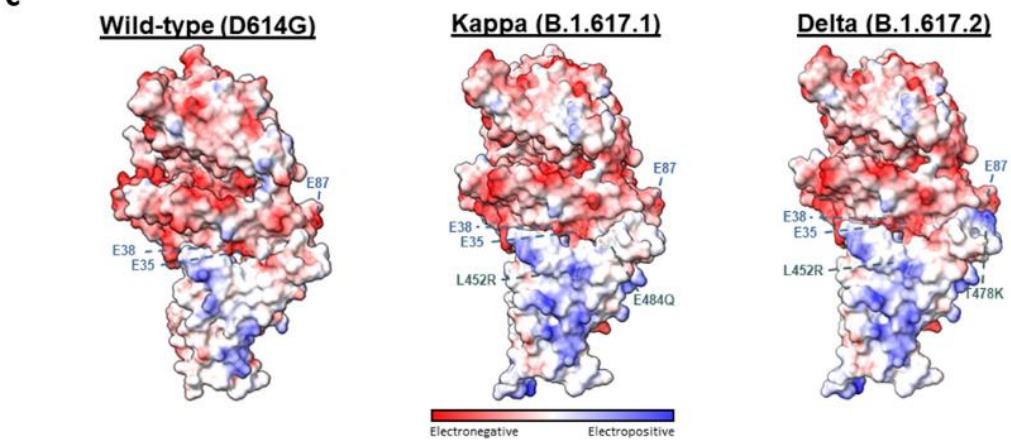

Figure 4.3. **Analysis of ACE2 binding by SARS-Cov-2 variant spike proteins.** (a) Fold increases in ACE2 binding affinities for different spike proteins compared to unmutated D614G spike measured via biolayer interferometry (BLI). Fold changes for variant spike proteins harbouring full sets of mutations (top) are compared with those from chapter 3 which incorporated only RBD mutations (bottom). Fold changes and comparison between these groups are tabulated on the right. (b) The global and focus-refined cryo-EM structures for the Kappa and Delta variant S proteins in complex with ACE2. (c) Electrostatic surface potentials for the wild-type, Kappa and Delta S protein–ACE2 complexes.

4.2.1.2 Antibody binding and Neutralization of Variant Spike Proteins

We next aimed to assess the antibody evasive properties of the selected variant spike proteins. We performed antibody binding and neutralisation studies using recombinant variant spike ectodomains and variant pseudo-typed viruses respectively. First, a panel of previously characterised monoclonal antibodies targeting epitopes in the spike RBD or NTD were assessed[104,105,110,127,137,144,159] (Figure 4.4a). S309 and CR3022 are RBD binding, cross-reactive SARS-CoV-1 directed antibodies. While S309 cross-neutralizes SARS-CoV-2[159], CR3022 binds but does not neutralize the SARS-CoV-2 spike protein[160–163]. Both S309 and CR3022 bind the SARS-CoV-2 spike protein in regions that do not span any variant mutations. Accordingly, CR3022 exhibited relatively unchanged binding across the variant spike proteins tested, and S309 bound and neutralized all variant pseudo-types tested although a modest reduction in binding and neutralization of the Kappa and Delta variants was observed (Figure 4.4b). In chapter 3 we characterized the mutational sensitivity of ab1, ab8, and S2M11 to spikes bearing only RBD mutations corresponding to those found in the Alpha, Beta, Gamma, and Epsilon variants, and the current analysis of antibody evasion using spikes bearing full sets of mutations (Figure 4.4b) is consistent with our previous studies: (1) The N501Y mutation within the Alpha variant reduces but does not abolish the neutralization potency of ab1, while dramatic loss of ab1 activity is seen in Beta and Gamma variants due to mutation of K417 to N or T, respectively; (2) The E484K

mutation abrogates ab8 and S2M11 activity in the Beta and Gamma variants; and (3) the L452R mutation reduces but does not abrogate activity of S2M11 in the Epsilon variant spike. Total escape of ab8 was achieved by the E484Q-bearing kappa spike protein, drawing similarity to the effect of the E484K mutation within the Beta and Gamma variants. In contrast to the complete loss of S2M11 activity for the E484K-bearing Beta and Gamma variants, binding and neutralisation of S2M11 was attenuated but not abolished by the E484Q mutation within the Kappa variant, suggesting tolerance for Q but not K at position 484. Despite falling within the footprint of ab1, the T478K mutation within the Delta variant does not result in antibody escape, suggesting accommodation of this mutation by ab1.

Evasion of NTD-directed antibodies was observed in cases when mutations were either within, or adjacent to, antibody footprints (Figure 4.4b). The W152C substitution within the Epsilon NTD is inside the footprints of 4A8 and 4–8, and both antibodies escaped by this variant spike. The Beta NTD contains a deletion (Δ242–245) which spans the 4–8 footprint, along with the R261I substitution spanning both 4A8 and 4–8 footprints, leading to escape from both antibodies. The footprint of 4A8 and 4–8 spans a deleted site within the Alpha NTD (Δ144–145) leading to escape. The Kappa variant spike harbours the E154K mutation which falls within the 4-8 footprint and evaded both 4-8 and 4A8. The Delta spike contains the R158G mutation which falls within both NTD directed antibody footprints, along with the deletion of E156, a residue within the 4A8 footprint, and accordingly both antibodies were completely evaded by the Delta spike protein. The Gamma spike protein uniquely retained susceptibility to both NTD directed antibodies, likely due to the absence of any NTD mutations falling directly within antibody footprints. Overall, these direct and allosteric mutational effects are consistent with other structural findings on NTD rearrangement within these variants[164–167] and demonstrate their antibody evasive properties.

Having characterized monoclonal antibody evasion by variant spikes, we extended our analysis to include polyclonal antibody escape from human sera. We utilized serum from the cohort introduced in chapter 2, comparing the ability of these sera to neutralize variant and Wild-Type (D614G) pseudo-typed viruses. We observed various effects on neutralization escape when sera samples were assayed using variant spike pseudo-typed viruses, obtaining overall statistically significant decreases in neutralization efficacy for the Beta, Gamma, and Delta variants relative to Wild-Type (Figure 4.4c).

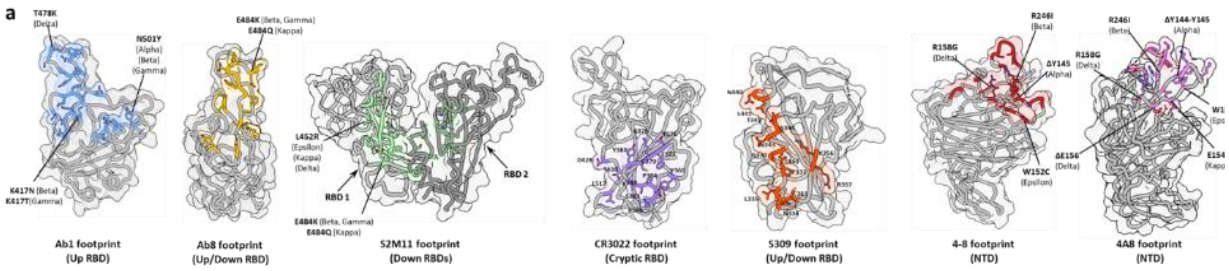

b

Antibody Binding

	RBD Directed					NTD Directed	
	ab1	ab8	S2M11	CR3022	S309	4A8	4-8
B.1.1.7 (Alpha)	0.63	3.47	0.26	0.53	1.29	N.B	N.B
B.1.351 (Beta)	N.B	N.B	N.B	1.24	2.40	N.B	N.B
P.1 (Gamma)	N.B	N.B	N.B	1.63	1.74	9.36	0.32
B.1.429 (Epsilon)	0.82	4.49	8.77	1.33	2.50	N.B	N.B
B.1.617.1 (Kappa)	0.32	N.B	N.B	n/a	5.30	N.B	N.B
B.1.617.2 (Delta)	0.16	2.07	7.82	n/a	5.19	N.B	N.B

Red: Resistance > 8 EC50 Fold change
NB: No Binding Detected

Antibody Neutralization

	RBD Directed				NTD Directed	
	ab1	ab8	S2M11	S309	4A8	4-8
B.1.1.7 (Alpha)	15.48	1.56	1.32	2.33	>100	>100
B.1.351 (Beta)	>100	>100	>100	2.20	>100	>100
P.1 (Gamma)	>100	>100	>100	0.93	1.85	0.84
B.1.429 (Epsilon)	2.80	1.46	4.10	2.46	>100	>100
B.1.617.1 (Kappa)	0.26	>100	>100	10.78	>100	>100
B.1.617.2 (Delta)	0.46	0.22	0.39	11.21	>100	>100

Red: Resistance > 3 EC50 Fold change

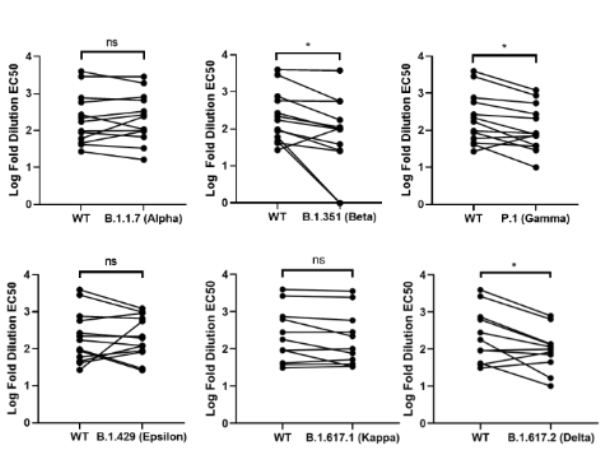

Figure 4.4. **Alpha, Beta, Gamma, Epsilon, Kappa, and Delta S proteins exhibit differences in monoclonal and polyclonal antibody escape.** (a) Antibody-binding footprints for monoclonal antibodies included in the study. Variant S protein mutations falling within each footprint are highlighted. (b) Fold-changes in antibody binding (top) and pseudovirus neutralization EC50s (bottom) for each variant spike relative to wild-type (D614G). Antibody binding was quantified by ELISA. (c) Log-fold EC50 dilutions of patient sera when neutralizing wild-type and variant spike pseudovirus. Statistical significance was tested via the Wilcoxon matched pairs test (*$p \leq 0.05$, ns, not significant)

These results confirm the antibody evasive nature of SARS-CoV-2 spike protein mutations within the RBD and NTD. While escape of monoclonal antibodies was striking in many cases, variant spike proteins generally displayed milder extents of escape from polyclonal sera. This is likely due to the enhanced epitope coverage afforded by multiple antibodies present in these samples and suggests the potential for broadly neutralizing antibodies against multiple variants.

4.2.1.3 Overall architecture of variant spike proteins

Having demonstrated mutational effects on antibody evasion and receptor engagement, we next sought to characterize the structural impacts of variant S protein mutations. To this aim, ectodomains bearing variant spike mutations were used for cryo-EM structural studies. Global 3D reconstructions were obtained at resolutions ranging from (2.25–3.16 Å) (Figure 4.5), yielding open trimers with one RBD in the up conformation and 2 RBDs in the down conformation for Alpha, Beta, Gamma, and Epsilon spike proteins, while the Delta spike protein was resolved with 1 RBD down and weak density for the remaining 2 RBDs, potentially due to averaging of these domains in both up and down states. The resolutions within the NTD and RBD regions were insufficient for accurate visualization of mutational impacts within these domains, likely due to high degrees of conformational heterogeneity. Unexpectedly, we observed a "head-to-head dimer of trimers" architecture for the Kappa variant spike protein (Figure 4.5). This dimer is mediated by RBD-RBD contacts between two S protein trimers, with one trimer offset at a 12° angle. This angle is a result of slightly asymmetric binding at each RBD-RBD contact. As the intrinsic ability to form such dimers has never been observed for any previous SARS-CoV-2 spike protein or any other coronavirus spike protein to our knowledge, we focused our structural efforts on resolving the interface of this unique assembly.

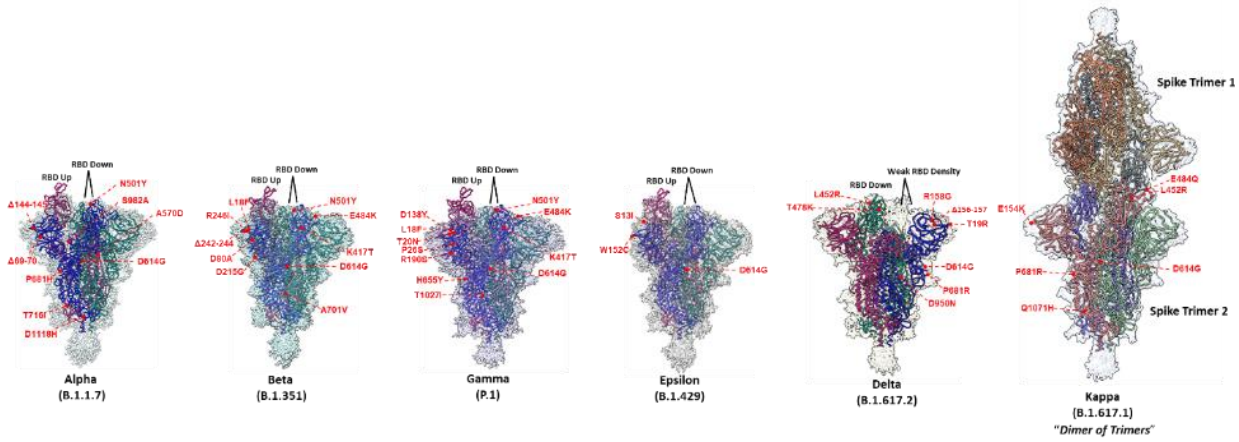

Figure 4.5. **Cryo-EM structures of Alpha, Beta, Gamma, Epsilon, Delta and Kappa spike glycoproteins.** Global cryo-EM maps and models for the Alpha (2.56 Å), Beta (2.56 Å), Gamma (2.25 Å), Epsilon (2.4 Å), Kappa (2.25 Å) and Delta (3.16 Å) variant S proteins. Mutational positions are indicated and labeled in red. Mutations that could not be modelled are placed at the nearest modelled residue.

4.2.1.4 Structural Studies on the Kappa Variant Spike Assembly

Focused refinement of the dimer-of-trimers interaction interface reveals an extensive binding interface involving all six RBDs (Figure 4.6). Each RBD interacts with two RBDs in the opposite trimer via two distinct interfaces, henceforth referred to as RBD1 and RBD2 (Figure 4.6 c-d). Interactions stabilising the RBD1 interface are primarily mediated by van der Waals interactions and hydrophobic contacts between residues across this interface. Additionally, homo- asparagine-asparagine and glutamine-glutamine hydrogen bonds at positions 440 and 506, respectively, and a backbone carbonyl oxygen–amide hydrogen bond between residues 372 and 445 further contribute to the RBD1 interface (Figure 4.6c).

The second RBD-RBD interface (RBD2), comprises multiple doubly-hydrogen bonded residues, between residues N487-N450 and between residues N450-Y489/N487 (Fig4.6c-d). Additionally, two homo- glutamine-glutamine hydrogen bonds are present between residues Q493-Q493 and

Q484-Q484 from each trimer. This latter interaction at position 484 is of particular interest as it is uniquely mutated from glutamic acid to glutamine (E484Q) in the Kappa variant. Given this unique substitution and the unique dimer-of-trimers phenotype seen only for the Kappa variant spike (and not for Alpha, Beta, Gamma, Epsilon and various RBD-mutated spike trimers), we identified position 484 as likely being crucial for S protein dimerization.

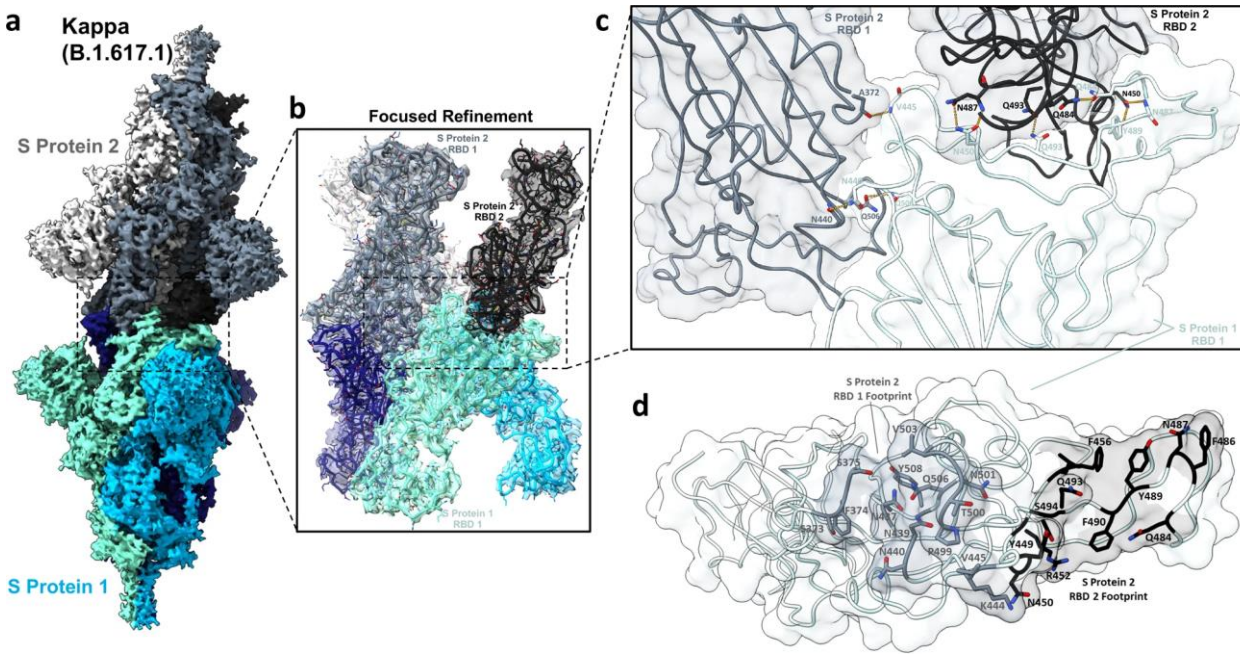

Figure 4.6. **The Kappa variant S protein exhibits a novel dimer-of-trimers phenotype.** (a) Side view of the global cryo-EM density map of the Kappa variant dimer-of-trimers complex. One trimer (S Protein 1, bottom) is displayed in various shades of blue, and the other trimer in grayscale (S Protein 2, top). (b) Focus-refined cryo-EM density map and fitted atomic model at the dimerisation interface. (c) Detailed view of the molecular interface between two RBDs in the grayscale trimer (top) and a single RBD in the blue shaded trimer (bottom). For amino acids involved in inter-residue hydrogen bonding, the backbone and sidechain atoms are displayed. Hydrogen bonds are indicated by yellow dashed lines. (d) The top-down view of the region in panel **c** is shown. The binding footprints of RBD1 and RBD2 are indicated by complementary shading and displaying the sidechain atoms of footprint residues.

Having identified that residue identity at position 484 likely affects head-to-head S protein oligomerization, we aimed to further probe the chemical properties at 484 that mediate this dimerisation. A focused view of the Q484-Q484 hydrogen bond (Figure 4.7a) shows the bond to be sandwiched by proximal bulky F490 aromatic sidechains. We therefore hypothesised that charge neutrality at position 484 (as seen in the Q484, but not E484 or the recently emerged K484 S proteins) may be sufficient to reduce charge–charge repulsion at this site and therefore allow dimerisation. To test this, we performed site-directed mutagenesis to substitute an alanine at position 484 (Q484A) in the Kappa S protein, purified the trimer, and performed structural studies. The cryo-EM reconstruction of Q484A spikes revealed no evidence of dimer-of-trimer assemblies, consistent with our previous results for wild-type and other variant of concern (VoC) spikes (Figure 4.7b). We next hypothesised that the homo-glutamine hydrogen bond conferred by the Q484 sidechain provided an additional contact critical for dimer formation. Accordingly, we introduced the amino acid isoleucine at position 484, which possesses a branched aliphatic sidechain capable of providing hydrophobic packing contacts. The cryo-EM reconstruction yielded a dimer-of-trimers phenotype for the Kappa + Q484I S protein variant, yet, with a reduced number of picked particles comprising the dimer class (46%), relative to the original Kappa variant with Q484 (74%) (Figure 4.7b-c). The Kappa and Kappa + Q484I dimer-of-trimers are structurally very similar, with RMSD values of 0.262 Å and 0.705 Å for the global and focus-refined atomic models, respectively. The oligomerization state of S proteins harbouring charged residues at 484 (E484, K484), along with the Q484A and Q484I mutations demonstrate that abrogation of charge at position 484 is necessary but not sufficient to permit dimerisation. Rather, a combination of charge neutralisation and additional contacts enabled by sidechains at position 484 is required for S protein dimerisation.

An analysis of the electrostatic surface potential at position 484 of the RBD reveals a unique property of the Kappa variant that may explain its propensity to dimerise. Figure 4.7d shows that the wild-type/Alpha/Delta variants and the Beta/Gamma variants may be binned into electronegative and electropositive surfaces at position 484, respectively, which would result in charge–charge repulsion if these variant S proteins were to dimerise in the same manner as the Kappa variant. The Kappa variant uniquely has an absence of charge at position 484 in its S protein, as reflected in the neutral surface potential shown in Figure 4.7d, consistent with its distinguishing ability to form head-to-head dimers.

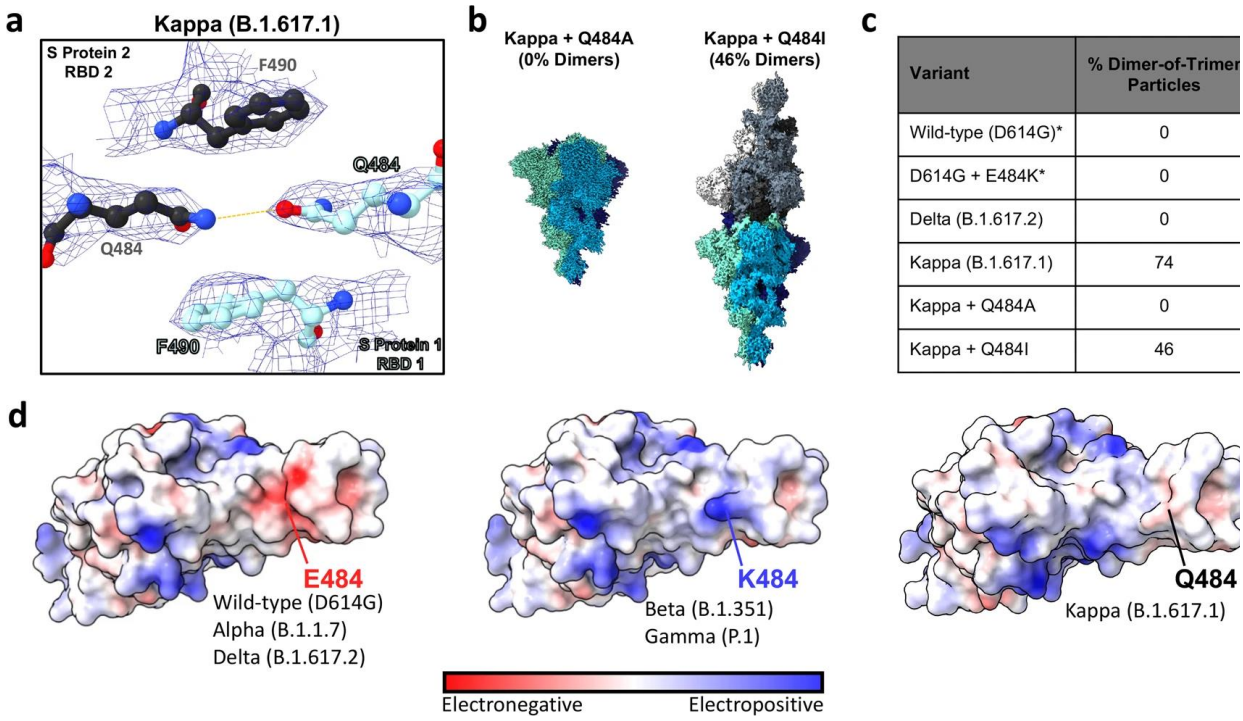

Variant	% Dimer-of-Trimer Particles
Wild-type (D614G)*	0
D614G + E484K*	0
Delta (B.1.617.2)	0
Kappa (B.1.617.1)	74
Kappa + Q484A	0
Kappa + Q484I	46

Figure 4.7. **Impact of residue identity at position 484 on S protein oligomerization.** (a) Detailed view of the Kappa (B.1.617.1) dimer-of-trimers cryo-EM density map and fitted model at the Q484-Q484 interaction site. The hydrogen bond formed between Q484 residues located in different S ectodomain trimers (S protein 2 RBD 2 in black, and S protein 1 RBD 1 in cyan) is indicated with a yellow dashed line. (b) Cryo-EM density maps for the Kappa + Q484A and Kappa + Q484I mutated S proteins. (c) Summary table of the proportion of dimerised particles in S proteins harbouring mutations at position 484. Asterisks indicate structures reported in chapter 3. (d) E484, K484, and Q484 RBD electrostatic surface potentials highlighting the surface potentials at position 484. The E484 surface potential was generated using the wild-type (D614G) + ACE2 focus-refined atomic model from chapter 3. The K484 surface potential was generated using the D614G + N501Y + E484K focus-refined atomic model from chapter 3. The Q484 surface potential was generated using the Kappa + ACE2 focus-refined atomic model.

Our synthetic mutation of Q484I in the Kappa variant background, which also resulted in dimerisation, suggests that the SARS-CoV-2 S protein may be a single amino acid substitution away from exhibiting this dimer-of-trimers phenotype. However, an analysis of mutational frequency at position 484 in globally deposited sequences reveals that only E484, K484 and Q484 S protein genotypes have ever been present at >1% of total deposited sequences, suggesting limited mutational flexibility at this position (Figure 4.8). We found this head-to-head dimerisation to be concentration-dependent, with no evidence of dimerisation in experiments conducted at <0.05 mg/mL during negative-stain electron microscopy (Figure 4.9). Thus, we hypothesise that if local spike concentrations reach high enough concentrations to dimerise at any point during the SARS-CoV-2 cell entry, replication and packaging events, this dimerisation phenomenon could have biological implications. When considering membrane-embedded S protein dimerisation, cryo-electron tomography results[65,66] suggest that the S protein adopts angles relative to the viral membrane that would be incompatible with intra-virion S protein dimerisation, therefore if dimerisation were to take place in physiological and membrane-embedded contexts, it would likely be limited to between viral particles (inter-virion).

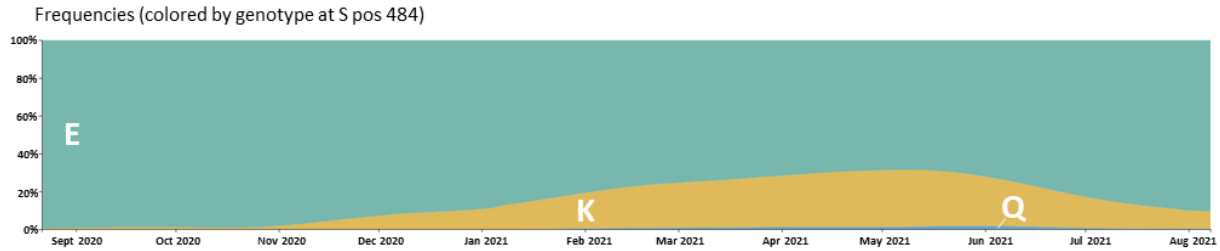

Figure 4.8. **Amino acid frequency at position 484 in global sequence deposits for the SARS-CoV-2 spike protein.** Residue frequency was derived from the Global Initiative on Sharing Avian Influenza Data (GISAID) database between September 2020 and August 2021.

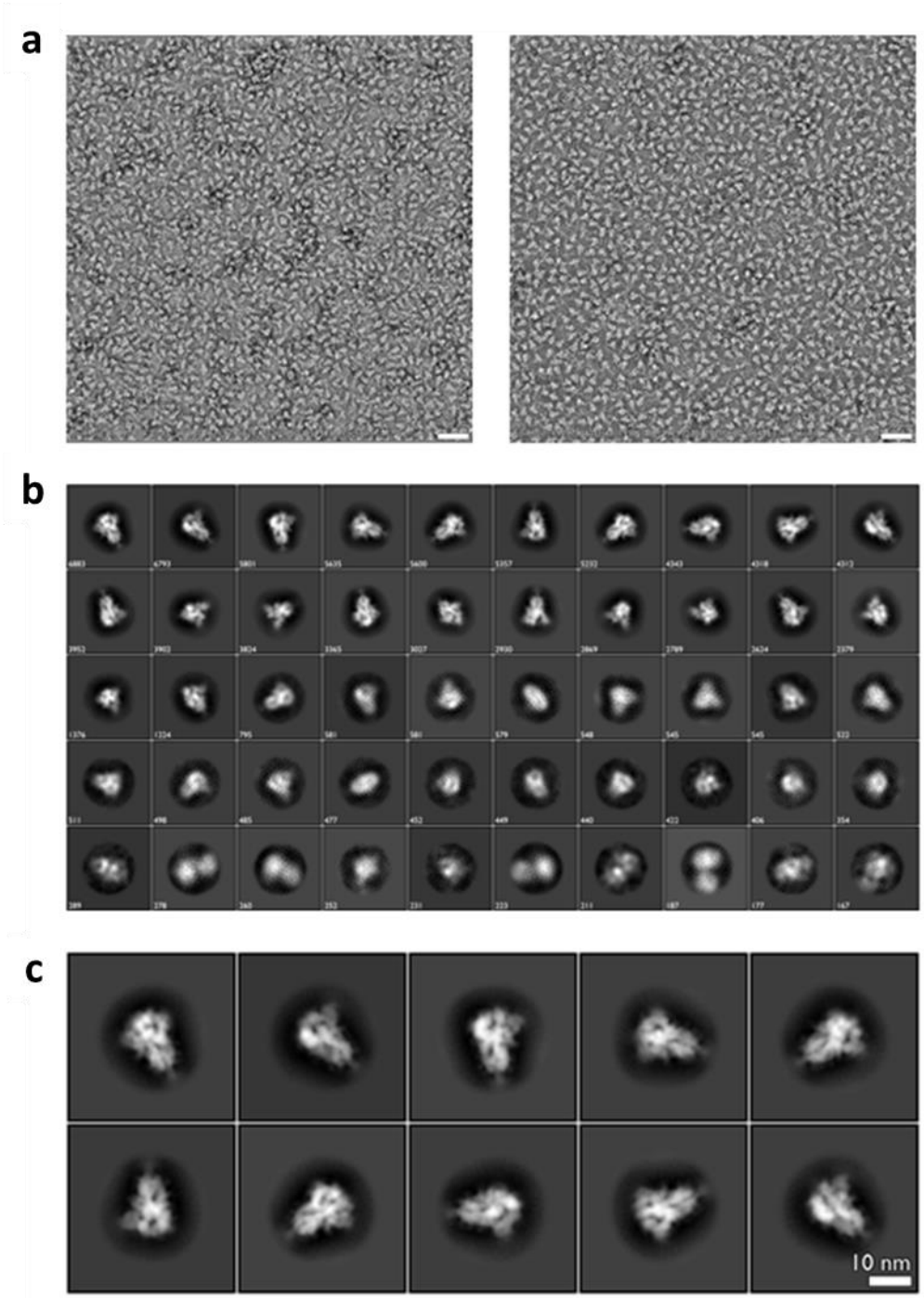

Figure 4.9. **The Kappa (B.1.617.1) variant S protein ectodomain reveals no dimerization under negative stain electron microscopy conditions. (**a) Two representative micrographs selected from the total dataset (1467 micrographs) for the Kappa (B.1.617.1) variant S protein ectodomain. (b**)** All 2D class averages derived from the micrographs as represented in (a). (c) The ten most highly populated 2D class averages from (b).

While future studies will be required to assess the potential biological relevance – if any – of the reported dimerisation of spike trimers, we speculate here on some mechanisms by which dimerised S proteins could theoretically result in increased or decreased viral fitness. Firstly, head-to-head S protein dimerisation buries much of the antibody-accessible surface area of the RBD (the predominant target of neutralising antibodies) and could shield this otherwise vulnerable neutralisation site[107]. Secondly, dimerised spikes - in the same manner as reported for the Kappa variant - would be unable to engage the ACE2 receptor and therefore not be able to enter host cells through the ACE2-dependent cell-entry pathway. These first two competing mechanisms resulting in increased and decreased viral fitness, respectively, could favour a spike protein with a finely tuned balance of dimerisation potential to both mask neutralising epitopes, but also to readily dissociate and permit engagement of ACE2. To this second point, we verified that the Kappa S protein dimer-of-trimers complex is labile enough to still permit ACE2 binding through our experimental derivation of the ACE2 bound structure. We saw no evidence of S protein dimer-of-trimer formation in our cryo-EM images upon introducing a modest excess of ACE2 (~1:1.25 S protein trimer : ACE2 molar ratio), despite an identical S protein concentration which resulted in the dimer-of-trimers reconstruction. Interestingly, two recent publications have independently described potent neutralising nanobodies with propensities to induce S protein dimers[168,169]. While the exact mode of neutralisation for these nanobodies remains unclear, this may suggest that S protein dimerisation has negative impacts on viral fitness. Further studies to elucidate the biological implications, if any, of this dimerisation phenomenon are therefore highly relevant in the rapidly evolving SARS-CoV-2 variant landscape.

4.2.2 Studies on the Omicron Lineage Spike Proteins

The studies up to this point have characterized the "first generation" variant spike proteins (Alpha, Beta, Gamma, Epsilon, Kappa, Delta). We now move to our efforts on the Omicron variant sub-lineages (BA.1 and BA.2) and their spike proteins. Sub-lineages will be addressed in chronological order of emergence, presented in the adapted form of 2 consecutive manuscripts. In the first manuscript the term Omicron is used to designate the initial BA.1 sub-lineage as no other sub-lineages had emerged at the time.

4.2.2.1 Studies of the Omicron (BA.1) Spike Protein

The Omicron (B.1.1.529) variant of SARS-CoV-2, first reported in November 2021, was quickly identified as a variant of concern with the potential to spread rapidly across the world. This concern was heightened because the Omicron variant quickly began circulating even among doubly vaccinated individuals.

The Omicron variant has 37 mutations (Figure 4.10a) in the spike protein relative to the initial Wuhan-Hu-1 strain, with 15 of them present in the RBD[170]. In comparison, the Delta variant, which was the predominant SARS-CoV-2 lineage until the emergence of Omicron, has only seven mutations in the spike protein relative to the Wuhan-Hu-1 strain, with only two mutations falling within its RBD. Of the Delta spike protein mutations, two [T478K (Thr^{478}→Lys) in the RBD and D614G (Asp^{614}→Gly) at the C terminus of S1] are shared with the Omicron strain. Analysis of the sequence of the Omicron genome suggests that it was not derived from any of the variants circulating at the time and may have had a different origin[171]. Currently, the two most likely hypotheses surrounding the origins of the Omicron variant are zoonotic transmission from a mouse adapted SARS-CoV-2 lineage[172], and evolution within immunocompromised individuals[172,173].

Cryo-EM structural analysis of the Omicron spike protein ectodomain shows that the overall organization of the trimer is similar to that observed for the ancestral strain and all earlier variants besides kappa (Figure 4.10b). The RBD in one of the protomers (protomer 1) is well-resolved and is in the down position, whereas the other two RBDs are less well-resolved because they are flexible relative to the rest of the spike protein polypeptide. Similarly, the amino terminal domain (NTD) is poorly resolved, reflecting the dynamic and flexible nature of this domain. The mutations in the Omicron variant spike protein are distributed both on the surface and the interior of the spike protein (Figure 4.10c), including the NTD and RBD regions. The mutations in the RBD are predominantly distributed on one face of the domain (Figure 4.10d), which spans regions that bind ACE2 as well as those that form epitopes for numerous neutralizing antibodies[174].

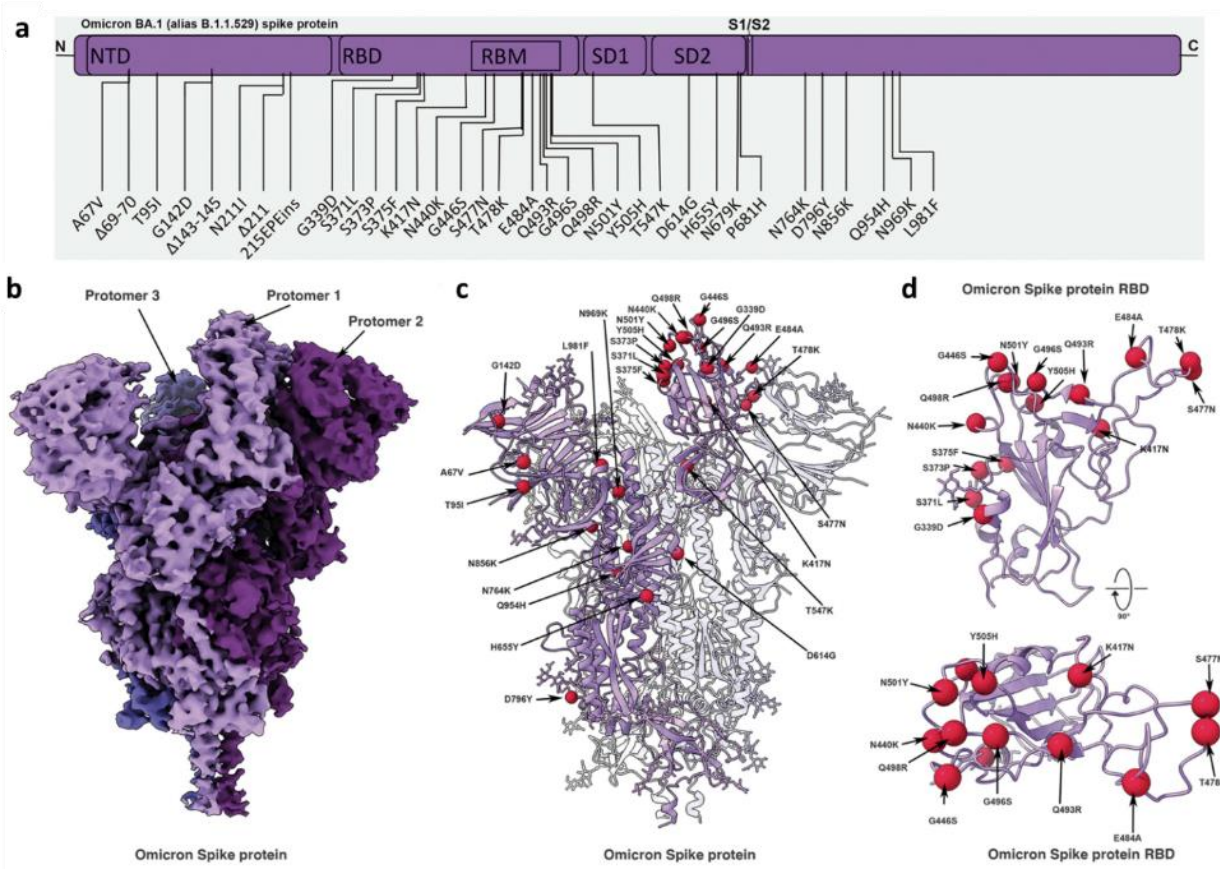

Figure 4.10. **Cryo-EM structure of the Omicron spike protein.** (a) A schematic diagram illustrating the domain arrangement of the spike protein. Mutations present in the Omicron variant spike protein are labeled. RBM, receptor binding motif. (b) Cryo-EM map of the Omicron spike protein at 2.79-Å resolution. Protomers are colored in different shades of purple. (c) Cryo-EM structure of Omicron spike protein indicating the locations of modeled mutations on one protomer. (d) The Omicron spike protein RBD shown in two orthogonal orientations with Cα positions of the mutated residues shown as red spheres.

The Omicron variant shares RBD mutations with previous variants of concern [K417N (Lys^{417}→Asn), T478K, and N501Y (Asn^{501}→Tyr)]. As shown in chapter 3, the N501Y and K417N mutations impart increased and decreased ACE2 binding affinities, respectively, and these mutational effects preserve the same general impact on ACE2 affinity when present in isolation or in combination with other RBD mutations. However, the Omicron RBD contains additional mutations, most of which have been shown to decrease receptor binding in a high-throughput

assay[117], with the exception of G339D (Gly[339]→Asp), N440K (Asn[440]→Lys), S447N (Ser[447]→Asn), and Q498R (Gln[498]→Arg)[117,139]. To measure the impact of Omicron spike protein mutations on human ACE2 binding affinity, we performed surface plasmon resonance (SPR) studies and compared the resulting apparent binding affinities ($K_{D,app}$) to wild-type and Delta spike proteins (Figure 4.11). "Wild type" is used in this work to refer to the ancestral Wuhan-Hu-1 strain with the addition of the D614G mutation. Although the Omicron spike protein exhibits a measurable increase in apparent affinity for ACE2 relative to the wild-type spike protein, the apparent ACE2 affinity is similar for both the Delta and Omicron variants (Figure 4.11d). Despite harboring several RBD mutations that decrease ACE2 binding, the preservation of overall ACE2 binding affinity for the Omicron spike protein suggests there are compensatory mutations that restore higher affinity for ACE2, similar to those explored in chapter 3. Such mutational effects should be possible to visualize in a high-resolution structure of the spike protein–ACE2 complex.

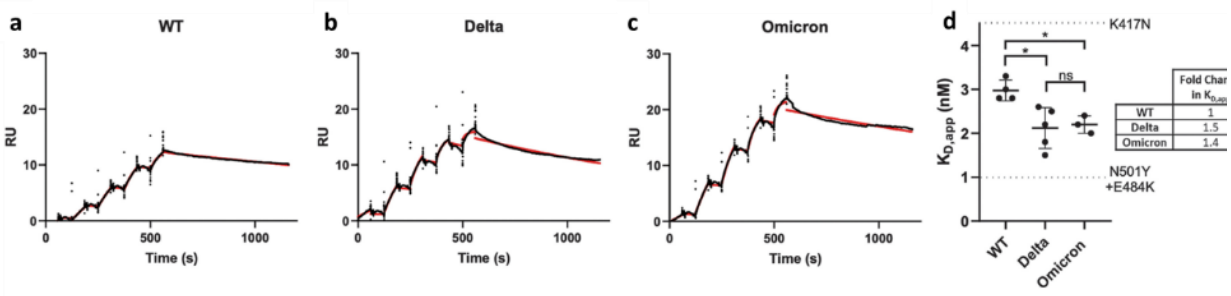

Figure 4.11. **SPR analysis of the wild-type, Delta, and Omicron spike protein affinities for human ACE2.** (a to c) Representative traces of single-cycle kinetic analyses of spike protein–ACE2 binding. The raw data (black) is fit (red) to a model using a 1:1 binding stoichiometry from which apparent dissociation constants were derived. The curves were obtained by injecting 6.25, 31.25, 62.5, 125, and 250 nM of each spike protein in successive cycles. RU, response units; WT, wild type. (d) Quantitation of apparent dissociation constants ($K_{D,app}$) for the wild-type, Delta, and Omicron spike protein–ACE2 interactions. The standard deviation obtained from at least three technical replicates is shown. Horizontal dotted lines are plotted for mutants carrying only K417N (top) or N501Y and E484K (Glu^{484}→Lys; bottom) mutations to demonstrate the range of this assay. A Tukey's multiple comparisons test was performed on the wild-type, Delta, and Omicron binding affinities (*$P \leq 0.05$; ns, not significant). A table highlighting the fold changes in $K_{D,app}$ for the Delta and Omicron spike protein–ACE2 interactions relative to wild type is shown.

Cryo-EM structural analysis of the human ACE2–Omicron spike protein complex shows strong density for ACE2 bound to the RBD of one of the protomers in the up position (Figure 4.12a). Weaker density is observed for a second bound ACE2, suggesting partial occupancy of a second RBD under our experimental conditions. We focus on the structure of the ACE2–spike protein interface in the most strongly bound ACE2 molecule. Focused refinement of the RBD-ACE2 region resulted in a density map with a resolution of 2.66 Å at the spike protein–ACE2 interface (Figure 4.12b), allowing the visualization of side chains involved in the interface (Figure 4.12c). In Figure 4.12d-f, we compare the key interactions at this interface in the Omicron variant with corresponding interactions for the Delta variant. In the Delta variant–ACE2 complex, there are hydrogen bonds formed by residues Q493 and Q498 on the spike protein with residues E35 (E, Glu) and Q42, respectively, on ACE2 (Figure 4.12d). In the Omicron variant, three mutations are

observed in this stretch: Q493R (Gln^{493}→Arg), G496S (Gly^{496}→Ser), and Q498R. Residue R493 replaces the hydrogen bond to ACE2 residue E35 with a new salt bridge, whereas residue R498 forms a new salt bridge with ACE2 residue D38 while maintaining a hydrogen bond interaction with ACE2 residue Q42. RBD residue S496 adds a new interaction at the interface by forming a hydrogen bond with ACE2 residue K353 (Figure 4.12d). Additionally, the mutated residue Y501 in the Omicron RBD makes π-stacking interactions with Y41 in ACE2, as previously seen in the Alpha (B.1.1.7), Beta (B.1.351), and Gamma (P.1) variants and in chapter 3.

These new interactions are offset by the loss of a key salt bridge between spike protein residue K417 and ACE2 residue D30 that is present in the Delta variant (Figure 4.12f). In isolation, the K417N mutant displays reduced ACE2 binding affinity (Figure 4.11d and as discussed in chapter 3), but our findings suggest that the new mutations in the Omicron interface have a compensatory effect on the strength of ACE2 binding, providing an explanation for the similar ACE2 binding affinities that are observed (Figure 4.11).

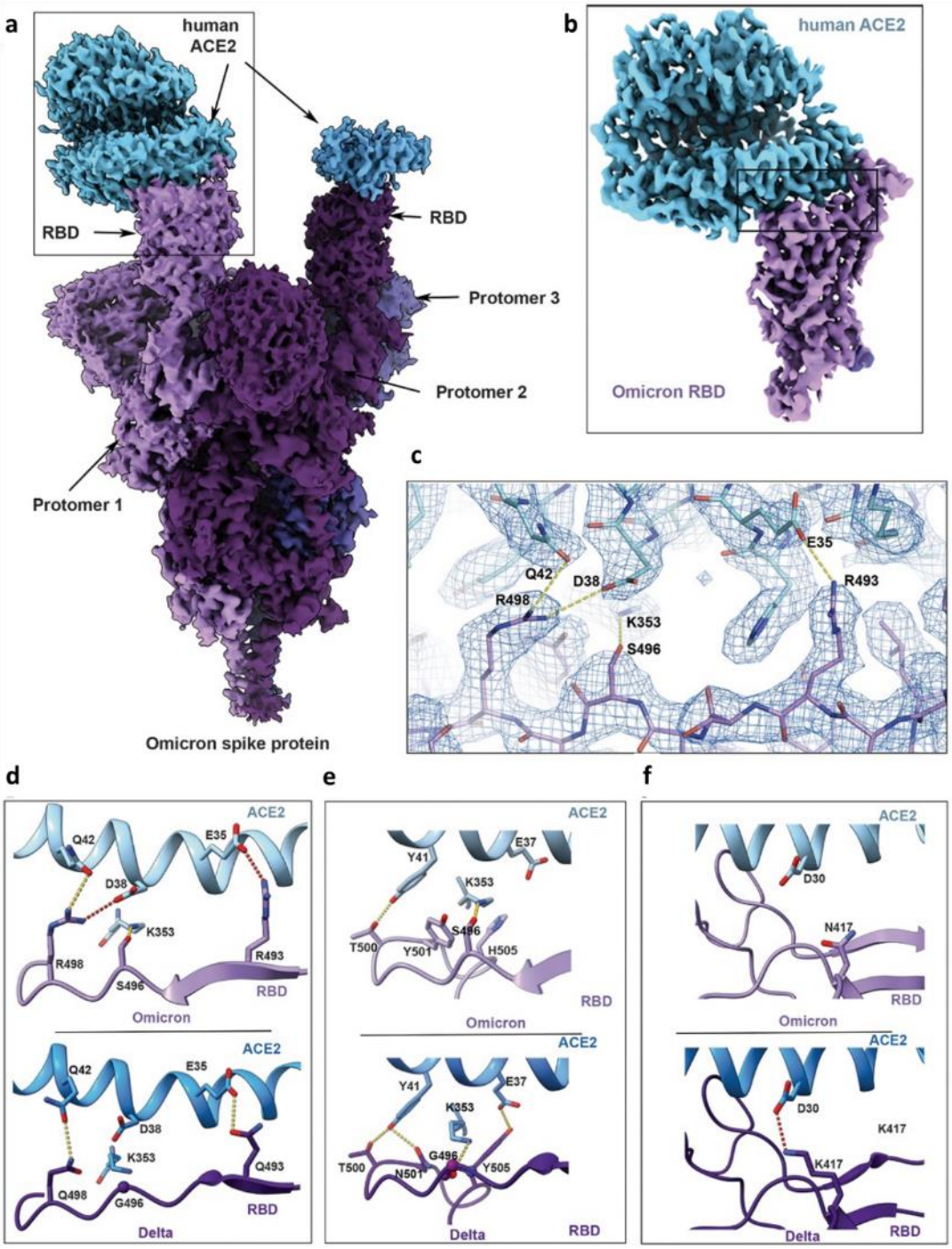

Figure 4.12. **Cryo-EM structure of the Omicron spike protein–ACE2 complex.** (a) Cryo-EM map of the Omicron spike protein in complex with human ACE2 at 2.45-Å resolution after global refinement. The three protomers are colored in different shades of purple, and the density for bound ACE2 is colored in blue. (b) Cryo-EM map of the Omicron spike protein RBD in complex with ACE2 at 2.66-Å resolution after focused refinement. The boxed area indicates the region highlighted in (c). (c) Cryo-EM density mesh at the Omicron spike protein RBD–ACE2 interface, with fitted atomic model. Yellow and red

dashed lines represent new hydrogen bonds and ionic interactions, respectively. (d to f) Comparison of the RBD-ACE2 interface between the Omicron (top) and Delta (bottom) variants. Compared with the Delta variant, new interactions are formed as a result of the mutations Q493R, G496S, and Q498R (d) and local structural changes owing to the N501Y and Y505H (Tyr^{505}→His) mutations (e) present in the Omicron variant. The salt bridge between Delta RBD K417 and ACE2 D30 that is present in the Delta variant spike protein but lost in the Omicron variant is highlighted in (f). Yellow and red dashed lines represent hydrogen bonds and ionic interactions, respectively.

We next investigated the effects of Omicron mutations on neutralization by (i) a selection of monoclonal antibodies, (ii) sera obtained from 30 doubly vaccinated individuals with no prior history of COVID-19 infection, and (iii) sera obtained from a set of 68 unvaccinated convalescent patients who recovered from infection with either the Alpha, Gamma, or Delta variants. (A summary of patient demographics is in tables 4.1 and 4.2). We performed neutralization experiments using pseudoviruses that incorporate the wild-type, Delta variant, or Omicron variant spike proteins and compared the ability of these pseudovirions to evade antibodies. We compare evasion relative to the Delta variant, given that the Omicron variant rapidly supplanted the Delta variant in global prevalence, and to wild-type SARS-CoV-2, given that most SARS-CoV-2 vaccine immunogens at the time were based on this sequence.

We used a panel of neutralizing monoclonal antibodies that include four RBD-directed antibodies (ab1, ab8, S309, and S2M11) and two NTD-directed antibodies (4-8 and 4A8) to investigate the impact of Omicron RBD and NTD mutations on monoclonal antibody escape. In contrast to wild-type SARS-CoV-2 and the Alpha (B.1.1.7), Gamma (P.1), Kappa (B.1.617.1), and Delta (B.1.617.2) variants studied earlier in this chapter, the Omicron variant could not be completely neutralized at maximum concentrations of five of the six antibodies tested (Figure 4.13a). The loss of neutralizing activity for both the NTD-directed antibodies (4-8 and 4A8) against Omicron is likely due to the Δ144-145 deletion, which falls within the footprint of both of these antibodies

(Figure 4.13b). The escape from RBD-directed antibodies S2M11, ab8, and ab1 is likely due to the numerous Omicron mutations that lie within their respective footprints (Figure 4.13b). By contrast, S309 (the precursor to the clinical monoclonal antibody sotrovimab for treatment of COVID-19) was able to fully neutralize the Omicron variant, consistent with previous reports that show retained binding and neutralization capacity of S309 despite a mild decrease in potency[175–177]. Given that that the only differences between S309 and sotrovimab are within the FC region (which was engineered for enhanced FC receptor binding in sotrovimab), this result suggests that sotrovimab will likely retain efficacy against the Omicron variant. The unusually high number of mutations in the Omicron variant spike protein thus appear to confer broad antibody escape relative to previously emerged variants of SARS-CoV-2.

Table 4.1. Summary of doubly vaccinated donor demographics

Sample ID	Sex	Age (Years)	Days between 1st dose and serum collection	Days between 1st dose and 2nd dose
81101	M	72	93	21
81102	F	85	98	17
81103	M	80	97	25
81106	F	63	107	17
81107	F	58	166	62
81108	F	67	154	27
81109	F	82	107	22
81110	F	50	197	153
81111	F	31	113	19
81112	F	33	148	39
81113	F	33	162	121
81114	F	37	136	33
81115	M	31	98	21
81116	F	35	156	112
81117	F	30	159	117
81201	F	54	93	15
81202	F	74	83	21
81203	F	31	86	16
81204	F	31	144	46
82101	M	57	133	21
82102	M	89	96	14
82103	M	73	88	23
82104	M	70	74	15
82105	F	89	81	15
83001	M	62	88	20
83002	F	43	97	22
84001	F	60	75	16
84003	F	52	79	15
84004	M	65	85	21

Table 4.2 Summary of convalescent donor demographics

Sample ID	Infecting Variant	Sex	Age (Years)	Days post infection to serum draw
B117-1	B.1.1.7	F	38	25
B117-10	B.1.1.7	M	53	15
B117-11	B.1.1.7	M	47	16
B117-13	B.1.1.7	M	59	17
B117-14	B.1.1.7	F	42	16
B117-15	B.1.1.7	F	37	29
B117-16	B.1.1.7	F	38	20
B117-17	B.1.1.7	M	49	19
B117-18	B.1.1.7	M	57	16
B117-19	B.1.1.7	M	34	54
B117-22	B.1.1.7	F	13	58
B117-23	B.1.1.7	M	50	17
B117-24	B.1.1.7	M	53	36
B117-25	B.1.1.7	M	30	21
B117-27	B.1.1.7	F	28	23
B117-3	B.1.1.7	M	55	15
B117-32	B.1.1.7	M	31	42
B117-36	B.1.1.7	M	50	21
B117-4	B.1.1.7	M	47	20
B117-45	B.1.1.7	M	35	27
B117-47	B.1.1.7	M	37	15
B117-5	B.1.1.7	M	18	22
B117-53	B.1.1.7	F	31	38
B117-55	B.1.1.7	F	68	59
B117-6	B.1.1.7	M	43	22

B117-7	B.1.1.7	M	16	16
B117-8	B.1.1.7	F	38	21
B1617-100	AY.25	F	34	33
B1617-101	B.1.617.2	F	54	18
B1617-104	AY.25	F	22	36
B1617-105	B.1.617.2	F	28	32
B1617-109	AY.27	F	28	46
B1617-111	AY.27	M	67	21
B1617-113	AY.27	F	26	19
B1617-2	B.1.617.2	F	37	27
B1617-35	B.1.617.2	F	31	17
B1617-40	B.1.617.2	F	79	115
B1617-51	B.1.617.2	F	25	57
B1617-52	B.1.617.2	F	16	14
B1617-55	B.1.617.2	F	27	29
B1617-57	B.1.617.2	F	36	27
B1617-60	B.1.617.2	F	60	22
B1617-61	B.1.617.2	M	31	25
B1617-62	B.1.617.2	F	44	20
B1617-66	B.1.617.2	F	22	14
B1617-69	B.1.617.2	M	28	40
B1617-70	B.1.617.2	F	25	37
B1617-74	B.1.617.2	M	50	20
B1617-83	AY.25	F	40	15
B1617-84	AY.27	M	36	39
B1617-85	AY.25	F	19	17
B1617-88	AY.25	F	21	24
B1617-92	AY.25	F	39	26

B1617-96	AY.27	M	25	37
B1617-97	AY.25	M	47	42
P1-10	P.1	M	38	23
P1-11	P.1	F	35	44
P1-12	P.1	F	24	37
P1-13	P.1	M	56	32
P1-2	P.1	M	35	21
P1-24	P.1	M	49	29
P1-26	P.1	F	21	18
P1-3	P.1	F	14	26
P1-30	P.1	F	55	25
P1-37	P.1	F	32	62
P1-38	P.1	F	27	60
P1-6	P.1	n/a	29	25
P1-7	P.1	M	28	31

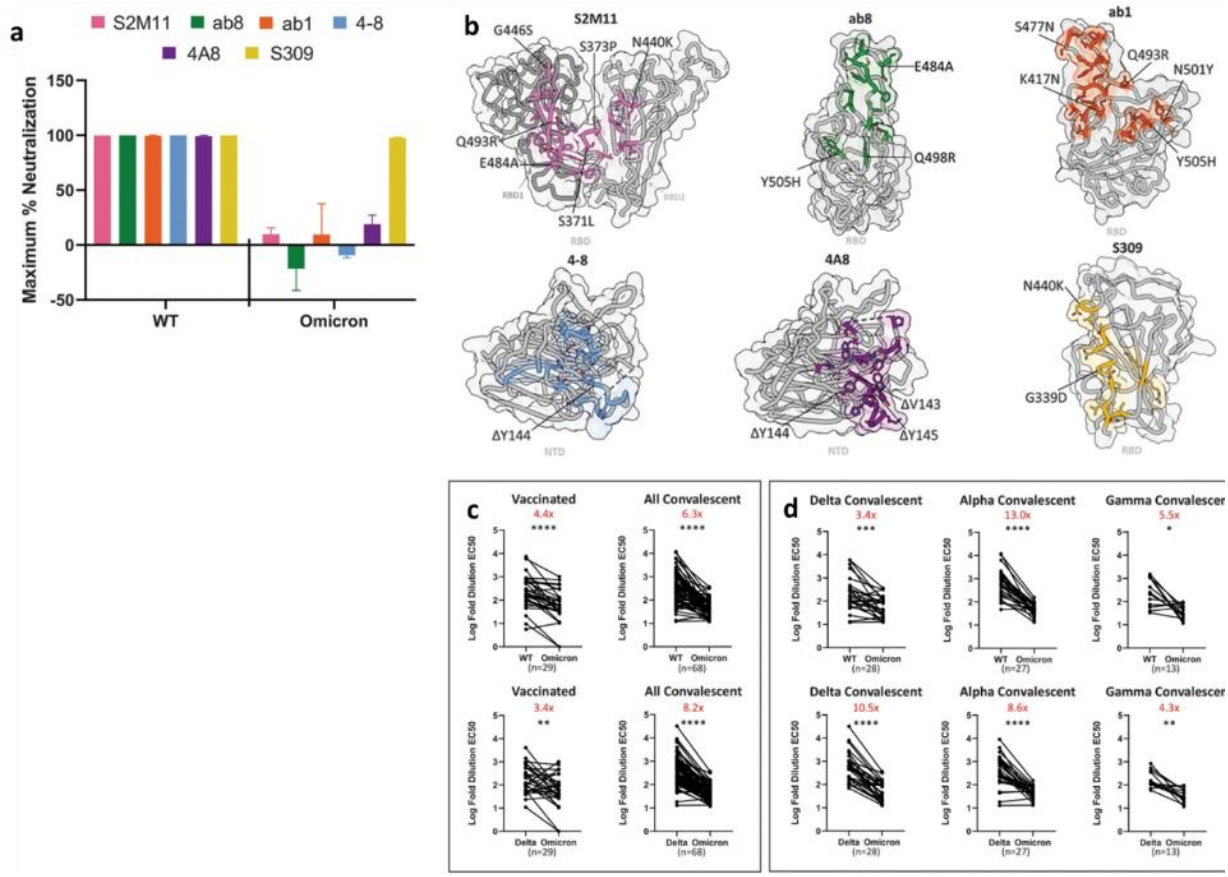

Figure 4.13. **Monoclonal antibodies and vaccinated and convalescent patient-derived sera exhibit decreased Omicron neutralization potency.** (a) Maximum neutralization achieved by the indicated monoclonal antibodies against wild-type and Omicron pseudoviruses (n = 3 technical replicates). Error bars denote standard deviation of the mean. (b) Antibody binding footprints for the monoclonal antibodies tested in this study. Omicron spike protein mutations that fall within each antibody footprint are labeled. (c) Log-fold 50% effective concentration (EC50) dilutions for vaccinated and convalescent patient sera for either wild-type (WT) versus Omicron variant pseudoviruses (top) or Delta versus Omicron variant pseudoviruses (bottom). (d) As in (c) but with a breakdown of the convalescent patients into previous infection with Delta, Alpha, or Gamma variants of concern. A pairwise statistical significance test was performed using the Wilcoxon matched pairs test (*$P \leq 0.05$; **$P \leq 0.01$; ***$P \leq 0.001$; ****$P \leq 0.0001$). The fold change in the geometric mean between the two groups is shown in red at the top of each plot.

Sera from either vaccinated or convalescent donors exhibited potent neutralization of wild-type pseudoviruses; sera from convalescent patients displayed, on average, a 6.3× decrease in ability to neutralize the Omicron variant relative to wild type (Figure 4.13c, top). Sera from the vaccinated cohort also displayed reduced neutralization ability (4.4× decrease on average) with a wider variation driven by some individuals that showed greater loss of neutralization ability against Omicron. The comparison of change in neutralization potential between the Delta and Omicron variants is perhaps more relevant given the previous worldwide dominance of the Delta variant. Sera from convalescent patients shows an even greater drop in neutralization potency relative to the Delta variant (8.2× decrease), whereas the vaccinated group also shows reduction in potency, although to a lesser extent (3.4× decrease) (Figure 4.13c, bottom).

A finer analysis of the unvaccinated convalescent cohort stratified into those who recovered from infection with either the Delta, Alpha, or Gamma variants (Figure 4.13d) highlights the reduction in neutralization potency against the Omicron variant relative to the Delta variant in all populations, with especially notable drops for patients who recovered from infection with the earlier Alpha and Delta variants.

The large number of mutations on the surface of the spike protein, including the immunodominant RBD, would be expected to help the virus escape antibodies elicited by vaccination or prior infection. It is interesting that the Omicron variant evolved to retain its ability to bind ACE2 efficiently despite these extensive mutations. The cryo-EM structure of the spike protein–ACE2 complex provides a structural rationale for how this is achieved: Interactions involving the new mutations in the Omicron variant at residues 493, 496, 498, and 501 appear to restore ACE2 binding efficiency that would be lost as a result of other mutations such as K417N. The Omicron variant thus appears to have evolved to selectively balance an increase in escape from

neutralization with its ability to interact efficiently with ACE2, consistent with the findings described in chapter 3. The increase in antibody evasion and the retention of strong interactions at the ACE2 interface are thus factors that likely contribute to the increase in transmissibility of the Omicron variant.

4.2.2.2 Studies on the Omicron BA.2 Spike Protein

Having characterized the initial BA.1 Omicron variant we now shift focus to the BA.2 sub-lineage spike protein. Initially, five sub-lineages of Omicron were identified as BA.1, BA.2, BA.3, BA.4, and BA.5. Lineages BA.1 and BA.1.1—a further sub-lineage of BA.1 that differs only by an additional R346K mutation in the spike (S) protein—comprised the vast majority of Omicron infections in late 2021 (Figure 4.14a)[170]. In early 2022, however, BA.2 infections began increasing and displacing the BA.1 lineages, with BA.2 constituting the majority of SARS-CoV-2 infections by March. The S protein mutational profile of sub-lineage BA.3 resembles the BA.1 mutational profile most closely, yet this variant never exceeded 1% of global SARS-CoV-2 infections at the time of study. The BA.4 and BA.5 sub-lineages share identical S protein mutations, which differ from the BA.2 S protein by only a few mutations (Δ69/70, L452R, and F486V), with these lineages combining to comprise less than 20% of global infections by the end of May 2022 (Figure 4.14a). BA.2 shares many S protein mutations with BA.1 with the exception of a number of unique mutations in the receptor-binding domain (RBD) and amino-terminal domain (NTD) (Figure 4.14b). Given the functional importance of the RBD and NTD in receptor engagement and their susceptibility to vaccine-elicited neutralizing antibodies, we sought to understand the molecular consequences of BA.2 S protein mutations within these two domains.

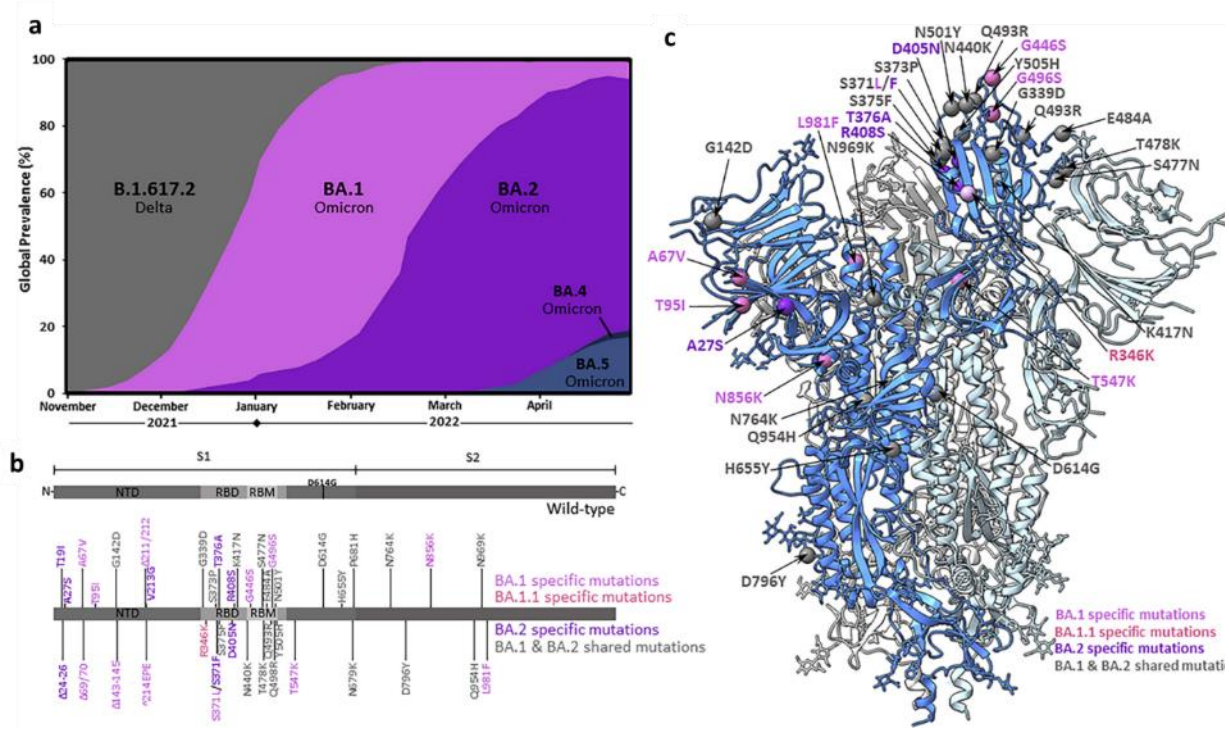

Figure 4.14. **Global prevalence and S protein mutations of the Omicron sub-lineages**. (a) Global prevalence of Omicron sub-lineages BA.1, BA.1.1, and BA.2 from November 2021 to March 2022. Only Omicron sub-lineages surpassing 1% global frequency are displayed. Sequence data were downloaded from the Global Initiative on Sharing All Influenza Data (GISAID) and graphed as weekly prevalence. (b) SARS-CoV-2 spike (S) protein amino acid sequence boxplots for the wild-type (D614G), BA.1/BA.1.1, and BA.2 Omicron sub-lineages. The BA.1.1 lineage is identical to BA.1 with the exception of an additional R346K mutation. NTD, N-terminal domain; RBD, receptor-binding domain; RBM, receptor-binding motif.
(c) Cryo-EM-derived atomic model of the BA.2 S glycoprotein. Each S protein protomer is colored in different shades of blue. The locations of modeled amino acid mutations are shown as spheres on one protomer. BA.1-, BA.1.1-, and BA.2-specific mutations are colored in magenta, light magenta, and purple, respectively. Shared mutations across BA.1, BA.1.1, and BA.2 sub-lineages are colored in gray.

cryo-EM structural analysis of the BA.2 S protein ectodomain (Figure 4.14c) reveals preserved overall architecture compared with the wild-type S, BA.1 S, and other previously emerged SARS-CoV-2 variant S structures besides the Kappa variant which was described earlier in this chapter. Similar to our observations for the BA.1 S trimer, the RBD of a single protomer within the BA.2 trimer is well resolved in the up position, with poor densities for the other 2 RBDs demonstrating flexibility of these regions relative to the rest of the trimer. This suggests a dynamic nature of the BA.2 RBD.

The unique BA.1 G496S mutation, which is the sole differentiating mutation between BA.1 and BA.2 within the receptor-binding motif, added a new hydrogen bonding interaction with human ACE2 (hACE2) residue K353 (Figure 4.12). We measured the affinity of the BA.2 S protein ectodomain or RBD binding to hACE2 using three different surface plasmon resonance approaches: (1) measurement of binding of dimeric hACE2 to immobilized WT, BA.1, and BA.2 RBDs (Figure 4.15a); (2) measurement of binding of WT, BA.1, and BA.2 RBDs to immobilized dimeric hACE2 (Figure 4.15b); and (3) measurement of binding of WT, BA.1, and BA.2 S protein ectodomains to immobilized dimeric hACE2 (Figure 4.15c). Collectively, these measurements reveal increased binding affinity of the BA.2 S protein to hACE2 relative to WT and is comparable to the increased binding affinity observed for BA.1.

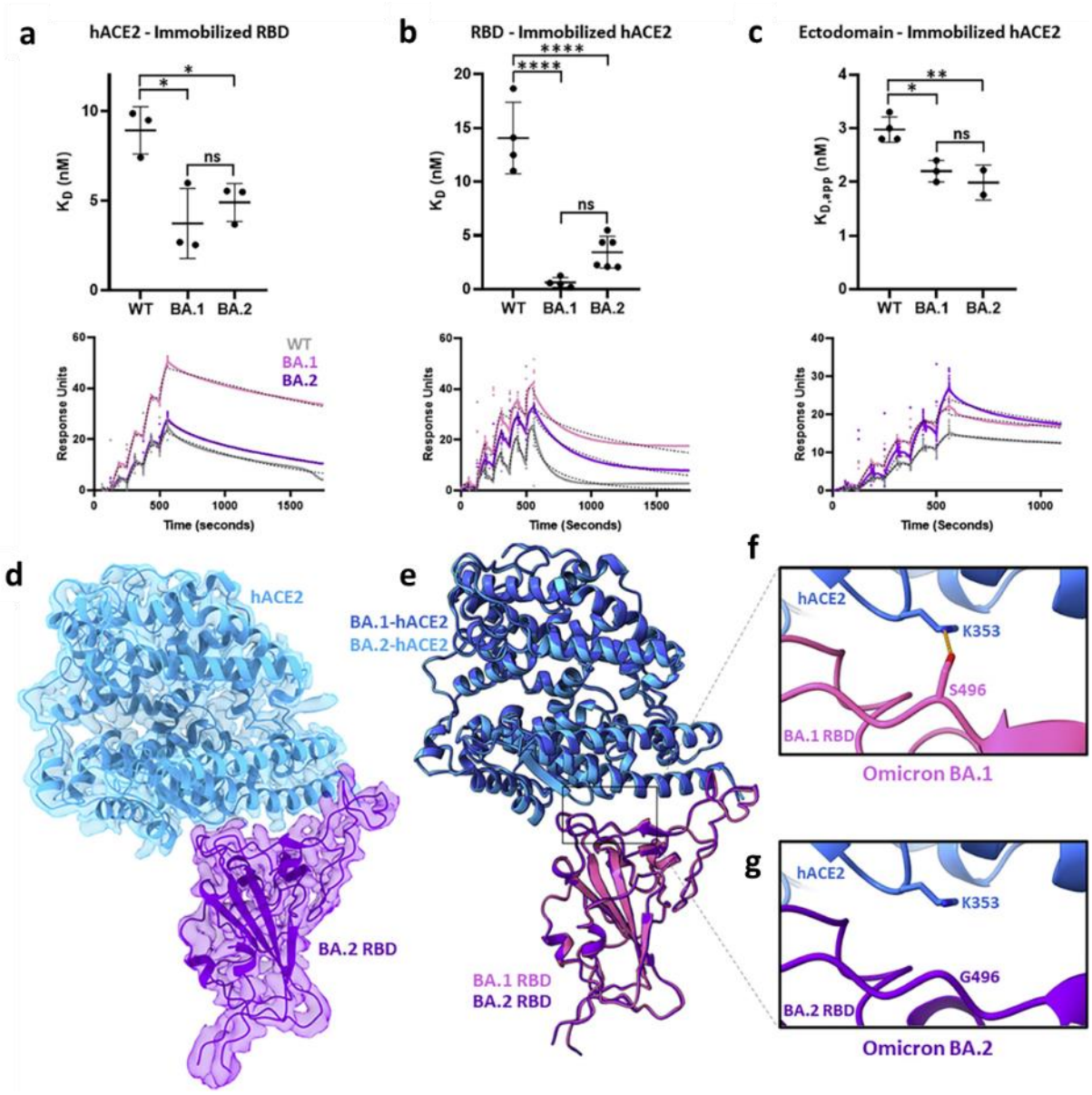

Figure 4.15. **Binding affinity and cryo-EM structure of the Omicron BA.2 S protein-human ACE2 complex.** (a) Surface plasmon resonance experiments measuring dimeric human ACE2 (hACE2) binding to immobilized wild-type (WT), BA.1, and BA.2 RBDs, performed in technical triplicates. Summary data are shown at the top with representative surface plasmon resonance (SPR)-binding curves (colored solid line), and fitted 1:1 binding models (black dashed line) are shown on bottom. (b) As in (a) but measuring WT, BA.1, and BA.2 RBDs binding to immobilized dimeric hACE2, performed in at least technical quadruplicates. (c) As in (a) but measuring WT, BA.1, and BA.2 ectodomains binding to immobilized dimeric hACE2, performed in at least technical duplicates. The WT and BA.1 data in (c) were taken from figure 4.11d. Pairwise statistical significance test was performed using a one-way ANOVA test (∗p ≤ 0.05; ∗∗p ≤ 0.01; ∗∗∗p ≤ 0.001; ∗∗∗∗p ≤ 0.0001, ns, not significant).
(d) Focus-refined cryo-EM density map and fitted atomic model of the BA.2 RBD in complex with hACE2 at 2.8 Å. (e) Aligned atomic models of hACE2 bound to BA.1 and BA.2 RBDs.

The BA.1 RBD (PDB: 7T9L) and complexed hACE2 atomic models are shown in magenta and dark blue, respectively. The BA.2 RBD and complexed hACE2 atomic models are shown in purple and light blue, respectively. (f) Atomic model of the BA.1 S protein-hACE2 complex, focused on residue S496. The hydrogen bonding interaction between BA.1 S protein residue S496 and hACE2 residue K353 is indicated by an orange dashed line. (g) As in (f) but for the BA.2 S protein-hACE2 complex, focused on residue G496.

To visualize the structural impacts of BA.2 RBD mutations on hACE2 binding, we performed cryo-EM analysis of the BA.2 S protein in complex with hACE2 (Figure 4.15d). Structural alignment of BA.1 and BA.2 RBD-hACE2 complexes demonstrates a high degree of structural similarity across both the RBDs and hACE2 molecules (0.97 Å root-mean-square deviation; Figure 4.15e). Seven mutations distinguish the BA.1 and BA.2 RBDs—BA.1 contains S371L, G446S, and G496S mutations and BA.2 contains S371F, T376A, D405N, and R408S mutations—yet only the G496S mutation makes differential interactions with hACE2 residues between these two sub-lineages (Figure 4.15f-g). The S496G revertant mutation present in the BA.2 receptor-binding motif (RBM) no longer makes a hydrogen bonding interaction that is present in the BA.1 RBD-hACE2 complex. However, the loss of this hydrogen bonding interaction in the BA.2 variant S does not impart a measurable difference in overall hACE2 binding (Figure 4.15a-c); therefore, we conclude that similar to BA.1, the numerous mutations within the BA.2 S protein enable enhanced hACE2 affinity relative to the WT S protein.

Given the suggestion that the Omicron variant originated within mice and achieved zoonosis[171], it is noteworthy that the BA.1 and BA.2 S proteins uniquely exhibit a significant increase in binding affinity for mouse ACE2 (mACE2) compared with previous SARS-CoV-2 lineages[176,178]. Additionally, increased cell entry relative to WT was observed in authentic BA.1 virus infecting cells overexpressing mACE2[179]. Mouse-adapted SARS-CoV-2, generated by the serial passaging of the virus in mice, reproducibly (across multiple studies) selected for mutations at positions Q493

and Q498[180,181], which are mutated sites in the BA.1 and BA.2 Omicron sub-lineages. We first confirmed the enhanced binding of mACE2 by the BA.1 and BA.2 ectodomains via ELISA, showing similar enhancements of mACE2 binding by both BA.1 and BA.2 relative to WT (Figure 4.16). To provide a structural basis for the increased mACE2 affinity exhibited by both the BA.1 and BA.2 Omicron variants, we solved cryo-EM structures of their S proteins in complex with the ectodomain of mACE2 (Figure 4.17a-c). mACE2 is observed to be similarly positioned in its binding of the BA.1 and BA.2 RBDs compared with hACE2 (Figure 4.17a-c). Focused refinement of the BA.1- and BA.2-mACE2 regions was possible, resulting in 2.8 and 2.7 Å local reconstructions, respectively, and allowing for side-chain placement at the RBD-mACE2 interfaces. As shown for the hACE2 structures, the BA.1- and BA.2-mACE2 focused refinements exhibit a high degree of structural similarity relative to one another (0.87 Å root-mean-square deviation), with identical side-chain interactions made at the RBD-mACE2 interface. In the BA.1 and BA.2 RBD-hACE2-bound structures, the sole differentiating mutation at this interface is the BA.1-specific G496S mutation, which makes a hydrogen bonding interaction with hACE2 residue K353. In mACE2, position 353 is a histidine residue that is not positioned to hydrogen bond with S496 (>4.8 Å distance) in BA.1, thus the BA.1-specific G496S mutation does not distinguish the BA.1 and BA.2 variants at the mACE2 interface as it did in hACE2. Our analysis proceeds with the higher-resolution BA.2-mACE2 focus-refined structure, with direct parallels possible for the BA.1-mACE2 structure.

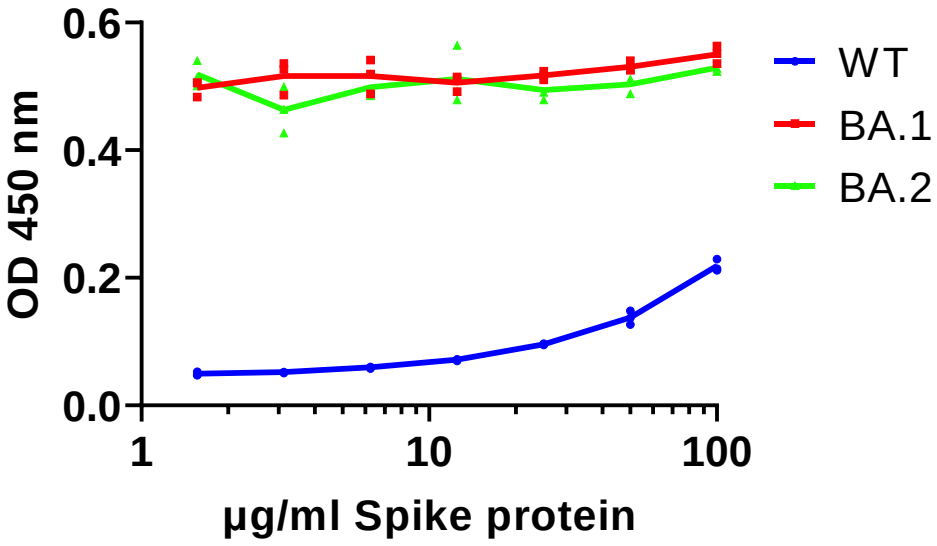

Figure 4.16**. ELISA analysis of mouse ACE2 binding by various spike protein ectodomains.** Monomeric mouse ACE2 (residues 1-615) was coated onto wells and serial dilutions of spike proteins were titrated to assess binding. Experiments were performed in technical triplicate (n=3) and are shown as points.

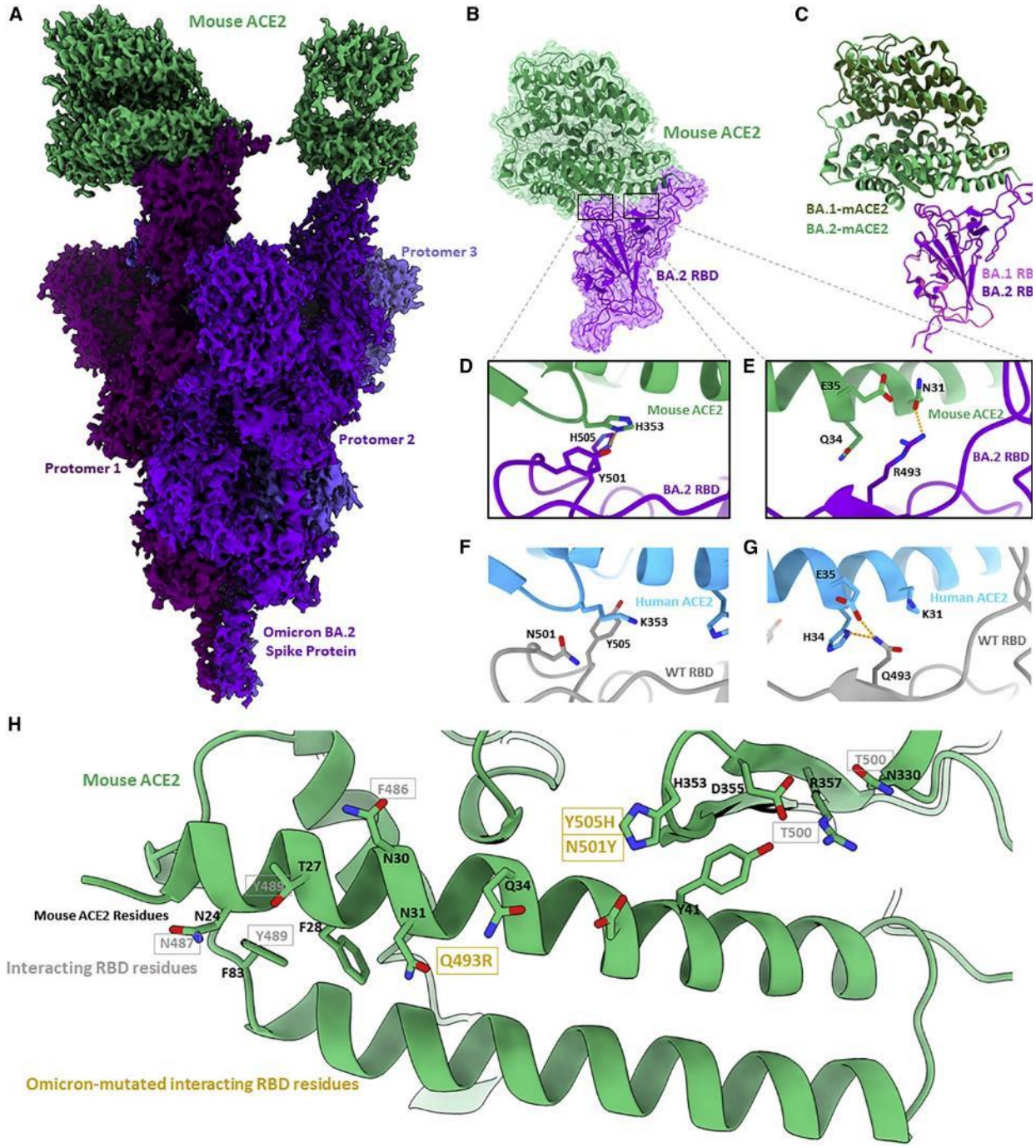

Figure 4.17. **Cryo-EM structure of the Omicron BA.2 S protein-mouse ACE2 complex.** (a) Cryo-EM density map of BA.2 S protein in complex with mouse ACE2 at 2.5 Å. Mouse ACE2 is shown in green, and protomers of the BA.2 S protein are shown in shades of purple.
(b) Focus-refined cryo-EM density map and fitted atomic model of the BA.2 RBD-mouse ACE2 (mACE2) complex at 2.7 Å. (c) Aligned atomic models of the BA.1 and BA.2 RBD-mACE2 complexes. The BA.1 RBD and complexed hACE2 atomic models are shown in magenta and dark green, respectively. The BA.2 RBD and complexed hACE2 atomic models are shown in

purple and light green, respectively. (d) Atomic model of the BA.2 RBD-mACE2 complex, focused on residues Y501 and H505.
(e) As in (d) but focused on residue R493.
(f) Atomic model of the WT RBD-hACE2, focused on residues N501 and Y505.
(g) As in (h) but focused on residue Q493.
(h) Atomic model of mACE2 from the perspective of a binding RBD. Black labels are mACE2 residues, and gray labels denote the interacting residues in a bound RBD. Gold labels denote the interacting residues in a bound RBD that are mutated in the BA.1 and BA.2 Omicron sub-lineages.

mACE2 has a high degree of overall amino acid sequence homology with hACE2 (82% identity), with lower sequence homology (73% identity) at the RBD-interaction interface comprising ACE2 amino acid residues 18–46, 78–91, 324–358, and 392–394[182]. There are two sites within the Omicron RBD-mACE2 interface that differ relative to the Omicron RBD-hACE2 interface. The first site (Figure 4.17d) involves residue H353 in mACE2 (K353 in hACE2) forming π-π stacking and hydrogen bonding interactions with Omicron-mutated RBD residues Y501 and H505, respectively. Both of these interactions are not possible in the WT RBD, which harbors N501 and Y505 residues at these positions (Figure 4.17f). Site two (Figure 4.17e) involves Omicron-mutated residue R493 forming a hydrogen bonding interaction with residue N31 of mACE2 (K31 in hACE2). Across these two sites, we see that non-conserved ACE2 residues between hACE2 and mACE2 (H353, N31, Q34) are complemented by mutated residues in the Omicron variants, providing us with the conclusion that the mutations Q493R, N501Y, and Y505H engage non-conserved ACE2 residues unique to mACE2, rationalizing the enhanced binding of mACE2 by the Omicron variant S proteins (Figure 4.17h).

Given that the vast majority of mutational differences between the BA.1 and BA.2 S proteins are within the immunogenic NTD and RBD regions, we sought to probe the antigenic differences between these proteins. We first assessed antibody binding of WT, BA.1, and BA.2 S proteins via ELISA using a small panel of RBD- and NTD-directed antibodies (Figure 4.18a). BA.1 and BA.2

S proteins exhibited similarly decreased binding by all antibodies compared with the WT S protein, with a pronounced decrease in BA.2 S binding by S309 compared with BA.1. S309 is the precursor to the clinical monoclonal antibody sotrovimab, which is the only FDA-approved monoclonal antibody that retained neutralization capability for the BA.1 variant. Both BA.1 and BA.2 share N440K and G339D mutations, which are within the S309 epitope, while the sub-lineages are differentiated by S371L (BA.1) and S371F (BA.2) mutations in an alpha helix close to the N343 glycan, an important feature of the S309 epitope[159]. A recent study showed that the S371F mutation alone was sufficient to decrease the neutralization potency of S309 by 20-fold, suggesting that this distal mutation may disrupt the S309-binding epitope via allosteric mutational mechanisms[183].

Superposition of WT, BA.1, and BA.2 RBDs reveals no prominent structural changes that could account for this finding, although a shift in the antigenic surface of these domains is evident upon mapping BA.1- and BA.2-specific mutations (Figure 4.18c-d). There is a distinct shift from the location of two BA.1-specific RBD mutations to three BA.2-specific RBD mutations, which are located within the footprints of different patient-derived antibodies.

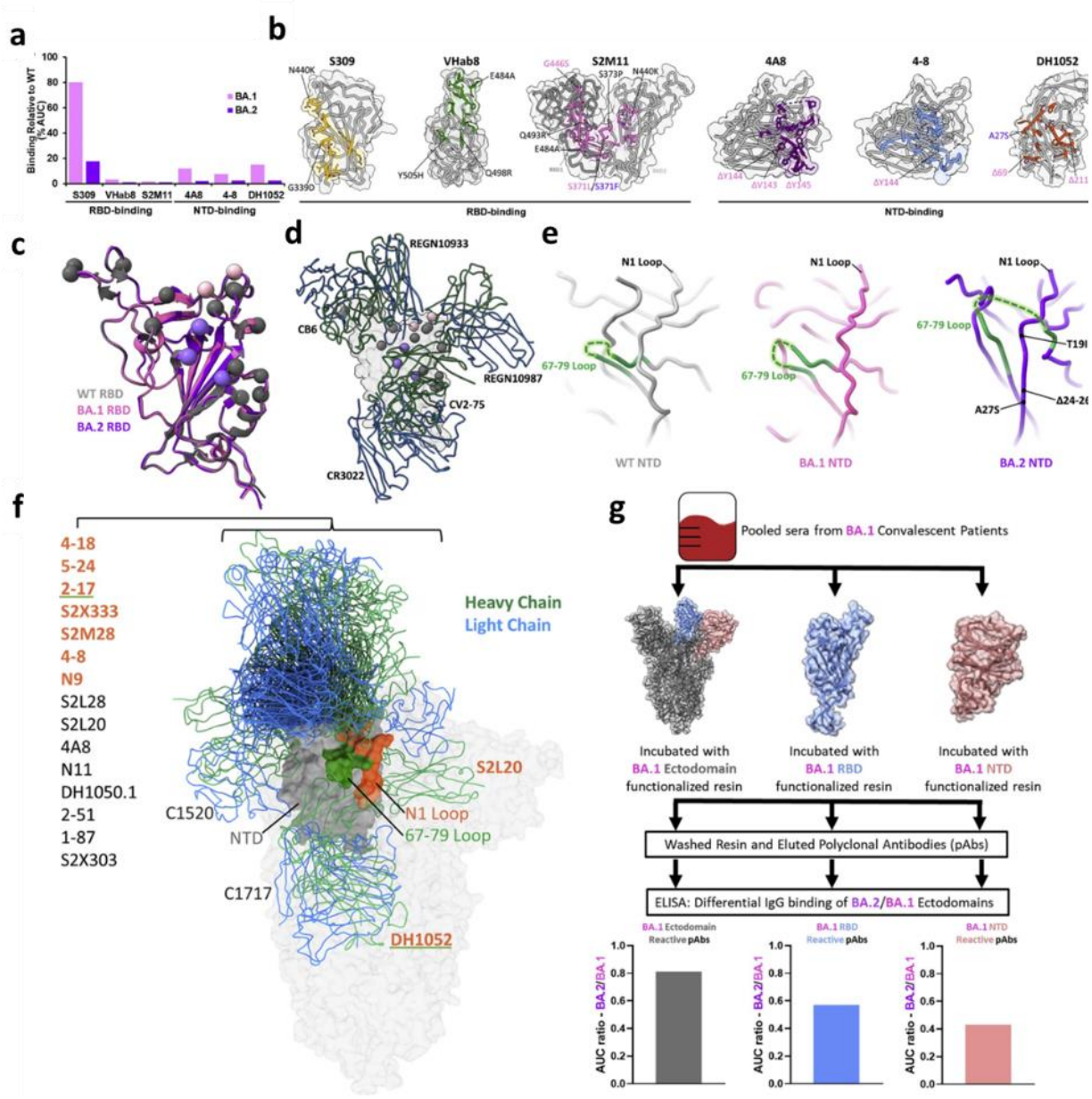

Figure 4.18. **Antigenic shift of the BA.2 S protein.** (a) Percentage of binding of monoclonal antibodies against the BA.1 and BA.2 S proteins relative to WT as assessed by ELISA, performed in technical triplicates. (b) Antibody epitopes with the side chains of contacted residues within the RBD or NTD shown and colored. BA.1- and BA.2-mutated residues are labeled within the antibody epitopes in magenta and purple, respectively, with shared mutations labeled in gray. (c) Alignment of WT, BA.1, and BA.2 RBDs, with shared, BA.1-specific, and BA.2-specific mutations labeled in gray, magenta, and purple, respectively. (d) Alignment of select patient-derived RBD-directed antibodies on the RBD. CB6, PDB: 7C01; REGN10933/REGN10987, PDB: 6XDG; CV2-75, PDB: 7M31; CR3022, PDB: 6YLA. (e) Side-by side comparison of WT (PDB: 7KRS), BA.1 (PDB: 7TNW), and BA.2 NTDs with a focused view on the structural rearrangement of the 67–79 loop and N1 antigenic loop. (f) Alignment of deposited patient-derived NTD-directed antibody atomic models. The labels of

antibodies that make intermolecular contacts with the N1 and/or 67–79 loop are colored in orange and/or underlined in green, respectively. The NTD is shown in gray with its N1 loop highlighted in orange and the 67–79 loop in green. (g) Schematic and BA.2/BA.1 antibody-binding ratio for domain-enriched (ectodomain, NTD, or RBD) BA.1-convalescent polyclonal sera. Serum was pooled from 18 BA.1-convalescent patients (16 breakthrough cases and 2 infections in non-vaccinated patients) prior to incubation with either BA.1 ectodomain, NTD, or RBD to enrich domain-specific BA.1-convalescent antibodies. The samples were washed prior to quantification of IgG binding by ELISA and plotting of the BA.2/BA.1 ratio of domain-specific antibody binding. Data are derived from serum from 18 pooled BA.1-convalescent patients, and the ELISA assays were performed in technical duplicates.

To assess structural differences within the flexible NTD region, we performed focused refinement on the NTD of the BA.2 S protein and were able to resolve a structure at 2.9 Å. In contrast to the RBD, inspection of the WT, BA.1, and BA.2 NTDs reveals a structural reordering of the immunodominant N1 loop within the BA.2 NTD (Figure 4.18e). While the N1 region is adjacent to the loop formed by residues 67–79 within the WT and BA.1 NTDs, the BA.2 N1 region is located between both ends of the 67–79 loop as a beta strand within an anti-parallel beta sheet, resembling a "threading" of the BA.2 N1 region within the 67–79 loop. Given the inability of proline to contribute favorable hydrogen bonding contacts within beta sheets[184], the structural rearrangement and ordering of the BA.2 N1 region is likely driven by the loss of two proline residues due to the BA.2-specific deletion of residues 24–26. This structural threading of the N1 loop is a distinguishing feature of the BA.2 variant and is significant given the inclusion of the N1 loop within the "NTD neutralization supersite"—designated for the propensity of patient-derived neutralizing antibodies to bind this location[108]. Figure 4.18f shows a comparison of PDB-deposited structures of patient-derived NTD binding antibodies aligned to a single NTD. From this alignment, one can see that a significant portion of NTD-binding antibodies contact the N1 and 67–79 loops, which are rearranged in the BA.2 NTD.

We hypothesized that the mutational changes in the antigenic surface of the RBD along with the structural reordering of the NTD represent an antigenic drift between the BA.1 and BA.2 S proteins. To test this, we purified BA.1 S ectodomain-, RBD-, and NTD-specific polyclonal antibodies from patients with a history of BA.1 infection and assessed the ability of the immunoglobulin G (IgG) component of these preparations to bind the BA.2 S ectodomain via ELISA (Figure 4.18g). The IgG component of all three polyclonal antibody preparations bound the BA.2 S ectodomain to a lower extent than BA.1. Interestingly, the disparity between BA.2 and BA.1 S ectodomain binding was greater for both RBD-specific antibodies (~40% decrease in BA.2 S binding) and NTD-specific antibodies (~60% decrease in BA.2 S binding) relative to whole S ectodomain-specific antibodies (~20% decrease in BA.2 S binding). This result suggests that antibodies targeting the BA.1 RBD and NTD are particularly sensitive to mutations within the BA.2 S protein, demonstrating an antigenic drift between BA.1 and BA.2 lineages that is driven by S protein RBD and NTD mutations.

To further characterize the antigenic differences between BA.1 and BA.2 spike proteins we measured the ability of antibodies in patient derived sera from 205 individuals to neutralize pseudoviruses harboring either the wild-type (WT), BA.1, or BA.2 spike proteins. Patients were stratified into different exposure groups by vaccination and infection history, with identification of infecting lineages verified by sequencing for 91% of infected patients (Figure 4.19a-b).

BA.2 and BA.1 spike pseudotyped viruses displayed similar extents of neutralizing antibody evasion relative to WT in patients with 2 vaccine doses (BA.1: 4-fold reduction in EC50, BA.2: 3-fold reduction in EC50), as well as in convalescent patients (BA.1: 5-fold reduction in EC50, BA.2: 4-fold reduction in EC50), and in patients with a single vaccine dose and previous infection (BA.1: 6-fold reduction in EC50, BA.2: 5-fold reduction in EC50) (Figure 4.19c). Similar trends were

observed when further stratifying each of these groups by identity of infecting variants (Figure 4.19d-e), with the exception of BA.1 convalescent patients with no vaccination history. Sera from these 2 patients exhibited lower neutralization potencies for WT spike bearing pseudovirus relative to BA.1 or BA.2, consistent with the large antigenic difference between WT and Omicron lineage spike proteins.

While sera from patients with two vaccine doses and a breakthrough infection exhibited decreased potencies for the BA.2 pseudotyped virus relative to WT (3-fold decrease in EC50), no statistically significant reduction in neutralization of BA.1 pseudotyped virus relative to WT was observed (Figure 4.19c). Stratification of these patients by the identity of infecting variant revealed a small decrease (3-fold decrease in EC50) in potency for BA.2, with no statistically significant evasion observed by BA.1 pseudovirus for sera from patients with Delta breakthrough infections (Figure 4.19f). Sera from patients with two vaccine doses and a breakthrough infection with BA.1 exhibited a statistically significant decrease in neutralization of BA.2 pseudotyped virus relative to WT (3-fold decrease in EC50), but not for BA.1 relative to WT (Figure 4.19f), consistent with the generation of a BA.1-specific neutralizing antibody response after BA.1 breakthrough infection. Importantly, sera from these patients neutralized BA.2 pseudovirus less potently on average than for BA.1 (3-fold decrease), demonstrating an antigenic difference between these Omicron sub-lineages, consistent with our structural and biochemical analyses which revealed an antigenic drift between BA.1 and BA.2 spike proteins.

a

	COVID-19	Vaccine 2 Doses	COVID-19 + 1 Dose	COVID-19 + 2 Doses
N	70	29	80	26
Average Age (Years)	37	56	43	38
Sex - N (%)				
Female	40 (57.1)	20 (69.0)	2 (2.5)	18 (69.2)
Male	30 (41.4)	9 (31.0)	1 (1.3)	8 (30.8)
Unknown	1 (1.4)	0 (0)	77 (96.3)	0 (0)
Vaccine Doses - N (%)				
Pfizer mRNA BNT162b2	N/A	42 (72.4)	58 (72.5)	38 (73.0)
Moderna mRNA-1273	N/A	9 (15.5)	10 (12.5	8 (15.4)
COVISHIELD	N/A	2 (3.5)	6 (7.5)	1 (1.9)
AstraZeneca ChAdOx1-S	N/A	5 (8.6)	6 (7.5)	5 (9.6)
Infecting Variant - N (%)				
Alpha	27 (38.6)	N/A	36 (45.0)	0 (0)
Gamma	13 (18.6)	N/A	25 (31.3)	0 (0)
Delta	28 (40.0)	N/A	3 (3.8)	10 (38.5)
BA.1	2 (2.9)	N/A	0 (0)	16 (61.5)
Unknown Variant	0 (0)	N/A	16 (20.0)	0 (0)
Breakthrough Infections - N (%)	N/A	N/A	42 (53)	26 (100)

b

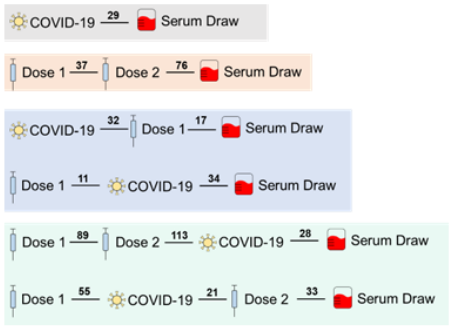

c

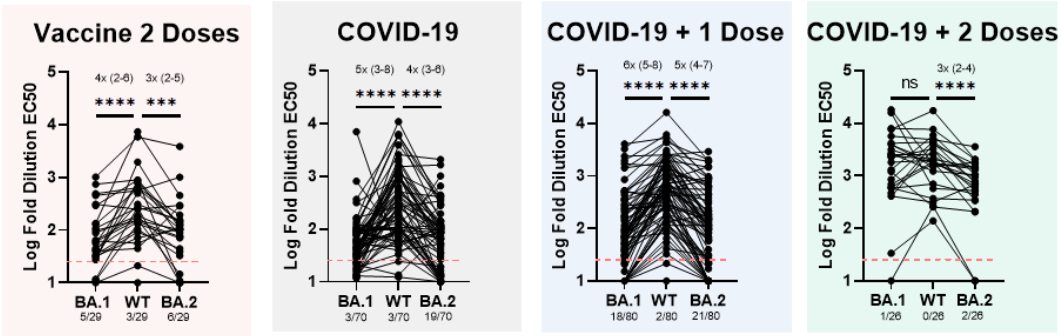

COVID-19: By Infecting Variant

d

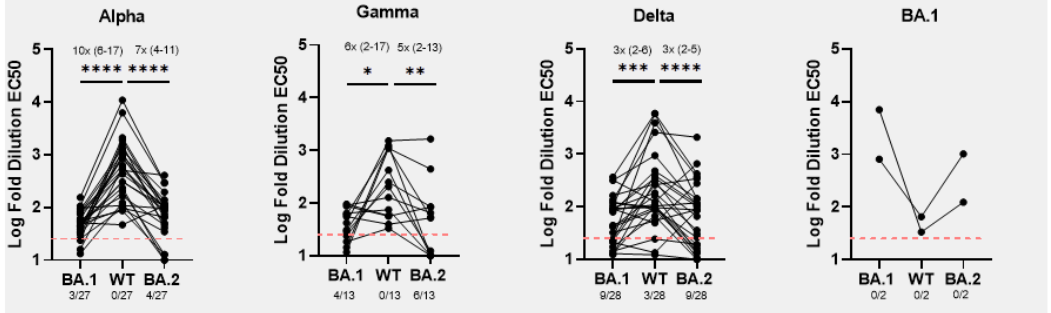

COVID-19 + 1 Dose: By Infecting Variant

e

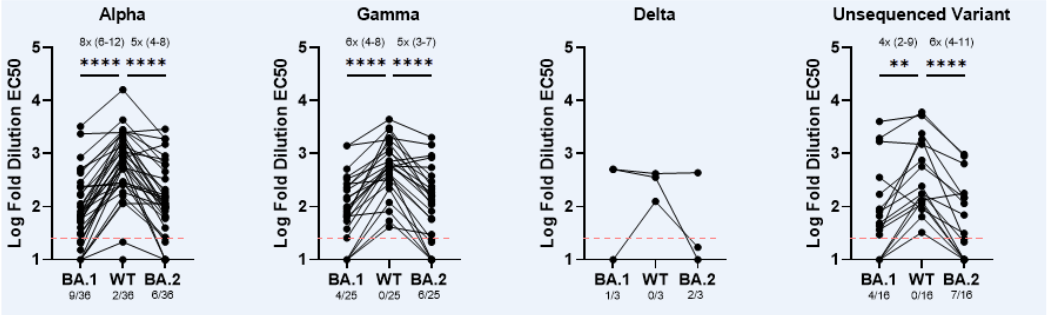

COVID-19 + 2 Doses: By Infecting Variant

f

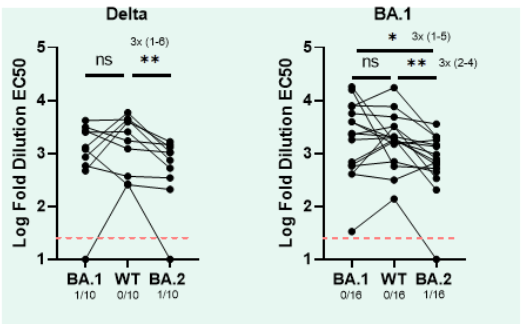

Figure 4.19. **Antibody evasion and cross neutralization of the Omicron BA.2 spike protein.** (a) Summary table detailing patient demographics for each exposure group category. (b) Schematic outlining exposure group categories in this study. Average time between each exposure is shown in days. (c) Pairwise comparisons of log-fold 50% effective concentration (EC50) dilutions for patient sera for either wild-type (WT), BA.1, or BA.2 variant pseudo-viruses. Aggregate comparisons for each exposure group are shown in (a) while panels (d-f) stratify samples by infecting variant for each exposure group. Dashed lines represent the limit of detection and the number of samples which fell below this limit is denoted beneath each graph. Fold changes in mean titers are shown with 95% confidence intervals in brackets above statistical descriptors. Pairwise statistical significance test was performed using the Wilcoxon matched pairs test (*P ≤ 0.05; **P ≤ 0.01; ***P ≤ 0.001; ****P ≤ 0.0001). Statistics were only calculated for groups with 10 or more samples. Data for the neutralization of WT and BA.1 pseudoviruses by sera from the non BA.1 convalescent COVID-19 patients (n=68) and the Vaccine 2 Doses patients (n = 29) is taken from a figure 4.13 and compared here in this analysis.

Herein, we have conducted a structural comparison of the spike proteins from the original Omicron BA.1 sub-lineage and the BA.2 lineage that replaced it. We provide a structural basis for the acquired ability of BA.1 and BA.2 S proteins to engage mACE2, finding Omicron mutations at the ACE2-binding site to complement non-conserved residues between hACE2 and mACE2. This finding has implications for potential future zoonotic transmission of these variants into mice reservoirs. As for BA.1, BA.2 exhibits dramatic escape from monoclonal antibodies through direct mutational effects within the RBD and allosteric mutational effects within the BA.2 NTD, for which we determined a structural basis. Finally, our discovery that BA.1 convalescent polyclonal sera exhibits decreased binding for the BA.2 ectodomain, RBD, and NTD relative to BA.1, and neutralizes BA.2 pseudo-viruses to a lower extent than BA.1, highlights the antigenic difference between the BA.1 and BA.2 S proteins. Our overarching finding is that the BA.1 and BA.2 S proteins do not differ greatly with regards to ACE2 binding (human or mouse) yet are distinguished by the arrangement of their NTDs, with implications for the evasion of serum antibodies.

4.2.3 Broad neutralization of the SARS-CoV-2 spike protein by an unconventional antibody fragment

Having demonstrated various extents of antibody escape due to mutational alterations of SARS-CoV-2 variant spike protein epitopes, we next sought to map out conserved vulnerabilities that could potentially enable broad targeting of variant spike proteins. We proceed here with our efforts to characterize a broadly neutralizing antibody fragment with unconventional properties and identify its molecular epitope on the SARS-CoV-2 spike protein.

V_H ab6 is a phage-display-derived antibody with the unusual biochemical property of exhibiting enhanced RBD affinity as a monomeric fragment as compared to a bivalent fusion[185] and was recently shown to exhibit tolerance to several circulating RBD mutations[186]. We first confirmed this anomalous property of ab6, showing that the bivalent V_H-Fc fusion has lower neutralization potency relative to the monovalent V_H construct in both pseudo-typed and live virus neutralization assays (Figure 4.20 a,c). Note the enhanced affinity of the bivalent V_H-Fc ab8 fusion relative to V_H ab8 as a typical example of increased affinity due to avidity (Figure 4.20b). We next assessed V_H ab6 neutralization of variant spikes, (Figure 4.21a). Ab6 neutralized all variant spike pseudo-typed viruses but exhibited 9–26-fold decreased potency for Epsilon, Kappa, and Delta and 4- and 3-fold lower potency for the BA.1 and BA.2 Omicron spikes respectively.

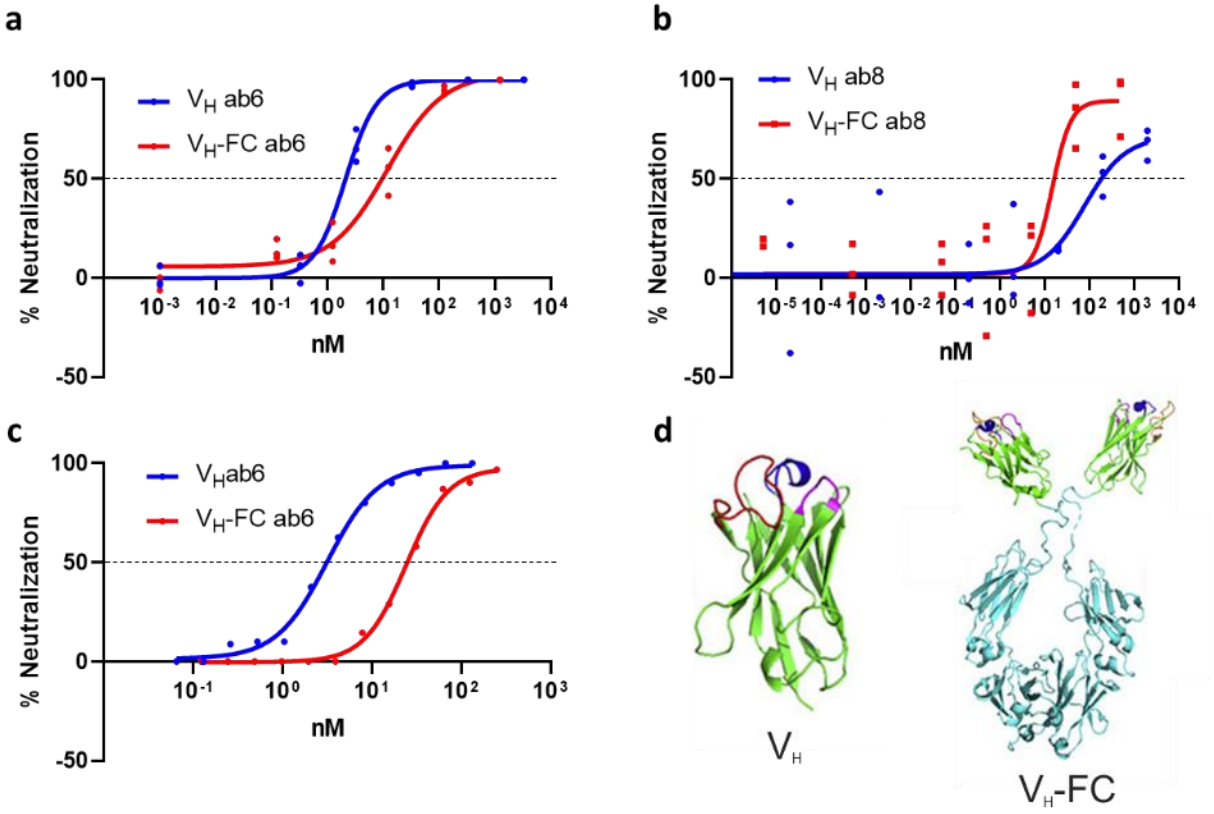

Figure 4.20. **Enhanced potency of V_H ab6 compared to V_H-FC ab6.** (a) Pseudoviral neutralization assay comparing neutralization activity of V_H and V_H-FC ab6. (b) Pseudoviral neutralization assay comparing neutralization activity of V_H and V_H-FC ab8. (c) Live viral neutralization assay comparing neutralization activity of V_H and V_H-FC ab6. (d) schematic highlighting the differences between minimal V_H constructs and V_H-FC constructs, adapted from Li *et al*[104]. All experiments were performed on the ancestral D614G spike protein/virus. Pseudovirus neutralization experiments were performed in technical triplicate (n = 3) and data are shown as points. Live virus neutralization assay was performed in technical singlicate (n = 1) and data are shown as points.

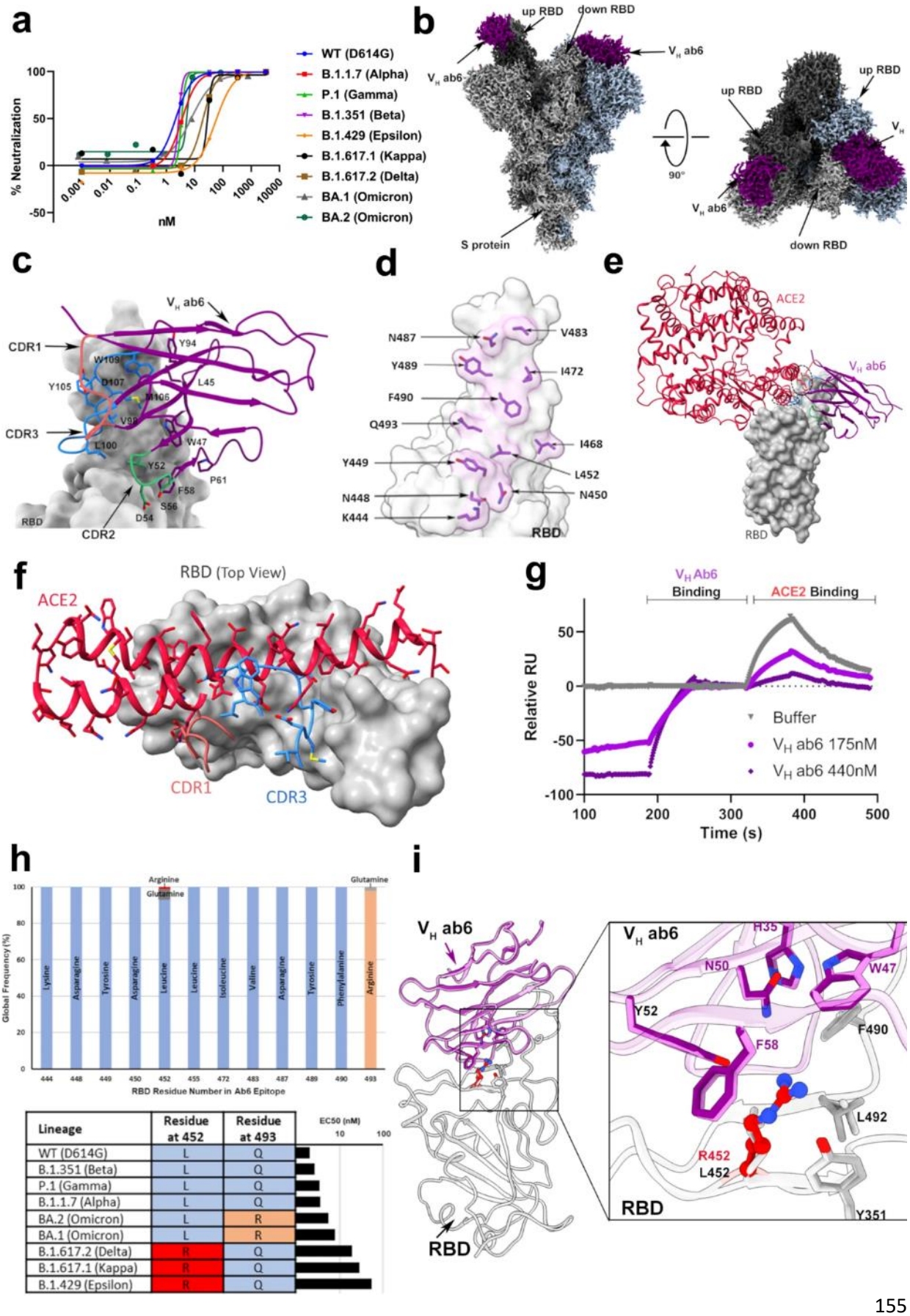
a
% Neutralization
nM
WT (D614G)
B.1.1.7 (Alpha)
P.1 (Gamma)
B.1.351 (Beta)
B.1.429 (Epsilon)
B.1.617.1 (Kappa)
B.1.617.2 (Delta)
BA.1 (Omicron)
BA.2 (Omicron)
b
up RBD
down RBD
V_H ab6
S protein
90°
c
CDR1
CDR2
CDR3
RBD
d
RBD
e
ACE2
RBD
f
RBD (Top View)
ACE2
CDR1
CDR3
g
V_H Ab6 Binding
ACE2 Binding
Relative RU
Time (s)
Buffer
V_H ab6 175nM
V_H ab6 440nM
h
Global Frequency (%)
RBD Residue Number in Ab6 Epitope
Lineage
Residue at 452
Residue at 493
EC50 (nM)
WT (D614G) L Q
B.1.351 (Beta) L Q
P.1 (Gamma) L Q
B.1.1.7 (Alpha) L Q
BA.2 (Omicron) L R
BA.1 (Omicron) L R
B.1.617.2 (Delta) R Q
B.1.617.1 (Kappa) R Q
B.1.429 (Epsilon) R Q
i
RBD
H35
N50
W47
Y52
F58
F490
L492
R452
L452
Y351

Figure 4.21. **Ab6 broadly neutralizes SARS-CoV-2 variants via a largely conserved molecular epitope.** (a) Pseudovirus neutralization of SARS-CoV-2 variants by V_H ab6, performed in at least technical triplicate ($n = 3$), the mean is plotted. (b) 2.4 Å global cryo-EM density map of V_H ab6 bound to wild-type S protein. Density corresponding to S protein protomers and ab6 are shown in grayscale and blue, respectively. (c) ab6 contact zones. The RBD and ab6 are shown as a gray surface and colorized cartoon, respectively. The ab6 scaffold is colored purple and complementarity determining regions (CDRs) of ab6 are colored as follows: CDR1—red; CDR2—green; CDR3—blue. (d) Footprint of ab6. The sidechains of footprint residues are shown in purple. (e) Overlap of ab6 and ACE2 binding footprints. The local refined model of the ab6-RBD interface was superposed with the crystal structure of the ACE2-RBD complex (PDB: 6M0J). ACE2 is shown in red while VH ab6 is shown as in **c**. The RBD is depicted as a gray surface. Models were aligned using the RBD. Ovals highlight steric clashing between ACE2 and V_H ab6. (f) Detailed view of clashes made by CDR3 and CDR1 of V_H ab6 with the N terminal helices of ACE2. (g) SPR-based spike protein competition assay between ACE2 and V_H ab6. Spike protein was loaded onto an SPR chip surface before buffer or indicated concentrations of V_H ab6 were injected, followed by injection of ACE2-FC. Relative response units (RUs) are plotted on the *Y* axis. (h) (Top) Global frequency of residue identity within the ab6 footprint in GISAID deposited sequences as of May 1st, 2022. (Bottom) Residue identity at positions 452 and 493 within SARS-CoV-2 variants and V_H ab6 half-maximal effective concentrations (EC50) from pseudoviral neutralization assays. (i) Focused view superpositions of the cryo-EM-derived atomic model of the Epsilon (B.1.429) and wild-type (D614G) S proteins bound to V_H ab6. Epsilon and wild-type RBDs are colored light and dark gray respectively, while purple and pink models refer to ab6-WT and ab6-Epsilon, respectively. The R452 mutation is highlighted in red

We next determined the cryo-EM structure of V_H ab6 bound to the WT spike at 2.57 Å, showing that ab6 binds to the RBD in both the up and down positions, via a unique binding mode (Figure 4.21b). Local refinement of the down RBD bound by V_H ab6 enabled visualization of the ab6-RBD interface at 3.21 Å and revealed that the ab6-RBD interaction is dominated by contacts with the ab6 beta-sheet scaffold, which wraps around the RBD, extending this large interface to include its CDR2 and CDR3 loops but leaving the CDR1 loop free (Figure 4.21c). This scaffold-mediated interaction necessitates a near perpendicular angle of approach for ab6 relative to the RBD, which likely can only be accommodated by a single V_H within a bivalent fusion construct. Furthermore, accessibility to the V_H scaffold may be limited within a bivalent fusion construct. Thus, the unusual angle of approach and dominance of scaffold-mediated contacts may account for the lower potency of the V_H-Fc ab6 construct relative to V_H ab6.

The ab6 footprint involves multiple RBD residues (Figure 4.21d) and overlaps that of ACE2, consistent with a mechanism of neutralization via ACE2 competition[185] (Figure 4.21e). The CDR1 and CDR3 loops of ab6 occupy positions that result in clashes with ACE2 upon superposition with an ACE2-bound RBD, with the CDR3 region directly competing with the amino terminal helix of ACE2 for RBD binding contacts, while the CDR1 loop poses a steric clash with the second helix of ACE2 without making RBD contacts (Figure 4.21f). To confirm the ACE2 competitive nature of ab6 we employed competition ELISA (Figure 4.22) and competitive SPR experiments (Figure 4.21g). Both experiments demonstrate the ability of ab6 to compete with ACE2 for spike protein binding.

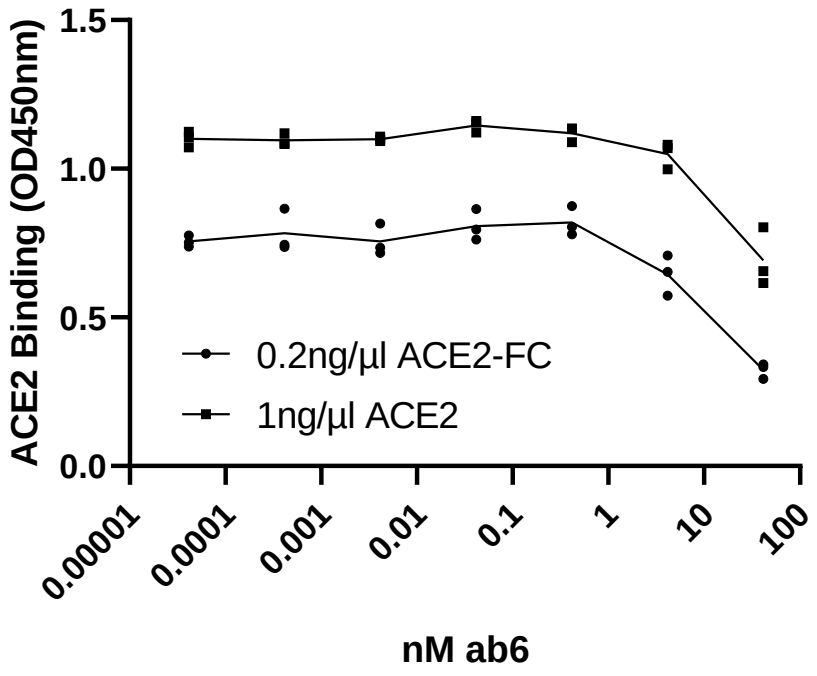

Figure 4.22. **ELISA based ACE2 competition assay.** The ability of VH ab6 to compete with the indicated concentrations of ACE2-FC was assessed via competition ELISA experiments. Experiments were performed in 3 technical replicates (n=3) which are shown as points.

Analysis of the ab6 footprint reveals the inclusion of L452 and Q493, consistent with the reduced potencies against the Epsilon, Delta, and Kappa spikes, which harbor the L452R mutation, along with the BA.1 and BA.2 Omicron sub-lineages which harbor the Q493R mutation (Figure 4.21d,h). Genomic sequences from the GISAID database confirm the conserved nature of the ab6 epitope, highlighting the Q493R mutation to have been the only significantly occurring variation in circulating variants as of May 1st, 2022. (Figure 4.21h). Analysis of the relative neutralization potencies of L452R and Q493R containing variants suggests that ab6 exhibits greater sensitivity to the L452R mutation (Figure 4.21h). To uncover the structural basis for the attenuation of ab6 potency by the L452R mutation, we obtained the cryo-EM structure of the Epsilon spike bound to ab6. Focused refinement enabled visualization of the ab6-Epsilon spike interface at 3 Å, revealing R452 to extend towards the ab6 scaffold (Figure 4.21i). This orientation places the positively charged R452 sidechain in close proximity to a hydrophobic portion of ab6, centered around F58. Thus, the reduced potency observed for R452-containing spikes is likely a result of unfavorable charge and steric effects. The Q493R mutation places R493 in close proximity to the ab6 CDR3 loop, and accommodation of this mutation may involve similar charge and steric penalties which give rise to the attenuation in ab6 potency against the BA.1 and BA.2 variant spike proteins.

A comparison of ab6 to several other reported RBD-directed V_H domains highlights the unique epitope and mechanism of binding exhibited by ab6 (Figure 4.23). While V_H fragments ab8[104], H3[187], and C5[187] approach the RBD with more acute angles relative to ab6, C1[187], and n3113[188] both exhibit near perpendicular angles of approach involving some scaffold interactions, similar to ab6. Although the H3 footprint overlaps significantly with that of ab6, it is completely escaped by mutations within the beta variant spike protein, unlike ab6. C1 binds an epitope distal to that of ab6 and the ACE2 binding site, yet is able to compete for ACE2 binding due to steric

effects, whereas n3113 binds an epitope which overlaps with that of ab6 but is non-competitive with regards to ACE2 binding. The neutralization breadth of n3113 extends to multiple variants[188], consistent with its epitope overlap to that of ab6. Of note, n3113 was shown to bind exclusively to the RBD in the up conformation[188] in contrast to ab6 which can recognize both down and up RBD conformations. Thus, distinguishing features of ab6 include its ability to adopt a near perpendicular angle of approach relative to the RBD in both up and down conformations via scaffold-mediated interactions, while also utilizing its CDR regions to compete with ACE2 via steric effects (CDR1) and direct binding of ACE2 interacting residues on the RBD (CDR3).

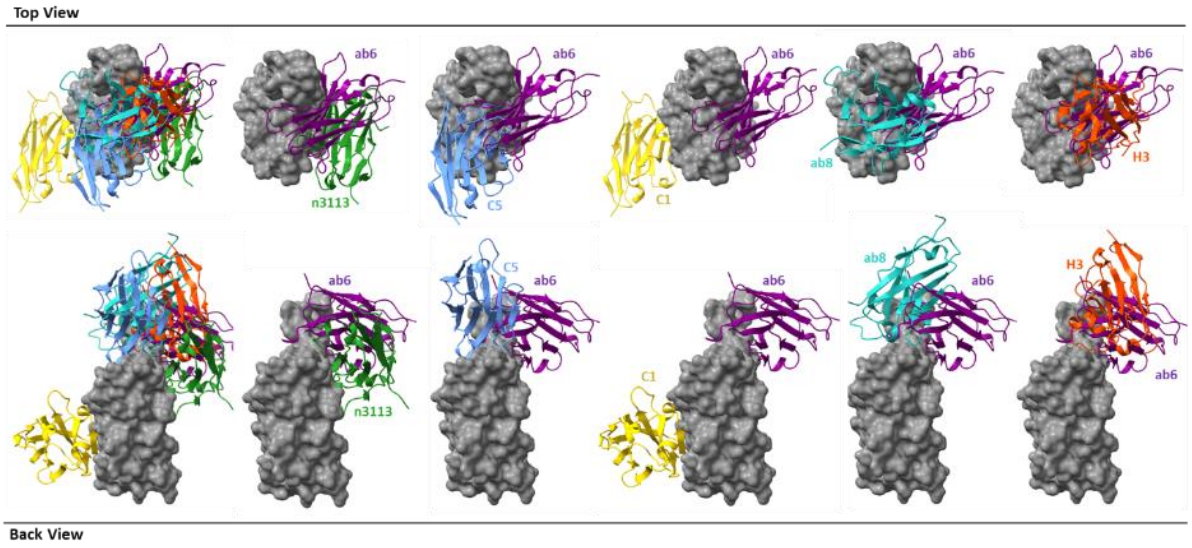

Figure 4.23. **Footprint comparison between ab6 and selected RBD-directed VH domains.** The RBD is depicted as a grey molecular surface and antibodies are depicted as colourized cartoon models. The following PDB files were utilized: 7VNB (n3113), 7OAP (H3 and C1), 7MJI (ab8), 7OAO (C5). The RBD model from the ab6-RBD complex is shown for all antibody complexes for ease of visualization. For superpositions, structures were aligned using the RBD.

Several RBD mutation-resistant antibodies against SARS-CoV-2 have been reported during the preparation of this thesis[174,189–192], providing additional context regarding the conserved epitope we report here. Antibodies DH1047[192] and STE90-C11[191] were isolated from convalescent

patients and SARS2-38[189] from immunized mice. All three antibodies are RBD directed and bind epitopes distal to that of ab6 (Figure 4.24). While STE90-C11 tolerated most circulating RBD mutations, it exhibited loss of activity against the K417T, K417N, and N501Y mutations[191], which are present in many VOC/VOI spike proteins. In contrast, SARS2-38 and DH1047 bind highly conserved epitopes, retaining potency across all VOC/VOI spikes, with DH1407 exhibiting cross-reactivity with additional sarbecoviruses[189,192]. V_H ab6 is distinguished from these previously reported antibodies by its unique angle of approach and binding mode involving multiple V_H scaffold - RBD contacts (Figure 4.21e), along with its small (15 kDa) size. Small antibody fragments are attractive therapeutic modalities given their enhanced tissue penetration compared to conventional monoclonal antibodies[193,194]. That being said, it should be noted that the half-lives of small antibody fragments is much shorter than that of traditional IgG molecules due to enhanced glomerular filtration, although there exist strategies to increase the size and hydrodynamic radius of such fragments to overcome this issue[195].

A recent study by a global consortium defined seven RBD binding antibody communities and showed broadly neutralizing antibodies either bind cryptic epitopes within the inner RBD face (communities RBD-6, RBD-7), or are non-ACE2 competing antibodies that bind the outer RBD face (community RBD-5)[196]. Ab6 binds the inner RBD face and contacts the RBM, enabling ACE2 competition, drawing similarity to the RBD-4 antibody community, which interestingly was not shown to contain any broadly neutralizing antibodies. Structural comparison of the ab6 footprint with a representative RBD-4 antibody (C002)15 reveals an overlapping footprint shared by the C002 heavy chain and ab6 despite differences in binding modes (Figure 4.24). C002 is derived from a convalescent patient, suggesting the potential for such an epitope to be recognized by

natural antibodies. This evidence further supports the potential value of focus on the ab6 binding epitope for future therapeutic design.

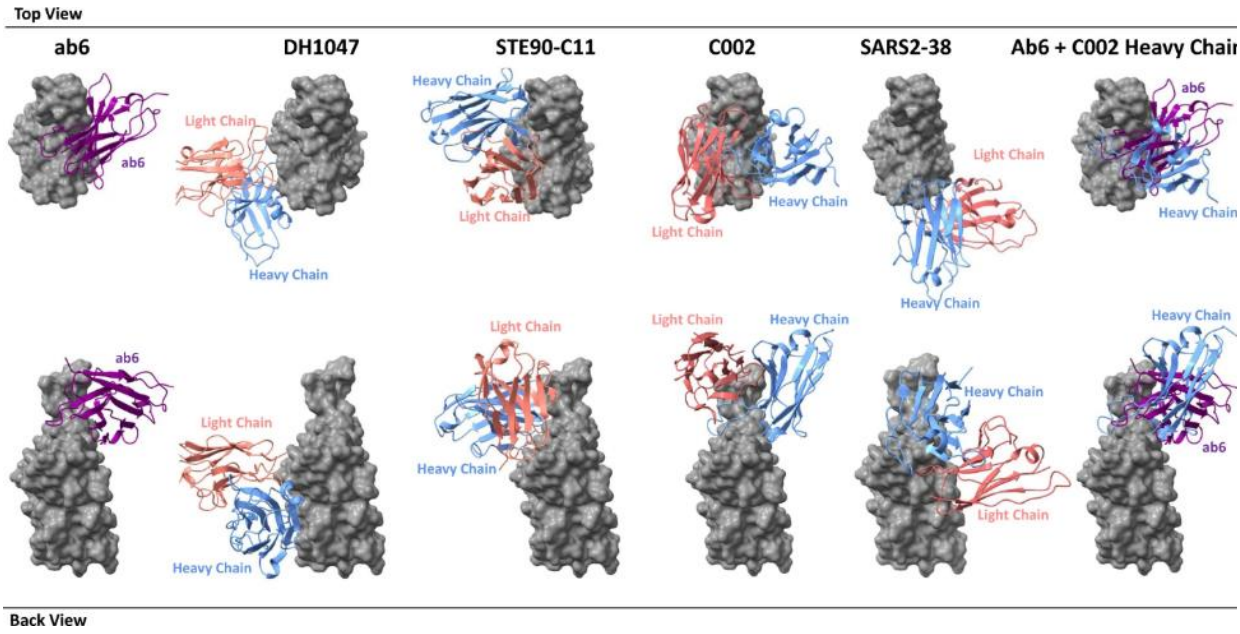

Figure 4.24. **Footprint comparison between ab6 and selected RBD-directed antibodies.** The RBD is depicted as a gray molecular surface and antibodies are depicted as colorized cartoon models. The following PDB files were utilized: 7LD1 (DH1047), 7B3O (STE90-C11), 7K8T (C002), 7MKM (SARS2-38). The RBD model from the ab6-RBD complex is shown for all antibody complexes for ease of visualization. For superpositions, structures were aligned using the RBD.

4.3 Methods

4.3.1 Cloning, expression, and purification of recombinant spike protein constructs

All variant spike protein hexapro genes and full length genes were synthesized and inserted into pcDNA3.1 (GeneArt Gene Synthesis, Thermo Fisher Scientific). RBD constructs were cloned as described in section 2.3.1. Human ACE2 (residues 1–615) with a C terminal 7x His tag was amplified from "hACE2", (Addgene plasmid # 1786) and cloned into pcDNA3.1 via BstXI and XbaI restriction enzyme cloning. Mouse ACE2 (residues 1-615) with a C terminal 8x His tag was amplified from (Addgene Plasmid #158087) and inserted into pcDNA3.1. human ACE2-FC plasmid was a kind gift from Dr. Zehua Sun. Mutational analysis of the kappa variant spike was performed using site-directed mutagenesis (Q5 Site-Directed Mutagenesis Kit, New England Biolabs). Successful cloning was confirmed by Sanger sequencing (Genewiz, Inc.).

All proteins were expressed in Expi293F cells (Thermo Fisher, Cat# A14527) under identical conditions to sections 2.3.3 and 3.3.1. All spike ectodomains were purified as described in those sections. All RBDs were purified as described in section 2.2.3 with the exception of the BA.1 RBD which was purchased from Sino Biological (Cat# 40592-V08H121). For monomeric human ACE2 (residues 1–615) purification, the supernatant was harvested by centrifugation and filtered through a 0.22-μM filter prior to loading onto a 5 mL HisTrap excel column (Cytiva). The column was washed for 20 CVs with wash buffer (20 mM Tris pH 8.0, 500 mM NaCl), 5 CVs of wash buffer supplemented with 20 mM imidazole, and the protein eluted with elution buffer (20 mM Tris pH 8.0, 500 mM NaCl, 500 mM imidazole). Elution fractions containing the protein were pooled and concentrated (Amicon Ultra 100 kDa cut off for ectodomain, 10 kDa for monomeric ACE2) before

gel filtration. Gel filtration was conducted using a Superose 6 10/300 GL column (Cytiva) pre-equilibrated with GF buffer (20 mM Tris pH 8.0, 150 mM NaCl). Peak fractions corresponding to soluble protein were pooled and concentrated to 4.5–5.5 mg/mL (Amicon Ultra 100 kDa cut off for ectodomain, 10 kDa for monomeric ACE2). Protein samples were flash-frozen in liquid nitrogen and stored at −80 °C.

For purification of dimeric human ACE2-FC, the supernatant was harvested after 6 days of expression and flowed through a gravity column containing over 400 µL of Protein A Plus Agarose (Thermo Fisher Cat# 22812) once. The column was washed once with 5 mL of PBS before elution with 0.1 M glycine pH3.5 and immediate neutralization with 1 M Tris pH 8.0. Elutions were pooled and concentrated using an Amicon Ultra 50 kDa cut-off concentrator before gel filtration. Gel filtration was conducted using a Superose 6 10/300 GL column (Cytiva) pre-equilibrated with GF buffer (20 mM Tris pH 8.0, 150 mM NaCl). Peak fractions corresponding to soluble protein were pooled and concentrated to 2–5 mg/mL (Amicon Ultra 50 kDa cut-off). Protein samples were flash-frozen in liquid nitrogen and stored at −80 °C.

4.3.2 Antibody Production

All antibodies were produced as described in section 3.3.2.

4.3.3 Pseudo-virus Neutralization Assay

Assays were conducted as described in section 2.3.8. In some cases, 384 well formats were employed and the following amendments were used: HEK293T-ACE2-TMPRSS2 cells (BEI

Resources cat# NR-55293) were seeded in 384-well plates at 20 000 cells. All other steps were identical.

4.3.4 Biolayer Interferometry (BLI)

BLI was performed as described in section 3.3.5. Concentrations of 125, 250, 500, and 1000 nM spike trimers were used.

4.3.5 Surface Plasmon Resonance (SPR)

A Biacore T200 instrument was used for all SPR experiments. All experiments were performed at 25°C, using 10 mM HEPES, 150 mM NaCl, 3 mM EDTA and 0.05% v/v Surfactant P20 as the SPR running buffer. The surface was regenerated using 10 mM glycine pH 1 for all experiments which strips all proteins from the SPR chip surface. Fresh protein was immobilized onto the SPR chip at the beginning of each experimental run. Reference-subtracted curves were fitted to a 1:1 binding model using Biacore evaluation software. Specific details pertaining to each experimental setup are described below.

ACE2-FC as ligand, RBD as analyte

Human ACE2 attached to a human FC tag (ACE2-FC) was immobilized using the series S protein A chip in SPR running buffer. Increasing concentrations of RBD protein constructs (6.25 nM, 31.25 nM, 62.5 nM, 125 nM, 250 nM) were flowed over the surface for single cycle kinetic experiments.

RBD as ligand, ACE2-FC as analyte

CM5 chips were functionalized with anti-his tag antibody (abcam Cat# ab18184) using an amine coupling kit (Cytiva) and used to capture his tagged RBD constructs. Increasing concentrations of ACE2-FC (2.5 nM, 25 nM, 50 nM, 100 nM, 200 nM) were flowed over the surface for single cycle kinetic experiments.

ACE2-FC as ligand, spike protein ectodomain as analyte

Human ACE2 attached to a human FC tag (ACE2-FC) was immobilized using the series S protein A chip in running buffer. Increasing concentrations (6.25 nM, 31.25 nM, 62.5 nM, 125 nM, 250 nM) of spike protein trimers were flowed over the surface for single cycle kinetic experiments.

Competition SPR

CM5 chips were functionalized with monoclonal anti-Strep-Tag antibody (BIO-RAD Cat# MCA2489) at a concentration of 50 μg/mL for the capture of spike protein ectodomains. After the capture of D614G hexapro ectodomain, either buffer, 175 nM, or 440 nM of VH ab6 was injected onto the chip, followed by 500 nM human ACE2-FC. Reference-subtracted curves were utilized for the qualitative assessment of ACE2 competition. Relative response units (RUs) were normalized to a value of 0 immediately before ACE2-FC injection for ease of ACE2-FC binding assessment.

4.3.6 Enzyme-linked immunosorbent assay (ELISA)

Experiments involving monoclonal antibodies and human ACE2 competition were performed as described in section 3.3.4

For mouse ACE2 binding experiments, 5 µg/ml of mACE2 was coated on the wells in PBST-2% casein overnight at 4 degrees Celsius. Washes were performed using PBST. Serial dilutions of spike protein ectodomains were incubated on the wells for 1 hour at room temperature. After washing, wells were incubated with a mouse anti-strep tag antibody (BIO-RAD Cat# MCA2489) at a 1:600 dilution in PBST-2% casein at room temperature for 1 hour. After washing, wells were incubated at a 1:5,000 dilution with Goat Anti-Mouse IgG Fc Secondary Antibody, HRP (Invitrogen) in PBS-T + 2% casein buffer for 1 h at room temperature. After washing signal was developed as described in section 3.3.4.

4.3.7 Authentic SARS-CoV-2 plaque reduction neutralization assay

Neutralization assays were performed using Vero E6 cells (ATCC CRL-1586) that were seeded 24 h prior to the assay in 24-well tissue culture plates at a density of 3×105 cells per well. Antibodies were serially diluted twofold (starting concentration of 4, 10, or 40 µg/mL, depending on the antibody being tested) and mixed with an equal volume of 30–50 plaque-forming units of SARS-CoV-2. This results in a final antibody concentration of 2, 5, or 20 µg/mL in the antibody–virus mixture. The following SARS-CoV-2 strain was used: isolate USA-WA1/2020 (NR-52281, BEI Resources). The antibody-virus mixture was then incubated at 37 °C in a 5% CO2 incubator for 1 h and added to the Vero E6 cell seeded monolayers, in duplicate. Plates were then incubated for 1 h at 37 °C in a 5% CO2 incubator. Following incubation, an overlay media with 1% agarose-containing media (2× Minimal Essential Medium, 7.5% bovine albumin serum, 10 mM HEPES, 100 µg/mL penicillin G, and 100 U/mL streptomycin) was added to the monolayers. The plates were incubated for 48–72 h (depending on the SARS-CoV2 variant) and then cells were fixed with formaldehyde for 2 h. Following fixation, agar plugs were removed, and cells were stained with crystal violet. In order to assess the input virus, a viral back-titration was performed using a culture

medium as a replacement for the antibodies. All assays were performed in the University of Pittsburgh Regional Biocontainment Laboratory BSL-3 facility.

4.3.8 Antigen Specific Polyclonal antibody purification and ELISA

BA.1 spike ectodomain, RBD, NTD, and irrelevant antibody functionalized resin were prepared using Pierce NHS-Activated Agarose Slurry according to manufacturer's instructions. Pooled sera from BA.1 convalescent patients was diluted by a factor of two in PBS, split into four batches, and incubated with each resin at 4°C overnight. After washing three times with PBS, antigen specific polyclonal antibody preparations were eluted from resin using 100 mM Glycine pH 2.5 and immediately neutralized using 1 M Tris pH 8 buffer. Polyclonal preparations were concentrated using 10 kDa cut off spin columns (Amicon).

For ELISA, 100 μL of either BA.1 or BA.2 spike protein ectodomain in PBS were coated on 96-well MaxiSorp plates at 2 μg/mL in PBS overnight. All washing steps were performed three times with PBS +0.05% Tween 20 (PBS-T). After washing, wells were incubated with blocking buffer (PBS-T + 1% casein) for 1 h at room temperature. Then polyclonal antibody preparations were serially diluted in PBS-T + 0.5% casein and incubated in wells for 1 h at room temperature. After washing, wells were incubated with goat anti-human IgG (Jackson ImmunoResearch) at a 1:5,000 dilution in PBS-T + 1% casein buffer for 1 h at room temperature. After washing, the substrate solution (Pierce 1-Step) was used for color development according to the manufacturer's specifications. Optical density at 450 nm was read on a Varioskan Lux plate reader (Thermo Fisher Scientific). An identical ELISA was performed using anti-his tag antibody (abcam Cat# ab18184) as a spike protein loading control. Area under the curve (AUC) was calculated for each experiment and normalized to the anti-his tag ELISA control for data analysis.

4.3.9. Cryo-EM sample preparation and data collection

Samples were prepared and data was collected as described in section 3.3.6. Mouse ACE2 was used at the same ratio as human ACE2 for complex formation (1:1.25 spike trimer to ACE2). 1:9 S protein trimer:VHab6 molar ratio was used for the ab6 complexes. 1:6.4 S protein trimer: 4A8 Fab was used for the BA.2-4A8 complex.

4.3.10 Cryo-EM Image Processing

Image processing was performed as described in section 3.3.7. In general, all data processing was performed in cryoSPARC v.3.2. For B.1.617.1 (Kappa) spike proteins, focused refinements were performed with a soft mask covering all six RBDs. For the complexes of spike protein ectodomain and VH ab6, a soft mask covering VH-ab6 and its bound RBD was used in focused refinement. For apo BA.2 spike protein and complexes of BA.2 spike protein with 4A8, to better resolve the N-terminal domain or the interface between the N-terminal domain and 4A8, particles were symmetry expanded after another round of global refinement with C3 symmetry, and then refined with a soft mask covering a single N-terminal domain or a single N-terminal domain and its bound 4A8.

4.3.11 Model Building and Refinement

For models of spike protein ectodomain alone, the SARS-CoV-2 HexaPro S trimer (PDB ID 7MJG) was used as an initial model and docked into the map. Then, mutation and manual adjustment were performed in COOT, followed by iterative rounds of real-space refinement in COOT and Phenix. For models of spike-ACE2/4A8 complex, the subcomplexes RBD-ACE2 or NTD-4A8 were built and refined against local refinement maps. The resulting models were then docked into global refinement maps together with the other individual domains of the spike

protein. Models were validated using MolProbity. Structural analyses and figure generation were performed in ChimeraX.

4.3.12 Negative Stain Electron Microscopy

Negative staining and image analysis was performed as described in section 2.3.9. Kappa spike trimers were used at 0.05mg/ml.

Chapter 5: Conclusion and Future directions

5.1 General Conclusions and Limitations

5.1.1 General Conclusions

Overall, the work presented in this thesis represents efforts to contribute to the global COVID-19 pandemic response. We identified vulnerable regions within the SARS-CoV-2 spike glycoprotein as primarily being within the NTD and RBD, determined the molecular impact of mutations within the SARS-CoV-2 RBD, and characterized variant spike proteins as they emerged in real time, demonstrating evolution towards both enhanced receptor binding and evasion of neutralizing antibodies. Structural studies revealed the structural plasticity of the NTD in comparison to the RBD, which appears to have evolved under more stringent structural constraints to preserve or enhance receptor binding but still permit antibody evasion. These insights provide the basis for continued study of this novel pathogen, which continues to exhibit antigenic drift within the spike glycoprotein to evade antibodies elicited by vaccination, natural infection, or clinical therapeutic antibodies. Despite the extensive antibody evasion exhibited by some variants, we identified a conserved epitope that may be exploited for broad neutralization of SARS-CoV-2 variants.

5.1.2 Limitations

We have assessed variant spike proteins for mutational impacts on overall architecture along with ACE2 and antibody binding, all of which are important but not comprehensive readouts on spike protein biology. Other critical aspects such as spike protein cleavage and protease preference, route of cell entry, recognition by cellular immunity, spike protein conformational dynamics (RBD up/down propensity in particular) have not been assessed and represent important outstanding areas of investigation. Our analyses make use of trimeric stabilized S protein ectodomain

constructs, which differ from native S protein trimers by the addition of six stabilizing proline mutations and the removal of the transmembrane domain, which may confound our analyses by altering spike protein conformation. Mutations in other viral proteins such as viral proteases and replication components may additionally contribute to increased viral fitness and have not been considered in the present work. Our reliance of pseudoviral systems, while permitting us to assay neutralization of ACE2 dependent cell entry, almost certainly does not recapitulate the full biology of SARS-CoV-2 cell entry due to the single cycle infectious nature of the experiment, along with the differing virion morphologies and spike protein densities of lentiviral particles compared to intact SARS-CoV-2 virions.

5.2 Future Directions

5.2.1 Monitoring of New Variants

SARS-CoV-2 will likely continue to evolve and more variants will emerge as we move into the endemic phase of this crisis[197], perhaps drawing some similarity to what has been observed with other endemic coronaviruses. In fact, at the time of writing this thesis there are several new variants that have emerged and are on track to achieve global dominance, likely due to enhanced immune evasion and/or infectivity. Retrospective analyses of antibody mediated neutralization of the endemic coronavirus 229E from serum collected during the 1980s has revealed a significant loss of neutralizing activity for subsequent variants that emerged and achieved global dominance 8-17 years later despite being endemic[198]. This was shown to be due to spike protein alterations within the RBD, and mirrors what is being seen with SARS-CoV-2 lineages[198]. Much like how circulating influenza strains are monitored, the future of our response to SARS-CoV-2 will likely necessitate continued genomic monitoring of viral sequences and where necessary, functional, structural, and antigenic studies such as those presented in this thesis. Genomic sequencing represents a critical

feature of the collective scientific effort to monitor new variants. Rapid sequencing technology and dedicated centers for viral sequencing, along with deposition of sequencing data into international databases such as the Global Initiative for Sharing Avian Influenza Data (GISAID) database, have enabled real-time surveillance of mutational drift and have provided the necessary motivation for many studies aimed at characterizing mutational features of emerging variants. Importantly, retrospective analysis of global SARS-CoV-2 sequencing data and confirmed clinical cases of COVID-19 has revealed a correlation between the rate of non-synonymous spike protein mutations and the rates of COVID-19 infection[199]. This observation has enabled *a priori* determination of infection case "surges" 10-14 days before occurrence as a function of the non-synonymous viral mutation rate across global viral sequences and provides valuable predictive insight with regards to preparing for future variants with increased transmissibility and/or virulence[199]. Continued international sequencing efforts, paired with geographic and epidemiological inferences based on the location and proportion of different sequences deposited into databases will allow a robust monitoring system to track new SARS-CoV-2 variants and identify concerning variants for additional study. Future efforts should attempt to combine sequencing and geographic data with real-time outcomes data that contains information on patient demographics and immunization status from health care centers, to enable rapid identification of variants with clinically significant levels of increased virulence, transmission, and immune evasion[200].

Of interest is the potential for new variants to achieve additional zoonotic transmission events. While it might be expected that the transition to endemicity for SARS-CoV-2 will necessitate lower viral pathogenicity, spillover and evolution in animal reservoirs allows the possibility of more pathogenic strains to emerge and begin circulating in humans. Our studies on the omicron

lineage spike proteins revealed the structural basis for their enhanced binding of mouse ACE2 and allow monitoring of key mutational hotspots in new variants. Given that earth's total mammal biomass is dominated by livestock with only a minor contribution from wild animals[201], it is sensible to monitor livestock for SARS-CoV-2 infection and circulation. However, it should be noted that studies thus far have found low susceptibility to SARS-CoV-2 infection in both domesticated cattle[202], domesticated pigs[203–205], and domesticated chickens[203,204]. Alarmingly, omicron spillover into non-human animals has been reported in white-tailed deer, minks, and cats.[206–209]. The acquired ability of SARS-CoV-2 variants to access animal reservoirs allows them to sample different evolutionary pressures in these organisms, with potential impacts on "spillback" transmission, which has recently been reported for deer-to-human transmission[207], even to the point where variants which previously became extinct in humans have been shown to circulate at alarming frequencies in deer populations[210]. Continued monitoring of new variants should therefore involve studies on ACE2 binding tropism across several animal reservoirs including deer. The structural and functional assays we describe in our study of mouse ACE2 binding can be easily adapted to suit a host of these animal ACE2 constructs, facilitating monitoring of this important aspect of SARS-CoV-2 evolution.

5.2.2 Developing Strategies for Broad SARS-CoV-2 Neutralization

As evidenced in this thesis, there is significant antigenic drift within the highly immunogenic NTD and RBD regions of the SARS-CoV-2 spike protein, rendering many neutralizing antibodies ineffective. Of some comfort is the discovery of several broadly neutralizing antibodies by us and other groups[169,174,189–192], and the definition of epitopes recognized by these antibodies provides the blueprints necessary for future therapy design. It is still unclear if vaccination can elicit a clinically meaningful level of antibodies which target these broadly neutralizing epitopes. To

answer this question, future efforts should employ serological studies assessing the ability for vaccinee and boosted sera to compete with a panel of these broadly neutralizing antibodies for spike protein binding. The extent of broadly neutralizing antibody competition by different sera should be correlated with in vitro neutralization assays, and prophylactic serum therapy studies in humanized mouse SARS-CoV-2 challenge models. Another related avenue of investigation is the ability to hyperfocus antibody responses to a selection of these broadly neutralizing epitopes within the SARS-CoV-2 spike protein. Antigens can be rationally engineered to present certain epitopes at high frequencies and have other epitopes immunologically "masked". This can be achieved by selective introduction of N-linked glycosylation sites to provide a "glycan shield" surrounding unwanted epitopes, while desirable epitopes can be presented via fusion to structural elements of scaffold proteins[211]. Proof of principle efforts towards leveraging such techniques within the context of COVID-19 have been recently published, demonstrating the ability to focus antibody responses on several RBD epitopes in mice using engineered chimeric RBD antigens[212]. It will be important to build on these results by adapting this technology to focus antibody responses on the ab6 epitope we defined, along with the growing list of other broadly neutralizing epitopes[174,176,189–192]. It should be noted that although antibody mediated immunity is a key component of antiviral responses, a key limitation of antibodies lies in the potential for inefficient localization and concentration to the respiratory mucosa within the context of respiratory infections. One potential strategy to overcome this issue involves delivery of vaccines directly to the respiratory mucosa. Indeed, studies on immunity to SARS-CoV-2 using bronchoalveolar lavage samples suggest the need for mucosal vaccine formulations rather than intra-muscular formulations to achieve meaningful levels of neutralizing antibodies within the respiratory mucosa[213]. Such vaccine formulations have been recently been developed for SARS-CoV-2, and hold great promise[214].

These intranasal vaccines elicit a substantial level of neutralizing mucosal IgA antibodies. Thus, future vaccination efforts should aim to both induce and enrich broadly neutralizing antibodies within the respiratory mucosa.

In addition to achieving broad neutralization via antibody activity, efforts have been made to utilize receptor decoys as agents of broad neutralization. The use of receptor decoys is motivated by the principle that spike protein evolution must always preserve receptor binding functionality to ensure viral survival. These efforts have included using soluble human ACE2 fusion constructs[215,216], engineering ACE2 constructs to optimize glycosylation[217] or increase the avidity via trimerization[218], and the development of affinity maturated, highly potent ACE2 decoys[150,219–221]. It should be noted that initial phase 2 trials using intravenously administered recombinant human ACE2 to treat COVID-19 failed, likely due to rapid clearance of the recombinant protein which was shown to have a half-life of ~3 hours, raising a fundamental barrier for therapeutic use[221]. However, fusion strategies aimed at tethering the extracellular domain of ACE2 to the FC region of an IgG have demonstrated decreased clearance with a half-life of ~30 hours[221]. An alternative strategy to administer receptor decoys is direct inhalation to the respiratory mucosa over intravenous injection. While the half-life of these decoys will still likely remain on the hour timescale[221], the localized delivery offers much higher concentrations at the relevant site of SARS-CoV-2 infection and replication. Future efforts should aim to optimize the pharmacokinetics and develop inhalable formulations of candidate ACE2 receptor decoys along with various broadly neutralizing antibody formats.

The significant antigenic changes and antibody escape observed for the omicron lineage spike proteins described in this thesis and by several other studies[176,222–224] has already caused a level of concern that warranted efforts to update the formulation of COVID-19 vaccines to include new

mutant spike proteins[225]. However research at this time does not generally support the notion that antibody responses to variant spike proteins are enhanced in potency or breadth when immunizing with ancestral spike versus including novel variant spike proteins in vaccine formulations[226–228]. Of note, a study funded by vaccine developers BioNTech and Pfizer seemed to contradict this notion showing a small benefit for bivalent vaccines which target both the ancestral and omicron (BA.4/5 sub-lineage) spike proteins with regards to neutralizing antibody breadth[229]. Nevertheless, these results suggest that immunity to SARS-CoV-2 can and has been imprinted against the ancestral and early variant spike proteins, to the point that antigenic stimulation with new variant antigens only elicits responses from a subset of previously activated B cells that are capable of inter-variant cross-reactivity[226]. A key question for future study surrounds methods to elicit new subsets of variant specific antibodies upon immunization with updated antigens. Central to this question is the need to structurally describe and differentiate newly elicited variant-specific antibodies from those which are previously existing and may recognize several antigens perhaps at lower affinities. The methods developed and utilized for structurally characterizing spike protein immune complexes in chapter 2 could hold great promise for addressing this aspect of the problem, enabling structural descriptions of epitope landscapes against several variant spike proteins in different immunization settings. Once we have achieved an understanding of the epitopes driving this imprinting of antibody responses, rational engineering of antigens to mask out these epitopes in subsequent variant specific vaccine formulations may hold great promise in enabling the elicitation of new and effective variant-specific antibody elicitation.

5.2.3 Understanding the Cellular Immune Response to Variant Spike Proteins

While we have investigated the antibody evasive nature of emerging SARS-CoV-2 variant spike proteins, our studies did not consider the cellular arm of the immune system. Immunity mediated by T cells has been shown to be critical in the clinical outcome after SARS-CoV-2 infection[230]. T cell responses to SARS-CoV-2 infection have been shown to recognize several viral antigens, including the spike protein, and there have been reports of diminished T cell reactivity towards variant spike proteins[231–233], although these effects are not generally thought to result in significant escape as seen with antibody mediated immunity[230]. However, future variants may arise which are capable of significant evasion of T cell mediated immunity. Furthermore, it is unclear if there exist phenotypic subsets of spike protein reactive T cells that are more prone to escape. Future work should therefore aim to continue monitoring new variant spike proteins for evasion of T cell responses, while also generating detailed phenotypic data of T cell subsets with retained or diminished reactivity. Such nuanced data can be obtained via stimulation of peripheral blood mononuclear cells with spike protein antigens, and subsequent analysis of T cell responses using activation induced marker (AIM) assays, which enable functional and phenotypic stratification of antigen specific T cells[234].

5.2.4 Structural Studies of Alternative SARS-CoV-2 Spike-Receptor Complexes

Although the interactions between human and murine ACE2 have been extensively characterized in the present work, there have been several alternative receptors or attachment factors that have been described in the literature to interact with the SARS-CoV-2 spike[235], but are not structurally well understood (Table 5.1). Some of these interactions have been shown to lead to productive cell entry, while others have not. These interactions range from moderate (mid nanomolar range) to low (micromolar range) affinity and vary in specificity of the spike protein sub-domains involved.

Many of these alternative receptors are expressed in extra-pulmonary tissues and could play key roles in infection of other organ systems, with direct relevance to more chronic post-COVID19 symptomatology, commonly referred to as “long COVID”. Future efforts should leverage single-particle electron microscopy to characterize the structural basis for these interactions will deepen our understanding of receptor tropism accessible to SARS-CoV-2, and shed light on structural requirements for interactions that lead to productive viral entry. Additionally, measurement of binding using all emerged variant spike proteins will provide insight into additional selection pressures during spike protein evolution.

Table 5.1. Human Host Cell Proteins that Bind the SARS-CoV-2 Spike Protein

Human Host Cell Protein	Spike Protein Binding Dissociation Constant/Binding Assay	Spike Protein Domains Involved	Productive Cell Entry	Reference
AXL	882nM/BLI	NTD	Yes	[236]
L-SIGN	1.8μM/SPR	Glycans across the whole spike protein	No	[237]
DCSIGN	11.9μM/SPR	Glycans across the whole spike protein	No	[237]
CLEC4G	259nM/SPR	Glycans within the RBD and other regions	n/a	[238]
KREMEN1	19.3nM/Flow Cytometry	RBD with minor contributions from NTD and S2	Yes	[239]
ASGR1	94.8nM/Flow Cytometry	RBD with minor contributions from NTD	Yes	[239]
LDLRAD3	293nM/SPR	NTD	Yes	[240]
TMEM30A	282nM/SPR	NTD	Yes	[240]
LRRC15	68.8nM/Flow Cytometry 263nM/ Flow Cytometry 104nM/ELISA	RBD	No	[241] [242] [243]
Neuropilin-1	20.1 μM /ITC	S1 (Furin Cleavage Site Residues)	Yes	[244]
Integrin α5β1	31.8nM/SPR	RBD	Yes	[245]

5.2.5 Understanding the SARS-CoV-2 Spike Pre-fusion to Post-fusion Transition

Although there is a wealth of structural information pertaining to both the pre-fusion and post-fusion conformations of the SARS-CoV-2 spike protein, the details of how this dramatic conformational change occurs is still not fully known. Detailed molecular dynamics simulations have suggested a plausible conformational trajectory for this event, positing that glycans within the S2 region provide a "pause" during this transition that enables correct positioning for the spike protein to embed itself in the host cell membrane upon refolding to the post-fusion state[246]. Preliminary low resolution cryo-electron tomography (cryo-ET) data has been generated on

SARS-CoV-2 spike harbouring particles incubated with ACE2 containing extracellular vesicles in the presence of a peptide inhibitor of viral fusion, demonstrating the presence of several distinct intermediates between pre- and post-fusion states[247]. Future studies should aim to build on these results, and achieve near atomic resolution descriptions of these intermediates, integrating single particle cryo-EM and cryo-ET techniques on similar biochemical experiments, both with genetic ablation of the key S2 glycan sites and with additional glycan site introduction at key positions, effectively testing the suggested role of these glycans in steering the conformational trajectory during this major architectural shift. High resolution insight into this process also offers the blueprint required for structure guided design of fusion inhibitors specific to the SARS-CoV-2 spike protein.

5.3 Concluding Remarks

The unfortunate reality is that SARS-CoV-2 will likely remain circulating within humans for the foreseeable future. Our efforts, along with those of the collective scientific community, provide the initial necessary steps for monitoring evolution of this new virus, combating new variants from a structural and molecular perspective, and hopefully, alleviating the burden of disease and death due to COVID-19 in the future. As discussed in this final chapter, we are only beginning to understand this new virus, which we must learn how to co-exist with as it joins the list of viruses that cause human disease.

Bibliography

1. Diehl, W. E., Patel, N., Halm, K. & Johnson, W. E. Tracking interspecies transmission and long-term evolution of an ancient retrovirus using the genomes of modern mammals. *Elife* **5**, e12704 (2016).

2. Mushegian, A. R. Are There 10(31) Virus Particles on Earth, or More, or Fewer? *J. Bacteriol.* **202**, (2020).

3. J., A. S. *et al.* A Strategy To Estimate Unknown Viral Diversity in Mammals. *MBio* **4**, e00598-13 (2013).

4. Forni, D., Cagliani, R., Clerici, M. & Sironi, M. Disease-causing human viruses: novelty and legacy. *Trends Microbiol.* **30**, 1232–1242 (2022).

5. Avendaño Carvajal, L. & Perret Pérez, C. Epidemiology of Respiratory Infections. *Pediatric Respiratory Diseases: A Comprehensive Textbook* 263–272 (2020) doi:10.1007/978-3-030-26961-6_28.

6. Monto, A. S. Epidemiology of viral respiratory infections. *Am. J. Med.* **112**, 4–12 (2002).

7. Paules, C. I., Marston, H. D. & Fauci, A. S. Coronavirus Infections—More Than Just the Common Cold. *JAMA* **323**, 707–708 (2020).

8. Hu, B. *et al.* Discovery of a rich gene pool of bat SARS-related coronaviruses provides new insights into the origin of SARS coronavirus. *PLOS Pathog.* **13**, e1006698 (2017).

9. Reusken, C. B. E. M., Raj, V. S., Koopmans, M. P. & Haagmans, B. L. Cross host transmission in the emergence of MERS coronavirus. *Curr. Opin. Virol.* **16**, 55–62 (2016).

10. Kutter, J. S., Spronken, M. I., Fraaij, P. L., Fouchier, R. A. M. & Herfst, S. Transmission

routes of respiratory viruses among humans. *Curr. Opin. Virol.* **28**, 142–151 (2018).

11. Payne, S. Family Coronaviridae. *Viruses* 149–158 (2017) doi:10.1016/B978-0-12-803109-4.00017-9.

12. Bai, C., Zhong, Q. & Gao, G. F. Overview of SARS-CoV-2 genome-encoded proteins. *Sci. China. Life Sci.* **65**, 280–294 (2022).

13. V'kovski, P., Kratzel, A., Steiner, S., Stalder, H. & Thiel, V. Coronavirus biology and replication: implications for SARS-CoV-2. *Nat. Rev. Microbiol.* **19**, 155–170 (2021).

14. Baranov, P. V *et al.* Programmed ribosomal frameshifting in decoding the SARS-CoV genome. *Virology* **332**, 498–510 (2005).

15. Brierley, I., Digard, P. & Inglis, S. C. Characterization of an efficient coronavirus ribosomal frameshifting signal: Requirement for an RNA pseudoknot. *Cell* **57**, 537–547 (1989).

16. Brierley, I. *et al.* An efficient ribosomal frame-shifting signal in the polymerase-encoding region of the coronavirus IBV. *EMBO J.* **6**, 3779–3785 (1987).

17. Denison, M. R. & Perlman, S. Translation and processing of mouse hepatitis virus virion RNA in a cell-free system. *J. Virol.* **60**, 12–18 (1986).

18. Snijder, E. J. *et al.* Unique and Conserved Features of Genome and Proteome of SARS-coronavirus, an Early Split-off From the Coronavirus Group 2 Lineage. *J. Mol. Biol.* **331**, 991–1004 (2003).

19. H., H. B. *et al.* Identification of Severe Acute Respiratory Syndrome Coronavirus Replicase Products and Characterization of Papain-Like Protease Activity. *J. Virol.* **78**,

13600–13612 (2004).

20. M., B. S., T., C. C., Tao, L. X. & R., D. M. Characterization of the Expression, Intracellular Localization, and Replication Complex Association of the Putative Mouse Hepatitis Virus RNA-Dependent RNA Polymerase. *J. Virol.* **77**, 10515–10527 (2003).

21. Gibson, B. A., H., C. R., Tao, L. X. & R., D. M. Four Proteins Processed from the Replicase Gene Polyprotein of Mouse Hepatitis Virus Colocalize in the Cell Periphery and Adjacent to Sites of Virion Assembly. *J. Virol.* **74**, 3379–3387 (2000).

22. Thiel, V. *et al.* Mechanisms and enzymes involved in SARS coronavirus genome expression. *J. Gen. Virol.* **84**, 2305–2315 (2003).

23. Sawicki, S. G. & Sawicki, D. L. A New Model for Coronavirus Transcription BT - Coronaviruses and Arteriviruses. in (eds. Enjuanes, L., Siddell, S. G. & Spaan, W.) 215–219 (Springer US, 1998). doi:10.1007/978-1-4615-5331-1_26.

24. Mortola, E. & Roy, P. Efficient assembly and release of SARS coronavirus-like particles by a heterologous expression system. *FEBS Lett.* **576**, 174–178 (2004).

25. Emily, C. & E., M. C. Infectious Bronchitis Virus E Protein Is Targeted to the Golgi Complex and Directs Release of Virus-Like Particles. *J. Virol.* **74**, 4319–4326 (2000).

26. Corse, E. & Machamer, C. E. The cytoplasmic tails of infectious bronchitis virus E and M proteins mediate their interaction. *Virology* **312**, 25–34 (2003).

27. Stohlman, S. A. *et al.* Specific interaction between coronavirus leader RNA and nucleocapsid protein. *J. Virol.* **62**, 4288–4295 (1988).

28. Molenkamp, R. & Spaan, W. J. M. Identification of a Specific Interaction between the

Coronavirus Mouse Hepatitis Virus A59 Nucleocapsid Protein and Packaging Signal. *Virology* **239**, 78–86 (1997).

29. Sturman, L. S. Characterization of a coronavirus: I. Structural proteins: Effects of preparative conditions on the migration of protein in polyacrylamide gels. *Virology* **77**, 637–649 (1977).

30. Sturman, L. S., Holmes, K. V & Behnke, J. Isolation of coronavirus envelope glycoproteins and interaction with the viral nucleocapsid. *J. Virol.* **33**, 449–462 (1980).

31. Masters, P. S. B. T.-A. in V. R. The Molecular Biology of Coronaviruses. in vol. 66 193–292 (Academic Press, 2006).

32. Stertz, S. *et al.* The intracellular sites of early replication and budding of SARS-coronavirus. *Virology* **361**, 304–315 (2007).

33. de Haan, C. A. M. & Rottier, P. J. M. B. T.-A. in V. R. Molecular Interactions in the Assembly of Coronaviruses. in *Virus Structure and Assembly* vol. 64 165–230 (Academic Press, 2005).

34. Klein, S. *et al.* SARS-CoV-2 structure and replication characterized by in situ cryo-electron tomography. *Nat. Commun.* **11**, 5885 (2020).

35. Li, G. *et al.* Coronavirus infections and immune responses. *J. Med. Virol.* **92**, 424–432 (2020).

36. Buchholz, U. J. *et al.* Contributions of the structural proteins of severe acute respiratory syndrome coronavirus to protective immunity. *Proc. Natl. Acad. Sci.* **101**, 9804–9809 (2004).

37. Du, L. *et al.* MERS-CoV spike protein: a key target for antivirals. *Expert Opin. Ther. Targets* **21**, 131–143 (2017).

38. Barry, R. *et al.* Structural Basis for Potent Cross-Neutralizing Human Monoclonal Antibody Protection against Lethal Human and Zoonotic Severe Acute Respiratory Syndrome Coronavirus Challenge. *J. Virol.* **82**, 3220–3235 (2008).

39. Pancera, M. *et al.* Structural basis for diverse N-glycan recognition by HIV-1 – neutralizing V1 – V2 – directed antibody PG16. *Nat. Publ. Gr.* **20**, (2013).

40. Duan, J. *et al.* A human SARS-CoV neutralizing antibody against epitope on S2 protein. *Biochem. Biophys. Res. Commun.* **333**, 186–193 (2005).

41. M., P. K. & S., L. A. Complexities of Viral Mutation Rates. *J. Virol.* **92**, e01031-17 (2018).

42. Banerjee, A., Mossman, K. & Grandvaux, N. Molecular Determinants of SARS-CoV-2 Variants. *Trends Microbiol.* **29**, 871–873 (2021).

43. Forni, D., Cagliani, R., Clerici, M. & Sironi, M. Molecular Evolution of Human Coronavirus Genomes. *Trends Microbiol.* **25**, 35–48 (2017).

44. Yang, Z. *et al.* Evasion of antibody neutralization in emerging severe acute respiratory syndrome coronaviruses. *Proc. Natl. Acad. Sci.* **102**, 797–801 (2005).

45. Zhu, Z. *et al.* Potent cross-reactive neutralization of SARS coronavirus isolates by human monoclonal antibodies. *Proc. Natl. Acad. Sci.* **104**, 12123–12128 (2007).

46. Huang, A. T. *et al.* A systematic review of antibody mediated immunity to coronaviruses: kinetics, correlates of protection, and association with severity. *Nat. Commun.* **11**, 4704

(2020).

47. L., G. R. & S., B. R. Recombination, Reservoirs, and the Modular Spike: Mechanisms of Coronavirus Cross-Species Transmission. *J. Virol.* **84**, 3134–3146 (2010).

48. Saladino, V., Algeri, D. & Auriemma, V. The Psychological and Social Impact of Covid-19: New Perspectives of Well-Being. *Front. Psychol.* **11**, 2550 (2020).

49. Kontis, V. *et al.* Magnitude, demographics and dynamics of the effect of the first wave of the COVID-19 pandemic on all-cause mortality in 21 industrialized countries. *Nat. Med.* **26**, 1919–1928 (2020).

50. Josephson, A., Kilic, T. & Michler, J. D. Socioeconomic impacts of COVID-19 in low-income countries. *Nat. Hum. Behav.* **5**, 557–565 (2021).

51. Parolin, Z. & Lee, E. K. Large socio-economic, geographic and demographic disparities exist in exposure to school closures. *Nat. Hum. Behav.* **5**, 522–528 (2021).

52. Shrestha, N. *et al.* The impact of COVID-19 on globalization. *One Heal.* **11**, 100180 (2020).

53. Ibn-Mohammed, T. *et al.* A critical analysis of the impacts of COVID-19 on the global economy and ecosystems and opportunities for circular economy strategies. *Resour. Conserv. Recycl.* **164**, 105169 (2021).

54. Dyer, O. Covid-19: Study claims real global deaths are twice official figures. *BMJ* **373**, n1188 (2021).

55. Walls, A. C. *et al.* Structure, Function, and Antigenicity of the SARS-CoV-2 Spike Glycoprotein. *Cell* **181**, 281-292.e6 (2020).

56. Shang, J. *et al.* Cell entry mechanisms of SARS-CoV-2. *Proc. Natl. Acad. Sci.* **117**, 11727 LP – 11734 (2020).

57. Scialo, F. *et al.* ACE2: The Major Cell Entry Receptor for SARS-CoV-2. *Lung* **198**, 867–877 (2020).

58. Hoffmann, M. *et al.* SARS-CoV-2 Cell Entry Depends on ACE2 and TMPRSS2 and Is Blocked by a Clinically Proven Protease Inhibitor. *Cell* **181**, 271-280.e8 (2020).

59. Johnson, B. A. *et al.* Loss of furin cleavage site attenuates SARS-CoV-2 pathogenesis. *Nature* **591**, 293–299 (2021).

60. Peacock, T. P. *et al.* The furin cleavage site in the SARS-CoV-2 spike protein is required for transmission in ferrets. *Nat. Microbiol.* **6**, 899–909 (2021).

61. Pallesen, J. *et al.* Immunogenicity and structures of a rationally designed prefusion MERS-CoV spike antigen. *Proc. Natl. Acad. Sci.* **114**, E7348–E7357 (2017).

62. Kirchdoerfer, R. N. *et al.* Stabilized coronavirus spikes are resistant to conformational changes induced by receptor recognition or proteolysis. *Sci. Rep.* **8**, 15701 (2018).

63. Hsieh, C.-L. *et al.* Structure-based design of prefusion-stabilized SARS-CoV-2 spikes. *Science (80-.).* **369**, 1501 LP – 1505 (2020).

64. Turoňová, B. *et al.* In situ structural analysis of SARS-CoV-2 spike reveals flexibility mediated by three hinges. *Science (80-.).* **370**, 203–208 (2020).

65. Ke, Z. *et al.* Structures and distributions of SARS-CoV-2 spike proteins on intact virions. *Nature* **588**, 498–502 (2020).

66. Yao, H. *et al.* Molecular Architecture of the SARS-CoV-2 Virus. *Cell* **183**, 730-738.e13

(2020).

67. Cai, Y. *et al.* Distinct conformational states of SARS-CoV-2 spike protein. *Science (80-.).* **369**, 1586–1592 (2020).

68. Liu, C. *et al.* The Architecture of Inactivated SARS-CoV-2 with Postfusion Spikes Revealed by Cryo-EM and Cryo-ET. *Structure* **28**, 1218-1224.e4 (2020).

69. Wrapp, D. *et al.* Cryo-EM structure of the 2019-nCoV spike in the prefusion conformation. *Science* **367**, 1260–1263 (2020).

70. Jackson, C. B., Farzan, M., Chen, B. & Choe, H. Mechanisms of SARS-CoV-2 entry into cells. *Nat. Rev. Mol. Cell Biol.* **23**, 3–20 (2022).

71. Burrell, L. M., Johnston, C. I., Tikellis, C. & Cooper, M. E. ACE2, a new regulator of the renin-angiotensin system. *Trends Endocrinol. Metab.* **15**, 166–169 (2004).

72. Crackower, M. A. *et al.* Angiotensin-converting enzyme 2 is an essential regulator of heart function. *Nature* **417**, 822–828 (2002).

73. Hofmann, H. *et al.* Human coronavirus NL63 employs the severe acute respiratory syndrome coronavirus receptor for cellular entry. *Proc. Natl. Acad. Sci. U. S. A.* **102**, 7988–7993 (2005).

74. Li, W. *et al.* Angiotensin-converting enzyme 2 is a functional receptor for the SARS coronavirus. *Nature* **426**, 450–454 (2003).

75. Hikmet, F. *et al.* The protein expression profile of ACE2 in human tissues. *Mol. Syst. Biol.* **16**, e9610 (2020).

76. Li, M.-Y., Li, L., Zhang, Y. & Wang, X.-S. Expression of the SARS-CoV-2 cell receptor

gene ACE2 in a wide variety of human tissues. *Infect. Dis. Poverty* **9**, 45 (2020).

77. Hamming, I. *et al.* Tissue distribution of ACE2 protein, the functional receptor for SARS coronavirus. A first step in understanding SARS pathogenesis. *J. Pathol.* **203**, 631–637 (2004).

78. Towler, P. *et al.* ACE2 X-Ray Structures Reveal a Large Hinge-bending Motion Important for Inhibitor Binding and Catalysis *. *J. Biol. Chem.* **279**, 17996–18007 (2004).

79. Wu, K., Li, W., Peng, G. & Li, F. Crystal structure of NL63 respiratory coronavirus receptor-binding domain complexed with its human receptor. *Proc. Natl. Acad. Sci. U. S. A.* **106**, 19970–19974 (2009).

80. Li, F., Li, W., Farzan, M. & Harrison, S. C. Structure of SARS Coronavirus Spike Receptor-Binding Domain Complexed with Receptor. *Science (80-.).* **309**, 1864–1868 (2005).

81. Shang, J. *et al.* Structural basis of receptor recognition by SARS-CoV-2. *Nature* **581**, 221–224 (2020).

82. Lan, J. *et al.* Structure of the SARS-CoV-2 spike receptor-binding domain bound to the ACE2 receptor. *Nature* **581**, 215–220 (2020).

83. Yan, R. *et al.* Structural basis for the recognition of SARS-CoV-2 by full-length human ACE2. *Science (80-.).* **367**, 1444–1448 (2020).

84. Bagdonaite, I. & Wandall, H. H. Global aspects of viral glycosylation. *Glycobiology* **28**, 443–467 (2018).

85. Doores, K. J. The HIV glycan shield as a target for broadly neutralizing antibodies. *FEBS*

J. **282**, 4679–4691 (2015).

86. Watanabe, Y., Allen, J. D., Wrapp, D., McLellan, J. S. & Crispin, M. Site-specific glycan analysis of the SARS-CoV-2 spike. *Science (80-.).* **369**, 330 LP – 333 (2020).

87. Acharya, P. *et al.* A glycan cluster on the SARS-CoV-2 spike ectodomain is recognized by Fab-dimerized glycan-reactive antibodies. *bioRxiv Prepr. Serv. Biol.* 2020.06.30.178897 (2020) doi:10.1101/2020.06.30.178897.

88. Trkola, A. *et al.* Human monoclonal antibody 2G12 defines a distinctive neutralization epitope on the gp120 glycoprotein of human immunodeficiency virus type 1. *J. Virol.* **70**, 1100–1108 (1996).

89. Walker, L. M. *et al.* Broad neutralization coverage of HIV by multiple highly potent antibodies. *Nature* **477**, 466–470 (2011).

90. Julien, J. *et al.* Broadly Neutralizing Antibody PGT121 Allosterically Modulates CD4 Binding via Recognition of the HIV-1 gp120 V3 Base and Multiple Surrounding Glycans. **9**, (2013).

91. Garces, F. *et al.* Affinity Maturation of a Potent Family of HIV Antibodies Is Primarily Focused on Accommodating or Avoiding Glycans Article Affinity Maturation of a Potent Family of HIV Antibodies Is Primarily Focused on Accommodating or Avoiding Glycans. *Immunity* **43**, 1053–1063 (2015).

92. Pejchal, R. *et al.* A potent and broad neutralizing antibody recognizes and penetrates the HIV glycan shield. *Science* **334**, 1097–1103 (2011).

93. Lee, J. H. *et al.* Model Building and Refinement of a Natively Glycosylated HIV-1 Env

Protein by High-Resolution Cryoelectron Microscopy Article Model Building and Refinement of a Natively Glycosylated HIV-1 Env Protein by High-Resolution Cryoelectron Microscopy. *Struct. Des.* **23**, 1943–1951 (2015).

94. Lee, J. H. *et al.* A Broadly Neutralizing Antibody Targets the Dynamic HIV Envelope Trimer Apex via a Long , Rigidified , and Anionic b -Hairpin Structure. *Immunity* **46**, 690–702 (2017).

95. Walker, L. M. *et al.* Broad and potent neutralizing antibodies from an African donor reveal a new HIV-1 vaccine target. *Science* **326**, 285–289 (2009).

96. Mclellan, J. S. *et al.* Structure of HIV-1 gp120 V1/V2 domain with broadly neutralizing antibody PG9. *Nature* (2011) doi:10.1038/nature10696.

97. Pan, J., Peng, H., Chen, B. & Harrison, S. C. Cryo-EM Structure of Full-length HIV-1 Env Bound With the Fab of Antibody PG16. *J. Mol. Biol.* **432**, 1158–1168 (2020).

98. Shingai, M. *et al.* Antibody-mediated immunotherapy of macaques chronically infected with SHIV suppresses viraemia. *Nature* **503**, 277–280 (2013).

99. Gristick, H. B. *et al.* Natively glycosylated HIV-1 Env structure reveals new mode for antibody recognition of the CD4-binding site. *Nat. Struct. Mol. Biol.* **23**, 906–915 (2016).

100. Huang, J. *et al.* Broad and potent HIV-1 neutralization by a human antibody that binds the gp41-gp120 interface. *Nature* **515**, 138–142 (2014).

101. Wu, X. *et al.* Rational design of envelope identifies broadly neutralizing human monoclonal antibodies to HIV-1. *Science* **329**, 856–861 (2010).

102. Reynolds, L. M., Henneberry, G. O. & Baker, B. E. Studies on Casein. II. The

Carbohydrate Moiety of Casein. *J. Dairy Sci.* **42**, 1463–1471 (1959).

103. Tropea, E. Kifunensine , a Potent Inhibitor Mannosidase I * of the Glycoprotein Processing. *J. Biol. Chem* **265**, 15599–15605 (1990).

104. Li, W. *et al.* High Potency of a Bivalent Human V(H) Domain in SARS-CoV-2 Animal Models. *Cell* **183**, 429-441.e16 (2020).

105. Li, W. *et al.* Rapid identification of a human antibody with high prophylactic and therapeutic efficacy in three animal models of SARS-CoV-2 infection. *Proc. Natl. Acad. Sci.* **117**, 29832 LP – 29838 (2020).

106. Barnes, C. O. *et al.* SARS-CoV-2 neutralizing antibody structures inform therapeutic strategies. *Nature* **588**, 682–687 (2020).

107. Piccoli, L. *et al.* Mapping Neutralizing and Immunodominant Sites on the SARS-CoV-2 Spike Receptor-Binding Domain by Structure-Guided High-Resolution Serology. *Cell* **183**, 1024-1042.e21 (2020).

108. McCallum, M. *et al.* N-terminal domain antigenic mapping reveals a site of vulnerability for SARS-CoV-2. *Cell* **184**, 2332-2347.e16 (2021).

109. Bianchi, M. *et al.* Electron-Microscopy-Based Epitope Mapping Defines Specificities of Polyclonal Antibodies Elicited during HIV-1 BG505 Envelope Trimer Immunization. *Immunity* **49**, 288-300.e8 (2018).

110. Chi, X. *et al.* A neutralizing human antibody binds to the N-terminal domain of the Spike protein of SARS-CoV-2. *Science (80-.).* **369**, 650 LP – 655 (2020).

111. Wu, Y. *et al.* A noncompeting pair of human neutralizing antibodies block COVID-19

virus binding to its receptor ACE2. *Science (80-.).* **368**, 1274 LP – 1278 (2020).

112. Zhou, D. *et al.* Structural basis for the neutralization of SARS-CoV-2 by an antibody from a convalescent patient. *Nat. Struct. Mol. Biol.* **27**, 950–958 (2020).

113. Kim, C. *et al.* A therapeutic neutralizing antibody targeting receptor binding domain of SARS-CoV-2 spike protein. *Nat. Commun.* **12**, 288 (2021).

114. Lauring, A. S. & Hodcroft, E. B. Genetic Variants of SARS-CoV-2-What Do They Mean? *JAMA* **325**, 529–531 (2021).

115. Davies, N. G. *et al.* Estimated transmissibility and impact of SARS-CoV-2 lineage B.1.1.7 in England. *Science (80-.).* **372**, eabg3055 (2021).

116. Gu, H. *et al.* Adaptation of SARS-CoV-2 in BALB/c mice for testing vaccine efficacy. *Science (80-.).* **369**, 1603–1607 (2020).

117. Starr, T. N. *et al.* Deep Mutational Scanning of SARS-CoV-2 Receptor Binding Domain Reveals Constraints on Folding and ACE2 Binding. *Cell* **182**, 1295-1310.e20 (2020).

118. Martinez, C. R. & Iverson, B. L. Rethinking the term “pi-stacking”. *Chem. Sci.* **3**, 2191–2201 (2012).

119. Wang, P. *et al.* Antibody resistance of SARS-CoV-2 variants B.1.351 and B.1.1.7. *Nature* **593**, 130–135 (2021).

120. Collier, D. A. *et al.* Sensitivity of SARS-CoV-2 B.1.1.7 to mRNA vaccine-elicited antibodies. *Nature* **593**, 136–141 (2021).

121. Laffeber, C., de Koning, K., Kanaar, R. & Lebbink, J. H. G. Experimental Evidence for Enhanced Receptor Binding by Rapidly Spreading SARS-CoV-2 Variants. *J. Mol. Biol.*

433, 167058 (2021).

122. Liu, H. *et al.* The basis of a more contagious 501Y.V1 variant of SARS-CoV-2. *Cell Res.* **31**, 720–722 (2021).

123. CDC. SARS-CoV-2 Variant Classifications and Definitions. SARS-CoV-2 Variant Classifications and Definitions (2021).

124. CDC. Science Brief: Emerging SARS-CoV-2 Variants. https://www.cdc.gov/coronavirus/2019-ncov/science/science-briefs/scientific-brief-emerging-variants.html (2021).

125. FDA. Genetic Variants of SARS-CoV-2 May Lead to False Negative Results with Molecular Tests for Detection of SARS-CoV-2 - Letter to Clinical Laboratory Staff and Health Care Providers. https://www.fda.gov/medical-devices/letters-health-care-providers/genetic-variants-sars-cov-2-may-lead-false-negative-results-molecular-tests-detection-sars-cov-2 (2021).

126. Moore, J. P. & Offit, P. A. SARS-CoV-2 Vaccines and the Growing Threat of Viral Variants. *JAMA* **325**, 821–822 (2021).

127. Tortorici, M. A. *et al.* Ultrapotent human antibodies protect against SARS-CoV-2 challenge via multiple mechanisms. *Science (80-.).* **370**, 950 LP – 957 (2020).

128. Lazarevic, I., Pravica, V., Miljanovic, D. & Cupic, M. Immune Evasion of SARS-CoV-2 Emerging Variants: What Have We Learnt So Far? *Viruses* vol. 13 (2021).

129. Chen, R. E. *et al.* Resistance of SARS-CoV-2 variants to neutralization by monoclonal and serum-derived polyclonal antibodies. *Nat. Med.* **27**, 717–726 (2021).

130. Dejnirattisai, W. *et al.* Antibody evasion by the P.1 strain of SARS-CoV-2. *Cell* **184**, 2939-2954.e9 (2021).

131. Liu, Z. *et al.* Identification of SARS-CoV-2 spike mutations that attenuate monoclonal and serum antibody neutralization. *Cell Host Microbe* **29**, 477-488.e4 (2021).

132. Wang, P. *et al.* Increased resistance of SARS-CoV-2 variant P.1 to antibody neutralization. *Cell Host Microbe* **29**, 747-751.e4 (2021).

133. Wibmer, C. K. *et al.* SARS-CoV-2 501Y.V2 escapes neutralization by South African COVID-19 donor plasma. *Nat. Med.* **27**, 622–625 (2021).

134. Yuan, M. *et al.* Structural and functional ramifications of antigenic drift in recent SARS-CoV-2 variants. *Science (80-.).* eabh1139 (2021) doi:10.1126/science.abh1139.

135. Upadhyay, V., Lucas, A., Panja, S. & Mallela, K. M. G. Interplay between protein stability, binding to ACE2 and escape from neutralizing antibodies determines the natural selection of SARS-CoV-2 receptor binding domain variants. *bioRxiv* 2021.05.23.445348 (2021) doi:10.1101/2021.05.23.445348.

136. Wang, R. *et al.* Analysis of SARS-CoV-2 variant mutations reveals neutralization escape mechanisms and the ability to use ACE2 receptors from additional species. *Immunity* (2021) doi:https://doi.org/10.1016/j.immuni.2021.06.003.

137. Yuan, M. *et al.* Structural basis of a shared antibody response to SARS-CoV-2. *Science (80-.).* **369**, 1119 LP – 1123 (2020).

138. Tanaka, S. *et al.* A recombinant 'ACE2 Triple Decoy' that traps and neutralizes SARS-CoV-2 shows enhanced affinity for highly transmissible SARS-CoV-2 variants. *bioRxiv*

2021.03.09.434641 (2021) doi:10.1101/2021.03.09.434641.

139. Zahradník, J. *et al.* SARS-CoV-2 RBD in vitro evolution follows contagious mutation spread, yet generates an able infection inhibitor. *bioRxiv* 2021.01.06.425392 (2021) doi:10.1101/2021.01.06.425392.

140. Shi, R. *et al.* A human neutralizing antibody targets the receptor-binding site of SARS-CoV-2. *Nature* **584**, 120–124 (2020).

141. Ju, B. *et al.* Human neutralizing antibodies elicited by SARS-CoV-2 infection. *Nature* **584**, 115–119 (2020).

142. Wu, N. C. *et al.* An Alternative Binding Mode of IGHV3-53 Antibodies to the SARS-CoV-2 Receptor Binding Domain. *Cell Rep.* **33**, 108274 (2020).

143. Hurlburt, N. K. *et al.* Structural basis for potent neutralization of SARS-CoV-2 and role of antibody affinity maturation. *Nat. Commun.* **11**, 5413 (2020).

144. Liu, L. *et al.* Potent neutralizing antibodies against multiple epitopes on SARS-CoV-2 spike. *Nature* **584**, 450–456 (2020).

145. Banach, B. B. *et al.* Paired heavy and light chain signatures contribute to potent SARS-CoV-2 neutralization in public antibody responses. *bioRxiv* 2020.12.31.424987 (2021) doi:10.1101/2020.12.31.424987.

146. Barnes, C. O. *et al.* Structures of Human Antibodies Bound to SARS-CoV-2 Spike Reveal Common Epitopes and Recurrent Features of Antibodies. *Cell* **182**, 828-842.e16 (2020).

147. Cao, Y. *et al.* Potent Neutralizing Antibodies against SARS-CoV-2 Identified by High-Throughput Single-Cell Sequencing of Convalescent Patients' B Cells. *Cell* **182**, 73-

84.e16 (2020).

148. Watanabe, C., Okiyama, Y., Tanaka, S., Fukuzawa, K. & Honma, T. Molecular recognition of SARS-CoV-2 spike glycoprotein: quantum chemical hot spot and epitope analyses. *Chem. Sci.* **12**, 4722–4739 (2021).

149. Glasgow, A. *et al.* Engineered ACE2 receptor traps potently neutralize SARS-CoV-2. *Proc. Natl. Acad. Sci.* **117**, 28046 LP – 28055 (2020).

150. Chan, K. K. *et al.* Engineering human ACE2 to optimize binding to the spike protein of SARS coronavirus 2. *Science (80-.).* **369**, 1261 LP – 1265 (2020).

151. Fantini, J., Yahi, N., Azzaz, F. & Chahinian, H. Structural dynamics of SARS-CoV-2 variants: A health monitoring strategy for anticipating Covid-19 outbreaks. *J. Infect.* S0163-4453(21)00281–4 (2021) doi:10.1016/j.jinf.2021.06.001.

152. Deng, X. *et al.* Transmission, infectivity, and neutralization of a spike L452R SARS-CoV-2 variant. *Cell* (2021) doi:https://doi.org/10.1016/j.cell.2021.04.025.

153. Motozono, C. *et al.* An emerging SARS-CoV-2 mutant evading cellular immunity and increasing viral infectivity. *bioRxiv* 2021.04.02.438288 (2021) doi:10.1101/2021.04.02.438288.

154. Schreiber, G., Haran, G. & Zhou, H.-X. Fundamental Aspects of Protein−Protein Association Kinetics. *Chem. Rev.* **109**, 839–860 (2009).

155. Laskowski, R. A., Jabłońska, J., Pravda, L., Vařeková, R. S. & Thornton, J. M. PDBsum: Structural summaries of PDB entries. *Protein Sci.* **27**, 129–134 (2018).

156. Harvey, W. T. *et al.* SARS-CoV-2 variants, spike mutations and immune escape. *Nat.*

Rev. Microbiol. **19**, 409–424 (2021).

157. Campbell, F. *et al.* Increased transmissibility and global spread of SARS-CoV-2 variants of concern as at June 2021. *Eurosurveillance* **26**, (2021).

158. Gao, S.-J., Guo, H. & Luo, G. Omicron variant (B.1.1.529) of SARS-CoV-2, a global urgent public health alert! *Journal of medical virology* vol. 94 1255–1256 (2022).

159. Pinto, D. *et al.* Cross-neutralization of SARS-CoV-2 by a human monoclonal SARS-CoV antibody. *Nature* **583**, (2020).

160. Wu, N. C. *et al.* A natural mutation between SARS-CoV-2 and SARS-CoV determines neutralization by a cross-reactive antibody. *PLoS Pathog.* **16**, e1009089 (2020).

161. Yi, C. *et al.* Key residues of the receptor binding motif in the spike protein of SARS-CoV-2 that interact with ACE2 and neutralizing antibodies. *Cell. Mol. Immunol.* **17**, 621–630 (2020).

162. Rogers, T. F. *et al.* Isolation of potent SARS-CoV-2 neutralizing antibodies and protection from disease in a small animal model. *Science* **369**, 956–963 (2020).

163. Yuan, M. *et al.* A highly conserved cryptic epitope in the receptor binding domains of SARS-CoV-2 and SARS-CoV. *Science* **368**, 630–633 (2020).

164. Gobeil, S. M.-C. *et al.* Effect of natural mutations of SARS-CoV-2 on spike structure, conformation, and antigenicity. *Science* **373**, (2021).

165. Cai, Y. *et al.* Structural basis for enhanced infectivity and immune evasion of SARS-CoV-2 variants. *Science* **373**, 642–648 (2021).

166. McCallum, M. *et al.* SARS-CoV-2 immune evasion by the B.1.427/B.1.429 variant of

concern. *Science* **373**, 648–654 (2021).

167. McCallum, M. *et al.* Molecular basis of immune evasion by the Delta and Kappa SARS-CoV-2 variants. *Science (80-.).* **374**, 1621–1626 (2021).

168. Hanke, L. *et al.* A bispecific monomeric nanobody induces spike trimer dimers and neutralizes SARS-CoV-2 in vivo. *Nat. Commun.* **13**, 155 (2022).

169. Sun, D. *et al.* Potent neutralizing nanobodies resist convergent circulating variants of SARS-CoV-2 by targeting diverse and conserved epitopes. *Nat. Commun.* **12**, 4676 (2021).

170. Elbe, S. & Buckland-Merrett, G. Data, disease and diplomacy: GISAID's innovative contribution to global health. *Glob. challenges (Hoboken, NJ)* **1**, 33–46 (2017).

171. Wei, C. *et al.* Evidence for a mouse origin of the SARS-CoV-2 Omicron variant. *J. Genet. Genomics* **48**, 1111–1121 (2021).

172. Sun, Y., Lin, W., Dong, W. & Xu, J. Origin and evolutionary analysis of the SARS-CoV-2 Omicron variant. *J. Biosaf. Biosecurity* **4**, 33–37 (2022).

173. Du, P., Gao, G. F. & Wang, Q. The mysterious origins of the Omicron variant of SARS-CoV-2. *Innovation (Cambridge (Mass.))* vol. 3 100206 (2022).

174. Hastie, K. M. *et al.* Defining variant-resistant epitopes targeted by SARS-CoV-2 antibodies: A global consortium study. *Science* **374**, 472–478 (2021).

175. McCallum, M. *et al.* Structural basis of SARS-CoV-2 Omicron immune evasion and receptor engagement. *Science (80-.).* **375**, 864–868 (2022).

176. Cameroni, E. *et al.* Broadly neutralizing antibodies overcome SARS-CoV-2 Omicron

antigenic shift. *Nature* **602**, 664–670 (2022).

177. VanBlargan, L. A. *et al.* An infectious SARS-CoV-2 B.1.1.529 Omicron virus escapes neutralization by therapeutic monoclonal antibodies. *Nat. Med.* **28**, 490–495 (2022).

178. Xu, Y. *et al.* Structural and biochemical mechanism for increased infectivity and immune evasion of Omicron BA.2 variant compared to BA.1 and their possible mouse origins. *Cell Res.* **32**, 609–620 (2022).

179. Hoffmann, M. *et al.* The Omicron variant is highly resistant against antibody-mediated neutralization: Implications for control of the COVID-19 pandemic. *Cell* **185**, 447-456.e11 (2022).

180. Gawish, R. *et al.* ACE2 is the critical in vivo receptor for SARS-CoV-2 in a novel COVID-19 mouse model with TNF- and IFNγ-driven immunopathology. *Elife* **11**, e74623 (2022).

181. Huang, K. *et al.* Q493K and Q498H substitutions in Spike promote adaptation of SARS-CoV-2 in mice. *eBioMedicine* **67**, (2021).

182. Conceicao, C. *et al.* The SARS-CoV-2 Spike protein has a broad tropism for mammalian ACE2 proteins. *PLOS Biol.* **18**, e3001016 (2020).

183. Iketani, S. *et al.* Antibody evasion properties of SARS-CoV-2 Omicron sublineages. *Nature* **604**, 553–556 (2022).

184. Fisk, J. D., Powell, D. R. & Gellman, S. H. Control of Hairpin Formation via Proline Configuration in Parallel β-Sheet Model Systems. *J. Am. Chem. Soc.* **122**, 5443–5447 (2000).

185. Sun, Z. *et al.* Potent neutralization of SARS-CoV-2 by human antibody heavy-chain variable domains isolated from a large library with a new stable scaffold. *MAbs* **12**, 1778435 (2020).

186. Sun, Z. *et al.* Neutralization of European, South African, and United States SARS-CoV-2 mutants by a human antibody and antibody domains. *bioRxiv* (2021) doi:10.1101/2021.03.22.436481.

187. Huo, J. *et al.* A potent SARS-CoV-2 neutralising nanobody shows therapeutic efficacy in the Syrian golden hamster model of COVID-19. *Nat. Commun.* **12**, 5469 (2021).

188. Yang, Z. *et al.* A non-ACE2 competing human single-domain antibody confers broad neutralization against SARS-CoV-2 and circulating variants. *Signal Transduct. Target. Ther.* **6**, 378 (2021).

189. VanBlargan, L. A. *et al.* A potently neutralizing SARS-CoV-2 antibody inhibits variants of concern by utilizing unique binding residues in a highly conserved epitope. *Immunity* (2021) doi:10.1016/j.immuni.2021.08.016.

190. Hyeseon, C. *et al.* Bispecific antibodies targeting distinct regions of the spike protein potently neutralize SARS-CoV-2 variants of concern. *Sci. Transl. Med.* **0**, eabj5413 (2021).

191. Bertoglio, F. *et al.* A SARS-CoV-2 neutralizing antibody selected from COVID-19 patients binds to the ACE2-RBD interface and is tolerant to most known RBD mutations. *Cell Rep.* **36**, (2021).

192. R., M. D. *et al.* A broadly cross-reactive antibody neutralizes and protects against

sarbecovirus challenge in mice. *Sci. Transl. Med.* **0**, eabj7125 (2021).

193. Jovčevska, I. & Muyldermans, S. The Therapeutic Potential of Nanobodies. *BioDrugs* **34**, 11–26 (2020).

194. Freise, A. C. & Wu, A. M. In vivo imaging with antibodies and engineered fragments. *Mol. Immunol.* **67**, 142–152 (2015).

195. De Vlieger, D., Ballegeer, M., Rossey, I., Schepens, B. & Saelens, X. Single-Domain Antibodies and Their Formatting to Combat Viral Infections. *Antibodies (Basel, Switzerland)* **8**, (2018).

196. M., H. K. *et al.* Defining variant-resistant epitopes targeted by SARS-CoV-2 antibodies: A global consortium study. *Science (80-.).* **0**, eabh2315 (2021).

197. Shaman, J. & Galanti, M. Will SARS-CoV-2 become endemic? *Science (80-.).* **370**, 527–529 (2020).

198. Eguia, R. T. *et al.* A human coronavirus evolves antigenically to escape antibody immunity. *PLOS Pathog.* **17**, e1009453 (2021).

199. Najar, F. Z. *et al.* Future COVID19 surges prediction based on SARS-CoV-2 mutations surveillance. *Elife* **12**, e82980 (2023).

200. Colijn, C. *et al.* The need for linked genomic surveillance of SARS-CoV-2. *Can. Commun. Dis. Rep.* **48**, 131–139 (2022).

201. Greenspoon, L. *et al.* The global biomass of wild mammals. *Proc. Natl. Acad. Sci. U. S. A.* **120**, e2204892120 (2023).

202. Falkenberg, S. *et al.* Experimental Inoculation of Young Calves with SARS-CoV-2.

Viruses vol. 13 (2021).

203. Shi, J. *et al.* Susceptibility of ferrets, cats, dogs, and other domesticated animals to SARS–coronavirus 2. *Science (80-.).* **368**, 1016–1020 (2020).

204. Schlottau, K. *et al.* SARS-CoV-2 in fruit bats, ferrets, pigs, and chickens: an experimental transmission study. *The Lancet Microbe* **1**, e218–e225 (2020).

205. Meekins, D. A. *et al.* Susceptibility of swine cells and domestic pigs to SARS-CoV-2. *Emerg. Microbes Infect.* **9**, 2278–2288 (2020).

206. Kuchipudi, S. V *et al.* Multiple spillovers from humans and onward transmission of SARS-CoV-2 in white-tailed deer. *Proc. Natl. Acad. Sci. U. S. A.* **119**, (2022).

207. Pickering, B. *et al.* Divergent SARS-CoV-2 variant emerges in white-tailed deer with deer-to-human transmission. *Nat. Microbiol.* **7**, 2011–2024 (2022).

208. Sánchez-Morales, L., Sánchez-Vizcaíno, J. M., Pérez-Sancho, M., Domínguez, L. & Barroso-Arévalo, S. The Omicron (B.1.1.529) SARS-CoV-2 variant of concern also affects companion animals . *Frontiers in Veterinary Science* vol. 9 (2022).

209. Oreshkova, N. *et al.* SARS-CoV-2 infection in farmed minks, the Netherlands, April and May 2020. *Euro Surveill. Bull. Eur. sur les Mal. Transm. = Eur. Commun. Dis. Bull.* **25**, (2020).

210. Caserta, L. C. *et al.* White-tailed deer (Odocoileus virginianus) may serve as a wildlife reservoir for nearly extinct SARS-CoV-2 variants of concern. *Proc. Natl. Acad. Sci. U. S. A.* **120**, e2215067120 (2023).

211. Ofek, G. *et al.* Elicitation of structure-specific antibodies by epitope scaffolds. *Proc. Natl.*

Acad. Sci. **107**, 17880–17887 (2010).

212. Hauser, B. M. *et al.* Rationally designed immunogens enable immune focusing following SARS-CoV-2 spike imprinting. *Cell Rep.* **38**, (2022).

213. Tang, J. *et al.* Respiratory mucosal immunity against SARS-CoV-2 after mRNA vaccination. *Sci. Immunol.* **7**, eadd4853 (2022).

214. Afkhami, S. *et al.* Respiratory mucosal delivery of next-generation COVID-19 vaccine provides robust protection against both ancestral and variant strains of SARS-CoV-2. *Cell* **185**, 896-915.e19 (2022).

215. Zhang, Z. *et al.* Potent prophylactic and therapeutic efficacy of recombinant human ACE2-Fc against SARS-CoV-2 infection in vivo. *Cell Discov.* **7**, 65 (2021).

216. Monteil, V. *et al.* Inhibition of SARS-CoV-2 Infections in Engineered Human Tissues Using Clinical-Grade Soluble Human ACE2. *Cell* **181**, 905-913.e7 (2020).

217. Capraz, T. *et al.* Structure-guided glyco-engineering of ACE2 for improved potency as soluble SARS-CoV-2 decoy receptor. *Elife* **10**, e73641 (2021).

218. Xiao, T. *et al.* A trimeric human angiotensin-converting enzyme 2 as an anti-SARS-CoV-2 agent. *Nat. Struct. Mol. Biol.* **28**, 202–209 (2021).

219. Chan, K. K., Tan, T. J. C., Narayanan, K. K. & Procko, E. An engineered decoy receptor for SARS-CoV-2 broadly binds protein S sequence variants. *Sci. Adv.* **7**, eabf1738 (2023).

220. Zhang, L. *et al.* Engineered ACE2 decoy mitigates lung injury and death induced by SARS-CoV-2 variants. *Nat. Chem. Biol.* **18**, 342–351 (2022).

221. Arimori, T. *et al.* Engineering ACE2 decoy receptors to combat viral escapability. *Trends*

Pharmacol. Sci. **43**, 838–851 (2022).

222. Cao, Y. *et al.* Omicron escapes the majority of existing SARS-CoV-2 neutralizing antibodies. *Nature* **602**, 657–663 (2022).

223. Cao, Y. *et al.* Characterization of the enhanced infectivity and antibody evasion of Omicron BA.2.75. *Cell Host Microbe* **30**, 1527-1539.e5 (2022).

224. Matthew, M. *et al.* Structural basis of SARS-CoV-2 Omicron immune evasion and receptor engagement. *Science (80-.).* **375**, 864–868 (2022).

225. Rubin, E. J., Baden, L. R. & Morrissey, S. Audio Interview: Updating and Standardizing Covid-19 Vaccines. *N. Engl. J. Med.* **388**, e21 (2023).

226. Offit, P. A. Bivalent Covid-19 Vaccines — A Cautionary Tale. *N. Engl. J. Med.* (2023) doi:10.1056/NEJMp2215780.

227. Wang, Q. *et al.* Antibody Response to Omicron BA.4–BA.5 Bivalent Booster. *N. Engl. J. Med.* (2023) doi:10.1056/NEJMc2213907.

228. Collier, A. Y. *et al.* Immunogenicity of BA.5 Bivalent mRNA Vaccine Boosters. *N. Engl. J. Med.* (2023) doi:10.1056/NEJMc2213948.

229. Zou, J. *et al.* Neutralization of BA.4–BA.5, BA.4.6, BA.2.75.2, BQ.1.1, and XBB.1 with Bivalent Vaccine. *N. Engl. J. Med.* (2023) doi:10.1056/NEJMc2214916.

230. Moss, P. The T cell immune response against SARS-CoV-2. *Nat. Immunol.* **23**, 186–193 (2022).

231. Riou, C. *et al.* Escape from recognition of SARS-CoV-2 variant spike epitopes but overall preservation of T cell immunity. *Sci. Transl. Med.* **14**, eabj6824 (2023).

232. Motozono, C. *et al.* SARS-CoV-2 spike L452R variant evades cellular immunity and increases infectivity. *Cell Host Microbe* **29**, 1124-1136.e11 (2021).

233. Zhang, H. *et al.* Profiling CD8+ T cell epitopes of COVID-19 convalescents reveals reduced cellular immune responses to SARS-CoV-2 variants. *Cell Rep.* **36**, 109708 (2021).

234. Poloni, C. *et al.* T cell activation induced marker assays in health and disease. *Immunol. Cell Biol.* (2023) doi:10.1111/imcb.12636.

235. Lim, S., Zhang, M. & Chang, T. L. ACE2-Independent Alternative Receptors for SARS-CoV-2. *Viruses* **14**, (2022).

236. Wang, S. *et al.* AXL is a candidate receptor for SARS-CoV-2 that promotes infection of pulmonary and bronchial epithelial cells. *Cell Res.* **31**, 126–140 (2021).

237. Thépaut, M. *et al.* DC/L-SIGN recognition of spike glycoprotein promotes SARS-CoV-2 trans-infection and can be inhibited by a glycomimetic antagonist. *PLOS Pathog.* **17**, e1009576 (2021).

238. Hoffmann, D. *et al.* Identification of lectin receptors for conserved SARS-CoV-2 glycosylation sites. *EMBO J.* **40**, e108375 (2021).

239. Gu, Y. *et al.* Receptome profiling identifies KREMEN1 and ASGR1 as alternative functional receptors of SARS-CoV-2. *Cell Res.* **32**, 24–37 (2022).

240. Zhu, S. *et al.* Genome-wide CRISPR activation screen identifies candidate receptors for SARS-CoV-2 entry. *Sci. China Life Sci.* **65**, 701–717 (2022).

241. Shilts, J. *et al.* LRRC15 mediates an accessory interaction with the SARS-CoV-2 spike

protein. *PLOS Biol.* **21**, e3001959 (2023).

242. Loo, L. *et al.* Fibroblast-expressed LRRC15 is a receptor for SARS-CoV-2 spike and controls antiviral and antifibrotic transcriptional programs. *PLOS Biol.* **21**, e3001967 (2023).

243. Song, J. *et al.* LRRC15 inhibits SARS-CoV-2 cellular entry in trans. *PLOS Biol.* **20**, e3001805 (2022).

244. Daly, J. L. *et al.* Neuropilin-1 is a host factor for SARS-CoV-2 infection. *Science (80-.).* **370**, 861–865 (2020).

245. Liu, J., Lu, F., Chen, Y., Plow, E. & Qin, J. Integrin mediates cell entry of the SARS-CoV-2 virus independent of cellular receptor ACE2. *J. Biol. Chem.* **298**, (2022).

246. Dodero-Rojas, E., Onuchic, J. N. & Whitford, P. C. Sterically confined rearrangements of SARS-CoV-2 Spike protein control cell invasion. *Elife* **10**, e70362 (2021).

247. Marcink, T. C. *et al.* Intermediates in SARS-CoV-2 spike–mediated cell entry. *Sci. Adv.* **8**, eabo3153 (2023).